UNIVERSITY OF SANNIO

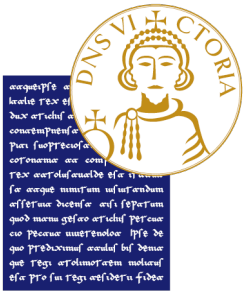

DEPARTMENT OF ENGINEERING

Ph.D. COURSE: "INFORMATION TECHNOLOGY FOR ENGINEERING" – XXXVI CYCLE

Ph.D. THESIS

APPLICATION OF REDUCED-ORDER METHODOLOGIES FOR THE SIMULATION AND OPTIMIZATION OF CHEMICAL PROCESSES FOR THE ENERGY INDUSTRY.

Author

ENRICO ALBERTO CUTILLO

Academic Supervisors:

Prof. GAETANO CONTINILLO

Prof. KATARZYNA BIZON

Ph.D. Program Coordinator

Prof. MASSIMILIANO DI PENTA

A.Y. 2025/2026

Chapter 1
Introduction

1.1 Heterogeneous chemical processes: key applications in the energy industry

This thesis presents a mathematical and simulation framework for the analysis and optimization of chemical processes occurring in heterogeneous systems. The applications examined emphasize relevant and contemporary research areas, such as self-ignition in stocks of flammable materials (Continillo, 1995; Continillo et al., 1996, 2000; Cutillo,Bizon, and Continillo, 2023; Cutillo, Mancusi et al., 2023), reactors for fuel synthesis (Bareschino et al., 2022a; Bizon et al., 2021; Cutillo et al., 2023) and adsorption columns (Cutillo, Neupaer et al., 2025; Gunia et al., 2023). These heterogeneous processes are all non-linear systems. The framework combines both traditional numerical methods and data-driven algorithms to efficiently solve the partial differential equations at the core of engineering problems. A more detailed discussion of the innovative methodology will be presented in Chapter 2 of this thesis.

1.2 Theories of self-heating and self-ignition

Self-ignition, also known as auto-ignition, refers to the phenomenon where a flammable material spontaneously combusts without any external ignition sources, such as a flame or spark. Both biomass and coal piles are characterized by the risks of hazards such as fire, explosions or toxic gas release occurring in combustion plants during storage. Discussions on the topic date back to ancient times; in fact, texts by Latin and Greek authors reports the observation of self-ignition in piles of vegetable materials, even providing remedies to avoid it. The causes were first attributed to friction and heat accumulation (Browne, 1929). In the late 1800s, researchers began to explore the phenomenon from a chemical perspective, relating self-heating to microbial metabolism and low-temperature oxidation or pyrophoricity, which is the tendency of a porous material to self-ignite due to high surface areas that easily come in intimate contact with ambient oxygen (Browne, 1929).

Inside a pile, self-heating due to exothermic phenomena such as low temperature oxidation, moisture adsorption or microbial metabolism can cause temperature rise (Sheng and Yao, 2022a; Zhang et al., 2016a).

The heat released from these reactions, under certain circumstances can exceed the heat dispersed to the ambient, allowing the temperature to reach the critical point of self-ignition.

Due to catastrophic consequences and financial losses, scientists and engineers have tried to study these events to predict them, trying to understand the mechanisms behind them and creating models of the phenomenon. Research into the spontaneous heating of piles of flammable materials has been concerned in literature with three well-defined problems. Those are definition and measurements of reaction rates, measurements of the heat produced by such reactions and establishment and solution of mathematical models describing heat and mass balances inside combustible materials to predict the sudden rise in temperature, to predict the explosion event (Stott, 1960).

1.3 Explosion theory and combustion models

The development of theories around self-heating and spontaneous ignition has seen major advancements through contributions from explosion theory (Frank-Kamenetskii, 2015; Gray and Lee, 1967; Hoff, 1884; Semenov, 1928). Explosion theory focuses on the balance between heat generation from exothermic reactions and heat dissipation to the surroundings. According to the theory, if heat generation exceeds the rate of heat loss, the system may undergo a runaway reaction, leading to self-ignition. Frank-Kamenetskii and Semenov seminal work on thermal explosion theory provides the mathematical framework to model this process through differential equations, considering parameters such as activation energy, material properties, and geometric factors of the storage pile. This theory has laid the groundwork for understanding how changes in pile geometry, material porosity, and environmental conditions influence the likelihood of spontaneous combustion.

1.4 Low-temperature oxidation and microbial influence

Studies on the low-temperature reactions that lead to self-heating emphasize the role of oxidation at sub-critical temperatures, particularly in coal and biomass materials. In coal stockpiles, the process of low-temperature oxidation occurs slowly but steadily, producing heat that accumulates over time. As moisture interacts with coal or biomass, heat is released not only from oxidation, but processes like water adsorption and evaporation can play a crucial role (Carras and Young, 1994). Microbial metabolism is another critical contributor, especially in biomass stockpiles where bacteria and fungi can thrive, producing additional heat through metabolic reactions (Sheng and Yao, 2022a). Biological and chemical processes can overlap, thereby creating a multi-phase heat generation system that has the potential to amplify self-heating to a degree that may ultimately result in auto-ignition, unless appropriate control measures are implemented.

1.5 Prediction and modeling of self-heating

Accurate prediction of self-heating phenomena remains a crucial challenge, particularly in large-scale industrial settings. Many effective methods have been developed to assess materials propensity for spontaneous combustion. They focus on two main factors: the rate of oxidation and the corresponding rate of heat release. Researchers employ models based on classical thermodynamics and kinetics, including the Frank-Kamenetskii theory, to estimate the critical pile size and temperature beyond which self-heating becomes uncontrollable (Carras and Young, 1994; Restuccia et al., 2019). Carras and Young, (1994) further highlight the importance of incorporating heat and mass transfer processes into these models, acknowledging that both natural convection and diffusion play significant roles in how heat accumulates within a coal stockpile. Their work critiques early models for oversimplifying or neglecting these transport processes, which can significantly alter the self-heating behavior of heterogeneous materials like coal. Furthermore, Carras and Young, (1994) underline the need to integrate the effects of moisture on heat generation and dissipation. They review the works of Brooks et al., (1988) and Nordon, (1979), to emphasize the importance of airflow dynamics and the effect of moisture in influencing the piles internal heat generation and how these factors could lead to ignition. In particular Nordon, (1979) discusses the need for a comprehensive modelling approach that includes the combined effects of water vapor sorption and oxidation. He highlights that while his model accounts for water vapor sorption, calculations involving both sorption and oxidation were not performed due to the complexity introduced in the resulting differential equations. Nordon, (1979) notes that the inclusion of these effects, especially convection, would require advanced computational methods beyond finite difference techniques, as the computing effort becomes prohibitive with traditional approaches. This complexity of the analysis is due to the highly non-linear nature of the self-combustion phenomenon, as will be pointed out in this paragraph. Therefore, alternative numerical methods need to be explored to accurately simulate the coupled processes. Advances in numerical techniques and computing power allowed researchers to simulate more complex models that consider two-dimensional geometry and the interplay between heat generated by metabolic activity, low-temperature oxidation and geometric factors in a composting pile of sewage sludge (Moraga et al., 2009). Nelson et al., (2007) focused on models for biomass systems, where microbial activity and moisture significantly affect heat accumulation developed a model to account for gas

diffusion, moisture interactions, and microbial kinetics with the aim of improving the accuracy of predictions for self-heating in compost stockpiles. Luangwilai et al., (2010) incorporated air flow and ambient temperature variations in a compost pile self-heating model, further demonstrating the importance of external environmental factors on ignition behavior in porous materials. The recent work of Cutillo et al., (2023) assesses a reaction-diffusion model exploring the effects of variable ambient temperature on self-ignition phenomena, employing parameters characteristic of biomasses. The study presents a reduced-order model (ROM) based on Proper Orthogonal Decomposition (POD) to reduce the computational burden of simulating the complex dynamics of self-ignition under variable temperature conditions, such as daily circadian cycles. This approach accurately reproduces the dynamic behaviors of more computationally intensive traditional models based on finite difference, while significantly reducing the number of state variables, making it practical for real-time control applications. By modeling time-varying boundary conditions, the work of Cutillo et al., (2023) highlights how daily fluctuations in ambient temperature can intensify self-ignition events, an aspect previously underexplored in classical models.

1.6 Self-ignition as a reaction-diffusion non-linear dynamical problem

Another key aspect of interest for predicting the evolution of the self-ignition problems is the study Kaganov, (1967) of the stability of the steady states, which has been a central focus in understanding self-heating and ignition phenomena. Kaganov, (1967) utilized the method of small perturbations to explore steady-state stability in the context of thermal explosions, introducing eigenvalue analysis to determine whether solutions remain stable or transition towards runaway heating. The nonlinear dynamical community has seen an increase in interest in reaction-diffusion and reaction-diffusion-convection problems due to their complex oscillatory and bifurcative behaviors. Matkowsky and Sivashinsky, (1978) demonstrated how oscillatory propagation arises through a Hopf bifurcation in gasless combustion systems, where the transition from a uniformly propagating front to a pulsating one occurs beyond a critical parameter threshold. Such bifurcations are indicative of the complex routes to instability and chaotic behaviour inherent in these systems. The work carried out by Continillo et al., (2000) expanded on these concepts by examining the dynamic characterization of self-ignition models, identifying period-doubling cascades and chaotic attractors through a detailed numerical analysis of reaction-diffusion-convection systems. Their studies revealed how natural convection and mass transport can significantly

affect stability, leading to a variety of dynamic regimes, including steady, periodic, and chaotic behaviours (Continillo, 1995). The application of singularity and degenerate Hopf bifurcation theory, as demonstrated by Luangwilai et al., (2013), has allowed for a deeper understanding of self-heating in biological systems, such as compost piles. The researchers identified regions of parameter space where steady-state solutions are stable and regions where oscillatory or runaway heating may occur. Such bifurcation analyses are crucial for distinguishing between desirable moderate-temperature regimes and hazardous conditions that could lead to spontaneous ignition.

These behaviours of a system characterized by self-heating and auto-ignition are clearly due to the non-polynomial nonlinearity that characterize most problems encountered in process engineering (for example, Arrhenius dependence on temperature of reaction rates, Langmuir-Hinshelwood expressions in catalytic processes and the non-linearity of arbitrary complexity in phase equilibrium models of a fluid) (Adrover et al., 2000). Self-ignition problems are characterized by the Arrhenius temperature dependence of elementary reaction rates, which is strongly non-linear (Gray et al., 1974).

Due to their intrinsic complexity and non-linear characteristics, reaction-diffusion systems, such as the models describing the self-ignition property of stockpiles, often serve as an important "benchmark" problem for the evaluation and advancement of innovative numerical methods.

Several advanced techniques have been developed to solve such infinite dimensional distributed partial differential problems (e.g. reaction-diffusion models), reducing their dimension to that of finite-dimensional system of ordinary differential equation while maintaining high accuracy levels.

One such approach is the inertial manifold theory (IMT), which seeks to approximate infinite-dimensional dynamical systems with finite-dimensional models by filtering out dynamically irrelevant modes. The wavelet-like collocation method uses localized trial functions to efficiently handle non-polynomial nonlinearities, providing a more flexible framework for capturing spatial variations and sharp gradients in self-igniting systems. In a series of works, the authors (Adrover et al., 2000; Russo et al., 2000) introduce this novel methodology to construct an approximate inertial manifold and study the self-ignition problem, comparing the results of this novel technique with classical methods. In the work of Adrover and Giona, (2003) the authors further refined these analyses introducing the

concept of Snapshots Archetypes. With the Snapshots Archetypes approach the system dynamics is projected onto a lower-dimensional space, facilitating the exploration of bifurcation structures and simplifying the study of steady-state solutions and oscillatory instabilities in a self-ignition model of coal stockpile. In the last decades, modal reduction strategies based on Proper Orthogonal Decomposition (POD) have become increasingly prominent (Bizon, 2010). This approach effectively reduces the dimensionality by identifying dominant modes that capture most the system energy and dynamics. For instance, Cutillo et al., (2023) demonstrated how combining POD with the Discrete Empirical Interpolation Method (DEIM) yields reduced-order models (ROMs) that capture complex behaviours, such as bifurcations and oscillations, in reaction-diffusion systems. The integration of DEIM addresses the computational challenges posed by non-linearities, while a k-means clustering-based snapshot selection further enhances the ROM accuracy and robustness. This methodological innovation enables a substantial reduction in computational time — up to 1020 times in some cases — without sacrificing the fidelity of the model in replicating bifurcation points and other critical feature. The relevance of these reduced-order models to the study of self-ignition is profound. By preserving the critical dynamics while simplifying the system's complexity, these models facilitate more in-depth analysis of the intricate processes driving self-ignition, such as low-temperature oxidation and variable ambient conditions. Furthermore, they provide practical advantages in real-time monitoring, control applications, and safety analysis, enabling researchers to explore parameter spaces and identify critical thresholds for ignition with greater efficiency. Consequently, the ongoing refinement of such modal reduction techniques underscores the synergy between advanced numerical methods and the study of self-ignition phenomena, advancing both theoretical understanding and practical safety measures. More details on these techniques and practical examples will be given both for self-ignition systems and fixed bed reactors during this thesis.

1.7 Introduction to fuel synthesis technologies

Fuel synthesis technologies have emerged as a cornerstone of the energy transition, offering viable pathways toward a carbon-neutral economy. These processes are particularly relevant in Power-to-X applications, where renewable electricity is converted into chemical fuels such as hydrogen, methane, methanol, and dimethyl ether (DME) (Dell'Aversano et al., 2024). Their strategic importance lies in their ability to provide long-term energy storage,

enhance grid flexibility, and enable carbon capture and utilization (CCU), thereby supporting the decarbonization of hard-to-abate sectors like aviation, shipping, and heavy industry (Colelli et al., 2026).

Fixed-bed reactors, among the most widely used configurations in fuel synthesis, are central to these technologies due to their simplicity, scalability, and efficiency in catalytic conversion (Levenspiel, 1998). However, the highly exothermic nature of many fuel synthesis reactions introduces significant challenges in terms of thermal management and process stability (Azizi et al., 2014). Although these reactions are governed by chemical equilibrium, they are not immune to dynamic instabilities or sudden temperature fluctuations, which can compromise reactor performance and safety (Bareschino et al., 2022a).

This aspect draws a compelling parallel with combustion systems, where runaway reactions and auto-ignition phenomena pose similar risks (Cutillo et al., 2023). In both cases, accurate modeling and control strategies are essential to predict and mitigate hazardous behavior, as will be shown in Chapter 5 of this thesis. The integration of advanced numerical techniques, such as reduced-order modeling (ROM), plays a crucial role in addressing these challenges (Cutillo et al., 2023). By simplifying complex reactor dynamics while preserving critical features, ROMs enable real-time simulation, optimization, and control, making them indispensable tools for the safe and efficient operation of fuel synthesis reactors in modern energy systems (Bizon and Continillo, 2020).

1.8 Technological landscape of fuel synthesis reactors

Fuel synthesis encompasses a wide range of reactor technologies; each tailored to specific chemical pathways and operational requirements. Among these, fixed-bed reactors stand out for their simplicity, scalability, and cost-effectiveness (Levenspiel, 1998). They are widely used in both laboratory and industrial settings, particularly for catalytic processes involving low to moderate heat release. In a typical fixed-bed configuration, a gaseous reactant flows through a packed column containing porous solid catalyst particles, facilitating efficient contact and reaction. The high surface-to-volume ratio of the catalyst enhances conversion rates, making fixed beds a preferred choice for many fuel synthesis applications (Bischoff, 1967).

However, fixed-bed reactors face limitations when dealing with highly exothermic reactions. Their inherently low thermal conductivity can lead to the formation of hot spots, risking

catalyst sintering and process instability. To mitigate these issues, advanced designs such as multi-tubular reactors with enhanced cooling surfaces or moving-bed configurations are employed. These alternatives retain the plug-flow characteristics of fixed beds while offering improved thermal management and catalyst regeneration capabilities (Levenspiel, 1998).

Slurry-phase reactors represent another class of fuel synthesis technology, particularly suitable for processes like direct dimethyl ether (DME) synthesis. These reactors operate with three phases: gas bubbles dispersed in a liquid solvent that suspends the solid catalyst. The solvent's high heat capacity allows for better temperature control, but mass transfer limitations between phases can reduce overall reaction rates. Additionally, slurry systems require complex auxiliary equipment, such as solvent recycling units and gas-liquid separators, which increase operational complexity (Azizi et al., 2014).

Fluidized-bed reactors offer a dynamic alternative, especially for fast and highly exothermic reactions. In these systems, solid catalyst particles are suspended by an upward flow of gas, creating a fluid-like behavior. This configuration enhances heat and mass transfer, reduces temperature gradients, and allows for quasi-isothermal operation. Fluidized beds are particularly advantageous for processes requiring precise thermal control or rapid reaction kinetics. However, they also pose challenges in terms of reactor design, particle attrition, and gas-solid separation, necessitating higher capital investment and sophisticated control strategies (Ray et al., 1987).

Micro-structured reactors, a more recent innovation, utilize sub-millimeter channels to achieve exceptional heat and mass transfer rates. Their compact design and high surface-to-volume ratio make them ideal for both exothermic and endothermic reactions. Microreactors offer precise control over reaction conditions and can be easily scaled through parallelization, making them attractive for modular fuel synthesis systems (Hayer et al., 2011).

Each reactor type presents a unique set of trade-offs between efficiency, scalability, thermal control, and operational complexity. As fuel synthesis technologies evolve to meet the demands of a renewable energy future, the integration of advanced reactor designs with robust modeling and control frameworks becomes increasingly essential.

1.9 Catalysts in fuel synthesis: functionality, design, and impact

Catalysts play a central role in fuel synthesis processes, enabling chemical transformations that would otherwise be too slow or inefficient under technologically and economically

sustainable operating conditions (Levenspiel, 1998). In heterogeneous catalysis, reactions occur on the surface of solid materials, where the catalyst facilitates the conversion of reactants into desired products without being consumed in the process. The effectiveness of a catalyst is primarily determined by two key properties: activity, which reflects its ability to accelerate reaction rates, and selectivity, which ensures that the reaction pathway favors the formation of specific target compounds (Levenspiel, 1998).

Industrial catalysts are typically engineered to operate under high temperatures and pressures, and their performance is closely linked to their physical structure. Porous pellets with high surface area are commonly used to maximize contact between the gas phase and the catalytic surface. Parameters such as surface area (expressed in m^2/g), particle porosity, pore volume, and pore size distribution are critical in defining the efficiency of a catalyst. Pellet shape and size also influence reactor performance, affecting pressure drop, flow dynamics, and mass transfer rates.

In fuel synthesis, particularly in the production of methanol and dimethyl ether (DME), bifunctional catalysts are often employed. These combine a metallic function - typically copper-based compounds such as $CuO\text{-}ZnO\text{-}Al_2O_3$ (CZA) - for methanol synthesis, with a solid-acid function - such as $\gamma\text{-}Al_2O_3$ or zeolites like H-ZSM-5-for methanol dehydration to DME. The integration of these functionalities can occur at both the reactor and pellet level, allowing for process intensification and improved efficiency. In direct DME synthesis, for example, the proximity of the two catalytic sites enhances reaction rates and reduces intermediate losses (Guffanti et al., 2020, 2021).

Despite their advantages, catalysts are subject to deactivation mechanisms, including sintering, poisoning, and structural changes due to temperature fluctuations. For instance, $\gamma\text{-}Al_2O_3$, while cost-effective and thermally stable, exhibits hydrophilic behavior that can negatively impact performance in CO_2-rich feeds by promoting the reverse water-gas shift reaction and generating excess water. This underscores the importance of careful catalyst selection and reactor design, especially when dealing with renewable feedstocks and dynamic operating conditions.

Advanced reactor configurations, such as adsorptive reactors, further enhance catalyst performance by integrating adsorption and reaction functionalities. These systems allow for in-situ removal of by-products like water or CO_2, shifting reaction equilibria and improving yield (Mancusi et al., 2025). The development of optimal distribution of functional sites such

as catalyst or adsorbent within the pellet or the reactor, tailored to enhance performance - adds another layer of control, enabling precise manipulation of reactors behavior as will be shown in Chapter 4 of this thesis (Cutillo et al., 2025; Grünewald and Agar, 2004).

As fuel synthesis technologies evolve, the role of catalysts becomes increasingly intertwined with reactor design, process control, and modeling strategies. Understanding the interplay between catalyst properties and reactor behavior is essential for optimizing performance, ensuring stability, and achieving the high selectivity and conversion rates required for sustainable fuel production.

1.10 Numerical modeling and reduced-order methods in Fuel Synthesis

Fuel synthesis reactors, particularly those involving heterogeneous catalysis, are governed by complex physical and chemical phenomena, including reaction kinetics, heat and mass transfer, and dynamic interactions between phases. Accurately capturing these behaviors requires detailed mathematical models, often formulated as systems of partial differential equations (PDEs). While high-fidelity models provide valuable insights into reactor performance, they are computationally intensive and often impractical for real-time simulation, optimization, or control-especially under dynamic operating conditions typical of renewable energy integration (Bremer et al., 2017a; Zimmermann et al., 2022a).

To address these challenges, reduced-order modeling (ROM) techniques have gained prominence. These methods aim to simplify complex models by projecting the system dynamics onto a lower-dimensional space, preserving essential features while significantly reducing computational cost. Among the most widely used ROM approaches are Proper Orthogonal Decomposition (POD) and the Discrete Empirical Interpolation Method (DEIM), which will be introduced in Chapter 2 of this thesis. POD identifies dominant modes that capture most of the system energy and behavior, while DEIM efficiently approximates nonlinear terms, enabling fast and accurate simulations (Chaturantabut and Sorensen, 2010).

In the context of fuel synthesis, ROMs have been successfully applied to fixed-bed reactors, where temperature control and reaction stability are critical (Cutillo et al., 2023). For example, in CO_2 methanation via the Sabatier reaction-a highly exothermic process-ROMs allow for the prediction and management of hot spots, enabling safer and more efficient reactor operation. Reduced-order models facilitate the optimization of reactor design and

operating conditions, accounting for the interplay between catalytic activity, heat transfer, and mass diffusion (Bizon et al., 2021; Bizon and Continillo, 2020).

These approaches are useful even in capturing bifurcation phenomena, oscillatory instabilities, and dynamic transitions, which are common in both combustion and catalytic systems (Cutillo, Bizon and Continillo, 2023; Cutillo, Mancusi et al., 2023). The ability to simulate such behaviors with reduced computational effort is essential for developing robust control strategies and ensuring process safety.

Moreover, ROMs support flexible operation, a key requirement for Power-to-X technologies that rely on intermittent renewable energy sources. By enabling fast simulations, these models allow for real-time adjustments in reactor conditions, facilitating start-ups, shut-downs, and load-following capabilities (Bremer et al., 2017a; Zimmermann et al., 2022a). This adaptability is crucial for integrating fuel synthesis processes into modern energy infrastructures, where responsiveness and efficiency are crucial.

In summary, reduced-order modeling represents a powerful tool for advancing fuel synthesis technologies. By bridging the gap between detailed physical models and practical engineering applications, ROMs enhance our ability to design, optimize, and control reactors under complex and variable conditions-ultimately contributing to the development of safer, more efficient, and more sustainable energy systems.

1.11 Brief outlook and scope of the thesis

The transition toward sustainable energy systems and carbon-neutral processes requires advanced modeling tools capable of accurately describing complex reactive and adsorptive systems. In this context, methane reactors for CO_2 methanation and hybrid adsorption-reaction systems represent promising technologies for carbon capture, utilization, and energy storage. However, their strongly nonlinear behavior, coupled mass and heat transport phenomena, and the possible occurrence of multiple steady states or oscillatory regimes make their numerical simulation and optimization computationally demanding.

This thesis addresses these challenges through the development and application of reduced order modeling (ROM) methodologies for the efficient simulation and optimization of heterogeneous chemical systems. The core focus of the research is the application of reduced-order modeling techniques based on empirical functional basis representations to problems characterized by high-dimensional systems of Ordinary Differential Equations (ODEs), which arise from the discretization of the underlying Partial Differential Equations

(PDEs). The problems and their solution through innovative methodologies are reported in Chapter 4 and 5 of this thesis, while Chapter 1, 2 and 3 include an introduction to the background, the mathematical models and the innovative methodologies applied in the thesis.

By combining Proper Orthogonal Decomposition (POD) and Discrete Empirical Interpolation Method (DEIM), the work demonstrates that high dimensional models are reduced while preserving their essential physical and dynamical features. The proposed approaches significantly decrease computational cost, enabling accurate prediction of stationary, periodic, and bifurcation behaviors in methane reactors, as well as facilitating optimization studies in non-isothermal reactors.

In addition to model-order reduction, the thesis explores the integration of data-driven surrogate models for multicomponent adsorption isotherms, which poses the basis for a hybrid modeling framework suitable for cyclic CO_2 capture and methanation processes. Overall, the research provides methodological advancements and practical tools that support efficient simulation, optimization, and control-oriented applications of complex reactive systems, contributing to the optimal design of energy conversion and carbon management technologies.

Moreover, the thesis advances the modeling of self-ignition phenomena in reaction-diffusion systems. Reduced-order models based on POD and POD-DEIM successfully reproduce complex oscillatory and bifurcation behaviors while reducing the dimensionality of the system by orders of magnitude. The incorporation of DEIM proves particularly effective in lowering the computational burden associated with nonlinear terms, enabling speedups exceeding three orders of magnitude in two-dimensional simulations.

These achievements demonstrate the robustness and versatility of the reduced-order model approach in both process design and safety-oriented analyses.

Chapter 2
Mathematical framework

2.1 Introduction to data-driven models

Real word physical problems are approximated accurately by numerical simulations of deterministic models, also known as mechanistic models, first-principles, white-box or phenomenological models, but requiring huge computing costs. To mitigate the computing cost, data-driven models, also called metamodels, surrogates, response surfaces, emulators or model-of-the-model, have gained great attention (Liu et al., 2018). The following chapter aims to explain the different data-driven methodologies employed in this thesis. Starting from a state of the art of the most important ones, followed by an in-depth formalization of the methodologies chosen and applied in this thesis. In particular, this thesis will focus on the application of data-driven methodologies such as Proper Orthogonal Decomposition (POD) to reduce the dimension of ordinary differential equations (ODEs) systems (Lu et al., 2019), and on response surface methodology based on Kriging to build fast and accurate data driven models (Forrester et al., 2008a). In addition, a series of case studies in the field of process engineering applied to renewable energy will be presented to demonstrate the effectiveness of these methodologies. It is important to note that the reported methodologies can be of heuristic nature in the sense that there is not a demonstrated way of building an optimal data-driven model and no strategy always outperforms the others, as reported in the work of (Liu et al., 2018). Nevertheless, their ability to reduce the complexity of a deterministic model, combined with the availability of huge amount of data, makes it possible to build such powerful tools that are nowadays pervasively used in the industry 4.0 sector (Tezzele et al., 2022).

2.2 Reduced-order models

Model reduction techniques can be broadly classified into conceptual approaches, which rely upon the physical interpretation of the system, and purely mathematical, numerical, and data-driven techniques. The first concept related to model reduction involves simplifying a detailed model based on physical principles, leading to the development of an approximate model or a sequence of interrelated simplified sub-models that adequately represent the system's states and dynamics. This process is known as physical reduction. Alternatively, or in addition, numerous formal mathematical methodologies have been developed to reduce the dimensionality of large-scale systems (Theodoropoulos, 2011).

In the case of mathematics-based reduction of mechanistic models, data of simulation origin are used to construct light yet robust numerical reduced-order models (ROMs) while preserving all the physics of the problem. Such ROMs are also called white-box data-driven reduced-order or super-reduced models (Bizon, 2023). When dealing with mechanistic models of engineering systems the mathematical formulation commonly takes the form of partial differential equations (PDEs). To address the solution of such infinite-dimensional mathematical models, they are, in most practical cases, reduced to a finite-dimensional form, such as systems of algebraic or ordinary differential equations. This is typically done with numerical approaches, such as the finite difference or finite volume methods, which can be seen as a model order reduction step from the infinite-dimensional PDEs system. Accurate solutions require the introduction of a fine grid discretization that results in high-dimensional and computationally onerous discretized models (Grossmann et al., 2007). To create simulation tools that are both computationally efficient and accurate, it is necessary to further reduce these high-dimensional discretized models. Therefore, in the literature, the term model-order reduction is commonly used rather to describe a broad class of techniques for obtaining low-dimensional approximations of the high-dimensional model (Bizon, 2023). One of the main advantages of reduced-order models compared to statistical data-fitting models is their explicit preservation of the underlying structure of high-fidelity numerical models, such structure in turns is grounded in physical principles (Kramer et al., 2024). Many of these purely mathematical model-order reduction techniques rely on projection methods.

All projection-based model order reduction (MOR) techniques aim to approximate the high-dimensional state space vector $\mathbf{u}(t) \in \mathbb{R}^n$ using a reduced-dimension vector $\mathbf{c}(t) \in \mathbb{R}^r$, where $r \ll n$. In the following, some of the most used techniques of projection-based model reduction of linear systems will be briefly introduced (Antoulas et al., 2015).

Krylov-based methods in MOR are based on a series expansion of the matrix-valued transfer function of the system. The idea is to construct a reduced-order model such that the series expansions of the reduced-order model transfer function and the original transfer function agree to a certain index of summation (e.g. $k = 1, \dots, q,\ q \in \mathbb{N}$). This is verified when the first moments of the series expansion are equal in both models (Antoulas et al., 2015).

Balanced truncation is perhaps one of the most popular projection-based model reduction schemes. The method was introduced in the work of Moore, (1981) and involves two main

steps. First, a variable transformation is applied to ensure that each state of the system is equally observable and controllable. Second, the states that exhibit a very weak relationship between the input and the output are truncated (Dones et al., 2011).

A combination of proper orthogonal decomposition (POD) and Galërkin projection has been used for decades to obtain reduced-order models. The POD technique was, in fact, proposed by Pearson in 1901, and depending on the field of application it is also known as Karhunen-Loéve (KL) decomposition (Karhunen, 1946; Loéve, 1945), principal component analysis (PCA) or Hotelling transformation (Hotelling, 1933). After its formulation, the method was rarely used because it required extensive calculations to determine the POD bases. It was reproposed in the 1940's independently by different mathematicians including Kosambi, (1943). A significant turning point in this regard was the introduction of the snapshot method, proposed by Sirovich in 1987. In combination with Galërkin projection this technique can be viewed as an empirically based spectral method (Lucia et al., 2004). Since the POD based reduced-order modeling is the one employed in this thesis to derive efficient data-driven models, more details are presented in the subsequent paragraphs.

More recent evolutions of the POD method include dynamic mode decomposition (DMD) (Schmid, 2010) and non-intrusive POD through operator inference (Peherstorfer and Willcox, 2016).

Operator inference is a technique designed to obtain reduced-order models directly from data, without the need to have direct access to the equations that constitute the discretized model. (Peherstorfer and Willcox, 2016). One of the major advantages of non-intrusive techniques is their ability to utilize data from obtained with computational fluid dynamics simulators, where the discretized equations are not readily available, or to employ data directly from experiments (Kramer et al., 2024). Among the non-intrusive techniques is dynamic mode decomposition (DMD), which is used for reducing complex dynamical models (Schmid, 2010). This method combines spatial-dimensionality reduction techniques like POD with Fourier transforms over time to create an optimum solution. By performing an eigen decomposition on a linear operator that best fits the data, this process allows to advance the measurements forward in time and helps in identifying important time-dependent features of the system (Brunton and Kutz, 2021). A much more challenging topic is model order reduction of nonlinear systems. In this context, model reduction techniques based on POD effectively handle nonlinearities, although also other projection techniques

have been modified to address nonlinearities. Recent advancements in this area will be discussed in a following paragraph.

2.2.1 Proper Orthogonal Decomposition - methodology fundamentals

The mathematical framework of POD lies in the solution of an optimization problem. The problem can be seen as building a set of basis functions $\varphi(x)$ such that the average squared error between the analyzed scalar field $u(x)$ and its projection into the subspace spanned by such basis is minimized. In a mathematical formulation, it is:

$$\min_{\varphi \in L^2} \left\langle \left\| u - \frac{(u,\varphi)}{\|\varphi\|^2}\varphi \right\|^2 \right\rangle \tag{2.1}$$

The aim is to obtain a finite-dimensional representation (i.e. an approximation or truncation) of the scalar vector $u(x)$ that is better approximation that can be obtained with any other basis. This problem can be seen as the maximization of the averaged projection of u onto φ with the constraint that $\|\varphi\|^2 = 1$, which means that the bases are orthonormal. It can be demonstrated (Holmes et al., 1996) that the solution to this minimization problem, in a continuous domain, reduces to the solution of the following integral eigenvalue problem:

$$\int_0^1 \langle (u(x)u*(x')) \rangle \, \varphi(x')dx' = \lambda\varphi(x) \tag{2.2}$$

where $\langle u(x)u(x') \rangle \triangleq R(x,x')$ is the averaged autocorrelation non-negative function. The optimal bases are the eigenfunctions obtained solving Eq. (2.2).

In practice, in the following thesis the aim is to reduce the dimension of ODEs system or system of nonlinear equations arising from the spatial discretization of initial/boundary value problems (IBVP). Therefore, dealing with a discretized domain, the derivation of the integral eigenvalue problem (2.2) can be generalized to functions of more than one variable and to vector-valued functions $\mathbf{u}(\mathbf{x},\boldsymbol{m})$, where $\mathbf{x}$ is the space variables vector, and $\boldsymbol{m}$ is a set of parameters (which could be physical parameters or time). The autocorrelation function can be replaced by the autocorrelation matrix:

$$\boldsymbol{C}(\boldsymbol{x},\boldsymbol{y}) = \frac{1}{M}\sum_{i=1}^{M} \boldsymbol{u}(\boldsymbol{x},\mu_i)\boldsymbol{u}^T(\boldsymbol{y},\mu_i) \tag{2.3}$$

or, in matrixial notation: $C = \frac{1}{M} UU^T$, where **U** is a matrix containing numerical solutions of the IBVP. The columns of the matrix **U** contain the state variable vectors of the discretized system $\boldsymbol{u}$, solved for a given value (or range of values) of the parameter space $(\mu_1 \dots \mu_M)$:

$$\mathbf{U} = [u_1(\mu_1) \cdots u_1(\mu_M) \vdots \ddots \vdots u_N(\mu_1) \cdots u_N(\mu_M)] \tag{2.4}$$

where *N* is the total number of discretization nodes.

Meanwhile, the integral eigenvalue problem given by Eq. (2.2) can be replaced by the eigenvalue problem:

$$\boldsymbol{C\Phi} = \boldsymbol{\Lambda\Phi} \tag{2.5}$$

where $\boldsymbol{\Phi}$, the eigenvectors of the matrix **C**, are the sought for set of basis functions, and $\boldsymbol{\Lambda}$ is the set of eigenvalues of **C**. The ordering of the computed eigenvalues from the largest to the smallest induces an ordering of the corresponding eigenvectors, i.e. the POD basis functions, from the most to the least important (Bizon et al., 2012a).

2.2.2 POD with Time series as Snapshots

For the construction of a Reduced-Order Model consider the general system of partial differential equations:

$$\frac{\partial \boldsymbol{u}(x,t)}{\partial t} = L\boldsymbol{u}(x,t) + \boldsymbol{f}\big(t, u(x,t)\big) \tag{2.6}$$

with boundary and initial conditions defined as

$$\boldsymbol{g}(\boldsymbol{u}(x,t)) = 0 \qquad x \in \partial\Omega \qquad t \geq 0 \tag{2.7}$$

$$\boldsymbol{u}(x,0) = \boldsymbol{u_0} \qquad x \in \Omega \tag{2.8}$$

where $\boldsymbol{u}$ is a function of a spatial coordinate *x* and time *t*, and *L* is a linear operator containing derivatives with respect to spatial variables x. Here *f* is the nonlinear term, and Ω and $\partial\Omega$ are respectively the domain and the border of the domain where the problem is defined. After spatial discretization, for example by finite differences, the following problem is obtained:

$$\frac{d}{dt}u(t) = Au(t) + F\big(t, u(t)\big) \tag{2.9}$$

$$u(0) = u_0 \tag{2.10}$$

The system of Equations (2.9-2.10) is solved by a suitable time integrator, for example with a variable-step, variable-order (VSVO) solver (Shampine and Reichelt, 2006). The set of solutions at time t_i are the snapshots $\mathbf{u}_i$ for the construction of the empirical basis. The solutions do not need to be equidistant, and in fact it is possible to employ only the most informative solutions by dividing them into clusters and employing the centroids of such clusters (Cutillo, Bizon and Continillo, 2023). In this case, it is possible to consider different time series for the construction of the snapshot matrix (Ullmann et al., 2014), and in fact the obtained solutions are collected as the columns of the snapshots matrix **U** (Eq. (2.4)).

2.2.3 Galërkin Projection

The Galërkin Projection method belongs to the groups of spectral methods. Such methods permit solving the problem of finding the best approximation of an unknown function - e.g. *u(x,t)* - that is, in practical cases, a solution to a system of PDEs. Without entering into the details, which are not in the scope of the thesis, and only to give a bigger picture to the reader, it must be said that spectral methods are characterized by test and trial functions. A linear combination of the trial functions offers an approximate representation of the unknown function *u(x,t)*, while test functions help verify that the differential equation and boundary conditions are closely met by the truncated series expansion. Spectral methods employ trial basis functions that span the entire domain of the problem. This approach differs significantly from finite-element or finite-difference techniques, which divide the domain into discrete, smaller sections such as elements or nodes. As a result, the trial basis functions used in finite-element methods, differently from the ones used in spectral methods, are local (Canuto et al., 2006). For example, the collocation method uses a unique set of test functions: shifted Dirac delta functions positioned at specific points called collocation points. This technique demands that the differential equation to be precisely solved at the collocation points (Finlayson, 2013). Meanwhile in the Galërkin (1915) approach, the test functions are the same as the trial functions.

The generic state variable vector **u**, following the Galërkin projection method, can be approximated as a linear combination of orthonormal basis vectors and time dependent coefficients:

$$\boldsymbol{u} \approx \tilde{\boldsymbol{u}} = \sum_{k=1}^{K} \phi_k c_k = \boldsymbol{\Phi}_K \boldsymbol{c}_K \quad \text{with} \quad \boldsymbol{\Phi}_K \in \mathbb{R}^{N \times K} \tag{2.11}$$

A group of applications of spectral methods, such as the Galërkin projection method, involves using empirically derived basis functions, such as those obtained through POD, as tests and trials functions (Bizon, 2010). In this case $\boldsymbol{\Phi}_K$ is the matrix containing the first K basis functions obtained applying the POD, and in particular Eq. (2.5), to an available empirical dataset representative of the variable $\boldsymbol{u}$. In fact, the aim of the approximation described above is to have $K \ll N$.

2.2.4 POD and Reduced-Order Models

In the literature there exist two main areas of applications of the POD methodology and its derivations. One is the analysis of data. In this area the POD is used to extract the coherent structures that emerge in physical phenomena, such as turbulent flows or turbulent reacting flows (Bizon et al., 2010; Holmes et al., 1996). Another area, that was grasped in the present thesis, is model order reduction. The POD methodology is applied for the reduction of the dimensions of numerical models arising from the discretization of partial differential equations, and it can be considered as a data-driven methodology for the construction of light and efficient models. As introduced in the previous sections, POD allows to build empirical basis functions that can be employed in the applications of spectral methods for the approximation of field variables using truncated expansion. The truncation is aimed at incorporating into the ROMs only the most important features, extracted from the original dataset. By applying the coordinate transformation defined in Equation (2.11), the reduction of the general nonlinear dynamical model defined in Equation (2.9) results in the following ROM:

$$\frac{d}{dt}\boldsymbol{c}_K(\boldsymbol{t}) = \widetilde{\mathbf{A}}\boldsymbol{c}_K(\boldsymbol{t}) + \widetilde{\boldsymbol{F}}\big(t, \boldsymbol{c}_K(\boldsymbol{t})\big) \tag{2.12}$$

$$\boldsymbol{c}_K(0) = \boldsymbol{c_0} \tag{2.13}$$

where $\widetilde{\mathbf{A}} = \boldsymbol{\Phi}_K^T \mathbf{A} \boldsymbol{\Phi}_K$ is the reduced-order dynamical matrix; $\widetilde{\boldsymbol{F}} = \boldsymbol{\Phi}_K^T \boldsymbol{F}$ is the reduced vector of non-linear terms; and $\boldsymbol{c_0} = \boldsymbol{\Phi}_K^T \boldsymbol{u_0}$ is the reduced vector on initial conditions. This transformation can be seen as the projection of the original full order model (FOM) defined in Equations (2.9-2.10), onto a low-dimensional subspace spanned by a few reduced-order basis functions (ROBFs) (Lu et al., 2019).

2.2.5 ROM of Steady-state problems

In the case of parameter-dependent steady state boundary value problems, which in the discretized form can be written as:

$$\mathbf{A}(\boldsymbol{\mu})\boldsymbol{u}(\boldsymbol{\mu}) + \boldsymbol{F}(\boldsymbol{u}(\boldsymbol{\mu}), \boldsymbol{\mu}) = \mathbf{0} \tag{2.14}$$

The matrix of the snapshots is composed of *M* solutions obtained from a set of simulations with *M* different values of the parameters (the coefficients of the PDE that constitutes the problem under examination). In such case, the reduced-order model takes the form of Equation 2.15:

$$\widetilde{\mathbf{A}}(\boldsymbol{\mu})\boldsymbol{c}_K(\boldsymbol{\mu}) + \widetilde{\boldsymbol{F}}(\boldsymbol{c}_K(\boldsymbol{\mu}), \boldsymbol{\mu}) = \mathbf{0} \tag{2.15}$$

2.2.6 Challenges of the POD

From the above discussion, it is evident that projection-based techniques, when combined with the POD methodology, offer an exceptional solution for developing reduced-order models. Over the years, various modifications of this methodology have emerged, enabling the solution of diverse problems, including steady-state and transient simulations, optimization, and optimal control. These data-enhanced, yet constitutive equation-based ROMs, have become a powerful simulation tool. Additionally, ROMs based on the POD-Galërkin approach are relatively easy to implement, as demonstrated by the simple matrix notations discussed earlier. Despite its advantages, challenges remain. The POD is a linear procedure that allows the approximation of the data through the projection into linear subspaces, optimal in the L_2 norm sense (Bizon, 2010). However, the dynamical systems that are projected into such linear spaces, or the source of the data that generate the empirical basis can be, and in most cases are, nonlinear. The POD advantages and constraints both stem from its linearity. Such linearity refers to the combination, through either a finite or infinite sum, of modal functions each multiplied by suitable coefficients (Holmes et al., 1996). When the data used to construct the bases of the linear space originate from the evolution of a non-linear system, it may lead to imprecise approximation of the system dynamics. This is because the orthogonal basis produced by the POD might not adequately capture the nonlinear interactions, hence the projection of the full-order model onto the reduced basis can introduce errors that can sum to the approximation errors. Moreover, computational time reduction, a key advantage of reduced-order models, can be compromised in the case of nonlinear systems because of the need of evaluating nonlinear

terms in the original, non-reduced space. This increase in computational time negates the benefits of the reduced-order model. To address these challenges, several alternative methodologies have been proposed in the literature.

Particular attention must also be paid to the fact that the response of a complex nonlinear dynamical system is closely related to the values of the system parameters; to the feasible values of the initial conditions; or more importantly to the boundary conditions. In principle, a new ROM must be built for a new set of parameters, however this is computationally impracticable (Lu et al., 2019).

One approach used in literature to circumvent this issue is called global POD. Global POD methods utilize a combination of snapshots collected for various (feasible) values of the key parameters to derive global basis functions. The construction of the set is instrumental in building global POD-ROMs that accurately span the region of the parametric domain of interest. The implementation of this method is straightforward and easily applicable; however, there is the issue of sampling the parameter space. This challenge, which is shared with any kind of technique used to build data-driven models, is related to the fact that no general rule dictates how the parameter space should be sampled (Bizon and Continillo, 2021a), in order to build a faithful and robust reduced-order model which can extrapolate to a wide range of parameters, initial conditions, or boundary conditions. This problem is known in literature as the sampling problem, and will be discussed in the following paragraph. The sampling problem is hindered when treating nonlinear systems, which can present multiple solutions and a wide range of different behaviors (Strogatz, 2024). For this reason, a substantial number of snapshots are required to accurately depict the original system. In such cases, previous knowledge of the system behaviors can be essential in building accurate ROMs.

Although the ROMs built with the global approach may result unreliable in a number of cases (Lu et al., 2019), the method has proven its validity in a variety of problems, for example in Bizon et al., (2012) the choice of sampling chaotic solutions of a reactive system was found to be the optimal choice, in terms of maximization of the information contained in the snapshots matrix, resulting in an accurate global ROM which could predict the system chaotic behavior accurately even if compared to standard spectral methods.

Another approach, which is particularly interesting for extending the validity of the ROM to a wider range of the parameters space, is the local-POD paradigm. The core idea relies on

the construction of multiple ROMs, each approximating the FOM in defined regions of the parameter space. In practice, multiple sets of snapshots, each belonging to a parametric domain, are used to build the local POD modes. This idea has been used by Sahyoun and Djouadi, (2013) to circumvent the issue that global nonlinear manifold geodesics are difficult to be quantified, but in general they can be approximated efficiently by local linear Euclidean distances, allowing the derived local ROMs to be more accurate than global ROMs. In the work of Aversano et al., (2019) the authors use local POD to obtain a surrogate model that allows performing parameter space exploration of a detailed model of the combustion of a methane laminar premixed flame, by varying different parameters such as the equivalence ratio, the inlet temperature and the fuel composition. They achieve a reduced computational cost thanks to their local-POD methodology, which allows to represent nonlinear manifolds as a combination of local-linear manifolds, providing a better representation with respect to the single hyper-planes derived through classical POD. In Narasingam et al., (2017) a version of local-POD, called time-dependent spatial domains, is presented and applied to the case study of a dynamic PDE system describing a hydraulic fracturing process. The application of techniques such as local proper orthogonal decomposition may not always bring to a more accurate result. In fact, in local POD approach the entire parametric domain is decomposed into multiple subdomains; consequently, it is difficult to obtain smooth approximate solutions (Lu et al., 2019).

A way to improve the local POD concept and make the ROMs more robust to the system parameter variation is the method of adaptive POD. With the adaptive method an optimal approximation of the original system is obtained by evolving the POD ROMs in the parametric domain “online” which means that the ROM evolve as the solutions are computed. Some of the adaptive ROM strategies are strictly tied to the adaptive sampling paradigm for building data driven models. Adaptive ROMs aim at leveraging a posteriori error estimation for the construction of the reduced-order models in the hope of reducing the computational cost for a given accuracy (Chinesta and Ladevèze, 2020). For example, this approach is employed in the works of Terragni and Vega, 2014a, 2014b, where reduced-order models are updated with solutions from the full-order model to bound the error of the ROM (estimated a posteriori). This technique has been applied to the study of bifurcations in a nonlinear dynamic system. Lass and Volkwein, (2014) employ an optimal control algorithm to sample the parameter space and to update the reduced-order model. Other

methods rely upon interpolation to adapt the original reduced-order model by constructing new reduced basis functions upon those already computed. For example, in the work of Amsallem and Farhat, (2012), the authors use the Grassmann manifold as a suitable framework for handling reduced-order bases. They interpolate the reduced basis in a flat space tangent to a Grassmann manifold, which in turn contains the subspaces generated by the POD bases of the initial reduced-order model.

In this thesis, the problem of broadening the range of validity of ROMs based on nonlinear systems is circumvented by employing global POD, which as the results will show is a viable and accurate solution for the reported case studies and is characterized by a straightforward application procedure.

2.2.7 Treating the non-linearities

Obtaining a simpler model that accurately represents the physics of the entire system is crucial for accelerating workflows that necessitate iterative model simulations. This scenario frequently occurs in parameter estimation and optimization problems (Kumar and Kostina, 2024).

Numerical methods can be used to achieve accurate approximate solutions of complex nonlinear problems, but it is necessary to introduce fine grid discretization, as demonstrated by convergence theorems (Grossmann et al., 2007), and this results in large-scale nonlinear system of equations. Hence reduced-order modeling through POD has been introduced, which has its advantages but nevertheless is characterized by limitations. A significant challenge in the POD method is assessing nonlinear terms, necessitating a projection back to the original large-scale state. This becomes evident when explicitly rewriting the nonlinear term of the previously introduced ROM, see Eq. (2.14):

$$\widetilde{\boldsymbol{F}}\big(t, \boldsymbol{c}_K(t)\big) = \boldsymbol{\Phi}_K^T \boldsymbol{F}\big(t, \boldsymbol{\Phi}_K^T \boldsymbol{c}_K(t)\big) \tag{2.16}$$

It can be noted that the function $\boldsymbol{F}\big(t, \boldsymbol{\Phi}_K^T \boldsymbol{c}_K(t)\big)$ must be evaluated in the original dimension of the full-order space (hereafter referred to as *N*); in fact, $\widetilde{\boldsymbol{u}} = \boldsymbol{\Phi}_K \boldsymbol{c}_K$ is the approximated state variable vector of *N* elements. To address the issue of increased computational time due to the evaluation of a nonlinear term, which would diminish the benefits of the ROM, numerous methodologies can be found in literature. The challenge of addressing the non-linear term extends beyond the POD-ROMs formulation discussed in this dissertation, and is common to other model order reduction techniques. In some cases, in fact, a method

initially designed for a different technique is later adapted for POD, or vice versa. This paragraph highlights several techniques from the literature that have been successfully combined with POD to address non-linear reduction problems. One of the latest approaches is the use of Graph Neural Networks (GNNs), which have been combined with classical reduced-order modeling frameworks to accelerate the numerical analysis of time-dependent partial differential equations (Matray et al., 2024). Additionally, data-driven algorithms such as sparse identification for nonlinear dynamics (Brunton et al., 2016) and neural networks (Kutz, 2023) have emerged as viable alternatives to projection-based ROMs. The method described in the work of (Gu, 2011) allows to represent a nonlinear system of differential algebraic equations (DAE) into an exact equivalent form of quadratic-linear differential algebraic equations (QLDAE) in which the differential equations are quadratic in their state variables and linear in their inputs. This representation has been originally combined with moment-matching model order reduction technique, in particular the author employed the Arnoldi algorithm to build a reduced-order model based on Krylov subspace projections and called quadratic linear model reduced-order model (QLMOR). This method subsequently inspired a series of works, all based on the reformulation of a nonlinear system in its equivalent quadratic-linear form, to address the evaluation of the nonlinearity (Benner et al., 2018; Benner and Breiten, 2015; Ghasemi and Gildin, 2016). Some methods, such as the one described by Kramer and Willcox (2019) employ QLDAE in combination with POD, thus extending the method to a broader class of systems. They use a multistep transformation called the lifting transformation and then, in combination with POD, build reduced-order models. The study demonstrates how the lifting transformation compares to the state-of-the-art Discrete Empirical Interpolation Method (DEIM) of Chaturantabut and Sorensen, (2010). The lifting transformation offers the advantage of not introducing additional approximations in the nonlinear terms of the reduced-order model. However, it requires extra initial effort to derive the so-called lifted system, including the matrices and tensors representing the lifted dynamics. Another drawback of this technique is that the introduction of auxiliary variables to transform the original nonlinear system into its lifted form increases the dimension of the state. This often requires a higher-dimensional ROM to achieve an acceptable error level, ultimately preventing the desired reduction in computational cost. In the context of Operator Inference, the Lift and Learn method introduced by Qian et al., (2020) uses the lifting

transformations to yield quadratic reduced-order models approximating complex nonlinear systems, such as combustion dynamics, from lifted data.

DEIM is one of the state-of-the-art algorithms for treating nonlinearities efficiently in reduced-order models Kramer and Willcox (2019). The DEIM approach allows for the construction of an approximation of the nonlinear function through the combination of projection and interpolation. It can be seen as a discrete variant of the empirical interpolation method (EIM) (Barrault et al., 2004) and is closely related to the Missing Point Estimation method (Astrid, 2004). In contrast to EIM, the DEIM was designed to be used in any system of ODEs, regardless of its origin. DEIM identifies a set of spatial grid points to bypass the costly evaluation of the nonlinear term across the entire domain of the PDE problem. Unlike the MPE approach, DEIM employs POD bases specific to each nonlinear function to precompute the coefficients for the nonlinear function's approximation. The reduced systems obtained from the POD-Galërkin approach with the DEIM approximation of the nonlinearities are usually called POD-DEIM. This thesis selects the POD-DEIM method due to its proven effectiveness in handling the nonlinearities of reaction-diffusion and reaction-convection-diffusion systems, which are the focus of the case studies analyzed (Bizon, 2017; Bizon and Continillo, 2020; Bremer et al., 2017; Cutillo et al., 2023; Nguyen et al., 2020).

In the work of Bizon (2017), the author applies the POD-DEIM approach to reduce the model of a single isothermal catalyst pellet in view of the potential application of the method to simulate multi-scale problems; the POD-DEIM methodology is later extended to the optimization of non-isothermal pellet model where the nonlinearities couple mass and heat diffusion phenomena (Bizon and Continillo, 2020). In the work of Bremer et al., (2017) the authors successfully reduce the model of a catalytic wall carbon dioxide methanator, allowing faster model evaluation for the analysis of the disturbed continuous operation and start-up of the reactor. Cutillo et al. (2023) employ the POD-DEIM methodology combined with a k-means clustering-based sampling technique to construct a reduced-order model for a reaction-diffusion problem, specifically modeling the self-ignition of a stockpile of solid fuel. The capabilities of the POD-DEIM method enables much faster computations and opens opportunities for various real-time control applications. This is demonstrated by the control scenarios performed in the work of Nguyen et al., (2020) on a plug flow reactor with coolant system. In the following thesis attention is focused on the possibility of increasing

the robustness and accuracy of POD-DEIM reduced-order models by exploring different sampling strategies of the snapshot matrix to build the empirical basis function set.

2.2.8 Sampling strategies

The construction of a model based on previously obtained data, derived from empirical measurements, or from computationally onerous numerical simulations, comes with the problem of sampling between all feasible values of the parameter space that are of interest for the designer (Forrester et al., 2008b). One of the challenges in constructing a global data-driven model is the need for a reasonably accurate predictive model, which requires a substantial amount of training samples from the parameter space. Uniformly filling this space and building an accurate model for each parameter is a computationally intensive task that is strictly correlated to the number of parameters of interest to the model designer. This task is known as the course of dimensionality (Forrester et al., 2008b). When dealing with parameter dependent steady problems or parametric analysis of dynamic systems, the global POD basis is generally derived by using a combination of snapshots collected for various values of the key parameters. Nevertheless, no general rule dictates how the parameters should vary. In the case of reduced-order models, several sampling strategies can be found in the literature, as shown in the review by Lu et al., (2019). Commonly used approaches include uniform, random and stratified sampling (Bizon and Continillo, 2021a). Liu et al., (2018), classify these strategies into static or sequential. Adopting the definition of Liu et al., (2018), static are those strategies that rely upon “one-shot” sampling methods. Where “one-shot” can be defined as a sampling scheme in which all evaluation points are selected in advance in a single step, without any subsequent adaptation based on intermediate model results. Two examples of one-shot methods are factorial design of experiments or Latin hypercube sampling (Bates et al., 2003; Eglajs and Audze, 1977), in which the decision of the quantity and position of samples in the parameter space is defined initially and is constant during model construction. This strategy is based on the idea of attempting to fill the parameter space uniformly, to capture all the features of a phenomenon necessary for the purpose of the application in which the reduced-order model will be used, to construct a model as general as possible. In the context of reduced-order models, it is possible to refer to this concept as to “global ROM” (Lu et al., 2019). On the other hand, sequential sampling approaches are classified into two categories: space-filling sequential sampling and adaptive sequential sampling Liu et al., (2018). Sequential space-filling shares the same properties of

one-shot methods and are usually derived from one-shot sampling criteria but with the difference that samples are simulated in a sequential manner. Meanwhile, adaptive sampling allows for the selection of informative points by iteratively analyzing the data-driven model and its respective reference dataset. In this way, adaptive sampling performs better with fewer points than space-filling sampling, thereby reducing the cost of expensive simulations. For example, instead of sampling data uniformly, it would make sense to increase sample density in regions where the data-driven model shows greater prediction errors. For this reason, it can be said that the data-driven model adapts to the properties of the system it is trying to reproduce. In the case of dynamical time-dependent systems, snapshots are classically sampled from the transient response, from steady state or oscillating regimes or, if they are available, from chaotic trajectories (Bizon et al., 2012a; Lu et al., 2019). In general, a potentially representative ensemble of data can be obtained by combining data from different simulations, run at different values of key parameters or with different initial conditions (Bizon et al., 2012a).

To seek ROM globality, in this thesis two sampling strategies are used and compared. The first one, the most straightforward, is uniform sampling, (e.g. taking samples of the dynamic FOM solutions with a uniform time interval). In the case of a dynamical system, the uniformly sampled snapshots include both the transient behavior of the system and its oscillating regimes when observed. Moreover, the system is simulated for a set of values of the parameter of interest. In general, a potentially representative ensemble of data can be obtained by combining data from different simulations, run for different values of key parameters or with different initial conditions. This, however, requires a comprehensive *a priori* knowledge about the system behavior, and involves relatively heavy computational work. For each system under study in this thesis, the parameters that are allowed to vary during the sampling process will be clearly defined. The solutions found for different values of the selected key parameters are then combined in a single dataset and, for the construction of the reduced-order model through the POD approach, they are arranged in the snapshot matrix, as shown in the following Eq. (2.17):

$$
\begin{aligned}
U = [u_1(t_1,\gamma_1) \cdots u_1(t_M,\gamma_1) \vdots \ddots \\
\vdots\ u_N(t_1,\gamma_1) \cdots u_N(t_M,\gamma_1)\ \ u_1(t_1,\gamma_2) \cdots u_1(t_M,\gamma_2) \vdots \ddots \\
\vdots\ u_N(t_1,\gamma_2) \cdots u_N(t_M,\gamma_2)\ \ u_1(t_1,\gamma_H) \cdots u_1(t_M,\gamma_H) \vdots \ddots \\
\vdots\ u_N(t_1,\gamma_H) \cdots u_N(t_M,\gamma_H)\ ]
\end{aligned}
\tag{2.17}
$$

To further increase the robustness of the ROM and while keeping computational resources to a minimum, another sampling strategy is introduced, consisting of the application of the k-means clustering algorithm to the uniformly sampled solutions. The employed methodology is akin to the approach proposed by Adrover et al., (2002) which uses snapshot archetypes as the basis for a linear subspace in the numerical solution of advection/diffusion/reaction equations. This approach involves projecting partial differential equations onto a linear subspace spanned by so-called snapshot archetypes.

The k-means algorithm is one of the most popular clustering techniques, widely applied in science and engineering. In the field of chemical engineering, for example, the procedure has proven successful in a series of studies on parameter-dependent stationary problems, such as optimization problems on multifunctional fixed-bed catalytic reactors (Bizon et al., 2021; Bizon and Continillo, 2021a). The algorithm is based on the so-called Lloyd method (Lloyd, 1982), which consists of an iterative expectation-maximization type approach that attempts to address the following objective: given a set of Euclidean points - which can be defined as a collection of vectors in R^n representing observations or samples in an n-dimensional space - and a positive integer number of clusters k, divide the points into k clusters so that the total sum of the squared Euclidean distances of each point to its nearest cluster center is minimized. Briefly, k-means operates a partition of the snapshot set by grouping together subsets of nearby observations from an ensemble; the observations are considered near in the sense of some mutual distance, for example, the Euclidean distance. The intuitive nature of the Lloyd method and the effectiveness of the k-means technique make this clustering algorithm the most popular and used in numerous applications in different fields of engineering.

However, the k-means clustering technique is not always applicable: for example, for systems with considerable amounts of data, the algorithm may not be particularly effective as it may be difficult to identify the relevant underlying structure (i.e., the k clusters). This may be due to the presence of many irrelevant characteristics in the initial dataset (Guyon et al., 2004). Furthermore, like many clustering methods, k-means clustering requires specification of the number of clusters k before starting the clustering procedure.

After partitioning the solutions profiles into k clusters, the snapshot matrix consists of the centroids of the clusters. The centroids are the arithmetic means of the solution profiles of a given cluster. The k-means clustering algorithm for generating centroids is shown in Fig.

2.1. The aim is employing such centroids to build more robust and reliable reduced-order models.

Consider the snapshots matrix **U**, of order [N x M] where N represents the order of the FOM and M is the number of samples. In the case of uniform sampling, M is the number of samples collected directly from the FOM solutions. When clustering is employed, M is the total number of clusters (and centroids), hence equal to k.

INPUT k number of clusters; solution profiles $\mathbf{U} = [\mathbf{u}(t_1,\gamma_1),...,\mathbf{u}(t_M,\gamma_H)] \in \mathbb{R}^{N\times M\cdot H}$

1) choose k initial guess centroids $\mathbf{Z} = [\mathbf{z}_1,...,\mathbf{z}_k]$ from the column of **U**

2) **while** not converged **do**

3) **for** $i = 1$ to $M \cdot H$

4) $\mathbf{a}_i \leftarrow 1$

5) **for** $j = 1$ to k

6) **if** $\|\mathbf{u}_i - \mathbf{z}_i\| < \|\mathbf{u}_i - \mathbf{z}_{\mathbf{a}_i}\|$

7) $\mathbf{a}_i \leftarrow j$

8) **end**

9) **end**

10) **for** $j = 1$ to k

11) move $\mathbf{z}_i$ to the mean of $\{\mathbf{u}_i : \mathbf{a}_i = j\}$

12) **end**

13) **end**

OUTPUT centroids of the k clusters: $\mathbf{Z} = [\mathbf{z}_1,...,\mathbf{z}_k]$

Figure 2.1. The k-means algorithm, adapted from (Hamerly and Drake, 2015).

2.2.9 The bottleneck of the evaluation of the nonlinear term: a hyper-reduction strategy via DEIM

The DEIM method aims at reducing the computational burden of evaluating the nonlinear term in the ROM introduced in Eq. (2.12 or 2.14) and shown in Eq. (2.16).

To proceed with DEIM, the first thing to do is the application of the POD method to approximate the nonlinear function, so, in the same way introduced earlier for the reduction of the model, here the matrix of snapshots of the nonlinear function is introduced:

$$\mathbf{U}_F = \left[\boldsymbol{F}_1, \ldots, \boldsymbol{F}_j, \ldots, \boldsymbol{F}_M\right] \tag{2.18}$$

where:

$$\boldsymbol{F}_j = \left[F\left(t_{\mathrm{j}}, \boldsymbol{c}_1(t_{\mathrm{j}})\right), F\left(t_{\mathrm{j}}, \boldsymbol{c}_2(t_{\mathrm{j}})\right), \ldots, F\left(t_{\mathrm{j}}, \boldsymbol{c}_{\mathrm{N}}(t_{\mathrm{j}})\right)\right]^{\mathrm{T}} \tag{2.19}$$

In Eq. (2.19) M is the total number of snapshots considered also in the construction of the POD basis. After solving the eigenvalue problem, the nonlinear function F can be approximated as:

$$\boldsymbol{F} \approx \widetilde{\boldsymbol{F}} = \boldsymbol{\Psi}_J \boldsymbol{q}_J \tag{2.20}$$

The unknown set of time-dependent coefficients $\boldsymbol{q}_J$ can be precomputed. They are calculated using the following equation:

$$\boldsymbol{P}^T \boldsymbol{F} = \left(\boldsymbol{P}^T \boldsymbol{\Psi}_J\right) \boldsymbol{q}_J \tag{2.21}$$

where P is the matrix of the interpolation indices defining the grid points at which the nonlinear function is evaluated. Eq. (2.22) can be rearranged as follows:

$$\boldsymbol{q}_J = \left(\boldsymbol{P}^T \boldsymbol{\Psi}_J\right)^{-1} \boldsymbol{P}^T \boldsymbol{F} \tag{2.22}$$

Considering that the following equality holds:

$$\boldsymbol{P}^T \boldsymbol{F}(\boldsymbol{u}(t)) = \boldsymbol{F}(\boldsymbol{P}^T \boldsymbol{u}(t)) \tag{2.23}$$

then Eq. (2.24) can be rewritten as:

$$\boldsymbol{q}_J = \left(\boldsymbol{P}^T \boldsymbol{\Psi}_J\right)^{-1} \boldsymbol{F}(\boldsymbol{P}^T \widetilde{\boldsymbol{u}}) \tag{2.24}$$

Matrix P contains the interpolation indices and can be found using the DEIM algorithm (Chaturantabut and Sorensen, 2010) reported in Fig. 2.2.

INPUT Projection basis of the nonlinear function $\boldsymbol{\Psi} = \left[\boldsymbol{\psi}_1, ..., \boldsymbol{\psi}_N\right] \in \mathbb{R}^{N \times N}$

1) $p_1 = i$ such that $\max\left\{\left|\boldsymbol{\psi}_1(\zeta_i)\right|,\ i = 1, ..., N\right\}$

2) $\boldsymbol{\Psi}_1 = \boldsymbol{\psi}_1 \in \mathbb{R}^N$, $\mathbf{p} = p_1 \in \mathbb{R}^N$, $\mathbf{P} = e_{p_1} \in \mathbb{R}^N$

3) **for** $j = 2$ to J

4) **solve** $(\mathbf{P}^{\mathrm{T}}\boldsymbol{\Psi}_j)\mathbf{q}_j = \mathbf{P}^{\mathrm{T}}\boldsymbol{\psi}_j$ for $\mathbf{q}_j$

5) $\mathbf{r} = \boldsymbol{\psi}_j - \boldsymbol{\Psi}_j\mathbf{q}_j$

6) $p_j = i$ such that $\max\left\{|\mathbf{r}|,\ i = 1, ..., N\right\}$

7) $\boldsymbol{\Psi}_j = \left[\boldsymbol{\psi}_1, ..., \boldsymbol{\psi}_j\right] \in \mathbb{R}^{N \times j}$, $\mathbf{p} = \left[p_1, ..., p_j\right]^{\mathrm{T}} \in \mathbb{R}^j$ $\mathbf{P} = \left[e_{p_1}, ..., e_{p_j}\right] \mathbb{R}^{N \times j}$

8) **end**

OUTPUT Vector of interpolation indices $\mathbf{p} = \left[p_1, ..., p_J\right]^{\mathrm{T}} \in \mathbb{R}^J$

Figure 2.2. The DEIM algorithm, adapted from (Bizon, 2017)

Finally, substituting Eq. (2.25) into Eq. (2.22) and then in the ROM Eqs. (2.12 or 2.15), the hyper-reduced POD-DEIM model is obtained:

$$\frac{d}{dt}\boldsymbol{c}_K = \boldsymbol{\Phi}_K^T \boldsymbol{A} \boldsymbol{\Phi}_K \boldsymbol{c}_K + \boldsymbol{\Phi}_K^T \boldsymbol{\Psi}_J \left(\boldsymbol{P}^T \boldsymbol{\Psi}_J\right)^{-1} \boldsymbol{F}(\boldsymbol{P}^T \boldsymbol{\Phi}_K \boldsymbol{c}_K) \tag{2.25}$$

In Eq. (2.26) the second term on the right-hand side $\boldsymbol{\Phi}_K^T \boldsymbol{\Psi}_J \left(\boldsymbol{P}^T \boldsymbol{\Psi}_J\right)^{-1} \boldsymbol{F}(\boldsymbol{P}^T \boldsymbol{\Phi}_K \boldsymbol{c}_K)$ contains two factors that can be computed offline: $\boldsymbol{\Phi}_K^T \boldsymbol{\Psi}_J \left(\boldsymbol{P}^T \boldsymbol{\Psi}_J\right)^{-1}$ and $\boldsymbol{P}^T \boldsymbol{\Phi}_K$ thus reducing the number of computation to be done while simulating the ROM. More importantly, the nonlinear function is evaluated only $J << N$ times, making the solution of the ODEs system much faster.

2.2.10 Tuning of the POD-DEIM model

The introduced POD-DEIM methodology comes with a price: there are two numerical parameters to be calibrated for each variable (in the case of this work the variables are two: concentration and temperature inside the pile). The numerical parameters are the number of POD modes K used to approximate the state variables, and the number of interpolation points J used to evaluate the nonlinear part of the operator. These parameters need be adjusted with the objective of building a fast and accurate ROM.

The accuracy of the model and the speed of the simulation are conflicting objectives: the search of the optimal ROM is a multi-objective optimization problem and as such there are infinitely many solutions to the problem. Most authors prefer to maintain low the number of J and K thus preserving the speed of the ROM (Sukuntee and Chaturantabut, 2020). Moreover, the accuracy and the speed of the simulation are not necessarily monotonous function of J and K. For this reason, the full space of parameters J and K must be investigated. This makes the tuning of the introduced numerical parameters a heavy task. Concerning the number of modes involved in the state variable approximation, there are mainly two methods to find the threshold eigenvalue that discriminates the most important modes that must be considered in the construction of the ROM from those that can be neglected: an a-priori method and an empirical method, the second one being more accurate but more expensive in terms of computational cost. The a-priori method consists of the evaluation of the so-called cumulative correlation energy defined as (Sirovich, 1987):

$$E_K = \frac{\sum_{k=1}^{K} \lambda_k}{\sum_{k=1}^{N} \lambda_k} \tag{2.26}$$

where λ_k are the ordered eigenvalues and Ek is usually chosen equal to at least 0.99 to build a sufficiently accurate model. The empirical method consists of the construction of different ROMs, which are built with an increasing number of modes. For each ROM, the error is calculated between full and truncated solutions. This error must be smaller than a predefined value, given by the designer of the reduced-order model or by the requirements of the application. At the end of the procedure, the ROM is chosen that, among the others, leads to sufficiently accurate solutions, and yet is computationally convenient (Bizon, 2017; Bizon and Continillo, 2021a). In this thesis, the empirical method will be employed also for the tuning of the nonlinear term approximation through DEIM.

2.3 Surrogate models

In situations when a first-principles model is not available, or is simply too complex, or when even greater computational efficiency is needed, yet another type of tool is required, namely surrogate or hybrid models, sometimes also referred to as equation-free models (Bizon, 2023). Surrogate modeling approaches extend the framework of classical model order reduction, which is typically applied to a state-space description. The surrogate approach provides tools for processing sequences of input-output data points and constructing an

approximate metamodel that explains and reproduces their relationship. By bridging the gap between control and system theory with statistics, computer science, and (big) data science, surrogates can be viewed as an extension of MOR and further demonstrate the pervasive key objectives that characterize MOR (Benner et al., 2021).

There is a wide selection of techniques for constructing data-driven models (Bizon, 2023). Among the most popular data-driven methodologies used to construct both surrogate models are artificial neural networks (ANN), Support vector machines (SVM) (Sansana et al., 2021), Radial basis functions (RBF) (Bárkán et al., 2021), Kriging (Wackernagel, 2003).

In this thesis, to explore innovative and computationally efficient solutions, two data-driven methods will be analyzed for building surrogate models (Forrester et al., 2008b), including artificial neural networks (ANN) and Kriging, known as Gaussian process regression (GPR), will be analyzed for building surrogate models (Forrester et al., 2008b).

ANNs, which emulate the learning process of biological neural systems, are recognized as a tool with great flexibility in approximating nonlinear functions. These can be characterized by a relatively simple structure of nodes, which can be adjusted during the training phase. ANNs are able to learn both correlations and patterns in the analyzed data, even in the presence of noise and uncertainty (Bizon et al., 2011). Unlike the reduced-order modeling approach, which in this work focuses on analyzing dynamical or steady-state systems described by partial differential equations, the surrogate approach is here demonstrated in studying multicomponent adsorption. Below is a brief overview of the literature concerning surrogate modeling in the field of multicomponent adsorption.

In the work of Ghalandari et al. (2020), a feed-forward neural network with a hidden layer was presented for the prediction of multicomponent adsorption of a mixture of N_2, CO_2 and CH_4 on activated carbon. The network was trained with experimental data of single-component isotherms and used to predict the amount adsorbed as temperature, pressure, gas type and specific surface area of the adsorbent varied. The results showed how a simple feed-forward network with just nine neurons can predict the data with a mean square error (MSE) of $4 \cdot 10^{-3}$. Nogueira and colleagues, (2022) investigated the dynamic behavior of the concentration profile of a fixed-bed isothermal adsorbent column by employing a neural network to replace multicomponent isotherms. The adsorbed amount of the single component at equilibrium was chosen as the output of the network, while the concentrations in the liquid phase of the two adsorbed components (propanol and n-propyl propionate) were

provided as input. The authors proposed feed-forward neural networks to calculate the adsorption equilibrium and mass transport coefficients. A neural network consisting of a hidden layer of seven neurons with hyperbolic tangent ('tansig') as the activation function was trained for each component. An MSE of 0.067 was obtained by comparing the results of the proposed hybrid model against experimental data. Kareem and colleagues (2018), employed ANN modeling to predict the adsorption of binary and ternary mixtures of CO_2, CH_4 and H_2O on zeolite 13x and demonstrated that a feed-forward neural network can fit the training data with a single hidden layer of 14 neurons, with sigmoidal activation functions. This network was trained using experimental data obtained with different compositions of the gas mixture and different operating conditions, namely a temperature of 343 K and a total pressure of up to 10 bar.

Kriging or GPR can be seen as empirical models. Their use is attractive when, due to limited time or resources, there can only be a limited number of sampling points. There are several methods for deriving accurate predictions from observations. In particular, Kriging also known as best linear unbiased predictor, has been initially employed in geostatistics since 1951 (Forrester et al., 2008a). The definition of "best linear unbiased predictor" is related to the minimum value of prediction variance that characterizes GPR compared with linear predictors (Forrester et al., 2008a). To predict a new function value at point $\mathbf{x}_0$ - that is, $Z^*(\mathbf{x}_0)$, the kriging model uses a weighted average of all known data (Wackernagel, 2003). Kriging uses most of the information in the data to obtain the new unknown value optimally. Therefore, the following relationship can be used to estimate the new value of the function (Wackernagel, 2003):

$$Z^*(\mathbf{x}_0) = \lambda_0 + \sum_{i=1}^{n} \omega_i \, Z(\mathbf{x}_i) \tag{2.27}$$

where n is the number of observations; ω_i are the weights; $Z^*(\mathbf{x}_0)$ is the estimated value of the function at a new location; meanwhile, $Z(\mathbf{x}_i)$ is the response of the function (or measure) at the sampled point with coordinates $\mathbf{x}_i$; and λ_0 is the mean or expected value of the function in the domain of interest. Finding the best linear unbiased prediction is equivalent to finding the optimal weights ω_i that minimize the variance of the prediction subject to the unbiasedness condition; therefore, the following minimization problem can be stated (Wackernagel, 2003):

$$\min_{\omega_i} \mathrm{Var}\left(Z(\mathbf{x}_0) - Z^*(\mathbf{x}_0)\right) \tag{2.28}$$

where $Z(\mathbf{x}_0)$ is the expected value of the function at the new point of coordinates $\mathbf{x}_0$.

Mukherjee et al. (2023) used Gaussian Process Regression (GPR) to obtain surrogate models of multicomponent adsorption through data obtained from Grand Canonical Monte Carlo (GCMC) simulations, which is a rigorous model of adsorption at the molecular level (Yun et al., 2002). Through GCMC, the authors generated a large number of data, in particular 5000 and 50000 cycles were used for initialization and generation of the data set, respectively. According to the authors, GPRs differ from other machine learning models in that they are flexible nonparametric models that can emulate any distribution with less starting data while providing an estimate of the standard deviation along with the required output. In addition, GPRs have shown better performance for smaller starting data sets than models such as Bayesian neural networks (BNNs) or neural network ensembles, which can also provide uncertainty estimates. Moreover, Mukherjee et al. (2023) have found that the best kernels for obtaining accurate models for their data are those based on Radial Basis Functions (RBF).

A combination of Kriging and multilinear free energy regression models was employed by Zhao et al. (2022) to predict the adsorption capacity of organic pollutants by bio-char and resin. After analyzing models built with neural networks as well, the authors concluded that the ones built with Kriging are more faithful with the measurements, allowing them to increase the accuracy in predicting the adsorption efficiency of pollutants in aqueous solutions by about 10 percent.

Chapter 3
Mathematical models of Fixed Bed Reactors and Self-ignition systems

3.1 Overview: Phenomenology of heterogeneous processes

This chapter introduces and analyzes the mathematical models that will be utilized in the thesis. The goal is twofold: first, to provide a rigorous formalization of the phenomena under investigation; and second, to identify the assumptions and operating conditions that underpin the simulations discussed in subsequent chapters.

Following a brief overview of the phenomenology, the main models found in literature will be described with a focus on their mathematical structure, the variables involved, and underlying assumptions. The validity of these models, potential simplifications, and their conceptual and computational limitations will also be discussed.

Reaction in heterogeneous systems involving a gaseous and a solid phase can be thought of as a network of different processes such as mass and heat transport and chemical reaction. For this reason, in this chapter more focus is posed on the mechanisms that take place in a catalyst pellet.

Considering a porous pellet particle inside a gas stream in which reactants are present, the rate of reaction for the whole particle (Figure 3.1) may depend on:

1. Surface kinetics, or what happens at the surface, interior or exterior of the particle. This may involve the adsorption of reactant A onto the surface, reaction on the surface, desorption of product back into the gas stream.
2. Pore diffusion resistance which may cause the interior of the particle to be starved for reactant. This causes concentration gradients inside the particle.
3. Temperature gradients within the particle, caused by large heat release or absorption during reaction, can influence the rate of the reaction.
4. Temperature and concentration gradients across the gas film surrounding the particle. Between the surface and the main gas stream there is a thin film of gas in which gradients of temperature and concentration may play a role in the rate of the reaction.

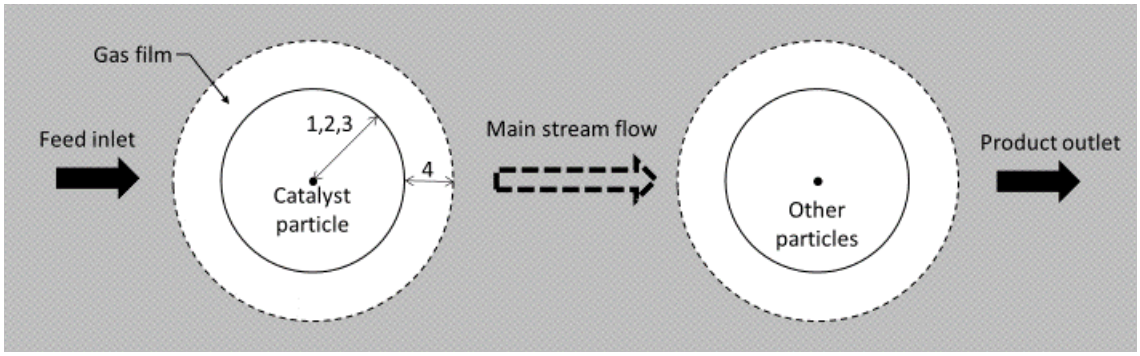

Figure 3.1. *Different aspects that influence a catalytic heterogeneous reaction*

The slowest step in a sequence is the one that is said to control the process. The overall rate can be thus controlled by external diffusion, internal diffusion, or surface reaction. If slow reactions are considered, the only element that influences the rate of the reaction is the surface kinetics. On the other hand, if fast reactions are considered, pore diffusion resistance may play a predominant role on the kinetic regime. Particles temperature gradients and film diffusion properties are unlikely to limit the overall rate (Levenspiel, 1998)

3.2 Mathematical models of Fixed Bed Reactors

Fixed Bed Reactor mathematical models are indispensable tools for predicting reactor behavior efficiently and cost-effectively. Such models guide industrial scaling, allow to optimize operations, and are used to assess reactor designs (Costa and Bagajewicz, 2019; Dixon et al., 2006). They are at the heart of numerical simulations that allow the computation of physical and chemical properties of the media that characterize the reactor. Numerical simulations are essential tools that simplify the analysis of the performance of a reactor, for example by providing estimation of conversion degree, yields, and thermal requirements. When validated against experimental data, numerical models allow rapid comparison of different reactor designs and provide guidance in selecting critical parameters, such as reactor and pellet geometry; the types of solid materials used as the reactor filling (e.g., catalyst type, adsorbent type, inert support); and the definition of operating conditions, including optimal inlet composition, gas flow rate, and temperature. Numerical simulations can thus substitute costly and time-consuming experimental runs with numerical sensitivity analysis (Kiewidt, 2017). Nevertheless, numerical simulations can be time-consuming, mainly due to the computational cost of solving highly non-linear systems of algebraic or differential equations. In this dissertation, various fixed bed reactor models have been

employed. Before describing the models used, this paragraph provides a brief description of the fixed bed reactor models employed in the literature. In a recent review, Stegehake et al., (2018) classify six modelling approaches based on four features: the application maturity, levels of simplifications, degree of detail and number of model parameters. The six types of models that are discussed range from the extremum of the estimation method to the extremum of the CFD (Computational Fluid Dynamics) particle-resolved modelling. To help the reader in the following Table 3.1 are listed six model types which are classified based on four features. The ordinal relationships are expressed with a scale of nominal categories ranging from Very High to Very Low.

Table 3.1: A qualitative assessment of modeling methods based on application maturity, abstraction level, detail, and model complexity. Higher abstraction favors simplicity and maturity, while greater detail enhances accuracy at increased computational cost, inspired from Figure 2 in (Stegehake et al., 2018).

Model Type	**Application Maturity**	**Level of simplifications**	**Degree of Detail**	**Number of Model Parameters**	**Computational cost**
Estimation Methods	Very High	Very High	Very Low	Minimal	Very Low
Pseudo-Homogeneous Continuum Model	High	High	Low	Low	Low
Heterogeneous Continuum Model	Medium-High	Medium-High	Medium-Low	Moderate	Medium-Low
Cell Model	Medium	Medium	Medium	Moderate to High	Medium
Stochastic Model	Low	Medium-Low	Medium-High	High	Medium-High
Particle-Resolved Modelling	Medium-Low	Very Low	Very High	Very High	Very High

In addition to the features cited in (Stegehake et al., 2019), in Table 3.1 is included the computational cost of solving the mathematical model. The computational cost depends on the resolution algorithm employed to solve the numerical representation of the model, but it is still possible to define ordinal relationships between the different types of models. It can be noted that the computational cost is directly proportional to the number of parameters and

the degree of detail, while it is inversely proportional to the level of simplifications and the application maturity.

3.3 Classification of Fixed Bed Reactor Models

Mathematical modelling of fixed bed reactors is characterized by a range of approaches that balance accuracy, computational efficiency, and applicability. The six main types of models reported in Table 3.1, range from highly simplified estimation methods to detailed particle-resolved simulations. These models differ in their assumptions regarding homogeneity, transport phenomena, and reaction kinetics, influencing their predictive power and computational cost.

The following paragraphs provide an overview of each model type, focusing on their key assumptions, applications, and computational implications.

3.2.1.1 Continuum models: The Heterogeneous Model

The heterogeneous continuum model captures distinct fluid and solid phases, involving mass and heat transfer. It requires solving separate balance equations for the catalyst and the reacting fluid, coupled through mass and heat exchange models - such as linear driving force formulations for interphase transfer - and appropriate boundary conditions required for solving the partial differential equations that describe the system. Although complex, these models offer greater accuracy. The equations include species and energy balances of the fluid and solid phases, as well as momentum balance. Heterogeneous models are essential for simulating catalytic reactors precisely. They show the location and intensity of hot-spots crucial for safety and allow a precise definition of optimization problem to design optimally distributed catalytic functions inside the reactor (Bizon and Continillo, 2021a). Table 3.2 shows an example of heterogeneous continuum model.

There are several possibilities for modeling the catalyst within the reactor. One of the simplest models treats the catalyst using a lumped parameter approach. The catalyst is modeled assuming that the state on the surface is approximately equal to the state of its innermost zones. The coupling between the solid and the gas phase is modeled accounting for mass and heat exchange between those phases. In the dynamic case, the catalyst behavior is described by a set of ordinary differential equations. In this model, therefore, internal gradients are neglected.

The heterogeneous model of the reactor that uses a lumped parameter model for the catalyst is formalized by Equations (1) to (4) reported in Table 3.2 and by the related initial and boundary conditions (Equations (7), (9) and (10) in Table 3.2).

Table 3.2 Examples of heterogeneous fixed-bed reactor models used in this doctoral dissertation

Description	**Governing Equation**	
Gas phase energy balance	$\left(\rho_g c_{p,g}\right)\frac{\partial T_g}{\partial t} = -\rho_g u_0 c_{p,g}\frac{\partial T_g}{\partial z} + K_{\text{ax}}\frac{\partial^2 T_g}{\partial z^2} + \alpha_p a_p\left(T_p - T_g\right) - \frac{h}{D_i}\left(T_g - T_w\right)$	(1)
Gas phase species balance	$\frac{\partial C_{i,g}}{\partial t} = -\frac{\partial\left(u_0 C_{i,g}\right)}{\partial z} + D_{\text{ax}}\frac{\partial^2 C_{i,g}}{\partial z^2} + k_g a_p\left(C_{i,g} - C_{i,p}\right)$ $\forall\ \text{i} = 1 \ \ldots\ \text{n species}$	(2)
Solid phase energy balance w/o internal limitations	$\left(\rho_p c_{p,p}\right)\frac{\partial T_p}{\partial t} = -\alpha_p a_p\left(T_p - T_g\right) + \rho_p \sum_{j=1}^{N_r}\left(-\Delta H_{R,j}\right)\ R_j$	(3)
Solid phase species balance w/o internal limitations	$\frac{\partial C_{i,p}}{\partial t} = -k_g a_p\left(C_{i,g} - C_{i,p}\right) - \rho_p \sum_{k=1}^{n} \nu_{i,k} R_k \quad \forall\ \text{i} = 1 \ \ldots\ \text{n species}$	(4)
Solid phase energy balance with internal limitations	$\left(\rho_p c_{p,p}\right)\frac{\partial T_p}{\partial t} = -\lambda_{eff,p}\frac{1}{{r_p}^m}\frac{\partial}{\partial r_p}\left({r_p}^m\frac{\partial T_p}{\partial r_p}\right) + \rho_p \sum_{j=1}^{N_r}\left(-\Delta H_{R,j}\right)\ R_j$	(5)
Solid phase species balance with internal limitations	$\frac{\partial C_{i,p}}{\partial t} = -D_{eff,i}\frac{1}{{r_p}^m}\frac{\partial}{\partial r_p}\left({r_p}^m\frac{\partial C_{i,p}}{\partial r_p}\right) - \rho_p \sum_{k=1}^{n} \nu_{i,k} R_k \ \forall\ \text{i} = 1 \ \ldots\ \text{n species}$	(6)
Gas phase Boundary Conditions	$T_g = T_0 \quad at \quad z = 0$ $\frac{\partial T_g}{\partial z} = 0 \quad at \quad z = L$ $C_{i,g} = C_{i,0} \quad at \quad z = 0.\ \forall\ \text{i} = 1 \ \ldots\ n\ \text{species}$ $\frac{\partial C_{i,g}}{\partial z} = 0 \quad at \quad z = 0.\ \forall\ \text{i} = 1 \ \ldots\ n\ \text{species}$	(7)
Solid phase Boundary Conditions (for Eq. 5 and 6)	$\alpha_p\left(T_p^{R_p} - T_g\right) = \lambda_{eff,p}\frac{\partial T_p}{\partial r_p} \quad at \quad r_p = R_p\ and\ \forall z \in [0, L]$ $k_g\left(C_{i,p}^{R_p} - C_{i,g}\right) = D_{eff,i}\frac{\partial C_{i,p}}{\partial r_p}\ at \quad r_p = R_p\ and\ \forall z \in [0, L]$ $\frac{\partial T_p}{\partial r_p} = 0 \quad at \quad r_p = 0\ and\ \forall z \in [0, L]$ $\frac{\partial C_{i,p}}{\partial r_p} = 0 \quad at \quad r_p = 0\ and\ \forall z \in [0, L]$	(8)
Reactor Initial conditions	$C_{i,g} = 0 \ \ and \ \ T_g = T_0 \ \ at \ \ t = 0\ and \ \ \forall z \in [0, L]$	(9)

Particle Initial conditions	$C_{i,p} = 0 \quad and \quad T_p = T_0 \quad at \quad t = 0$ (for Eq. 3 and 4) $C_{i,p} = 0 \quad and \quad T_p = T_0 \quad at \quad t = 0 \; and \quad \forall r_p \in [0, R_p]$ (for Eq. 5 and 6)	(10)

A more complex heterogeneous model, on the other hand, accounts for internal gradients within the particles. This model integrates the balance Equations (5) and (6), as reported in Table 3.2. These equations describe the spatial variation of temperature and concentration inside the catalyst pellets, typically requiring the solution of partial differential equations in radial coordinates. Such models are essential when intra-particle transport limitations significantly affect reaction rates and thermal behavior. In Equations (5) and (6) of Table 3.2, the variable r_p is a radial coordinate in the case of cylinder or sphere geometry and a coordinate normal to the two flat faces of a flat plate, measured from an origin in the center plane, in the case of slab geometry. For these three geometries the exponent m refers to the catalyst pellet geometry and has the value of 0 in a slab, 1 in a cylinder and 2 in a sphere (Jackson, 1977).

Building upon this framework, it is also essential to consider how mass diffusion is modeled within porous media, particularly under multicomponent conditions.

To clarify this section, the species balance equation for the particle (represented by Equation 6 in the approximated model of Table 3.2) can be rewritten as follows:

$$\varepsilon c \frac{\partial x_i}{\partial t} + u_c^s \frac{\partial x_i}{\partial r} = -\frac{1}{r^2}\frac{\partial}{\partial r}(r^2 J_i^e) + S_i - \sum_{i=1}^{n} S_i \text{ (mole based)} \tag{3.1}$$

In this formulation:

- The term $-\frac{1}{r^2}\frac{\partial}{\partial r}(r^2 J_i^e)$ represents diffusive transport, describing the radial flux of species i due to concentration gradients.
- The term $u_c^s \frac{\partial x_i}{\partial r}$ accounts for convective transport, associated with the movement of species i due to the superficial velocity within the particle.
- The source terms S_i represent generation or consumption of species due to chemical reactions occurring within the particle.
- The term $\sum_{i=1}^{n} S_i$ stems from the enforcement of the continuity equation inside the mass species balance equation.

For completeness, a brief review of the most used multicomponent diffusion flux models for porous media is presented here. The choice of the model affects the description of mass transport within catalytic pellets, as transport in such systems is often limited by diffusion phenomena occurring at the pore scale, frequently under multicomponent conditions. Depending on the assumptions made, one can adopt a more or less accurate closure of the diffusive flux, using models that may or may not account for species interactions, molecular collisions with the pore walls (Knudsen diffusion), or the geometry of the porous medium (Solsvik and Jakobsen, 2012a).

The simplest model is Fick's law, which assumes that the diffusive flux of a species is proportional to the gradient of its concentration (Equation (1) of Table 3.3). This approach is valid for binary or dilute mixtures but neglects multicomponent interactions. The more general Maxwell-Stefan model describes such molecular interactions through a coupled system of nonlinear equations using the so-called effective diffusivities and becomes essential in the presence of multiple chemically active species (Equation (2) of Table 3.3). The Wilke model is a Fick type model that estimates the effective diffusivity of a species in a multicomponent gas mixture assuming that each species diffuses through a stagnant gas mixture composed of other species, and calculates the apparent diffusivity as a weighted average of the binary diffusivities, considering the mole fractions. The model is simple to implement and useful when a complete Maxwell-Stefan model would be too expensive to compute (Equation (3) of Table 3.3).

The Dusty Gas model extends the Maxwell-Stefan formulation by also including Knudsen diffusion, which becomes significant when the pore size is comparable to the mean free path of the gas molecules (Equation (4) of Table 3.3). The Wilke-Bosanquet model characterizes intermediate diffusion regimes by employing a reciprocal summation of molecular and Knudsen diffusion, drawing an analogy with electrical conductivity (Equation (5) of Table 3.3).

Table 3.3 Diffusion models of chemical species inside a mixture of at least two components, adapted from (Solsvik and Jakobsen, 2012b)

Model	Description	Mathematical formulation	
Fick	Simple to use; valid for binary or very dilute mixtures; assumes constant binary diffusivity.	$\mathbf{J}_\mathrm{i} = -D_{ij}\nabla c_i$	(1)
Maxwell-Stefan	Accounts for interactions among all species; more accurate for multicomponent systems; mathematically more complex.	$\mathbf{J}_\mathrm{i} = \frac{-\mathrm{c}\nabla \mathrm{x}_\mathrm{i} + \sum_{\mathrm{j}=1,\,\mathrm{j}\neq\mathrm{i}}^{\mathrm{n}} \frac{\mathbf{J}_\mathrm{j}\mathrm{x}_\mathrm{i}}{\widetilde{\mathrm{D}_{\mathrm{ij}}}}}{\sum_{\mathrm{j}=1,\,\mathrm{j}\neq\mathrm{i}}^{\mathrm{n}} \frac{\mathrm{x}_\mathrm{j}}{\widetilde{\mathrm{D}_{\mathrm{ij}}}}}$	(2)
Wilke	Fick-type model using an effective diffusivity (or Wilke diffusivity) derived assuming diffusion of a component i in a mixture of stagnant gases	$D_{i,mix} = \frac{1 - x_i}{\sum_{j=1,\,j\neq i}^{n} \frac{x_j}{\widetilde{D_{ij}}}}$ $\mathbf{J}_\mathrm{i} = -D_{i,\mathrm{mix}}\nabla c_i$	(3)
Dusty Gas	Includes both molecular and Knudsen diffusion; requires many parameters; suitable when both mechanisms are relevant.	$\boldsymbol{J}_i = \frac{\sum_{j\neq i}^{n} \frac{J_j x_i}{\widetilde{D_{ij}}} - \frac{c_i V^*}{D_{iK}} - c\nabla x_i}{\sum_{j\neq i}^{n} \frac{x_j}{\widetilde{D_{ij}}} + \frac{1}{D_{iK}}}$	(4)
Wilke-Bosanquet	Fick-type model, the effective diffusivity is determined from the reciprocal sum of the Wilke diffusion coefficient and Knudsen contributions.	$\frac{1}{D_i'} = \frac{1}{D_{iW}} + \frac{1}{D_{iK}}, D_{\mathrm{eff,i}} = \frac{\varepsilon_p D_i'}{\tau}$ $\mathbf{J}_\mathrm{i} = -D_{eff,i}\nabla c_i$	(5)

The models of Table 3.3 are written on molar basis. In the work of (Solsvik et al., 2012) the differences between the mass and molar formulation of such models are analyzed.

In the dusty gas model, a term proportional to the convective velocity of the gas within the particle (V*) appears. This convective phenomenon, which develops due to pressure gradients inside the particle - caused by temperature gradients or changes in the number of moles resulting from the ongoing chemical reaction - is typically accounted for by applying a momentum balance, often approximated using Darcy's law:

$$v = -\frac{B}{\mu}\nabla p \tag{3.2}$$

In this study, each of the introduced models will adopt the simplified Fickian diffusion model. This choice is supported by the findings of (Guffanti et al., 2020), who demonstrated that, under comparable operating conditions, the use of more complex diffusion-reaction models yields results that are nearly indistinguishable from those obtained with Fick-type formulations. Their analysis of methanol synthesis and dehydration processes showed that

the average reaction rate profiles remained consistent across both modeling approaches, with negligible differences.

- *The linear driving force models*

Returning briefly to the heterogeneous reactor model (Table 3.2), a common aspect between the two particle models presented in Equations (3) to (6) of Table 3.2 includes heat and mass exchanges between the catalyst and the bulk gas.

The heat and mass exchanges are modelled by the linear driving forces. The mass and heat fluxes between the bulk gas and the particles (reported as N_i and q in the following Equation 3.3) are proportional to the concentration and temperature gradients across the stagnant gas film surrounding each pellet. Under the linear driving-force assumption, the molar flux of each species and the heat flux are expressed, respectively, as

$$N_i = k_m \cdot \left(C_{i,p}^{R_p} - C_{i,g}\right), \qquad q = k_q \cdot \left(T_p - T_g\right) \tag{3.3}$$

The mass and heat transfer coefficients, k_m and k_q, are related to the dimensionless Sherwood and Nusselt numbers by

$$k_m = \left(Sh \cdot D_{i,mix}\right)/\left(2R_p\right), \qquad k_q = \left(Nu \cdot \lambda_G\right)/\left(2R_p\right) \tag{3.4}$$

where R_p is the particle radius, $D_{i,mix}$ the diffusivity of species i in the gas mixture, and λ_g the gas thermal conductivity. The Sherwood and Nusselt numbers are obtained from empirical correlations of the form $Sh = f(Re, Sc), \quad Nu = f(Re, Pr)$ in which $Re = (\rho \cdot u \cdot L)/\mu, \quad Pr = \left(\mu \cdot c_p\right)/k, \quad Sc = \mu/\left(\rho \cdot D_{i,mix}\right)$ are, respectively, the Reynolds, Prandtl and Schmidt numbers (with ρ fluid density, u superficial velocity, L characteristic length, μ viscosity, c_p heat capacity, k fluid conductivity).

Most experimental heat and mass transfer data for multiparticle systems like fixed and fluidized beds are reported in the literature as plots of a dimensionless *j-factor* versus Reynolds number. Notably, under conditions of fully developed turbulent flow or, more generally, in many gas-solid systems, it is often found that mass and heat transfer are analogous. This is captured by the Chilton-Colburn analogy (Perry and Green, 1997), which states that:

$$j_H = Nu/\left(Re \cdot Pr^{1/3}\right) = Sh/\left(Re \cdot Sc^{1/3}\right) = j_D \tag{3.5}$$

where j_H and j_D are the *j-factors* or correlation factors for which empirical fit of experimental data can be found in the literature as functions of the *Re* number (Pfeffer, 1964).

Although the Chilton-Colburn analogy was originally formulated for fully developed turbulent flow in tubes ($Re > 10^4$), it has been shown to hold with good accuracy in packed beds over much lower Reynolds numbers. For example, (Wakao et al., 1979) correlated both heat and mass transfer in spherical-particle beds by:

$$Nu = 2 + 1.1 \cdot Re^{0.6} \cdot Pr^{1/3}, \quad Sh = 2 + 1.1 \cdot Re^{0.6} \cdot Sc^{1/3} \tag{3.6}$$

and (Malling and Thodos, 1967) demonstrated the equivalence of j_H and j_D in beds of spheres for 185 < Re < 8500. Thus, by invoking the Chilton-Colburn analogy, one may infer mass-transfer coefficients directly from heat-transfer data (or vice versa), significantly streamlining the modeling of transport phenomena in fixed-bed catalytic reactors.

Each parameter appearing in the equations presented in this section is defined in the nomenclature. Building on this foundation, additional closure models will be introduced in the sections describing the specific models employed in this thesis, if necessary.

3.3.1.2 Continuum Models: The Pseudo-Homogeneous Model

Although homogeneous systems are, by definition, those in which the reactants, catalyst, and inert material all exist in a single phase within the reactor, the terms pseudo-homogeneous and homogeneous are often used interchangeably when referring to fixed-bed reactor models. (Stegehake et al., 2019).

Pseudo-homogeneous models are employed when mass and heat transfer between the fluid and solid phase can be assumed to occur instantaneously, leading to a temperature and concentration field throughout the reactor which is equal both for the gas and the solid phases. These models are often used when inter- and intra- particle mass and heat transfer resistances are negligible.

Table 3.4 summarizes a set of governing equations which are an example of a one dimensional (1-D) pseudo-homogeneous model used to formalize mass and energy transport in a fixed bed reactor.

Equation (1) of Table 3.4 represents the gas-phase energy balance, accounting for axial dispersion, convective heat transport, heat exchange with the wall, and the heat released or absorbed by chemical reactions occurring within the catalyst pellets. Equation (2) of Table 3.4 describes the species mass balance in the gas phase, including axial dispersion,

convection, and the net rate of consumption or production due to chemical reactions. The corresponding boundary conditions, presented in Equation (3) of Table 3.4, define the behavior of temperature and species concentrations at the reactor inlet and outlet, assuming Danckwerts type conditions (Danckwerts, 1953). Finally, Equation (4) of Table 3.4 specifies the initial conditions, with uniform temperature and zero species concentration throughout the reactor domain at the start of the process. This system of partial differential equations forms the basis for the numerical simulation of the reactor's dynamic behavior under non-isothermal conditions.

Table 3.4 1-D Pseudo-homogeneous fixed-bed reactor models example used in this doctoral dissertation

Description	**Equations**	
Gas-phase energy balance	$\left(\rho_p c_{p,p}(1-\varepsilon_b)+\rho_g c_{p,g}\varepsilon_b\right)\frac{\partial T}{\partial t} = K_{\text{ax}}\frac{\partial^2 T}{\partial z^2}-\rho_g u_0 c_{p,g}\frac{\partial T}{\partial z}-h_{ov}\frac{4}{D_i}(T-T_w)+\eta\rho_p\sum_{j=1}^{N_{r,i}}\left(-\Delta H_{R,j}\right)R_j$	(1)
Gas-phase species balance	$\varepsilon_b\frac{\partial C_i}{\partial t}=\varepsilon_b D_{\text{ax}}\frac{\partial^2 C_i}{\partial z^2}-\frac{\partial(u_0 C_i)}{\partial z}-\eta\rho_p\sum_{k=1}^{N_{r,i}}\nu_{i,k}R_k$	(2)
Boundary conditions	$-D_{ax}\frac{\partial C_i}{\partial z}=\frac{u}{\varepsilon_b}\left(C_{f,i}-C_i\right)\quad at\quad z=0$ $\frac{\partial C_i}{\partial z}=0\quad at\quad z=L$ $-K_{ax}\frac{\partial T}{\partial z}=u\rho_g c_g\left(T_f-T\right)\quad at\quad z=0$ $\frac{\partial T}{\partial z}=0\quad at\quad z=L$	(3)
Initial conditions	$C_i(z,0)=0$ and $T(z,0)=T_0\quad \forall z\in[0,L]$ and $\forall r\in[0,R_r]$	(4)

In Equation (1) of Table 3.4 the coefficient ($4/D_i$) arises from the surface-area to volume ratio of a cylindrical geometry. In Equation (1) and (2) of Table 3.4, the production terms incorporate the effectiveness factor η to address internal diffusion limitations. In the pseudo-homogeneous formulation, the effectiveness factor quantifies both intra-particle and inter-particle transport resistances. It represents the ratio of the actual reaction rate within a catalyst pellet to the reaction rate assuming uniform bulk conditions throughout the particle. This ratio is also called global effectiveness factor (Froment et al., 2011; Solsvik and Jakobsen, 2012b).

Table 3.5 presents an extended formulation for a pseudo-homogeneous model that accounts for radial non-uniformities in concentration and temperature. In fact, the model includes both axial and radial transport phenomena. Compared to the simplified one-dimensional model of Table 3.4, this two-dimensional (2-D) model provides a more detailed representation of the system. Specifically, the gas-phase energy balance now includes a radial conduction term with effective radial thermal conductivity K_{rad}, while the species balance includes radial dispersion via the term with radial dispersion D_{rad}. These additions allow the model to capture radial gradients in temperature and concentration, whose relevance depends on a combination of geometric and physical factors, such as reactor diameter, transport properties, and reaction exothermicity, and can be assessed through criteria based on dimensionless numbers, such as the Biot number, or through criteria like those proposed by Mears (1976) or Dixon (1996).

Moreover, the heat balance boundary conditions include h_w, the wall heat transfer coefficient, which accounts for convective heat exchange between the reactor wall and its surroundings (Dixon, 2012). This differs from the 1-D formulation, where the heat exchange with the environment is included directly within the energy balance equation through an overall heat transfer coefficient h_{ov},. It is also important to note the distinction between h_{ov}, representing the overall heat transfer coefficient in the 1-D model (which accounts for both the effective radial thermal conductivity K_{rad} and the wall heat transfer coefficient h_w (Dixon, 1996)), and h_w, which refers specifically to the local convective exchange at the reactor wall in the 2-D model.

This type of model is computationally more demanding, but when the assumptions for applying a pseudo-homogeneous model are met (Mears, 1976; Stegehake et al., 2019), it becomes necessary to evaluate phenomena such as the cooling effect of a reactor jacket.

Moreover, a two-dimensional model is particularly well-suited for reactor design studies, especially for optimizing the radial distribution of active sites, adsorbents, or inert materials, as demonstrated in the work by Cutillo et al., 2025.

Table 3.5 2-D Pseudo-homogeneous fixed-bed reactor models example used in this doctoral dissertation.

Description	Governing Equations	
Gas-phase energy balance	$\left(\rho_p c_{p,p}(1-\varepsilon_b)+\rho_g c_{p,g}\varepsilon_b\right)\frac{\partial T}{\partial t} = K_{\text{ax}}\frac{\partial^2 T}{\partial z^2}+K_{\text{rad}}\frac{1}{r}\frac{\partial}{\partial r}\left(r\frac{\partial T}{\partial r}\right)-u_0\rho_g c_g\frac{\partial T}{\partial \text{z}}+\eta\rho_p\sum_{j=1}^{N_r}\left(-\Delta H_{R,j}\right)R_j$	(1)
Gas-phase species balance	$\varepsilon_b\frac{\partial C_{\text{i}}}{\partial t}=\varepsilon_b D_{\text{ax}}\frac{\partial^2 C_{\text{i}}}{\partial z^2}+\varepsilon_b D_{\text{rad}}\frac{1}{r}\frac{\partial}{\partial r}\left(r\frac{\partial C_{\text{i}}}{\partial r}\right)-u_0\frac{\partial C_{\text{i}}}{\partial \text{z}}-\eta\rho_p\sum_{k=1}^{n}\nu_{i,k}R_k$	(2)
Boundary conditions	$-D_{ax}\frac{\partial C_i}{\partial z}=\frac{u}{\varepsilon_b}\left(C_{f,i}-C_i\right)\quad at\quad z=0\quad and\quad \forall r\in[0,R_r]$ $\frac{\partial C_i}{\partial z}=0\quad at\quad z=L\quad and\quad \forall r\in[0,R_r]$ $\frac{\partial C_i}{\partial r}=0\quad at\quad r=0\quad and\quad \forall z\in[0,L]$ $\frac{\partial C_i}{\partial r}=0\quad at\quad r=R_r\quad and\quad \forall z\in[0,L]$ $-K_{ax}\frac{\partial T}{\partial z}=u\rho_g c_g\left(T_f-T\right)\quad at\quad z=0\quad and\quad \forall r\in[0,R_r]$ $\frac{\partial T}{\partial z}=0\quad at\quad z=L\quad and\quad \forall r\in[0,R_r]$ $-K_{rad}\frac{\partial T}{\partial r}=h_w(T-T_w)\quad at\quad r=0\quad and\quad \forall z\in[0,L]$ $\frac{\partial T}{\partial r}=0\quad at\quad r=R_r\quad and\quad \forall z\in[0,L]$	(3)
Initial conditions	$C_i(z,r,0)=0$ and $T(z,r,0)=T_0\quad \forall \text{z}\in[0,L]$ and $\forall r\in[0,R_r]$	(4)

3.3.1.3 Continuum Models: Criteria for their choice

To further support the choice of the most appropriate reactor model, the literature provides well-established criteria to assess whether heat and mass transfer resistances can be neglected (Froment et al., 2011; Stegehake et al., 2019). These criteria, derived from simplified transport-reaction models, help identify whether the system can be considered under purely kinetic control or whether transport limitations must be explicitly modeled. They cover intraparticle and interparticle transport for both heat and mass, as well as axial and radial dispersion phenomena. Table 3.6 summarizes some of the most widely adopted criteria, reported by classical sources such as (Mears, 1971), (Weisz and Hicks, 1962), (Froment et al., 2011), and (Carberry, 2001). Each criterion is expressed in an inequality or dimensionless form, involving measurable or estimable parameters. By evaluating these

relationships, the relative importance of transport processes can be systematically screened before kinetic parameter estimation or scale-up, ensuring that the selected model accurately captures the controlling phenomena. Selecting the most appropriate model requires a careful assessment of which effects can be neglected in the governing equations.

For instance, considering the heterogeneous model equations - formalized in Table 3.2 - one can determine whether to account for concentration gradients within the catalyst pellet (i.e., intraparticle mass transfer) by applying the (Weisz and Prater, 1954) criterion, as presented in Equation (2) of Table 3.6. Similarly, to decide whether radial mass dispersion should be considered, the criterion proposed by (Mears, 1976), shown in Equation (8) of Table 3.6, can be used.

The second column of Table 3.6 indicates which effect can be considered negligible when the corresponding criterion - expressed as the inequality reported in the third column - is satisfied. In addition to these specific criteria, dimensionless numbers are often employed to understand which phenomenon most influences the process, i.e. the so-called "limiting step." Examples include the Biot number, which compares internal to external heat transfer resistance; the Thiele modulus, relating reaction rate to diffusivity (Equation (2) of Table 3.6 is the extended Thiele modulus proposed by Bischoff, (1967)); and the Péclet number, assessing the relative importance of convection and diffusion.

Table 3.6 Criteria for selecting among different reactor models.

Reference/Author	Can be neglected	Criteria formulation	
(Froment et al., 2011; Mears, 1971)	Intraparticle heat transfer	$\frac{(-\Delta H)(r_A \rho_s)_{obs}(R/3)}{h_f T} < 0.05\frac{RT}{E}$	(1)
(Bischoff, 1967; Weisz and Hicks, 1962; Weisz and Prater, 1954),	Intraparticle mass transfer	$\Phi = \frac{(r_A \rho_s)_{obs} L^2 g(C_s^s)}{2\int_{C_{s,eq}}^{C_s^s} D_{eA}(C)\ g(C)\, dC} \ll 1$	(2)
(Mears, 1971)	Interparticle heat transfer (gas-solid film)	$\frac{(-\Delta H) r_A \rho_B d_p}{2 h_f T} < 0.15\frac{RT}{E}$	(3)
(Carberry, 2001)	Interparticle mass transfer (gas-solid film)	$Ca = \frac{\mathrm{r_{obs}}}{\mathrm{k_g}\, a'\, \mathrm{c_b}} = \frac{\mathrm{c_b} - \mathrm{c_s}}{\mathrm{c_b}} \ll 0.05$	(4)
(Young and Finlayson, 1973)	Axial dispersion mass transfer	$\frac{r_{A0} \rho_B d_p}{u_s C_0} \ll Pe_{ma}$	(5)
(Young and Finlayson, 1973)	Axial dispersion heat transfer	$\frac{(-\Delta H) r_{A0} \rho_B d_p}{(T_o - T_w) u_g \rho_g c_p} \ll Pe_{ht}$	(6)

(Mears, 1976; Stegehake et al., 2019)	Radial dispersion heat transfer	$\left\lvert\frac{\Delta H\,\mathcal{R}\,d_t^2}{k_{e,r}\,T_w}\right\rvert\frac{E}{RT} < \frac{1.6}{1+\frac{8}{Bi_w}}$	(7)
(Mears, 1976)	Radial dispersion mass transfer	$\frac{d_t}{d_p} > 8$	(8)

Another reason for selecting one model over another is the opportunity to introduce additional degrees of freedom in reactor design. By employing models that account for the spatial distribution of state variables within the catalyst, it becomes possible to formulate optimization problems that extend beyond conventional structural parameters, such as residence time or operating temperature. For example, more advanced models enable the analysis of factors such as the distribution of active sites within the catalyst or the particle size, which can be deliberately tailored to improve overall reactor performance (Bizon et al., 2021; Cutillo et al., 2025; Guffanti et al., 2020, 2021).

3.3.1.4 Continuum Models: Gas phase momentum balance and pressure drop

In the mathematical modeling of fixed-bed reactors, the momentum balance equation governs the pressure distribution along the reactor and is essential for predicting flow behavior, particularly in systems where pressure drop may influence reaction kinetics or transport phenomena. However, due to the complexity of solving the full Navier-Stokes equations in porous media, this balance is often approximated using empirical correlations. The most widely adopted formulation is the Ergun equation, which provides a semi-empirical relationship between pressure drop and flow rate, accounting for both viscous and inertial contributions. For a cylindrical packed bed under steady-state conditions, the Ergun equation is expressed as (Ergun and Orning, 1949):

$$\frac{dP}{dz} = -\left(\frac{150\mu(1-\varepsilon)^2}{\varepsilon^3 d_p^2}\right)u - \left(\frac{1.75\rho(1-\varepsilon)}{\varepsilon^3 d_p}\right)u\cdot|u| \tag{3.7}$$

The first term corresponds to viscous losses, dominant at low Reynolds numbers, while the second term accounts for inertial losses, which become significant at higher flow rates. The Ergun equation is valid across a wide range of Reynolds numbers and is particularly suitable for modeling gas-phase flow in packed beds.

Despite its utility, in the models employed throughout this dissertation, the pressure drop along the reactor is assumed negligible. This is justified by the operating conditions and reactor geometry considered, which lead to low Reynolds numbers, moderate flow rates, and

minimal pressure gradients as predicted by the Ergun equation. As noted by Froment, (1972), in most cases the pressure drop is sufficiently small to allow the use of a mean value for the total pressure in the calculations. Neglecting the momentum balance therefore reduces computational complexity without compromising the accuracy of the predicted concentration and temperature profiles.

3.3.2 Estimation Methods for Predicting Operating Limits of Fixed Bed Reactors

Fixed-bed reactors operating under highly exothermic reactions require accurate safety assessments to prevent thermal runaway. The estimation methods provide a rapid and practical approach to identifying safe operating limits by employing simplified mathematical models or empirical correlations, avoiding the complexity of solving full reactor models. These methods rely on sensitivity analysis, which evaluates how variations in kinetic, transport, operating or geometric parameters affect the reactor. They require minimal computational effort and are commonly used for quick preliminary assessments. There are various methods to predict the safety limits of fixed-bed reactors, differing in complexity and accuracy. The Empirical Safety Indices (SREST, Simplified Reactor Safety Estimation Technique) uses historical data. With this method, safety conditions must meet inequality constraints based on dimensionless groups like Damköhler, Stanton, Lewis numbers, or safety indices. Constraints can substitute systematic model-based analysis and vary in complexity. Less computationally demanding indices utilize direct practical tests under non-adiabatic conditions, which involve significant costs. Such tests help characterize the hazards related to primary (desired) and secondary (undesired) reactions. More elaborated reaction hazards try to characterize the interactions between primary and secondary reactions (Maria and Stefan, 2010; Nicolae and Maria, 2007). In summary, estimation methods have the benefits of low computational requirements and ease of application. However, they tend to be less accurate and necessitate a detailed understanding of the process, typically gained through experimental data or numerical simulations (Froment et al., 2011). More precise methods for predicting safety limits can be developed using a process/reactor model, depending on the available information about kinetics, thermodynamics, and reaction pathways (Maria and Stefan, 2010).

3.3.4 Cell models, Stochastic models and Particle resolved models

Below are reported additional fixed-bed reactor modeling techniques used in the literature.

Cell models represent fixed-bed reactors as a discrete structure composed of several simpler subsystems, such as assemblies of CSTRs (Continuous Stirred-Tank Reactors). These models have been used relatively rarely in the literature and, in recent years, have seen only limited development (Elnashaie and Elshishini, 1994).

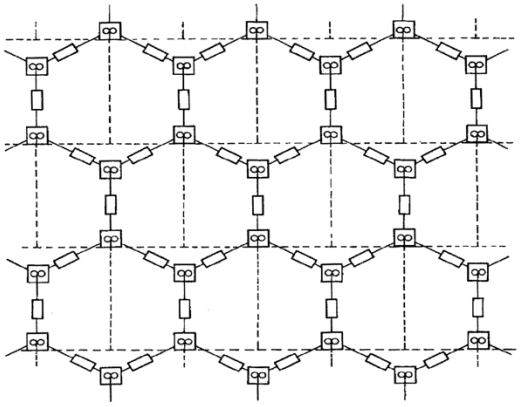

Figure 3.2 Examples of cell model (Schnitzlein and Hofmann, 1987).

Stochastic models, on the other hand, describe the process occurring within a fixed-bed reactor as random. In a first attempt to achieve this goal, researchers postulated that the parameters of deterministic models would match a random distribution. The integration of random variables to represent the parameters of deterministic models does not result in a modification of the fundamental characteristics of the model; however, it does introduce a substantial degree of variation (Schnitzlein and Hofmann, 1987). Another approach to stochastic models is to use stochastic reactor models in which fluid flows through several randomly selected paths. (Patak, 1973). Although stochastic models provide a more realistic description of a packed bed, the rapidly growing complexity of the mathematical problem makes these models less attractive. (Schnitzlein and Hofmann, 1987).

The *particle-resolved modeling* approach involves detailed computational fluid dynamics (CFD) simulations that account for the complex geometry of fixed-bed reactors. This is achieved by first generating a 3D structure of the packed bed using the discrete element method (DEM) or alternative tools like the Bullet physics library for collision detection. The resulting geometry is then processed through CAD and meshed for CFD simulations, enabling the simultaneous solution of heat, mass, and momentum balances (Partopour and Dixon, 2017). Particle-resolved modeling offers high accuracy by capturing multiscale transport and reaction phenomena through detailed CFD simulations. However, a

comprehensive understanding of the complex physical and chemical interactions across all relevant scales is still lacking, often necessitating simplifications in diffusion and reaction modeling (Das et al., 2018; Dixon, 2017). This limitation, combined with the method's high computational demands, restricts its application to simplified or small-scale systems (Dixon, 2017). Many models simplify catalyst particles as non-porous solids, ignoring important intra-particle mass transport effects, while modelling intra-particle heat transfer (Eppinger et al., 2016). While pore-resolved simulations have been developed for individual particles (Wehinger et al., 2017), they often rely on simplified kinetics (Dixon, 2017). Coupling CFD with microkinetic and pore-scale models has shown success in simpler systems like monolithic catalysts (Wehinger et al., 2017), but applying this to industrial-scale random beds remains difficult due to their geometric complexity and the lack of unified multiscale solvers. Despite these challenges, particle-resolved modelling continues to be a valuable tool for exploring heterogeneous catalysis.

3.4 Surface kinetics

Surface kinetics, also referred to as intrinsic kinetics, represent the fundamental mechanism by which heterogeneous catalytic reactions occur. These reactions take place at the active sites located on the surface of the catalyst, including both external surfaces and internal pore walls. When the control volume is restricted to the catalyst surface and a defined composition of reactant gases is present within the pellet, the influence of mass transport from the bulk gas phase to the particle core is neglected. This allows the focus to be placed exclusively on the elementary steps of the surface reaction mechanism.

A typical heterogeneous catalytic reaction proceeds through three sequential steps:

Step 1. Chemisorption of reactant molecule. The reactant molecule (e.g., species A) is adsorbed onto the catalyst surface, binding to an active site. This step, known as chemisorption, is distinct from physical adsorption due to the formation of a strong chemical bond. It is characterized by a significant activation energy, typically exceeding 80 $kJ \cdot mol^{-1}$ and occasionally reaching values above 400 $kJ \cdot mol^{-1}$.

Step 2. Surface reaction. Once adsorbed, the molecule undergoes transformation via surface reaction. This may involve interaction with another adsorbed species (dual-site mechanism), reaction with a molecule from the gas phase (single-site mechanism), or decomposition directly on the site. The reaction kinetics depend on the nature of the active site and the local concentration of reactants.

Step 3. Desorption of product molecule. The final step involves the desorption of the product molecule from the surface, thereby regenerating the active site and allowing the catalytic cycle to continue.

To illustrate these steps, consider a reversible reaction A ↔ P occurring on a catalyst with a defined concentration of active sites. The reaction mechanism and corresponding rate expressions are summarized in Table 3.7.

Table 3.7 example of the three steps of the intrinsic kinetic

Steps	**Equation**	**Rate equation**
Chemisorption of A	$A^g + S_S \leftrightarrow AS_S$	$r_1 = k_a C_A \sigma_S - k'_a \sigma_{AS}$
Surface reaction	$AS_S \leftrightarrow PS_S$	$r_2 = k\sigma_{AS} - k'\sigma_{PS}$
Desorption of P	$PS_S \leftrightarrow P^g + S_S$	$r_3 = k_d \sigma_{PS} - k'_d C_P \sigma_S$

Where:

- the concentration of A, P are C_A, C_P ;
- the concentration of S (catalyst active sites) in moles per surface area is σ_S
- the concentration of the absorbed molecule in moles per surface area is σ_{AS}
- the concentration of product still attached on the active site in moles per surface area is σ_{PS}

Depending on which step is rate-limiting, the overall reaction rate can be approximated by a simplified expression derived from the dominant elementary step. The kinetic constants involved are typically determined through experimental data fitting.

To enhance the intrinsic reaction rate, increasing the concentration of active sites is essential. This is commonly achieved by enlarging the catalyst surface area, which can be done by reducing pore size or increasing pore tortuosity. However, this strategy introduces a trade-off: while a higher surface area promotes reaction kinetics, it simultaneously impairs mass transport within the pellet due to increased diffusion resistance. Therefore, an optimal balance must be established between surface area and diffusivity to maximize overall reactor performance.

3.5 Mathematical models of Self-Ignition

An additional line of research developed in this work concerns the modeling of auto-ignition phenomena in heterogeneous reactive systems.

These models are essential for analyzing catastrophic events characterized by so-called run-away reactions. In such processes, the reactants are almost entirely converted into products in a sudden and uncontrolled manner, releasing a significant amount of energy in a very short time.

Unlike the fixed-bed reactors previously described, these systems spontaneously evolve toward auto-ignition. Therefore, accurately predicting this behavior is crucial for the safe design and optimization of the involved industrial processes.

3.5.1 Classification of Self-Ignition models

Among the earliest adopted models for predicting self-ignition phenomena in porous reactive media is the Frank-Kamenetskii theory (Frank-Kamenetskii, 1955). This model provides a simplified framework for assessing the thermal stability of a self-igniting system by analyzing the balance between heat generation and heat dissipation. It is particularly suited for systems where reaction kinetics follow a single-step Arrhenius-type mechanism and heat transfer occurs primarily by conduction, as these represent the core assumptions upon which the model is built.

Furthermore, the model assumes that the activation energy is sufficiently high, such that $E/RT_0 \ll 1$; heat transfer within the material occurs exclusively by conduction, while heat exchange at the boundaries is governed by convection and radiation. It also assumes a high value of the Biot number ($Bi \to \infty$) ensuring that the surface temperature matches the ambient temperature. Additionally, the material is considered isotropic and homogeneous, with constant physical properties. Under the assumption of steady-state conditions and slab geometry, the governing energy balance equation simplifies to those reported in Table 3.8

Table 3.8 Frank-Kamenetskii simplified model of self-ignition

Description	Equations	
	$C_p \rho \frac{\partial T}{\partial t} = \lambda \frac{\partial^2 T}{\partial x^2} + q$	(1)
Energy balance	$\frac{d^2T}{dx^2} = \dot{q}'''$	(2)
Heat generation term	$\dot{q}''' = \rho Q A e^{-E/RT}$	(3)
Frank-Kamenetskii parameter	$\delta = \frac{QA\rho L^2}{\lambda} \cdot \frac{E}{RT_0^2} \cdot e^{-E/RT_0}$	(4)
Critical dimension for self-ignition	$L_{\text{crit}} = \sqrt{\frac{\lambda}{QA\rho} \cdot \frac{RT_0^2}{E} \cdot e^{E/RT_0} \cdot \delta_c}$	(5)

The approach introduces a dimensionless parameter, known as the Frank-Kamenetskii parameter (δ), which represents the ratio between heat generation and heat dissipation. When δ exceeds a critical value δ_c, the system no longer admits a stationary solution, and self-ignition is expected to occur.

The Frank-Kamenetskii model is a fast and widely used tool for estimating ignition thresholds in engineering safety assessments. Its simplicity enables analytical solutions and quick evaluations. However, the model presents several limitations arising from its simplifying assumptions. In certain cases, these limitations can be mitigated by applying corrections to the Frank-Kamenetskii parameter δ. For instance, reactant consumption effects have been addressed by Adler and Enig, (1964) through the introduction of the adiabatic temperature rise parameter, meanwhile Takeno and Sato, (1980) studied the dependence of the critical self-ignition parameter δ_c in situations where oxygen diffusion limitations cannot be neglected. These extensions enhance the applicability of the model to more realistic scenarios, although they still rely on the foundational assumptions of the original formulation.

The corrections to the Frank-Kamenetskii parameter δ originate from simplified analyses of more complex models. As an example, the work of Takeno and Sato, (1980) addresses a more advanced formulation by analytically solving a stationary reaction-diffusion problem that includes spatial distributions of both temperature and oxygen concentration.

However, even this improved analysis relies on simplifying hypotheses. The analytical solution derived by Takeno and Sato, (1980) is valid only within a limited range of the oxygen diffusion parameter and becomes less accurate as it increases. In more critical scenarios-such as low oxygen diffusivity or high reaction rates-numerical solutions of the full boundary value problem are required to accurately capture the ignition and extinction behavior. An adaptation of the model employed by Takeno and Sato, (1980) is reported in Table 3.9.

Table 3.9 Steady-state model of self-ignition with

Description	Equations	
Energy balance	$\frac{d^2T}{d\xi^2}+\frac{j}{\xi}\frac{dT}{d\xi}+B\,c^{\,n}\,\exp\left(-\frac{E_n}{T}\right)=0$	(1)
Oxygen balance	$\frac{d^2c}{d\xi^2}+\frac{j}{\xi}\frac{dc}{d\xi}-\gamma\,B\,c^{\,n}\,\exp\left(-\frac{E_n}{T}\right)=0$	(2)
Boundary condition	$T'(0)=0, T(1)=1;$ $c'(0)=0, c(1)=1$	(3)
Dimensionless variables	$\xi=\frac{x}{L}, T=\frac{\Theta}{T_0}, c=\frac{C}{C_0}$	(4)
Dimensionless parameters	$B=\frac{C_0^n A\,p\,Q\,L^2}{\lambda\,T_0}, E_n=\frac{E}{R\,T_0}, \gamma=\frac{\lambda\,T_0}{C_0\,Q\,D}$	(5)
c-T relation	$c(\xi)=1-\gamma\,[T(\xi)-1]$	(6)
Reduced equation in T	$\frac{d^2T}{d\xi^2}+\frac{j}{\xi}\frac{dT}{d\xi}+\delta\,[1-\gamma\,(T-1)]^n\;exp\left(-\frac{E_n}{T}\right)=0$	(7)
Geometric parameter	$j=0\,(flat\ plate),\ j=1\,(cylinder),\ j=2\,(sphere)$	(8)

Moreover, Table 3.9 presents the model reduced to the single state variable *T*, by exploiting the relationship between the variables *c* and *T*.

With the advancement of computational technologies, qualitative analyses based on approximate analytical solutions have gradually given way to more detailed investigations derived from simulation data. In this context, increasingly sophisticated mathematical models have been employed to describe self-heating and self-ignition phenomena.

The description of this phenomenon has attracted increasing interest within the scientific community. As highlighted in the recent review by, research efforts have progressively focused on a detailed analysis of the influence of various factors on pile behavior. Specifically, the following aspects have been investigated:

- Effect of convection
- Effect of the material used (e.g., coal, biomass)
- Effect of water vapor
- Effect of microbial growth
- Effect of variable environmental conditions
- Effect of pile geometry

Representative examples of models developed to describe these phenomena are presented below.

- *Effect of pile geometry and variable environmental conditions*

Table 3.10 presents the governing equations of a reaction-diffusion model used to describe self-ignition phenomena in reactive systems. The model couples mass and energy balances, incorporating nonlinear source terms that account for temperature-dependent reaction kinetics. Although the governing equations and boundary conditions are expressed in general form - applicable to any geometry - the specific definition of the Laplacian operator (∇^2) and the domain boundary ($\partial\Omega_a$) ultimately determines the actual geometry being analyzed. This geometry may take various forms, as illustrated in Figure 3.3.

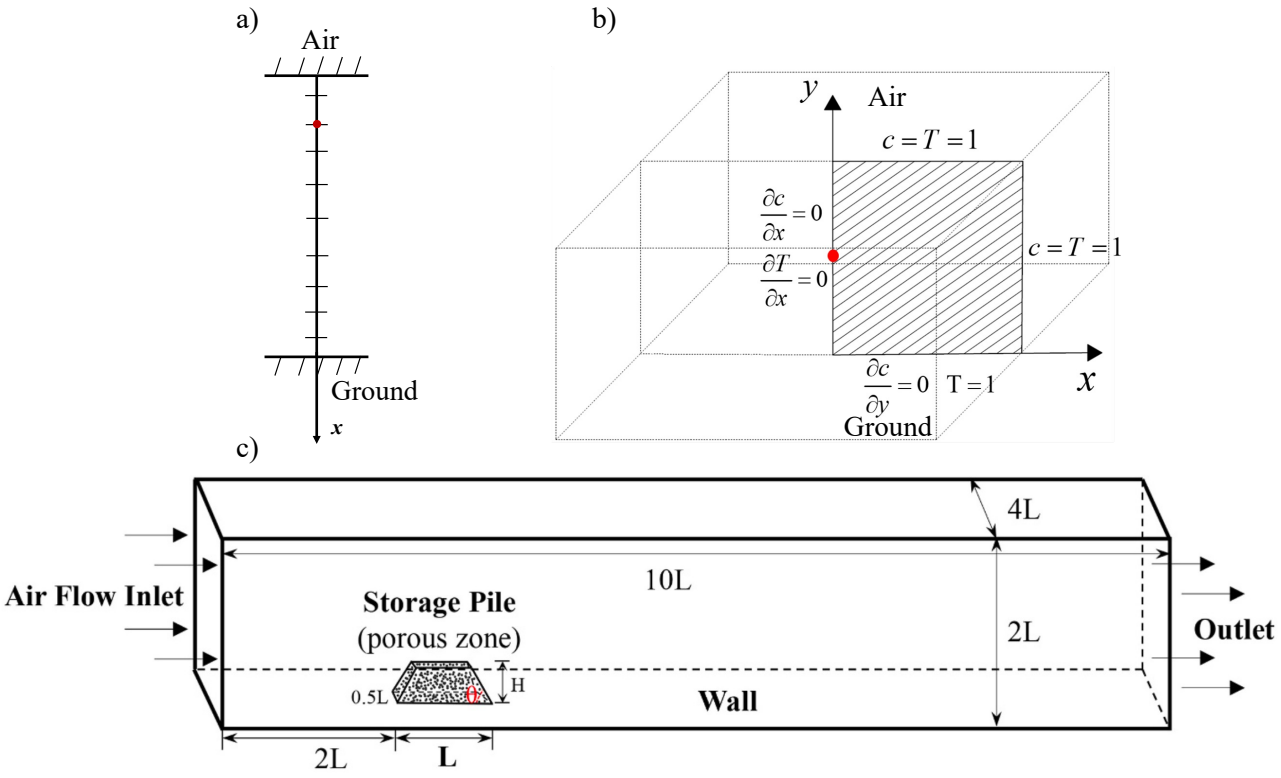

Figure 3.3 Geometrical models used in simulations of self-heating in a storage pile; a) 1-D pile; b) 2-D pile; c) 3-D pile adapted from (Yin et al., 2024).

The boundary conditions (Equations (3) to (6) of Table 3.10) account for both permeable and insulated concentration interfaces, depending on the side of the pile being considered - whether in contact with the atmosphere or with the ground. Meanwhile the initial conditions

(Equations (7) and (8) of Table 3.10) assume a steady-state distribution of temperature and reactant concentration. Notably, the imposed sinusoidal temperature variation at the boundary (Equation (4) of Table 3.10), that depends on the pulsation parameter ω, can be used to model either circadian temperature oscillations or long-term seasonal variations. This model enables the simulation of transient thermal behaviors and ignition dynamics under heterogeneous and time-varying conditions.

Table 3.10 Governing equations of a reaction-diffusion model of the self-ignition phenomena with time dependent boundary conditions.

Description	Equations	
Mass balance	$\frac{\partial c(\boldsymbol{x},t)}{\partial t} = Le\nabla^2 c(\boldsymbol{x},t) - \Phi^2 c(\boldsymbol{x},t)\exp\left(-\frac{\gamma}{T(\boldsymbol{x},t)}\right)$	(1)
Energy balance	$\frac{\partial T(\boldsymbol{x},t)}{\partial t} = \nabla^2 T(\boldsymbol{x},t) + \beta\Phi^2 c(\boldsymbol{x},t)\exp\left(-\frac{\gamma}{T(\boldsymbol{x},t)}\right)$	(2)
Boundary conditions	$c(\boldsymbol{x},0)\|_{\partial\Omega_a} = c_0$	(3)
	$\nabla c\|_{\partial\,\Omega_g} = 0, t > 0$	(4)
	$T\|_{\partial\Omega_a} = T_0\sin(\omega t)$	(5)
	$T\|_{\partial\Omega_g} = T_0$	(6)
Initial Conditions	$T(\boldsymbol{x},0) = T_{ss}, \boldsymbol{x}\in\Omega$	(7)
	$c(\boldsymbol{x},0) = c_{ss}, \boldsymbol{x}\in\Omega$	(8)

Table 3.11 Dimensionless parameters of the reaction diffusion model reported in Table 3.10

Dimensionless parameter	Description	Formula
Le	Lewis number	D / α
T	Dimensionless temperature	T / T_0
t	Dimensionless time	$t\,\alpha / L^2$
Y	Dimensionless concentration	c / c_0
β	Dimensionless heat of reaction	$(-\Delta H\, c_0) / (\rho\, c_P\, T_0)$
γ	Dimensionless activation energy	$E / (R\, T_0)$

- Effect of convection

Building on the previous discussion of heat and mass transfer mechanisms, it is essential to consider the role of convective phenomena in self-ignition models. While many simplified

approaches neglect momentum transport, as if heat transfer occurred exclusively by conduction, this assumption can lead to significant inaccuracies under realistic conditions. Numerous self-ignition models decouple mass and energy balances from the momentum balance, whereas more advanced formulations explicitly account for convection. This inclusion is crucial because convection can significantly influence the thermal stability of reactive systems. Several studies have demonstrated that natural convection exerts a stabilizing effect on potentially explosive systems. For instance, (Merzhanov and Shtessel, 1973), (Jones, 1974), and (Shtessel' et al., 1979) investigated ignition in homogeneous systems and concluded that buoyancy-driven flow can delay the onset of thermal runaway.
Two main approaches are found in the literature:

- *Forced Convection Models*: Some models assume a constant gas velocity within the fuel bed, effectively representing a forced convection regime (Salinger et al., 1994). For example, (Nordon, 1979) and (Schmal et al., 1985) analyzed forced convection through the packed bed by arbitrarily varying the airflow velocity as a system parameter. This type of model is conceptually similar to the pseudo-homogeneous axial-dispersion model of a packed-bed reactor (Table 3.4), where a predefined velocity field is imposed and the pressure drop is estimated using the Ergun equation (Equation (3.8)) (Brooks et al., 1988).
- *Natural Convection Models:* Other models incorporate buoyancy-driven flow. Such models account for density variations resulting from changes in temperature distribution. This approach captures the coupling between thermal gradients and fluid motion, which is essential for accurately predicting ignition thresholds under realistic conditions (Salinger et al., 1994).

An example of a model that accounts for natural convection is presented in Table 3.12. This is a dynamic model that simultaneously considers the transport of energy, mass, and momentum within the stock-pile. In particular, the momentum balance incorporates viscous effects, represented by the term $\mu\nabla^2\mathbf{v}$; inertial effects, expressed through the convective term $\rho(\mathbf{v}\cdot\nabla)\mathbf{v}$; buoyancy effects, modeled as $\rho g\beta(T-T_\infty)$.
To fully define the problem, the system of partial differential equations must be complemented with appropriate initial and boundary conditions. A typical set of boundary conditions includes prescribed temperature and concentration at the external surfaces in contact with the atmosphere, and no-flux conditions at insulated boundaries.

Table 3.12 Governing equations of a reaction-diffusion-convection model of the self-ignition phenomena with corresponding boundary and initial conditions.

Description	Equations	
Mass balance	$\frac{\partial Y}{\partial t} + v \cdot \nabla Y = \epsilon D \nabla^2 Y - \frac{M}{\rho} r$	(1)
Energy balance	$pc\left(\frac{\rho_p C_p}{pc}\frac{\partial T}{\partial t} + v \cdot \nabla T\right) = k\nabla^2 T + (-\Delta H) r$	(2)
Momentum balance	$\rho \frac{\partial v}{\partial t} + \rho v \cdot \nabla v = -\nabla p + \rho g \beta (T - T_\Lambda) - \frac{\mu}{K} v$	(3)

In practice, this comprehensive formulation is often simplified by neglecting certain terms to reduce computational complexity. For example, inertial terms may be omitted under low-velocity regimes. Brooks et al., 1988, adopted such an approach, leading to the simplified model reported in Table 3.13.

Table 3.13 Example of a simplified reaction-diffusion-convection model with buoyancy effects. Adapted from Brooks et al. (1998)

Description	Equations	
Mass balance	$\frac{u_0 \rho_a}{M}\frac{dy}{dx} = -r$	(1)
Energy balance	$k_e \frac{d^2 T}{dx^2} - u_0 \rho_a c_p \frac{dT}{dx} + (-\Delta H) r = 0$	(2)
Momentum balance	$\frac{dP^*}{dx} = -f_p + \rho_a g\left(1 - \frac{T_a}{T}\right) - \frac{\rho_a u_0^2}{T_a}\frac{dT}{dx}$	(3)

Another critical aspect that differentiates convection-inclusive models is whether the external environment is explicitly considered. Accounting for ambient conditions - such as external temperature fluctuations or wind-driven airflow - can significantly affect the prediction of self-ignition behavior. Several studies have highlighted that neglecting these interactions may lead to underestimating ignition delays or misrepresenting the stability of the system.

- *Heat Generation Mechanisms in Stockpiles*

Finally, a brief overview is provided on the mechanisms responsible for heat generation in stockpiles of different materials.

Heat generation within stockpiles can arise from multiple factors, which vary significantly depending on the nature of the material. In the literature, two main research directions can be identified:

- *Biomass-based stockpiles*, where biological and microbial activity plays a dominant role (Zhang et al., 2016b);
- *Coal stockpiles*, where oxidation reactions and moisture effects are the primary contributors (Sheng and Yao, 2022b).

As highlighted in the review of Sheng and Yao, (2022), the behavior of coal stockpiles is influenced not only by oxidation reactions but also by physical phenomena associated with moisture content. Water can affect the self-heating process through several mechanisms: evaporation and condensation phenomena, as well as absorption and desorption within the porous structure of the material. These processes introduce additional heat sources or sinks, which must be accounted for in mathematical models. To capture these effects, advanced models include specific terms in the energy balance representing the latent heat associated with phase changes of water vapor.

An example of a model that accounts for moisture influence is presented in Table 3.14, which couples chemical heat generation with moisture transport, condensation or evaporation.

Table 3.14 reports a dynamic model adapted from (Monazam et al., 1998), which simultaneously describes oxygen transport, moisture transport, and heat transfer within a reactive porous medium. The formulation captures the coupling between chemical reactions and physical processes, including oxidation, water absorption/desorption, and associated latent heat effects. The governing equations are summarized below. The latent heat effect (ΔH_{O_2}) is calculated using the Clapeyron equation (Keenan and Keyes, 1936).

Table 3.14 Adaption of the model proposed by (Monazam et al., 1998) to account for moisture effects

Description	Equations	
Oxygen mass balance	$(1-\alpha)\frac{\partial \rho_{O_2}}{\partial t}+\frac{\partial(\rho_{O_2}u)}{\partial x}+\frac{\partial(\rho_{O_2}v)}{\partial y}=D_{O_2}^{(e)}\frac{\partial^2 \rho_{O_2}}{\partial x^2}-\alpha\eta r_{O_2}$	(1)
Moisture mass balance	$(1-\alpha)\frac{\partial \rho_w}{\partial t}+\frac{\partial(\rho_w u)}{\partial x}=D_w^{(e)}\frac{\partial^2 \rho_w}{\partial x^2}+\alpha r_w$	
Energy balance	$\left(\rho_p c_{p,p}\alpha+\rho_g c_{p,g}(1-\alpha)\right)\frac{\partial T}{\partial t}=K_{ax}\frac{\partial^2 T}{\partial x^2}-\rho_g c_{p,g}u\frac{\partial T}{\partial x}-\eta\Delta H_{O_2}r_{O_2}+\alpha\Delta H_w r_w$	(2)

The term (r_w) represents the rate of water absorption or desorption within the solid matrix and is defined as:

$$r_w=\frac{3rv^2}{R0^3}M_e\rho_c\frac{dr_v}{dt} \tag{3.8}$$

where (r_v) is the instantaneous radius of the sorption front, (R_0) the initial particle radius, (M_e) the equilibrium moisture content, and (ρ_c) the coal density. The evolution of (r_v) is governed by:

$$\frac{dr_v}{dt}=\frac{{R_0}^2K_g\left(\rho_v^g-\rho v^{r_v}\right)}{M_e\rho_c r_v^2\left(1+Bi_m\left(\frac{R0}{rv}-1\right)\right)} \tag{3.9}$$

where (K_g) is the mass transfer coefficient, (Bi_m) the mass transfer Biot number, and (ρ_v^g) and ($\rho_v^{r_v}$) the vapor densities in the bulk gas and at the sorption front, respectively. This detailed formulation highlights the strong coupling between moisture dynamics and thermal behavior, as water absorption/desorption significantly influences the energy balance through latent heat effects. Accurate modeling of (r_w) and (r_v) is therefore essential for predicting self-heating and ignition thresholds in coal stockpiles.

In biomass piles, heat originates from physical, biological, and chemical processes, which occur sequentially and often overlap. At low temperatures, physical mechanisms dominate, mainly involving moisture migration and water exchange with the environment. Adsorption

and condensation effects are particularly relevant below 20 °C and can raise the temperature to about 40-50 °C As the pile warms, biological activity becomes the primary heat source. This includes plant cell respiration and the metabolic activity of microorganisms, fungi, and bacteria. These processes are strongly exothermic and operate between 0-75 °C, with maximum intensity from 20-60 °C, limited by microbial heat tolerance.

At higher temperatures, chemical reactions prevail, such as oxidation, pyrolysis, and hydrolysis of organic matter, as well as oxidation of inorganic components. These reactions span from near ambient conditions to ignition, with direct oxidation starting around 30-50 °C and cellulose or lignin oxidation occurring above 100 °C.

The thermal evolution of a biomass pile reflects this progression: an initial mesophilic phase with rapid heating, followed by a thermophilic stage where temperature stabilizes at higher levels, and finally a decline as nutrients are depleted, leading to a second mesophilic phase. If ignition does not occur, the system cools gradually.

Figure 3.4 qualitatively illustrates this progression, and experimental studies, such as those reported in Miyawaki et al., (2021) and Wei et al., (2023), confirm this multi-phase thermal behavior.

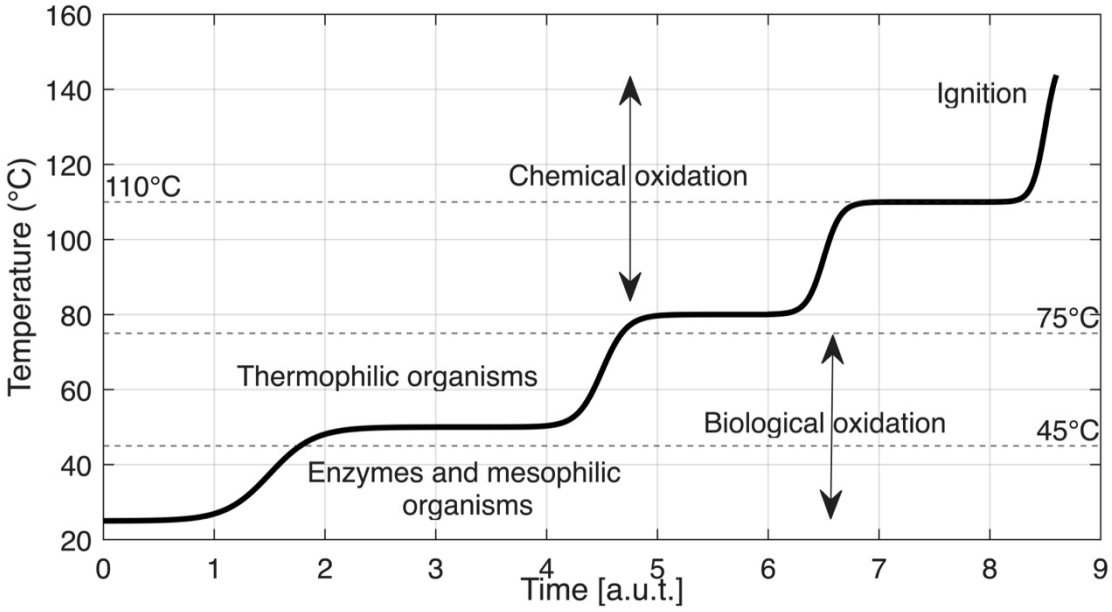

Figure 3.4 Main sources of heat generation in stockpiles of biomass

Advanced models often incorporate multiple heat-generation mechanisms with distinct kinetics, including microbial growth terms based on Monod-type formulations. An example of such a simplified model is presented in Table 3.15, which introduces a temperature-dependent microbial growth rate to capture the biological contribution to self-heating.

Microbial activity in biomass piles is a key contributor to self-heating and is commonly modeled through a specific growth rate (μ) that depends on temperature. A widely used formulation, proposed by (Esener et al., 1981), accounts for both activation and inactivation effects:

$$\mu_m = \frac{A\ \exp\left(-E_1/(R_u T)\right)}{1 + B\ \exp\left(-E_2/(R_u T)\right)} \tag{3.10}$$

where (A) and (B) are pre-exponential factors, (E_1) and (E_2) the activation enthalpies, (R_u) the universal gas constant, and (T) the absolute temperature. This model, although simplified, is considered an effective tool for representing the temperature dependence of the maximum growth rate. The actual biomass growth rate is often expressed as:

$$RX = \frac{dX}{dt} = \mu X \left(1 - \frac{X}{Xm}\right) \tag{3.11}$$

where (X) is the microorganism concentration, (X_m) its maximum attainable value, and (μ) the specific growth rate. This logistic formulation accounts for nutrient limitation, predicting an initial exponential phase followed by a slowdown as (X) approaches (X_m). Combining this with the temperature-dependent (μ_m) enables models to capture both thermal effects and substrate constraints on microbial growth.

Chapter 4
Results: Fixed beds analysis and optimization through Full and Reduced-Order Models

4.1 Periodic Oscillations in Methane Reactor: Effects of the Main Operating Parameters[1]

Piero Bareschino[a,b], **Alberto. E. Cutillo[a]**, Claudio Tregambi[a,b], Francesco Pepe[a], Gaetano Continillo[a], Erasmo Mancusi[a]

[a]*Dipartimento di Ingegneria, Università degli Studi del Sannio, Benevento 82100, Italy.*
[b]*Istituto di Scienze e Tecnologie per l'Energia e la Mobilità Sostenibili - Consiglio Nazionale delle Ricerche, Italy*
erasmo.mancusi@unisannio.it

Abstract

Biogas is widely considered as one of the most promising renewable energy resources and the most environmental-friendly energy source. Biogas produced through anaerobic digestion contains many impurities and a high percentage of CO_2. Thus, upgrade and purification of the raw biogas by capturing CO_2 before its application is necessary. In this work a catalytic methanation process of biogas was proposed and numerically analyzed. It appears that sustained periodic oscillations occur in a wide range of operating parameters. A detailed nonlinear analysis is performed, and the information produced can be useful for effective plant design and adequate plant control and operation.

Keywords: Biomethane, Power-to-Methane, fixed bed reactor, periodic oscillations, non-linear dynamics.

4.1.1 Introduction

Due to the continuous increase in energy demand and to mitigate environmental problems related to greenhouse gas emissions, the research towards non-fossil and renewable energy sources is continuously increasing (Kapoor et al., 2019). In this respect, production of biomass-derived biofuels has emerged as one of the most promising non-conventional energy resources (Mancusi et al., 2021a; Tursi, 2019). Among biofuels, biogas from the anaerobic digestion of organic wastes stands out as an attractive way of reducing landfilling while producing energy. However, the CH_4 content in biogas usually reaches about 70% at

[1] Published in: *Computer Aided Chemical Engineering*. Vol. 51. Elsevier, 2022. 1-6. https://doi.org/10.1016/B978-0-323-95879-0.50001-1

most, so that it needs to be purified (removal of trace components) and upgraded (removal of CO_2) before utilization. The most used carbon dioxide separation technologies are based on absorption, adsorption, cryogenic distillation, and membrane separation, all of them being highly energy consuming (Zhang et al., 2020). In this work, the upgrading process by direct methanation of biogas is analyzed. Particularly, we envision using surplus electrical energy from renewable sources to produce, via electrolysis, the required hydrogen to be fed, along with the biogas, into the methanation reactor (Bareschino et al., 2020). Methanation enables the conversion of H_2 and CO_2 into methane ranking among the power-to-gas technologies that represent the best solution for the energy storage. Several studies show that methanation has a very high CO_2 conversion degree, close to the removal efficiencies of traditional upgrading techniques (e.g. Mhadmhan et al., 2022). In the present work, the proposed methanation process involves simultaneous biogas upgrading and methane enrichment of the leaving gas. The process is carried out in an adiabatic fixed bed reactor with a nickel-based catalyst, and a recycle loop is used for diluting the inlet reactants concentration, to limit the maximum adiabatic temperature increase (Bareschino et al., 2021). The effects on the feed temperature and recycling ratio (R) are considered. Periodic oscillations are predicted over a wide range of the investigated parameters. The main cause of the sustained periodic oscillations can be found in the feedback from the mass recycle coupled with the typical phenomena of fixed bed reactors, i.e. the inverse response (Luyben, 2007). Although the maximum temperature reached during the oscillations is limited by the thermodynamic equilibrium, the system temperature oscillates remarkably, with a period of about 10 minutes and in a range of $\pm$150°C. This behavior must be avoided to prevent catalyst damage. Non-linear analysis is performed to characterize the stability range of periodic regimes and to identify domains of coexistence of multiple stable regimes. This information can be useful for effective plant design and adequate plant control and operation (Mancusi et al., 2007).

4.1.2 Mathematical Model

The biogas upgrading process is carried out in a single adiabatic fixed bed reactor with a nickel-based catalyst. Figure 1 reports a schematic layout of the methanation process under study.

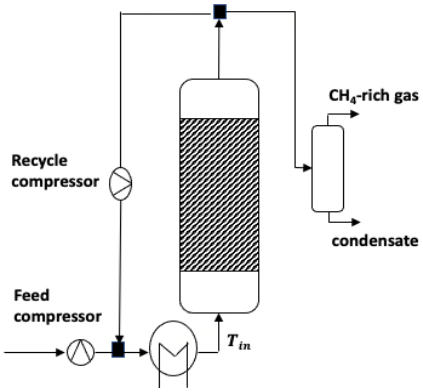

Figure 1 Adiabatic fixed bed methanation with recycle.

The biogas fed to the reactor is produced by anaerobic digestion of food waste. Purified from all impurities (H_2S), it contains CH_4 and CO_2 at 65% and 35% respectively (Tursi, 2019). This stream is enriched with H_2 produced by renewable sources according to a stoichiometric CO_2:H_2 ratio of 1:4 (R_3 in Tab. 1). The complete CO_2/CO methanation reaction mechanisms for syngas methanation over Ni-based catalyst proposed by Xu and Froment (Xu and Froment, 1989a) is considered. For readers convenience, Table 1 summarizes the adopted reactions and associated enthalpy variations.

Table 1 – Reactions scheme and associated standard enthalpies of reactions.

Reaction	ΔH_{298} (kJ.kmol^{-1})	
$CO + 3H_2 \Leftrightarrow CH_4 + H_2O$	-206	R_1
$CO_2 + H_2 \Leftrightarrow CO + H_2O$	41	R_2
$CO_2 + 4H_2 \Leftrightarrow CH_4 + 2H_2O$	-165	R_3

To limit an increase in temperature due to the strong exothermicity of the methanation reactions, the water content in the feed is increased by adopting gas recirculation (Rönsch et al., 2016a). While the presence of water in the feed stream due to recycle shifts the chemical balance towards the products, it is essential to keep the temperature below 600° C and reduce carbon formation (Rönsch et al., 2016a). Moreover, since the process is exothermic and reactions R_1 and R_3 take place with increasing volumes, the process benefits from high pressures and low temperatures.

The fixed bed reactor is modeled by a 1D pseudo-homogeneous and adiabatic model (Bareschino et al., 2021). The material balances for each gas component (i=CH_4, CO, CO_2, H_2, H_2O) and the energy balance are reported in Table 2 with the initial and boundary conditions:

Table 2 – Governing equations.

Mass Balance	$\varepsilon_g \frac{\partial c_i}{\partial t} = -u_{sg} \frac{\partial c_i}{\partial z} - (1-\varepsilon_g)\rho_c r_i$
Heat Balance	$\left(\varepsilon_g \rho_g c_{pg} + (1-\varepsilon_g) c_{pc}\right) \frac{\partial T}{\partial t} = -u_{sg}\rho_g c_{pg} \frac{\partial T}{\partial z} - \rho_c \sum_{j=1}^{3} \Delta H_{Rj} R_j$
Initial conditions	$c_i(z,0) = 0, T(z,0) = T_0$
Boundary conditions	$c_i(0,t) = c_{i,in}, T(z,0) = T_{in}$

where z is the axial position along each reactor belonging in [0, L], and r_i the rate of consumption or formation of i-species (i=CH_4, CO, CO_2, H_2, H_2O) determined by summing up the reaction rates of those species in all the reactions R_j (see Table 1) according to the stoichiometric coefficients (ν) as follows:

$$r_i = \sum_{j=1}^{3} \nu_{i,j} R_j \quad (1)$$

The gas superficial velocity (u_{sg}) was calculated as follows:

$$u_{sg}(z,t) = \frac{PM_{in}}{PM} u_{sg,in} \quad (2)$$

where PM is the molecular weight and the subscript *in* represents inlet conditions. Operating conditions, reactor volumes, and catalyst properties used in the simulations are reported in Table 3.

Table 3 – Parameters values used in the simulations.

Parameter	Value	Parameter	Value
P, bar	15.0	$y_{CO2,in}$	0.145
T_{in}, °C	280	$y_{H2,in}$	0.585
L, m	1.5	c_{pc}, $J.kg^{-1}.K^{-1}$	1100
d_r, m	0.225	ρ_c $kg.m^{-3}$	2350
$y_{CH4,in}$	0.27	ε_g	0.4

The method of lines is applied to solve the partial differential equations (PDEs) in two steps: the spatial derivatives are approximated by finite differences over a uniform grid of 200 discretization nodes, and the resulting system of 1200 ODEs is integrated in the initial value variable (Bareschino et al., 2021).

4.1.3 Results

The non-linear features of the fixed bed reactor give rise to phenomena such as the inverse response (a temporary behavior contrary to that expected). Figure 2 reports the reactor output according to the legend, for a step decrease (10°C) of the inlet temperature. It is apparent that the first effect observed at the reactor exit is a temperature increase. Since higher temperatures decrease the equilibrium conversion, the temperature increase is followed by an increase in the reactant concentrations. Thus, although the inlet heat exchanger cancels out temperature variations, recycle still provides feedback.

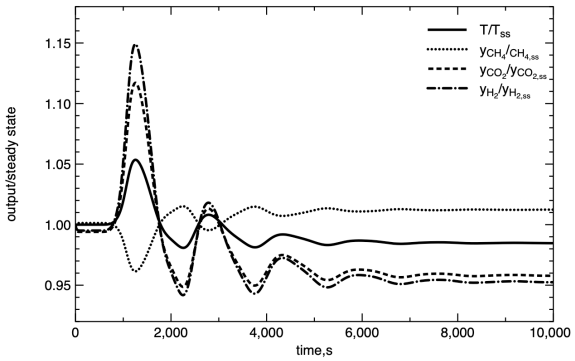

Figure 2 Reactor response to a step decrease of inlet temperature. Subscript *ss* refers to unperturbed steady-state. R=1.6 whereas the other parameters are those reported in Tab. 3.

The combination of this feedback due to mass recycle and the inverse response can result in sustained oscillatory behavior (Luyben, 2007). Numerical simulations using non-linear dynamical model reproduce periodic oscillations in the reactor. Figure 2 reports a simulation showing time series of the outlet gas temperature and composition.

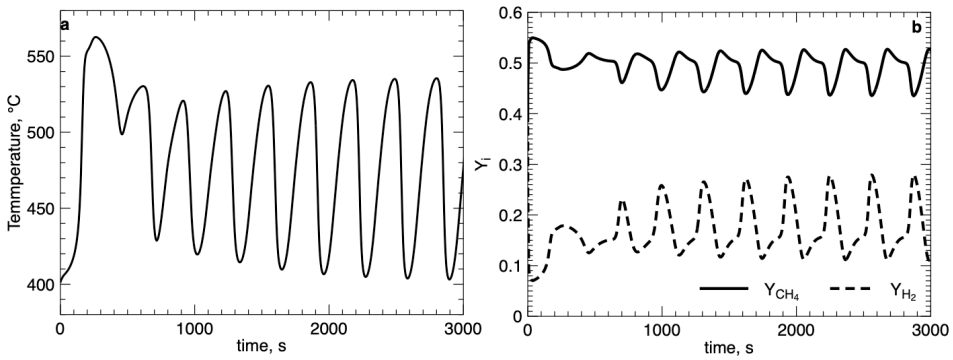

Figure 3 (a) Temperature at reactor exit vs time, (b) CH_4 and H_2 molar fraction at reactor exit vs time for R=1.6, whereas the other parameters values are those reported in Tab. 3.

Although the maximum temperature is limited by thermodynamic equilibrium, the system, as it can be seen, oscillates with a period of about 10 minutes and in the range of ±150°C. The amplitude of temperature oscillations is wide, and this could cause thermal stress of the catalyst. We now use a linear analysis to study more carefully the cause of the instability induced by the recycle operation. Close to an operating point, the dynamics of a system are well described by its linearized model. The model of the reactor was linearized numerically at this operating point, yielding a standard linear state space model with 1200 state variables in the form:

$$\frac{dx}{dt} = Jx \tag{2}$$

where J is the Jacobian matrix calculated at the steady state solutions. Computing steady state solution implies solving the nonlinear system of equations as reactor parameters vary (Mancusi et al., 2015). Once the steady state solution was calculated, the eigenvalues are computed by employing the *eig* function in MATLAB.

The largest eigenvalues of J for several values of R were calculated and depicted in Fig. 4. The reactor with no recycle (R=0) has a stable stationary response, i.e., all the eigenvalues have a negative real part. As R increases, the real part of the eigenvalues increases until R=1.5, where a couple of eigenvalues cross the imaginary axis. In these conditions the stable static regime solution becomes unstable, and periodic oscillations occur due to a Hopf bifurcation (Kuznetsov, 1998).

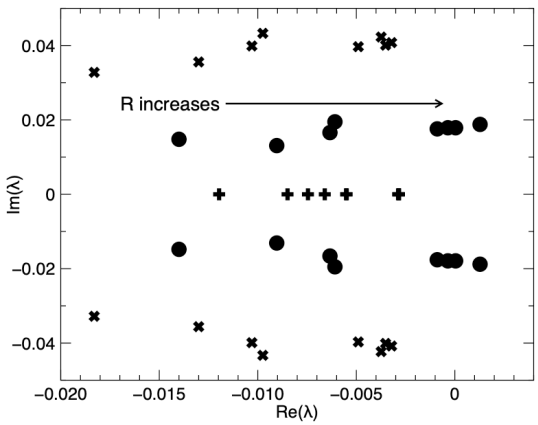

Figure 4 Imaginary and real part of the largest eigenvalues for several R.

The effect of the inlet temperature and recycle ratio is addressed by a bifurcation diagram (Fig. 5) where the locus of all Hopf bifurcation points is reported in the plane R-T_{in}. In this plot, the lines partition the parameter space into regions characterized by qualitatively similar

phase portraits, that is the region characterized by stable steady state and region in which stable periodic oscillations exist (Kuznetsov, 1998).

4.1.4 Conclusions

The paper reports a dynamical study of an adiabatic fixed bed reactor for the catalytic methanation of biogas. The complete dynamical characterization of a model is very useful to study the existence of periodic regimes and its influence on plant design, control, and operation. For the problem at hand, complex periodic regimes are due to the interaction of feedback induced by the mass recycle and by the inverse response typical of fixed bed reactors. The emergence of periodic oscillations is due to a Hopf bifurcation. The effect of both the inlet temperature and the recycle ratio was investigated. The knowledge of the global dynamics can be helpful in designing an effective control strategy.

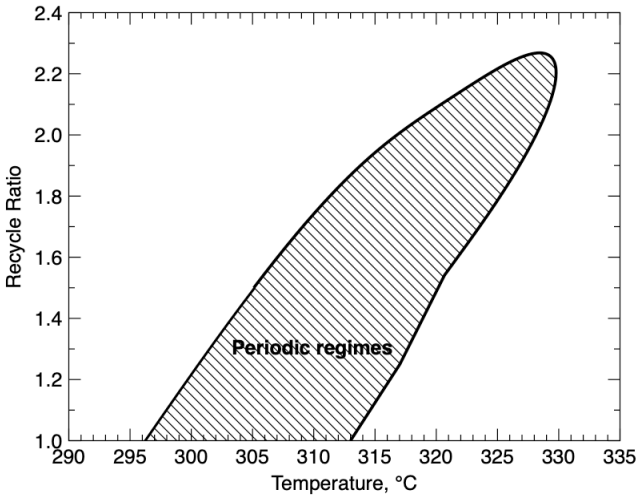

Figure 5 The bifurcation diagram in the R-T_{in} plane.

4.2 A Reduced-Order Model for the Prediction of the Dynamics of a Methane Reactor[2]

Enrico A. Cutillo,[a*] Erasmo Mancusi,[a] Katarzyna Bizon,[b] Piero Bareschino,[a,c] Gaetano Continillo,[a]
[a]*Dipartimento di Ingegneria, Università degli Studi del Sannio, Benevento 82100, Italy*
[b]*Faculty of Chemical Engineering and Technology, Cracow University of Technology, ul. Warszawska 24, 31-155 Kraków, Poland*
[c]*Istituto di Scienze e Tecnologie per l'Energia e la Mobilità Sostenibili - Consiglio Nazionale delle Ricerche, Italy*
[*]*cutillo@unisannio.it*

Abstract

The present work studies fixed-bed methanation reactor for the upgrading of biogas, that is expected to provide the chemical energy storage for nonprogrammable sources. The reactor has been described using a pseudo-homogeneous model. The dynamics of such systems can exhibit complex behaviors, that could make the numerical solution computationally expensive. Therefore, in view of building a fast and accurate numerical model able to predict the dynamics of the reactor, in this work the influence of both the inlet temperature and the recycle ratio on the reactor dynamics are studied employing a reduced-order model. A sensible reduction of computational time is achieved in this application because the applied methodology allows significant reduction of the dimension of the resulting system. Moreover, an assessment of the accuracy of the proposed reduced-order model enables its use within real time control applications, or in speeding up the resolution of time-consuming optimization.

Keywords: reduced models, POD, methanation, step response, Power-to-Methane.

4.2.1 Introduction

Numerical simulation of high-fidelity models of complex systems can take hours or even days. Some applications, such as parametric studies or optimization, often require thousands of those simulations, and for this reason overall CPU time rapidly increases. Anyhow, simulations enable to optimize process parameters in order to reduce economical costs or maximize the productivity of the studied process (Bizon and Continillo, 2021b) without the need for time-consuming and expensive experimental work but, most importantly, permit to

[2] Published in: *Computer Aided Chemical Engineering*. Vol. 52. Elsevier, 2023. 1199-1204. https://doi.org/10.1016/B978-0-443-15274-0.50191-8

predict unwanted behaviors and adopt adequate control strategies (Bareschino et al., 2022b). In this work, the studied process is related to sustainable energy conversion and reduction of CO_2 emissions, which are challenges that cannot be procrastinated any further and, moreover, this is in line with the core principles of the European Green Deal and Power-to-Gas concept. Particularly, the production of biofuels as green energy resource is very promising (Mancusi et al., 2021b). Among biofuels, biogas from anaerobic digestion of organic waste stands out as an attractive way to reduce landfilling and to produce energy. However, the CH_4 content in biogas usually never reaches values above 70%, so it needs to be purified (removal of trace components) and improved (removal of CO_2) before it can be used. One of the most widely studied upgrading processes involves the methanation of CO_2 (Mancusi et al., 2021b). Recently, modeling studies on the methanation process have allowed to address specific aspects such as the dynamical characterization of methanation reactors (Zimmermann et al., 2022b). In this work, the simulations of a dynamical system that describes the methanation of biogas in an adiabatic fixed-bed reactor with a nickel-based catalyst and a recycle loop are carried out by applying classical proper orthogonal decomposition (POD) for the model-order reduction. This methodology enables the use of the previously derived robust numerical model (Bareschino et al., 2022b) for more computationally intensive applications. POD is a popular model reduction technique that, combined with Galërkin projection, is widely applied in the field of chemical engineering and many other fields to alleviate the computational expense required for the solution of very high-dimensional systems (Sahyoun and Djouadi, 2013b). Both methanation and fixed-bed reactors with recycle have been simulated successfully with this methodology (Bizon and Continillo, 2012; Bremer et al., 2017).

To understand if the proposed POD/Galërkin-based reduced-order model (ROM) can correctly predict the dynamics of the methanation reactor, in this work a step response analysis is performed in a region of the space of the parameters where periodic solutions are encountered, and in its vicinity. Temperature oscillations inside the reactor can lead to catalyst permanent deactivation, thus generally must be avoided, and outlet concentration variations are also generally inconvenient. Therefore, the ROM developed here can be useful if incorporated in the design of a control system that allows avoiding those unwanted regimes.

4.2.2 Mathematical model and computational methods

- *Mathematical model of an adiabatic fixed bed reactor for biogas upgrading*

The methanation reactor investigated is a fixed-bed adiabatic reactor with mass recycle. The catalyst considered is a nickel-based catalyst and the kinetic model employed is the one proposed by Xu and Froment (Xu and Froment, 1989). The chosen model is one-dimensional pseudo-homogeneous with axial dispersion (Rönsch et al., 2016b). Gas recycle is necessary to keep the temperature inside the reactor within an acceptable limit, determined by catalyst deactivation and carbon formation. The model is mathematically formalized by Eq. (1)-(2) that are, respectively, the species and heat balances:

$$\varepsilon_g \frac{\partial c_i}{\partial t} = D_{ax} \frac{\partial^2 c_i}{\partial z^2} - u_{sg} \frac{\partial c_i}{\partial z} - \left(1 - \varepsilon_g\right) \rho_c r_i \tag{1}$$

$$\left(\varepsilon_g \rho_g c_{pg} + \left(1 - \varepsilon_g\right) c_{pc}\right) \frac{\partial T}{\partial t} = \lambda_{eff} \frac{\partial^2 T}{\partial z^2} - u_{sg} \rho_g c_{pg} \frac{\partial T}{\partial z} - \rho_c \sum_{j=1}^{3} \Delta H_{Rj} R_j \tag{2}$$

where:

$$r_i = \sum_{j=1}^{3} \nu_{i,j} R_j \tag{3}$$

with R_j being the reaction rates as in (Xu and Froment, 1989b), and:

$$c_i(0,t) = c_{i,in}(t)\,; \;\; T(0,t) = T_{in} \tag{4}$$

where:

$$c_{i,in}(0,t) = \frac{c_{i,0}}{1+R} + R \frac{c_{i,out}(t)}{1+R} \tag{5}$$

To solve the above system of partial differential equations, the method of lines was initially employed: spatial derivatives were approximated using finite differences over a uniform grid of 200 discrete nodes, yielding a system of 1200 ordinary differential equations (ODE) that was solved with MATLAB solver for stiff ODEs. To simplify the description of the reduction method, and to efficiently code the system of ODEs in MATLAB, the following matrix notation is employed:

$$\frac{d}{dt}\boldsymbol{c}_i = \boldsymbol{A_c c}_i + \boldsymbol{B_c c}_i \odot \boldsymbol{u} + \boldsymbol{F}_{\boldsymbol{c}_i}(\boldsymbol{c}_i, \boldsymbol{T}) \tag{6}$$

$$\frac{d}{dt}\boldsymbol{T} = (\boldsymbol{A_T T} + \boldsymbol{B_T T} \odot \boldsymbol{u}) \odot \frac{1}{\varepsilon_g \rho_g(\boldsymbol{c}_i, \boldsymbol{T}) c_{pg} + \rho_c c_{pc}\left(1 - \varepsilon_g\right)} + \boldsymbol{F_T}(\boldsymbol{c}_i, \boldsymbol{T}) \tag{7}$$

where **A** and **B** are the coefficient matrices discretizing spatial derivatives which include also the terms resulting from the outlet boundary conditions, whereas the nonlinear functions F_c and F_T incorporate the inlet boundary conditions (Eq. (4) and Eq. (5)). The discretized system above is hereafter referred to as the full-order model (FOM).

- *Reduced-order model formulation*

The POD method allows to extract a set of empirical basis functions from observations originating from experiments or numerical simulation (Sahyoun and Djouadi, 2013). The observations, often referred to as snapshots, are collected in the snapshots matrix **Y**. The choice of the most relevant snapshots is often driven by the knowledge of the spatiotemporal complexity of the system and its variability when changing key parameters of the model. In this work, the most straightforward strategy (uniform sampling) is employed (Bizon et al., 2012b). After collecting the snapshots, the POD basis is determined by solving the eigenvalue problem:

$$\boldsymbol{C\Phi} = \boldsymbol{\Lambda\Phi} \tag{8}$$

In Eq. (8) **C** is the autocorrelation matrix defined as $\mathbf{Y}\mathbf{Y}^{\mathrm{T}}/M$, where M is the number of observations used for the construction of the basis, while **Φ** and **Λ** are, respectively, the matrix containing basis functions and the relevant eigenvalues. The magnitude of each eigenvalue indicates the contribution of the corresponding POD mode to the "information" content of the original data. Using the POD basis, the generic state variable vector **y** can be expressed in truncated form as:

$$\boldsymbol{y} \approx \tilde{\boldsymbol{y}} = \sum_{k=1}^{K} \phi_k x_k = \boldsymbol{\Phi}_K \boldsymbol{x}_K \tag{9}$$

Where $K \leq N$ is the dimension of the reduced-order model and $\boldsymbol{\Phi}_K \in \mathbf{R}^{\mathrm{N}\times K}$ is a matrix composed of the first K columns of the matrix **Φ**. In Eq. (9), the unknowns are the K time-dependent coefficients $\mathbf{x}_K$. They can be determined by resolving the following ROM obtained after substitution of Eq. (9) into Eq. (6)-(7), followed by Galërkin projection onto $\boldsymbol{\Phi}_K$:

$$\frac{d}{dt}\boldsymbol{x}_K = \boldsymbol{\Phi}_K^T \boldsymbol{A}\boldsymbol{\Phi}_K \boldsymbol{x}_K + \boldsymbol{\Phi}_K^T \boldsymbol{B}\boldsymbol{\Phi}_K \boldsymbol{x}_K \odot \boldsymbol{u} + \boldsymbol{\Phi}_K^T \boldsymbol{F}(\boldsymbol{\Phi}_K \boldsymbol{x}_K) \tag{10}$$

The state variables vector has been divided into six sets of variables, associated with the species concentrations and temperature. Each one of these sets has been reduced with its own POD basis.

4.2.3 Results and discussion

The values of the main operating conditions and parameters characterizing the reactor geometry used in both FOM and ROM simulations are reported in Table 1. Figure 1 reports a schematic of the system (a) and the grid of parameters explored (b). Before starting the construction and validation of the reduced-order model, several simulations of FOM were performed for the different values of the three parameters analyzed in this work, namely: T_{in} – the inlet temperature assumed to calculate the steady state, ΔT_{in} – the amplitude of the step forcing, and R – the value of the recycle ratio used for both steady state and step response calculations.

Table 1. Main model parameters

Parameter	Value	Parameter	Value
L_r [m]	7	d_r [m]	1.2
P [atm]	20	ρ_c [kg·m^{-3}]	2350
c_c [J·kg^{-1}·k^{-1}]	1107	$y_{CH4,in}$	0.271
Q_{in} [Nm^3·s^{-1}]	1	$y_{CO2,in}$	0.146
D_{ax} [m^2·s^{-1}]	10^{-2}	$y_{H2,in}$	0.583

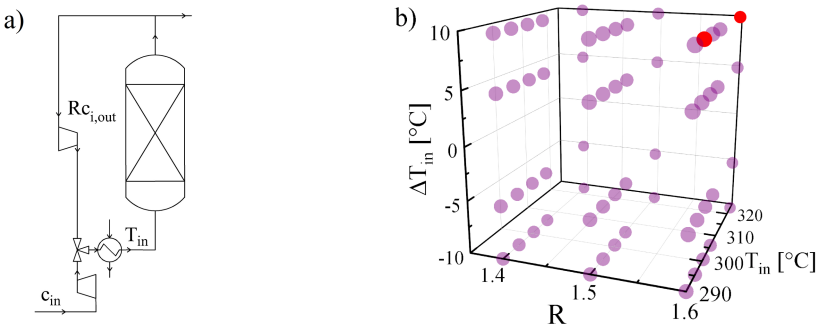

Figure 1. Scheme of methanation reactor (a) and values of the parameters used in simulations performed with the FOM (b). The two red dots correspond to the set of parameter values employed in the construction of the ROM.

The simulations were carried out in two steps: First, the steady state (ss) solution is determined for different values of T_{in} and R; then, a step change ΔT_{in} of the inlet temperature is introduced and the response of the reactor is simulated. Different values of ΔT_{in} are considered. The whole set of FOM simulations performed is represented inside the space of the studied parameters (Fig. 1b). The snapshots matrix is built with the spatial profiles of the step response of the FOM simulations, sampled uniformly in time. To build the snapshots matrix, different sampling strategies in the parameter space have been evaluated, but only the one that has given the best results in terms of ROM accuracy is reported in this work. Particularly, the snapshots matrix is built using only two FOM step response solutions. Those

solutions were obtained for the values of the parameters highlighted in red in Fig. 1b, that is T_{in}= [295.3, 323] °C, ΔT_{in}=10 °C and R=1.6. After computing the set of basis functions, the truncation order was set to K=35 for each state variable. Solution obtained using FOM and ROM are shown in Fig. 2. Before the step forcing, the system was simulated only using FOM, whereas after the forcing both FOM and ROM solutions are determined and reported here. This is because the ROM was built to reproduce only the step response of the system. As an interesting case study, to assess the ROM accuracy, a step forcing was applied to the operating conditions for which the oscillatory regime (or) was encountered. The parameters used in the simulation are T_{in}=306 °C and R=1.4. In fact, as reported in a previous study (Bareschino et al., 2022b), this set of parameters is inside a region of periodic regimes. To move outside this region, that corresponds to unwanted behavior, the inlet temperature can be reduced, for instance, by 10 °C. In fact, forcing the system with a step of ΔT_{in}= −10 °C results in a steady-state solution. As can be seen from the overlapping curves shown in Fig. 2a, the ROM predicts even the steepest transient oscillations quite accurately.

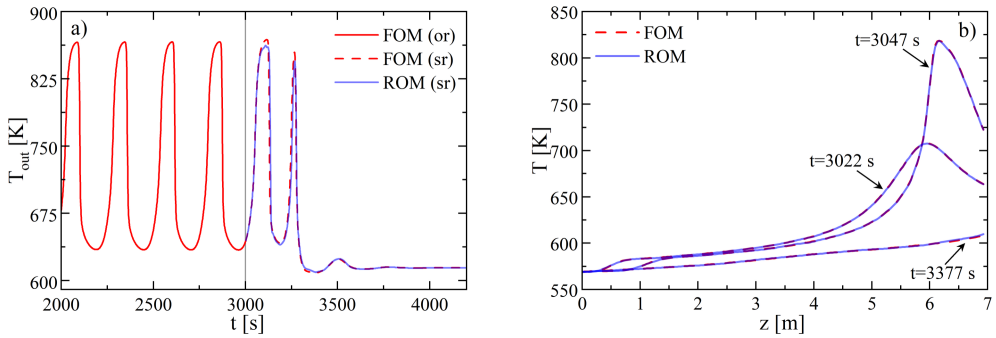

Figure 2. Time series (a) of the outlet temperature as computed with FOM before the step forcing (in the legend, or: oscillatory regime), and with both FOM and ROM after the step forcing (in the legend, sr: step response); (b) spatial profile of the temperature at different time instants confirming the accuracy of the ROM solution inside the reactor.

The choice of approximating the state variables with K=35 POD modes was made to achieve a sufficient reduction of CPU time and to maintain suitable accuracy of the obtained ROM. The resulting ROM has 210 degrees of freedom, that is one order of magnitude lower than the corresponding FOM. The simulation of the step response toward a stable steady state is less computationally expensive, and in this case the speed up (the ratio of CPU time of ROM simulation over FOM simulation) of the analyzed ROM is of 15. For the chosen approximation, the computed relative root mean squared error (RMSE) between FOM and ROM (calculated for the solutions described in Fig. 2) is of the order of 10^{-3} with a maximum

value of the error in correspondence of the peak value of T (at 3130 s) of $1.9 \cdot 10^{-2}$ and a steady state error of $6.5 \cdot 10^{-5}$.

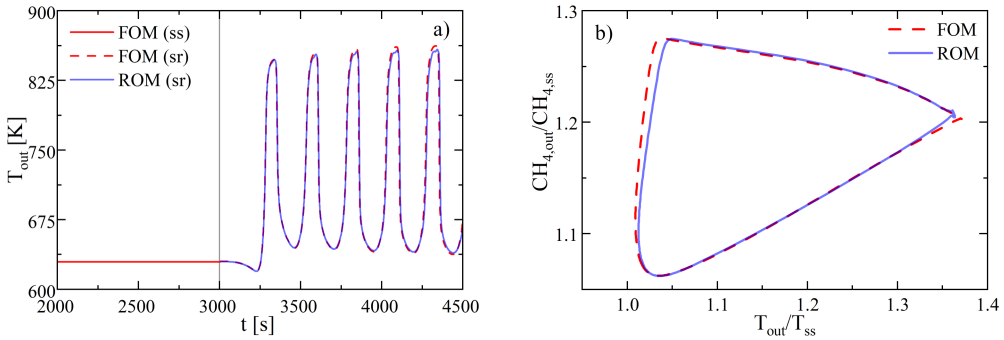

Figure 3. Time series as computed with FOM before the step forcing (in the legend, ss: steady state), and with both FOM and ROM after the step forcing – after the vertical line – (a); and phase space to highlight the accuracy of the ROM predicting the oscillatory regime (b.

Although the ROM was built without taking into account periodic regime solutions, it can be used to predict such regimes accurately. This is demonstrated in Fig. 3, in fact as it can be seen, if the system is forced to go from a stable steady state (ss) regime, toward oscillatory regime, the ROM correctly predict periodic oscillations. The parameter values used in the simulation are T_{in}=300.7, R=1.6, ΔT_{in}=10 °C. In Fig. 3b to highlight the accuracy of the ROM the limit cycle obtained using both models are reported. In this case the simulation is more expensive in terms of CPU time both for FOM and ROM because the solution is characterized by steep gradients that slow the convergence of the employed stiff-stable solver. Nonetheless, the ROM achieves a speed up of 5 with a computed RMSE of $4 \cdot 10^{-3}$.

4.2.4 Conclusions

The objective of the study was to develop an efficient reduced-order model (ROM) for the simulation of the complex system that describes the methanation of biogas in a fixed-bed reactor with mass recycle. For the case analyzed in this study, it has been shown that a sufficiently reliable POD basis can be obtained using two solutions obtained from FOM simulations. Despite the nonlinear nature of the reactor model, the adopted approach has resulted in a substantial savings in calculation time of the step response of the system. The obtained speed up for the analyzed ROM has been of 15 in the case of a stationary regime solution and of 5 in the case of a more computationally intensive periodic solution. The order of the system has been reduced of one order of magnitude going from 1200 ODEs to 210 ODEs. This reduction obviously brings along a loss in the accuracy, but, as shown from the

reported figures, it can be said that the ROM predicts quite accurately both stationary and periodic solutions, with a relative error of the order of 10^{-3}. After assessing the accuracy of the proposed ROM, a more efficient optimization or a real time control application can be developed. A considerably larger benefit in terms of reduction of CPU time is expected if the methodology is applied to reduce more complex models such as those considering the radial distribution of temperature and concentration.

4.3 A POD-ROM Methodology for Optimal Structuring of a Non-isothermal Fixed-bed Reactor for Process Integration[3]

Katarzyna Bizon[a], Gaetano Continillo[b,*], **Enrico Alberto Cutillo**[b], Alfonso D'Onofrio[b]

[a]*Faculty of Chemical Engineering and Technology, Cracow University of Technology, ul. Warszawska 24, 31-155 Kraków, Poland*

[b]*Dipartimento in Ingegneria, Università degli Studi del Sannio, Piazza Roma 21, 82100 Benevento, Italy*

gaetano.continillo@unisannio.it

Abstract

The structure of a catalytic reactor integrating two reactions is yield-optimized in terms of distribution of active sites of two catalysts in a hybrid pellet, using a two-scale (pellet and reactor) approach. POD-Galërkin model reduction is adopted to reduce the burden of the optimization algorithm. Results show that optimal structuring can have a key role in catalyst process intensification, in terms of yield, chosen as the performance indicator and thus also as the objective function for the optimization problem.

Keywords: hybrid catalyst pellet, process integration, optimal reactor structuring.

4.3.1 Introduction

A catalytic fixed-bed reactor integrating two or more reactions poses a problem of performance optimization in terms of best selection of its structural parameters. Beyond temperature and residence time, the distribution of the catalytic active sites in the solid as well as the size of the pellets play a key role. In an earlier work, the yield-optimal distribution of catalytic active sites was determined for a single spherical hybrid pellet where two consecutive isothermal chemical reactions with one reversible step under arbitrary kinetics occur (Bizon and Continillo, 2019). A Proper Orthogonal Decomposition (POD) model reduction approach was employed to limit the computational effort related to the resolution of the optimization problem. Later on, the non-isothermal case of a hybrid pellet was tackled (Bizon and Continillo, 2020), and a Discrete Empirical Interpolation Method (DEIM) approach was combined with POD-Galërkin to best deal with the strong non-linearities due to the presence of the Arrhenius terms. In this work, the study is extended to the whole reactor, and the optimal distribution of catalytic active sites within a single pellet is

[3] Published in: *Computer Aided Chemical Engineering*. Vol. 50. Elsevier, 2021. 307-312. https://doi.org/10.1016/B978-0-323-88506-5.50049-8

determined with reference to the process enhancement on the apparatus level. This is a multiscale problem, in that the state variables are distributed along the reactor length and within the pellets, thus, to limit the computational expenses, the discretized model of the pellet is reduced using POD.

4.3.2 Mathematical model and solution methodology

Two reversible chemical reactions of the first order in a catalytic fixed-bed reactor made of spherical hybrid pellets take place under non-isothermal and steady-state conditions:

$$A \overset{k_1 k_{-1}}{\longleftrightarrow} B \overset{k_2 k_{-2}}{\longleftrightarrow} C \tag{1}$$

The mass and energy balance equations for a pellet, written in dimensionless form, are:

$$\frac{d^2\beta_A}{d\xi^2} + \frac{2}{\xi}\frac{d\beta_A}{d\xi} - \Phi_1^2 f_1 \frac{\tilde{r}_1}{\tilde{r}_{1,ref}} = 0 \tag{2a}$$

$$\frac{d^2\beta_B}{d\xi^2} + \frac{2}{\xi}\frac{d\beta_B}{d\xi} + \Phi_1^2 f_1 \frac{\tilde{r}_1}{\tilde{r}_{1,ref}} - \Phi_2^2 f_2 \frac{\tilde{r}_2}{\tilde{r}_{2,ref}} = 0 \tag{2b}$$

$$\frac{d^2\beta_C}{d\xi^2} + \frac{2}{\xi}\frac{d\beta_C}{d\xi} + \Phi_2^2 f_2 \frac{\tilde{r}_2}{\tilde{r}_{2,ref}} = 0 \tag{2c}$$

$$\frac{d^2\theta_p}{d\xi^2} + \frac{2}{\xi}\frac{d\theta_p}{d\xi} + \delta_1 \Phi_1^2 f_1 \frac{\tilde{r}_1}{\tilde{r}_{1,ref}} + \delta_2 \Phi_2^2 f_2 \frac{\tilde{r}_2}{\tilde{r}_{2,ref}} = 0 \tag{2d}$$

where $\beta_i = C_{p,i}/C_{ref}$ denotes reactant concentration within the pellet, $\theta_p = T_p/T_{ref}$ is the temperature of the pellet and $\xi = r/R_p$ is the radial coordinate with R_p being the pellet radius. Symbols f_1 and f_2 in Eq. (2) are the local volume fractions of the pellet occupied by active sites catalyzing, respectively the first and the second step of the process described by Eq. (1). The boundary conditions associated with the above balances are:

$$\left.\frac{d\beta_i}{d\xi}\right|_{\xi=0} = 0, \quad i = A,\ B,\ C; \qquad \left.\frac{d\vartheta_p}{d\xi}\right|_{\xi=0} = 0 \tag{3a}$$

$$\left.\frac{d\beta_i}{d\xi}\right|_{\xi=1} = \mathrm{Bi}_m(\alpha x_i - \beta_i(1)); \qquad \left.\frac{d\vartheta_p}{d\xi}\right|_{\xi=1} = \mathrm{Bi}_q\left(\vartheta_g - \vartheta_p(1)\right) \tag{3b}$$

Under the assumptions that the gas, flowing in a plug flow through the catalytic bed, obeys the ideal gas law and that the pressure drop can be neglected, the component mass balances, the continuity equation and the energy balance for the gas are:

$$\frac{d}{d\zeta}(\alpha x_i v) + \Gamma_m[\alpha x_i - \beta_i(1)] = 0, \quad i = A, B, C \tag{4a}$$

$$\frac{d}{d\zeta}(\alpha v) + \Gamma_m \sum_i [\alpha x_i - \beta_i(1)] = 0 \tag{4b}$$

$$v\frac{d\theta_g}{d\zeta} + \Gamma_{q1}\left[\theta_g - \theta_p(1)\right] + \Gamma_{q2}(\theta_g - \theta_q) = 0 \tag{4c}$$

with x_i being component molar fraction, $v = u/u_{ref}$ - dimensionless interstitial gas velocity and $\zeta = z/L_r$ – dimensionless reactor length. The conditions at the reactor inlet are:

$$x_i|_{\zeta=0} = x_{in,i}; \quad \alpha|_{\zeta=0} = \alpha_{in}; \quad \vartheta_g\big|_{\zeta=0} = \vartheta_{in}; \quad v|_{\zeta=0} = v_{in} \tag{5}$$

More details on the model formulation are in (Bizon and Continillo, 2021a). The optimization problem is to find f_1 maximizing the yield of C with respect to A, defined as:

$$\max_{f_1} Y_{CA,r} = \frac{\dot{n}_{C,out}}{\dot{n}_{A,in}} \text{ subject to } 0 \le f_1 \le 1 \text{ and } f_2 = 1 - f_1. \tag{6}$$

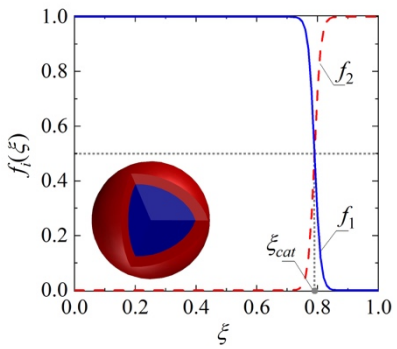

Figure 1. Distribution of f_1 and f_2 within the pellet for $\xi_{cat} = 0.7937$.

Considering that the core-shell arrangement of the active sites within bifunctional pellets is a promising approach to process integration and intensification (Bizon et al., 2020; Sánchez-Contador et al., 2019), the optimization procedure seeks the optimal radius of the pellet core ξ_{cat}. Functions f_1 and f_2 are defined by sigmoid functions as:

$$f_1(\xi) = \frac{1}{1+exp[-A\cdot(\xi-\xi_{cat})]} \text{ and } f_2(\xi) = 1 - f_1(\xi) \tag{7}$$

Figure 1 shows the distribution of f_1 and f_2 determined according to Eq. (7) with A = 100 and ξ_{cat} = 0.7937, that gives equal pellet volume occupied by each of the two catalysts. Considering that the catalyst arrangement with the active sites enhancing the first step of the process located in the pellet core proved to overperform the reverse arrangement, only the arrangement with catalyst one located in the pellet core and catalyst two in the shell is considered in this study. The solution of the optimization problem given by Eq. (6) requires the resolution of the two-scale reactor model. The most straightforward approach consists in the transformation of the infinite-dimensional problem (Eq. (2)-(5)) into a finite-dimensional form using the finite difference method. Given the core-shell nature of the pellet, as many as N = 101 discrete nodes are necessary to obtain satisfactory solution accuracy for the pellet sub-model. On the other hand, to account for possible hot spots, M = 501 discrete nodes along the reactor are needed to discretize the gas phase balance equations. Thus, to reduce the computational effort related to resolution of the optimization problem, a model-reduction technique is adopted. In this study, Proper Orthogonal Decomposition (POD) combined with Galërkin projection (Holmes et al., 1996) helps reduce the dimensionality of the smaller scale model, i.e. the pellet sub-model. The POD-Galërkin procedure consists in the orthogonal projection of the full-order finite-dimensional system onto a low number of POD modes generated from the full-order model (FOM) snapshots. Consider the following parameter-dependent system of N algebraic equations resulting from the discretization of the boundary value problem (Eq. (2)-(3)):

$$\boldsymbol{A}\boldsymbol{y}(\mu) + \boldsymbol{F}(\boldsymbol{y}(\mu)) = 0 \tag{8}$$

For the case here considered, the model μ represents the location of pellet within the bed and the value of ξ_{cat} for which the FOM was resolved. The POD basis, $\boldsymbol{\Psi} = [\psi_1, \psi_2, ..., \psi_N] \in \tilde{}^{N\times N}$, is then determined by solving the eigenvalue problem:

$$\boldsymbol{C\Psi} = \boldsymbol{\Lambda\Psi} \quad \text{where} \quad \mathbf{C} = \frac{1}{M_s}\boldsymbol{YY}^T \tag{8}$$

where **Y** is the matrix of snapshots obtained from FOM simulation and M_s is the number of snapshots used for the determination of the POD basis. Since in this study POD-Galërkin is used to reduce the pellet model coupled with the gas model, both embedded in the optimization algorithm, it is necessary to construct a POD basis that is able to approximate accurately the system behavior as it develops with the variation of the decision variable. Over the years, different sampling strategies were proposed to construct the so-called global POD basis (Lu et al., 2019), however, until now there is no reliable sampling policy. In this study, the procedure based on *k*-means clustering (Bizon and Continillo, 2021a) is employed to extract the most informative snapshots from a large number of solution profiles within the pellet. Considering that the optimal value of ξ_{cat} is expected to be close to 0.7937 (radius at which core and shell have equal volume in a sphere), the FOM was simulated for three values of ξ_{cat}, i.e. 0.75, 0.8, 0.85, 0.9 and 0.95, and then the *k*-means algorithm was run on the ensemble of intrapellet solution profiles collected along the reactor for all values of ξ_{cat}. For each state variable, a separate POD basis was determined using the $M_s = 100$ most informative snapshots.

4.3.3 Results and discussion

The values of the main parameters used in the simulations are summarized in Table 1.

Table 1. Main model parameters used in the numerical simulations.

Parameter	Value	Parameter	Value
D_{eff}	10^{-6} m^2·s^{-1}	R_p	$2.5 \cdot 10^{-3}$ m
$k_1(T_{in}) = k_2(T_{in})$	2.95 s^{-1}	T_{in}	400 K
$k_{-1}(T_{in}) = k_{-2}(T_{in})$	0.15 s^{-1}	u_{in}	0.7 m·s^{-1}
L_r	8 m	λ_{eff}	10^{-4} kW·m^{-1}·K^{-1}

Representative centroid of clusters employed to construct the POD basis for the concentration of intermediate product B within the pellet are shown in Fig. 2a, whereas Fig. 2b. shows the leading POD modes determined for β_B. The intrapellet solution profiles vary with the location of the pellet in the reactor, due to ongoing chemical process and variation of the composition of the flowing gas, and also with the variation of the catalyst arrangement represented by the variable ξ_{cat}. As shown in Fig. 2a, the *k*-means procedure permits to select

the most informative profiles while skipping those that are practically the same, and thus do not contribute, in terms of information content, to the POD basis.

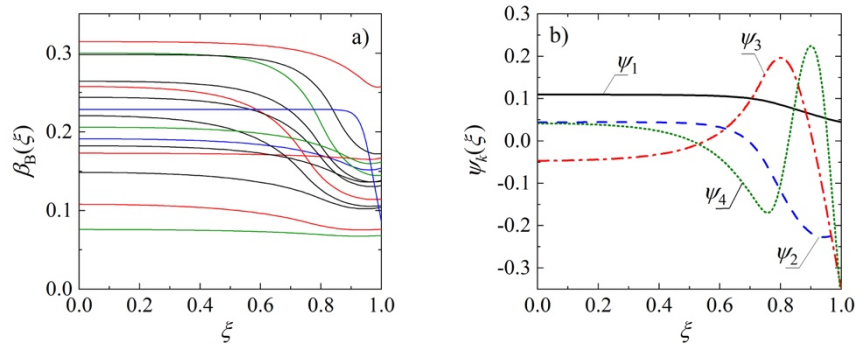

Figure 2. Representative solution profiles of $\beta_B(\xi)$ within the pellet selected using *k*-means clustering (a) and leading POD modes for the concentration of component B (b).

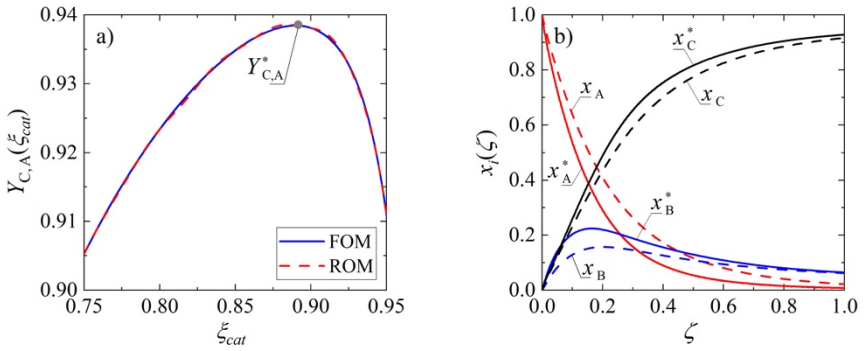

Figure 3. Values of the objective function YC,A determined using FOM and ROM (a), and molar fractions of the reactants in the gas phase along the reactor determined using ROM for optimal value of ξ^*_{cat} (solid lines) and for reference value $\xi_{cat} = 0.7937$ (dashed lines).

After analysing the accuracy of the ROM constructed using different truncation order, the value of $K = 19$, for each intrapellet state variable, was selected to run the optimization algorithm. Figure 3a shows the comparison of the objective function determined using FOM and ROM, together with the location of the optimum, determined by the MATLAB *fmincon* function with the submerged *fsolve* function for the resolution of the full- and reduced-order reactor model. It can be observed that the ROM approximates very accurately both the objective function and the location of the optimum. The optimal value of ξ_{cat} results to be higher than the one corresponding to the 1:1 volume ratio, $\xi_{cat} = 0.7937$, of the pellet occupied by the first and the second type of the catalytic active centers. Increasing the value of ξ_{cat} from the reference value equal to 0.7937 to optimal value, i.e. $\xi^*_{cat} = 0.8901$, permits in fact (Fig. 3b) to enhance the conversion of A near the reactor inlet. Values of the optimum location and corresponding values of the objective function are in Table 2 together with the

computational time expenses. Despite the relatively high number of the POD modes used to build the ROM, mainly because of the core-shell structure of the pellet, the ROM still allows considerable time saving, both when performing a single simulation and computing the optimization of the pellet structure.

Table 2. Comparison of optimal values and computational time of FOM and ROM (K = 19).

Model	ξ_{cat}^{*}	$Y_{C,A}^{*}$	Single sim. time, s	Optimization time, s
FOM	0.8901	0.9384	88.064	1573
ROM	0.8846	0.9386	18.904	385

4.3.4 Conclusions

Adopting the optimal structuring found in this study will positively impact the production and is foreseen as a practical gain in many processes of industrial interest. Although more detailed than most literature models, this approach has still some limitations in that it does not address reactor non-idealities: the hybrid plug-flow fixed-bed reactor model is in fact adopted. The model reduction procedure helps even though, with this particular problem, accuracy requires a relatively large number of POD modes to be included in the ROM.

Acknowledgments

G.C. is grateful to Università del Sannio for granting a sabbatical leave that made this and other research works possible. The research was partly financed by the Polish National Science Centre, project number 2017/26/D/ST8/00509.

4.4 Enhancing carbon dioxide adsorption in a hybrid fixed bed via structuring and thermal management: a numerical study[4]

Enrico A. Cutillo[a], Krzysztof Neupauer[b], Gaetano Continillo[c], Katarzyna Bizon[d]

[a] *Department of Engineering, Università degli Studi del Sannio, Piazza Roma 21, 82100 Benevento, Italy cutillo@unisannio.it, ORCID number 0000-0002-9991-7489*

[b] *Faculty of Chemical Engineering and Technology, Cracow University of Technology, ul. Warszawska 24, 31-155 Kraków, Poland, krzysztof.neupauer@pk.edu.pl, ORCID number: 0000-0002-1504-8686*

[c] *Department of Engineering, Università degli Studi del Sannio, Piazza Roma 21, 82100 Benevento, Italy continillo@unisannio.it, ORCID number: 0000-0002-6012-3999*

[d] *Faculty of Chemical Engineering and Technology, Cracow University of Technology, ul. Warszawska 24, 31-155 Kraków, Poland, katarzyna.bizon@pk.edu.pl, ORCID number: 0000-0001-7600-4452*

Corresponding author: Katarzyna Bizon, katarzyna.bizon@pk.edu.pl

Abstract.

Systems based on physical sorption are an attractive solution for CO_2 capture from flue gases, biogas upgrading or gas storage. Besides the sorbent choice, one of the most important factors to the design of such systems is proper heat management. Commonly used sorbents typically have low thermal conductivity. Nevertheless, catalyst particles characterized by high conductivity are inherently present in adsorptive (hybrid) reactors. Thus, appropriate structuring of hybrid beds can be used for controlling temperature profiles and improving the bed performance. In this study, the behaviour of a nonadiabatic adsorptive reactor described by a two-dimensional model was analysed for the adsorption step. The effect on the CO_2 adsorption performance of different spatial distributions of functionalities in the bed was investigated. The optimality problem for nonuniform radial distribution of sorbent and catalyst in the bed was solved, indicating that such a configuration is a potentially important direction for structuring hybrid beds. Results demonstrate that the optimal configuration of radially distributed functionalities significantly increases the amount of CO_2 absorbed under identical boundary and initial conditions for the bed. It appears that precise control of the heat generated and removed from the bed is achievable. Such control could be advantageous for the regeneration phase.

[4] Published in: *Chemical and Process Engineering: New Frontiers* 45.4 (2024).
DOI: 10.24425/cpe.2024.149471

Keywords: CO_2 sequestration, hybrid fixed bed, structured bed, thermal management, adsorptive reactor optimization

4.4.1 Introduction

The need for deceleration of ongoing global warming and the urgency for energy transition demand the development of new technologies as well as the advancement of existing ones. Among the techniques that undoubtedly require rapid development are various methods for separating carbon dioxide and other greenhouse gases, including volatile organic compounds (VOCs), from flue gases and ambient air. Another important and urgent problem to be addressed is the issue of treating fuels of biological origin, and in particular, the upgrading of biogas to biomethane. Ultimately, in light of the pursuit of widespread use of hydrogen and methane as fuel, it is also necessary to develop safe and viable (in terms of energy density) methods of both stationary and on-board storage of these fuels. An attractive solution suitable for CO_2 capture (Ben-Mansour et al., 2020), biogas upgrading (Ali Abd et al., 2024) or gas storage (Grande et al., 2023) are undoubtedly adsorption-based systems. Another example of the use of adsorption systems that is in line with eco-friendly and sustainable development concepts are adsorption-based cooling systems (Chauhan et al., 2022; Szyc and Nowak, 2014).

It is worth noting that physical adsorption together with chemisorption, membrane and cryogenic separation (Kammerer et al., 2022) provide the foundation for carbon capture and storage (CCS) and carbon capture and utilization (CCU) methods (Leonzio and Shah, 2024; McLaughlin et al., 2023a). Three fundamental storage methods for CO_2 falling under the CCS concept are generally available, namely oceanic, geological and mineral storage (Lin et al., 2024). In recent years the latter, also known as mineral carbonation, gained particular attention. It involves the binding of CO_2 with alkali and alkaline earth metal oxides, such as magnesium oxide and calcium oxide. Unlike geological storage, the process of carbonation takes place on the ground and yields a product that is stable over a long period. While the method itself is very attractive, primarily due to its safety, its application on a larger scale requires further intensive work. This is primarily due to the low reaction rate of mineral carbonation (Lin et al., 2024). On the other hand, CCU techniques involve reusing CO_2 and converting it into valuable chemicals, including fuels, polymers or feedstock chemicals such

as formic acid (McLaughlin et al., 2023b). Among the various options, the conversion of CO_2 to methane provides both a way to prevent its emission to atmosphere and to chemically store surplus energy generated from renewable sources (Miguel et al., 2017). There are three basic modes of implementation of CO_2 methanation, that is: direct methanation, sorption-enhanced methanation with in-situ water removal, and the recently proposed cyclic capture of CO_2 and its conversion in the same unit. In particular, the latter approach still requires research centered on the appropriate combination of adsorptive and catalytic functions in the apparatus.

Although studies involving the use of adsorbents for gas separation and storage have been the subject of extensive research for many decades, there are still many challenges in this field. They are strongly aligned with the goals and requirements imposed on the technologies under development. In fact, the crucial features that are expected to accompany the technologies of the future are essentially process integration and intensification, miniaturization, energy efficiency and zero waste. In this regard, one aspect that needs to be further researched extensively is increasing the capacity of adsorption systems, which can be realized both through the preparation of novel sorbents and, at the apparatus level, by choosing appropriate conditions for the execution of the process. Given that adsorption is an exothermic process and desorption is an endothermic process, the critical element that determines the efficiency of the sorption process is the heat removal and supply at the adsorption and desorption stages, respectively (Ben-Mansour et al., 2020; Kwan and Yao, 2022). Gas uptake and sorption efficiency are heavily influenced by heat transport in the bed of a solid sorbent, which is significantly hindered because of the low values of thermal conductivity of typical adsorbents (Saha et al., 2019).

To address the aforementioned problem, various heat management concepts aimed at improving heat transfer in granular beds were proposed and studied (Ben-Mansour et al., 2020; Demir et al., 2010; Grande et al., 2023), ranging from external (Fig. 1a), annular (Fig. 1b) and internal (Fig. 1c) water-cooling systems, or various combinations of them (Fig. 1d), longitudinal (Fig. 1e) or transversal fins (Fig. 1f), 3D printed metal lattices (Fig. 1g) or use of metal additives in the form of tiny chips. Also, the geometry of the apparatus itself affects the uptake of adsorbate captured from the gas being purified. In addition to obvious features

such as the ratio of the apparatus diameter to its length, which, as shown in the literature (Lian et al., 2019), significantly affects the removal of heat from the bed generated in the exothermic adsorption process, an interesting solution is the structuring of the walls of the apparatus (Fig. 1h). In fact, it is known that in fixed beds randomly filled with particles, the bed void fraction near the walls is higher than in the axis of the apparatus, which negatively affects the heat transfer process (Van Antwerpen et al., 2010). Hence, the design of a properly structured wall makes it possible to equalize the distribution of porosity in the radial direction of the apparatus, which, as a result, improves the heat removal rate from the bed (Eppinger et al., 2021).

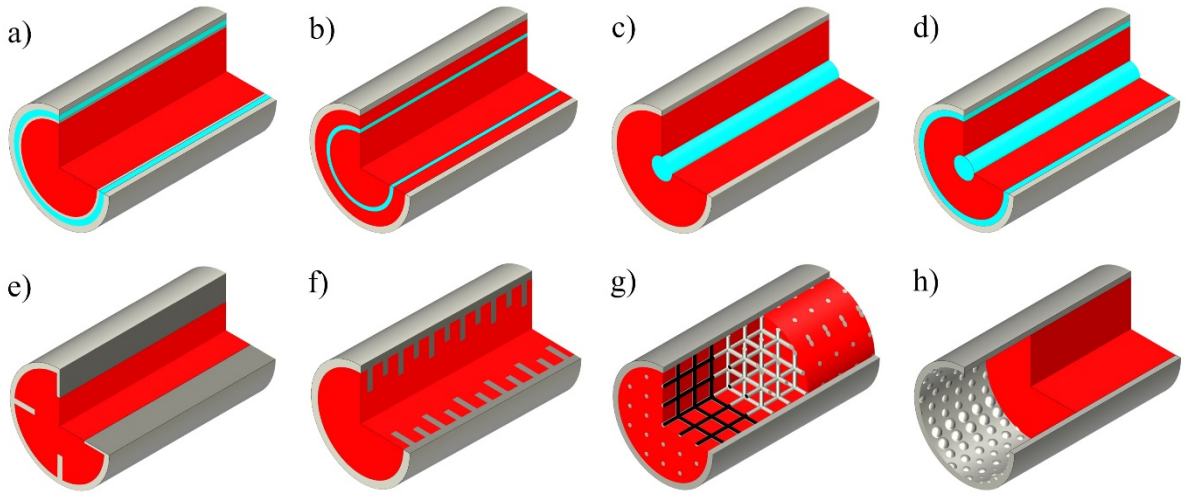

Fig. 1. Schematic of different configurations of fixed-bed adsorbent column: (a) bed with cooled wall, (b) bed with annular cooling, (c) bed with inner cooling, (d) bed with cooled wall and inner cooling, (e) bed with longitudinal fins, (f) bed with annular fins, (g) bed with internal lattice, (h) bed with structured wall.

Referring to bed additives (e.g. aforementioned metal chips) characterized by high conductivity and acting as a heat sink, in addition to inert materials, it is also worth mentioning hybrid beds consisting of an adsorbent and a catalyst. The latter can be used, for example, to conduct cyclic processes of CO_2 adsorption and its subsequent methanation in the Sabatier reaction (F. D. Martins et al., 2022). Another example of the use of adsorptive reactors for the capture of one compound in the first step, followed by a second step in which the conversion of the captured compound takes place, is the process of VOCs capture,

followed by their catalytic oxidation as described by(Jarczewski et al., 2022). Appropriate tailoring of hybrid fixed beds in adsorptive (hybrid) reactors, e.g. in terms of the ratio of adsorbent to catalyst or in terms of the spatial arrangement of the various functionalities, can also help to control the temperature profiles in the apparatus and thus improve process performance.

Given the above, the aim of this study was to assess the performance of a nonadiabatic adsorptive reactor operating at the CO_2 adsorption step and characterized by different spatial distributions of functionalities, which are zeolite 13X adsorbent and nickel catalyst. The evaluation of the spatial arrangement of particles characterized by different values of thermal conductivity and heat capacity was conducted by means of dynamic simulations using a two-dimensional model. Moreover, the optimality problem for radially nonuniform adsorbent distribution in the bed was solved. To find the global optimum that meets the constraints, a numerical method was implemented by discretizing the feasible space of the control variables using a uniform grid. Strictly speaking, this allowed to find a sub-optimal solution in the set of values of the discretized variables.

4.4.2 Mathematical model and numerical procedure

While in a previous study (Gunia et al., 2023), the effect of the macrostructure of an adiabatic hybrid fixed bed on carbon dioxide adsorption efficiency was evaluated using one-dimensional mathematical model, in this study the analysis was further extended to the nonadiabatic two-dimensional case to account for both longitudinal and radial distributions of concentration and temperature.

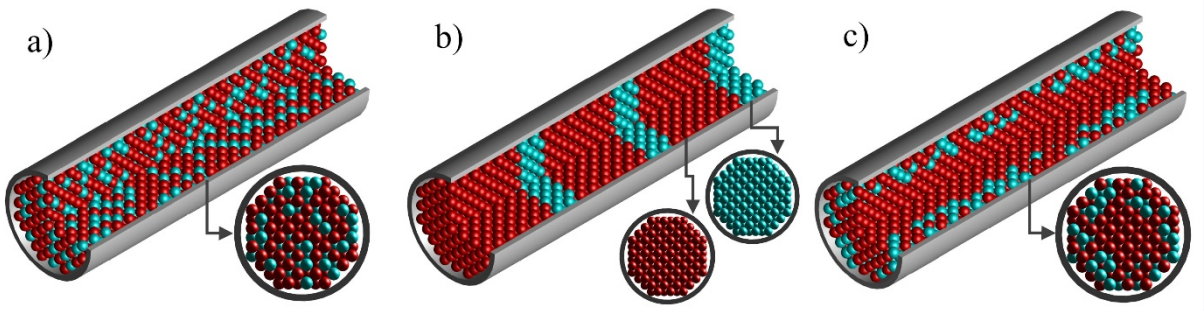

Fig. 2. Different configurations of a hybrid bed formed of adsorbent and catalyst particles: (a) uniform mixture of particles, (b) bed made of alternating layers of adsorbent and

catalyst, and (c) radially nonuniform distribution of both types of particles. Blue spheres indicate catalyst and red spheres indicate adsorbent.

The impact of different spatial arrangements of sorbent and catalyst in the hybrid bed on its performance at the CO_2 adsorption step was investigated. The arrangements analysed are as follows:

- a bed made of a uniform physical mixture of adsorbent and catalyst particles (Fig. 2a),
- a bed composed of alternating layers of adsorbent and catalyst particles (Fig. 2b),
- a bed with radially nonuniform distribution of adsorbent and catalyst particles (Fig. 2c).

- *Model assumptions and governing equations*

The following simplifying assumptions were adopted to formulate the mathematical model of the hybrid bed:

- a cylindrical fixed-bed hybrid apparatus is described using a two-dimensional axisymmetric model, thus both axial and radial variations of concentration and temperature are considered,
- the system is assumed to be adiabatic, with bed-to-wall heat transport being described by the α_w-model (Yagi and Kunii, 1960; Stegehake et al., 2018),
- there is a local thermal equilibrium of the gas phase and the solid phase, i.e. adsorbent and catalyst particles, consequently, from the thermal point of view, the model has a pseudo-homogeneous character,
- the gas mixture being separated via adsorption contains only CO_2 and N_2, moreover the inlet concentration of the component that is adsorbed (CO_2), is low enough to assume a constant gas velocity during its flow through the bed,
- the gas obeys the ideal gas law, and the pressure drop is low enough to be neglected,
- the gas flow is accompanied by both axial and radial dispersion of the mass,
- the Toth isotherm is employed to describe the adsorption equilibrium, and the rate of mass transfer is given by the linear driving force (LDF) model,

- in the energy balance, in addition to the convective component, axial and radial heat conduction resulting from the thermal conductivity of solid particles and gas, as well as from gas motion, is also considered,
- values of physical, thermal and transport properties are independent of temperature and calculated with respect to averaged concentrations and temperatures.

Under the above assumptions, the mass and energy equations describing the analysed system are as follows:

$$\frac{\partial C_{\mathrm{CO_2}}}{\partial t} = \frac{1}{\Gamma_{mass}}\left[\varepsilon_b D_{ax}\frac{\partial^2 C_{\mathrm{CO_2}}}{\partial x^2} + \frac{\varepsilon_b D_{rad}}{r}\frac{\partial}{\partial r}\left(r\frac{\partial C_{\mathrm{CO_2}}}{\partial r}\right) - u\frac{\partial C_{\mathrm{CO_2}}}{\partial x} - \rho_{b,ads} f_{ads}\frac{\partial q_{\mathrm{CO_2}}}{\partial t}\right] \tag{1}$$

$$\frac{\partial T}{\partial t} = \frac{1}{\Gamma_{heat}}\left[K_{ax}\frac{\partial^2 T}{\partial x^2} + \frac{K_{rad}}{r}\frac{\partial}{\partial r}\left(r\frac{\partial T}{\partial r}\right) - u\rho_g c_g\frac{\partial T}{\partial x} + \rho_{b,ads} f_{ads}(-\Delta H_{ads})\frac{\partial q_{\mathrm{CO_2}}}{\partial t}\right] \tag{2}$$

where:

$$\Gamma_{mass} = \varepsilon_{t,ads} f_{ads} + \varepsilon_{t,cat} f_{cat} \tag{3}$$

$$\Gamma_{heat} = \left(\varepsilon_{t,ads} f_{ads} + \varepsilon_{t,cat} f_{cat}\right)\rho_g c_g + \rho_{b,ads} f_{ads}\left(c_{s,ads} + c_{g,ads}\right) + \rho_{b,cat} f_{cat} c_{s,cat} \tag{4}$$

where f_{ads} denotes the volume fraction of adsorbent particles, whereas $f_{cat} = 1 - f_{ads}$ is the volume fraction of catalyst particles in the hybrid bed.

The adsorption rate $\partial q_{\mathrm{CO_2}}/\partial t$ was described by the linear driving force (LDF) model (Glueckauf and Coates, 1947), namely:

$$\frac{\partial q_{\mathrm{CO_2}}}{\partial t} = k\left(q^*_{\mathrm{CO_2}} - q_{\mathrm{CO_2}}\right) \tag{5}$$

where:

$$k = \frac{15 D_e}{r_p^2} \quad \text{and} \quad D_e = \frac{\varepsilon_p}{\tau_p}\frac{D_K D_m}{D_K + D_m} \tag{6}$$

with the molecular diffusion coefficient, D_m, calculated from the formula proposed by Chapman and Enskog (Poling et al., 2001), and Knudsen diffusion coefficient, D_K, calculated using the formula based on the kinetic theory of gases (Do, 1998).

The equilibrium concentration in Eq. (5) was described with Toth isotherm for zeolite 13X (Wang and LeVan, 2009) given by the following equation:

$$q^*_{CO_2} = \frac{a p_{CO_2}}{\left[1 + \left(b p_{CO_2}\right)^{\tau}\right]^{1/\tau}} \tag{7}$$

where:

$$a = a_0 exp\left(\frac{E}{T}\right), \quad b = b_0 exp\left(\frac{E}{T}\right), \quad \tau = \tau_0 + \frac{c}{T} \tag{8}$$

The coefficient of axial mass dispersion, D_{ax}, which appears in the mass balance given by Eq. (1) was calculated based on the following correlation (Wakao and Funazkri, 1978):

$$D_{ax} = \frac{D_m}{\varepsilon_b}\left(20 + 0.5 \mathrm{Sc} \mathrm{Re}_p\right) \tag{9}$$

while the radial dispersion coefficient, D_{rad}, was calculated using the following expression (Tsotsas and Schlünder, 1990):

$$D_{rad} = D_m\left(1 - \sqrt{1 - \varepsilon_b}\right) + \frac{u d_p}{8} \tag{10}$$

To simplify the calculations, constant values of density, ρ_g, and viscosity, μ_g, (determined based on the average composition and temperature of the gas mixture) were used to determine Schmidt and Reynolds numbers in Eq. (9). An analogous approach was made for the specific heat capacity of the gas phase, c_g, and adsorbed phase, $c_{g,ads}$, and for the enthalpy of adsorption, ΔH_{ads}. The latter was calculated, for the averaged saturation of the solid, from the Clausius-Clapeyron equation, which is (Do, 1998):

$$-\Delta H_{ads} = \frac{RT^2}{p_{\mathrm{CO_2}}}\left(\frac{\partial p_{\mathrm{CO_2}}}{\partial T}\right)_{q^*_{CO_2}} \quad \text{where} \quad p_{CO_2} = \frac{q^*_{\mathrm{CO_2}}}{\left[a^{\tau} - \left(q^*_{\mathrm{CO_2}}\right)^{\tau}\right]^{1/\tau}} \tag{11}$$

The values of axial, K_{ax}, and radial, K_{rad}, effective thermal conductivities were determined from the following correlations (Kunii and Smith, 1960; Yagi et al., 1960):

$$K_{ax} = K^0_{ax} + \lambda_g a_{ax} \mathrm{Pr} \mathrm{Re}_p \tag{12}$$

$$K_{rad} = K^0_{rad} + \lambda_g a_{rad} \mathrm{Pr} \mathrm{Re}_p \tag{13}$$

In the above equations (Eq. (12) and (13)), the first term denotes the so-called stagnant thermal conductivity, while the second term accounts for the effect of gas flow motion on heat transport. The parameters a_{ax} and a_{rad} are empirical parameters; in the present study,

following the literature results (Díaz-Heras et al., 2020), values equal to $a_{ax} = 0.5$ and $a_{rad} = 0.1$ were adopted. The stagnant thermal conductivity was calculated assuming that the medium is isotropic, therefore the radial and axial stagnant thermal conductivities were considered equal (Díaz-Heras et al., 2020) and were calculated as follows (Kunii and Smith, 1960):

$$K_{ax}^0 = K_{rad}^0 = \varepsilon_b + \frac{\beta(1-\varepsilon_b)}{\psi_t + \gamma/\kappa} \quad \text{where} \quad \beta = 0.9 \quad \text{and} \quad \kappa = \frac{\lambda_s}{\lambda_g} \tag{14}$$

whereas ψ_t depends on the bed porosity and the number of contact points between particles; for details on determining this quantity, see (Kunii and Smith, 1960; Díaz-Heras et al., 2020; Gunia et al., 2023).

The solution of the system of partial differential equations (PDEs) given by Eq. (1) and (2), together with Eq. (5), which was also used to determine the amount of CO_2 adsorbed, requires the definition of appropriate boundary conditions and initial conditions. Therefore, the boundary conditions (for the adsorption step) were defined as:

$$-D_{ax}\frac{\partial C_{\mathrm{CO_2}}}{\partial x} = \frac{u}{\varepsilon_b}\left(C_{f,\mathrm{CO_2}} - C_{\mathrm{CO_2}}\right) \quad \text{at} \quad x = 0 \quad \text{and} \quad \forall r \in [0, R_r] \tag{15}$$

$$\frac{\partial C_{\mathrm{CO_2}}}{\partial x} = 0 \quad \text{at} \quad x = L \quad \text{and} \quad \forall r \in [0, R_r] \tag{16}$$

$$\frac{\partial C_{\mathrm{CO_2}}}{\partial r} = 0 \quad \text{at} \quad r = 0 \quad \text{and} \quad \forall x \in [0, L] \tag{17}$$

$$\frac{\partial C_{\mathrm{CO_2}}}{\partial r} = 0 \quad \text{at} \quad r = R_r \quad \text{and} \quad \forall x \in [0, L] \tag{18}$$

$$-K_{ax}\frac{\partial T}{\partial x} = u\rho_g c_g\left(T_f - T\right) \quad \text{at} \quad x = 0 \quad \text{and} \quad \forall r \in [0, R_r] \tag{19}$$

$$\frac{\partial T}{\partial x} = 0 \quad \text{at} \quad x = L \quad \text{and} \quad \forall r \in [0, R_r] \tag{20}$$

$$-K_{rad}\frac{\partial T}{\partial r} = h_w(T - T_w) \quad \text{at} \quad r = 0 \quad \text{and} \quad \forall x \in [0, L] \tag{21}$$

$$\frac{\partial T}{\partial r} = 0 \quad \text{at} \quad r = R_r \quad \text{and} \quad \forall x \in [0, L] \tag{22}$$

Assuming that, initially, interparticle voids and intraparticle pores are filled with an inert gas, the initial conditions are:

$$C_{CO_2}(x,r,0) = q_{CO_2}(x,r,0) = 0 \text{ and } T(x,r,0) = T_0 \quad \forall x \in [0,L] \text{ and } \forall r \in [0,R_r] \tag{23}$$

The Robin-type boundary condition defined by Eq. (21) used to describe the energy exchange between the bed and the wall originates from the so-called α_w-model (Yagi and Kunii, 1960; Stegehake et al., 2018), which constitutes one approach for modelling cooled fixed-bed. The simplifying hypothesis behind the α_w-model implies that porosity, flow, and effective heat and mass dispersion are independent of radial position. Although the α_w-model exhibits inherent limitations that cannot be overcome by more accurate estimation of transport parameters, such as the unphysical temperature gradient between the near-wall region and the reactor wall, it is commonly used in practical applications due to its relatively low computational burden (Stegehake et al., 2018) and the possibility of obtaining an analytical solution of the heat transfer equation under certain simplifying hypotheses (Dixon et al., 1978; Jorge et al., 2010). The selection of the α_w-model in this study was further justified by the fulfilment of two conditions: first, the inner diameter of the reactor significantly exceeds the diameter of the particles ($D_r/d_p > 15$) (Stegehake et al., 2019); second, the adsorption process is not highly exothermic.

The apparent wall heat transfer coefficient, h_w, found on the right side of Eq. (21) was calculated according to the following formula recommended by Dixon (2012):

$$\mathrm{Nu_w} = \mathrm{Nu_{w0}} + \frac{1}{(1/\mathrm{Nu_w^*}) + (1/\mathrm{Nu_m})} \tag{24}$$

where:

$$\mathrm{Nu}_{w0} = \left(1.3 + \frac{5}{D_r/d_p}\right)\left(\frac{K_{rd}^0}{\lambda_g}\right) \tag{25}$$

$$\mathrm{Nu}_w^* = 0.3\,\mathrm{Pr}^{1/3}\,\mathrm{Re}_p^{0.8} \tag{26}$$

$$\mathrm{Nu}_m = 0.054\mathrm{PrRe}_p \tag{27}$$

Substituting Eq. (25)-(27) into Eq. (24) and using the definition of Nusselt number yields the formula:

$$h_w = \frac{\lambda_g}{d_p}\left(\mathrm{Nu}_{w0} + \frac{1}{(1/\mathrm{Nu}_w^*) + (1/\mathrm{Nu}_m)}\right) \tag{28}$$

- *Numerical solution of the model and employed parameters*

To solve numerically the equations of the model, which consist of two PDEs (Eq. (1) and (2)), an ordinary differential equation (ODE, Eq. (5)) to be solved at each position of the domain, with the associated boundary (Eq. (15)-(22)) and initial conditions (Eq. (23)), the method of lines was applied. It consists in approximating the derivatives with respect to spatial variables at discrete grid nodes using finite differences. The resulting large system of ODEs is then solved using an appropriate solver. In the present study, the spatial domain, that is, half of the cross-section of a tubular reactor, was discretized using $N_{ax} \cdot N_{rad} = 251 \cdot 51 = 12801$ nodes, where N_{ax} refers to the number of nodes along the bed length and N_{rad} along its radius. The obtained system of ODEs was then solved using the *ode15s* solver of the MATLAB software. To improve the reliability and efficiency of stiff ODE solvers (such as *ode15s*), providing information about the Jacobian matrix is crucial. The open-source "*ADiGator*" package developed in MATLAB was therefore used to generate the Jacobian sparsity pattern of the obtained ODEs system, which is useful to numerically calculate a sparse Jacobian, significantly reducing the computational time (Weinstein and Rao, 2017).

In the case of the bed made of alternating layers of adsorbent and catalyst (Fig. 2b), f_{ads} is solely a function of axial coordinate, x, and it was defined as in the previous work (Gunia et al., 2023) as a combination of double sigmoid functions:

$$f_{ads}(x) = 1 - \sum_{i=1}^{M/2-1} \frac{1}{1+\exp[-A(x-x_{2i-1})]} \cdot \frac{1}{1+\exp[A(x-x_{2i})]} - \frac{1}{1+\exp[-A(x-x_{M-1})]} \tag{29}$$

where M denotes the total number of layers of different material within the bed, x_i is the endpoint coordinate of the layer, whereas A is the sigmoid slope. In this study the value of A was set to 10000. This choice was guided by the objective of defining a function that closely resembles a step function while avoiding convergence errors.

The adsorbent distribution, $f_{ads}(x)$, defines the fraction of the reactor volume dedicated to the presence of the adsorbent. Its complement to unity represents the distribution function of the catalyst (or inert) material, i.e. $f_{cat}(x) = 1 - f_{ads}(x)$. It is important to note that f_{ads} is

not simply the ratio of adsorbent volume to total reactor volume, but rather the ratio of the reactor volume dedicated to adsorbent particles to the total reactor volume, $V_{tot} = L\pi R_r^2$. The expression "dedicated volume" includes both solid particles and voids. When filled with adsorbent, this designated volume of the reactor includes both the actual sorbent material (solid fraction) and the interparticle voids (void fraction).

For the case of the bed with radially nonuniform distribution of both types of particles, only the cases that are assumed feasible under practical conditions were adopted. Namely, it was assumed that the bed consists of an inner cylindrical core with a diameter of $R_c < R_r$, in which $f_{ads,1}$ and, consequently, $f_{cat,1}$ are constant values, encircled by a cylindrical shell, in which the distributions of individual functionalities ($f_{ads,2}$, $f_{cat,2}$) are also constant, but with values different from those in the core. Such a distribution, which in this case is only a function of the radial coordinate, is described by the following function:

$$f_{ads}(r) = \frac{f_{ads,1}}{1 + \exp[A(r - R_c)]} + \frac{f_{ads,2}}{1 + \exp[A(r - R_c)]} \tag{30}$$

Figure 3a shows representative distributions of both materials in the bed corresponding to the optimal case described later in this study. It is important to underline that in the configuration where the distribution of functionalities varies radially, once the adsorbent-to-catalyst ratio is defined and $f_{ads,1}$ are defined, the other constant $f_{ads,2}$ is also determined indirectly as a function of the other two parameters. This relation is crucial for the optimization process because it reduces the number of feasible solutions, i.e. it represents a constraint of the optimization problem.

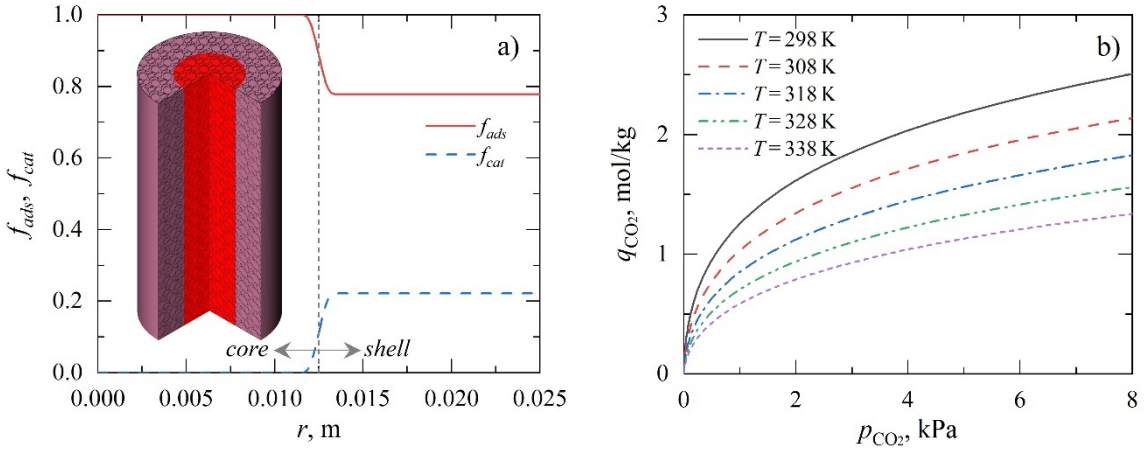

Fig. 3. Radial distributions of adsorbent and catalyst volume ratio in configuration with the radially nonuniform sorbent distribution (a), and adsorption isotherms of CO_2 on zeolite 13X (b) determined for different temperatures based on parameters from Wang and LeVan (2009).

The main parameters of the mathematical model used in the numerical simulations are summarized in Table 1. In addition, Fig. 3b graphically shows the isotherms of CO_2 adsorption on zeolite 13X, which were calculated based on the parameters given in the work of Wang and LeVan (2009). The physical parameters of the second granular material, i.e. nickel catalyst, which has an inert character during the adsorption stage, were taken from Bremer et al. (2017).

Table 1. The main parameters of the mathematical model.

Parameter	Value	Parameter	Parameter	Value	Parameter
a_0	$6.509 \cdot 10^{-3}$ mol/(kg·kPa)	L	1 m	$\varepsilon_{p,ads}$	0.54
b_0	$4.884 \cdot 10^{-4}$ 1/kPa	P	101325 Pa	$\varepsilon_{p,cat}$	0.6
C	3.805·10 K	r_p	10^{-3} m	$\lambda_{s,ads}$	0.15 W/(m·K)
$c_{s,ads}$	1100 J/(kg·K)	$T_f = T_w$	298.15 K	$\lambda_{s,cat}$	0.84 W/(m·K)
$c_{s,cat}$	1107 J/(kg·K)	u	0.2 m/s	$\rho_{p,ads}$	1085 kg/m^3
d_{pore}	10^{-9} m	$y_{CO_2,in}$	0.05	$\rho_{p,cat}$	2355 kg/m^3
D_r	$5 \cdot 10^{-2}$ m	ΔH_{ads}	$-3.898 \cdot 10^4$ J/mol	τ_0	$7.487 \cdot 10^{-2}$
E	$2.991 \cdot 10^3$ K	ε_b	0.45	τ_p	3

4.4.3 Results and discussion

Given that, in general, adsorbents and catalysts differ significantly in their thermal conductivity values, this factor, combined with the bed structure and the exothermic nature of adsorption, determines the efficiency of the sorption process. This is due to the significant influence of the structure of the hybrid bed on the axial and radial temperature profiles. In the present study, the average concentration of adsorbed carbon dioxide in the solid phase at the time of bed breakthrough was used as an index of the efficiency of the adsorption process. The breakthrough time, t_b, was defined as:

$$t_b = \min\{ t: \bar{y}_{\mathrm{CO_2},out}(t) = c_{lim} \cdot y_{\mathrm{CO_2},in}\} \tag{31}$$

which states that t_b is the minimum time at which the average molar fraction of adsorbate at the reactor outlet, $\bar{y}_{\mathrm{CO_2},out}(t)$, reaches a predefined ratio, c_{lim} (here set to 1%), of the molar fraction of CO_2 in the gas feed to the apparatus, $y_{\mathrm{CO_2},in}$. Meanwhile, the average concentration at the breakthrough time, $Q_{\mathrm{CO_2}}(t_b)$, was calculated from the equation:

$$Q_{\mathrm{CO_2}}(t_b) = \frac{2\pi}{\pi {R_r}^2 L} \int_0^L \int_0^{R_r} f_{ads}\, q_{CO_2}\big|_{t_b}\, r dr dx \tag{32}$$

Comparative analysis of sorption dynamics was performed for three different bed configurations described in the previous section and shown in Fig. 2. For the bed made of uniform physical mixture of adsorbent and catalyst particles (Fig. 2a) and for the layered bed (Fig. 2b), numerical simulations were conducted for both the adiabatic and nonadiabatic (with T_w = 298.15 K) case. In these calculations, following the results of earlier work (Gunia et al., 2023), where the one-dimensional adiabatic case was analysed, the volume ratio of adsorbent to catalyst was also varied (i.e. *ads-to-cat* = {1:1, 2:1, 3:1, 4:1, 5:1, 6:1}), moreover, for a layered bed the number of layers was changed as well (M = {2, 4, 6, 8, 10}). The calculations concerning the case of the bed with radially nonuniform sorbent distribution were limited to nonadiabatic case, and as specified above (Fig. 3a) two zones in such a bed were distinguished, i.e., a cylindrical core and a cylindrical shell, characterized by constant but different (among the zones) distributions of functionalities.

Figure 4 compares the results obtained for two values of the adsorbent to catalyst ratio versus the number of layers in the layered bed obtained for the adiabatic and nonadiabatic case. The last (from the right) symbols corresponding to each analysed process case refer to a bed made of physical mixture of particles. As expected, the introduction of bed cooling (nonadiabatic case) enables a significant increase in bed breakthrough time (Fig. 4a) and

raises the corresponding amount of adsorbed CO_2 (Fig. 4b). While the configuration with six alternating layers of adsorbent and catalyst performs best in the case of a process conducted without heat exchange, for the nonadiabatic case a mixed bed behaves slightly better.

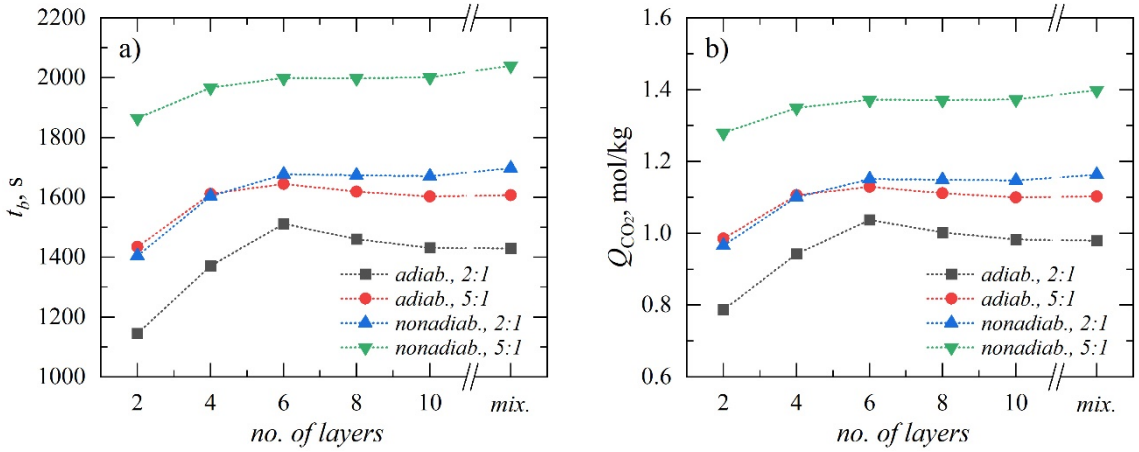

Fig. 4. Bed breakthrough time, t_b (a), and corresponding values of the average adsorbate concentration in the sorbent, Q_{CO_2} (b), determined for adsorbent-to-catalyst ratios equal to 2:1 and 5:1, for both adiabatic and nonadiabatic (T_w = 298.15 K) bed vs. number of alternating layers.

Both in the adiabatic case and in the nonadiabatic case, the most significant increase in breakthrough time and the amount of adsorbed CO_2 is observed when moving from two to four zones. This is because the two-layer configuration behaves like a standard adsorption column, but with an additional sorption-inactive zone located near the outlet. In the case of catalyst (or inert) layers sandwiched between the sorbent layers (e.g. 4 to 10 layers), the initially cold sorption-inactive particles function as a heat sink for the gas being warmed up due to exothermic sorption. Thus, the t_b value is significantly lengthened and the Q_{CO_2} value is increased even in the absence of bed cooling (Fig. 4). The improvement of the bed behavior under adiabatic conditions, achieved by structuring the bed with alternating layers of adsorbent and inert material, was described in a previous work where the characteristic formation of heat waves was analyzed, allowing the inert layer to be considered as a heat sink (Gunia et al., 2023). In addition, the same work by Gunia et al. (2023) showed that the optimal number of layers under adiabatic conditions is six. However, Fig. 4a and 4b show that when the cooling effect of a wall maintained at a lower temperature is added, the adoption of a uniform mixture configuration improves the bed performance, and the optimal

number of layers is no longer equal to six. This is because the phenomenon that affects the bed sorption efficiency is not only the presence of a thermal flywheel, but also the enhanced ability of the bed to transport heat out of the reactor. This effect is consistent with the experimental results shown in the work of Demir et al. (2010) and Ben-Mansour et al. (2020). Specifically, in the work of Demir et al. (2010), it was experimentally shown that mixing metal pieces uniformly with the adsorbent improves the conductivity of the bed and thus the removal of heat generated during adsorption. Unlike Demir et al. (2010), the present work aims to understand not only the variability of the adsorption efficiency while varying the ratio of the amount of adsorbent to inert material, but also to push the analysis towards the bed structure, which can be of fundamental importance in adsorption processes, as shown in the experimental work of Jarczewski et al. (2022).

The heat sink effect is still dominant in the layered nonadiabatic configuration and is shown in more detail in Fig. 5, for the number of layers $M = 6$ and the nonadiabatic case with adsorbent to catalyst ratio equal to 5:1. The left column of Fig. 5 illustrates the spatial distributions of temperature, $T(x, r)$, at several representative time instants, while the right column shows the concentration of CO_2 adsorbed in the solid per unit volume of the reactor, determined according to the formula:

$$\tilde{q}_{\mathrm{CO_2}} = \rho_{b,ads} f_{ads} q_{\mathrm{CO_2}} \tag{33}$$

As shown in Fig. 5a, the adsorption process is accompanied by the formation of a classical thermal wave. However, once the wave front reaches the boundary of the first zone of the sorbent and catalyst (vertical dashed line), due to the absence of adsorption occurring in the catalyst (Fig. 5b), a drop in temperature is observed, which is due to the large heat capacity of the bed material within this zone. As a result, the influent gas on the subsequent second sorbent zone is slightly cooler (Fig. 5c), and the adsorption equilibrium is more favorable (Fig. 5d). Moving forward in time, the effect of heat uptake by the catalyst (inert) layer diminishes due to its heating and the flattening of the thermal waves resulting from axial heat conduction throughout the bed (Fig. 5e).

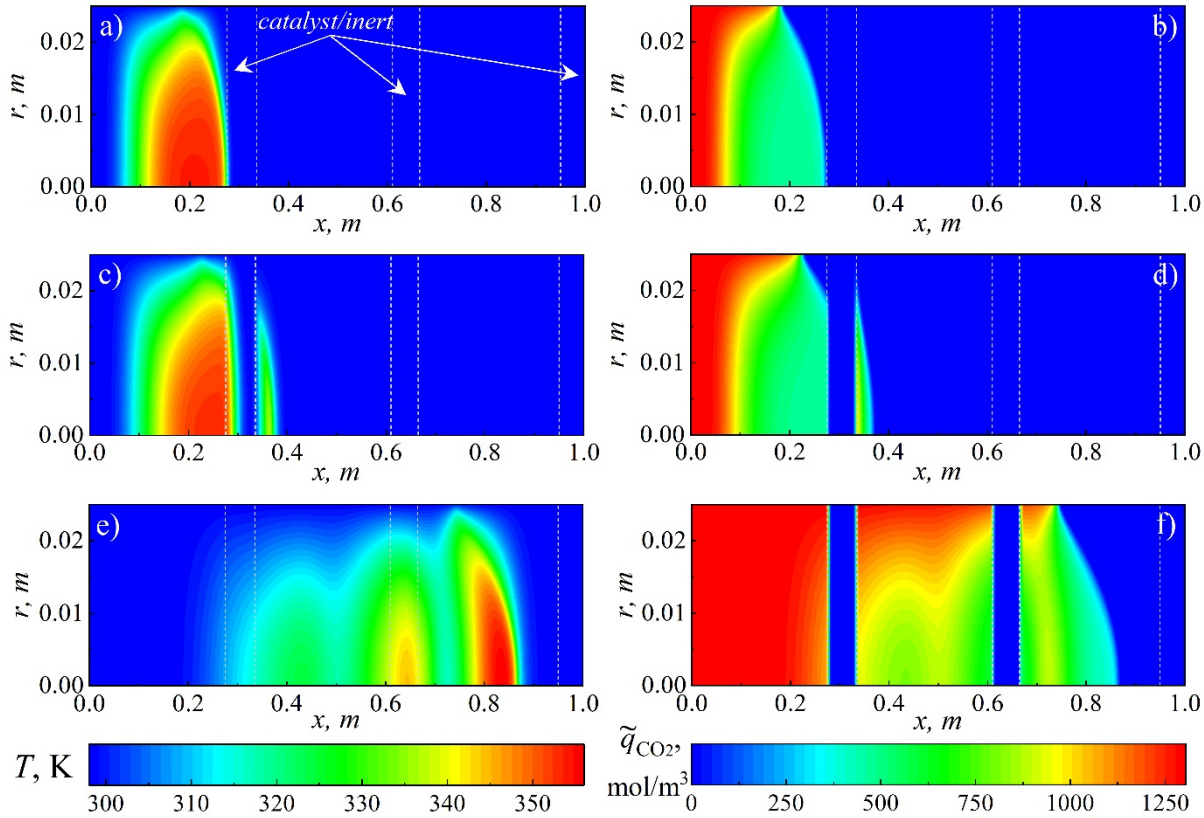

Fig. 5. Spatial distributions of temperature (left column) and solid-phase concentration of CO_2 (right column) expressed in moles per cubic meter of hybrid reactor determined for nonadiabatic (T_w = 298.15 K) hybrid bed with six alternating layers of adsorbent and catalyst, and with adsorbent-to-catalyst ratio equal to 5:1 at: (a)-(b) t = 8 min, (c)-(d) t = 10 min, and (e)-(f) t = 30 min.

Figure 6 shows a comparison of the spatial distributions of the temperature and the variable $\tilde{q}_{CO_2}$ at t_b obtained for different bed configurations, i.e.: layered bed with M = 2 (Fig. 6a and 6b), bed made of uniform mixture of particles (Fig. 6c and 6d), and layered bed with M = 6 (Fig. 6e and 6f). As mentioned earlier, a uniform nonadiabatic bed slightly outperforms a multilayer bed regarding breakthrough time, that is t_b = 1999.36 s for the latter and t_b = 2039.97 s for uniformly mixed sorbent and catalyst particles. Furthermore, analyzing Figures 6a, 6c and 6e, it is evident that higher temperatures are observed near the outlet section when dealing with a layered configuration, compared to the uniform mixture configuration. This may be related to the fact that the preferred path for heat exchange is where the catalyst is present. In the case of the layered configuration, the catalyst is not present where adsorption occurs, making it difficult for heat to be removed from the bed due

to the higher resistance compared to the uniform case, especially near the wall. In fact, heat removal through the wall of the apparatus in the sorption zones, where the actual process takes place, is hindered due to the lower heat conductivity value of zeolite 13X compared to the nickel catalyst (respectively, $\lambda_{s,ads} = 0.15$ W/(m·K) and $\lambda_{s,cat} = 0.84$ W/(m·K)). Consequently, the physical mixture of adsorbent and catalyst exhibits an improvement of the apparent wall heat transfer coefficient (h_w) and of the effective radial thermal conductivity (K_{rad}) (see Eq. (14) and (28)), thereby facilitating heat extraction. Hence, with the aim of enhancing the cooling effect, a configuration with a radially nonuniform distribution of the sorbent volume fraction is considered in the next step.

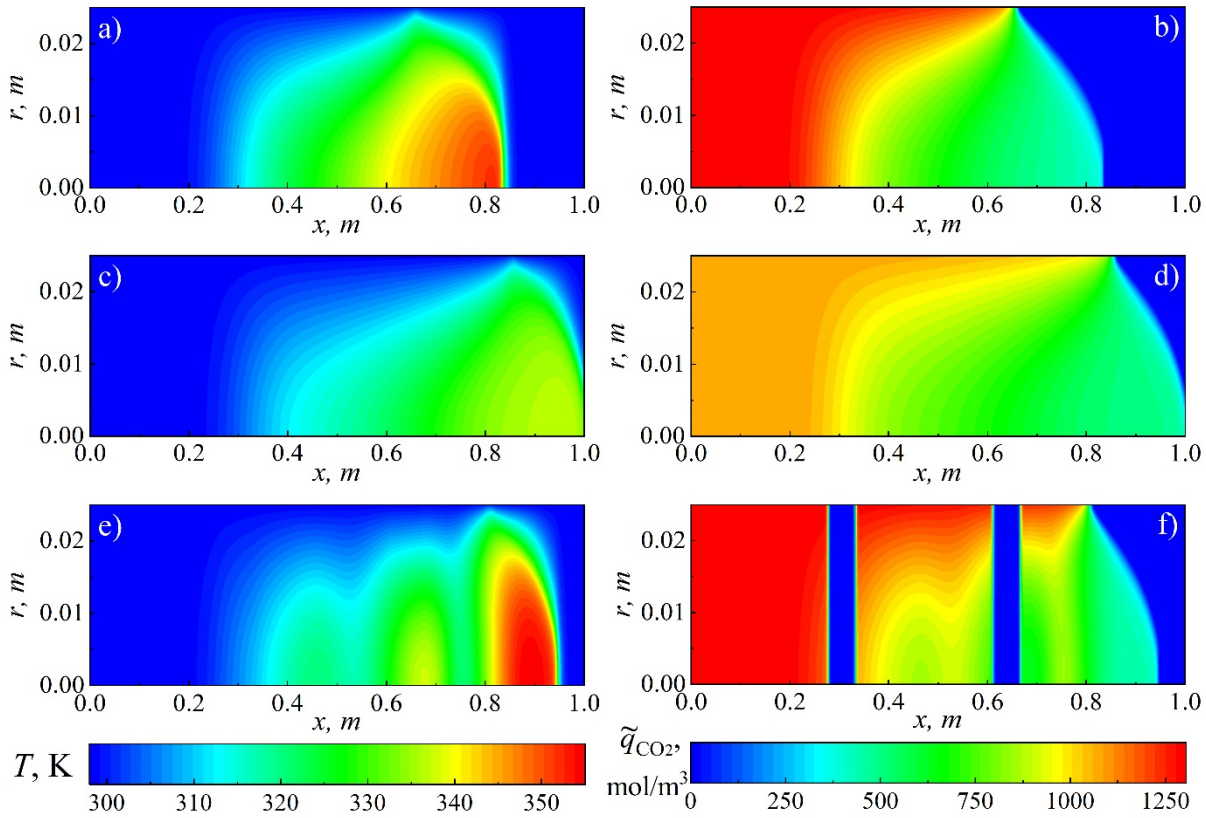

Fig. 6. Spatial distributions of temperature (left column) and solid-phase concentration of CO_2 (right column) expressed in moles per cubic meter of hybrid reactor at t_b for: (a)-(b) bed with two layers (t_b = 1864.93 s), (c)-(d) bed made of uniform mixture of particles (t_b = 2039.97 s), and (e)-(f) bed with six layers (t_b = 1999.36 s). In all cases, the bed is nonadiabatic (T_w = 298.15 K), and adsorbent-to-catalyst ratio is 5:1.

The analysis of the temperature distributions shown in Fig. 6a, 6c and 6e suggests that for the bed configuration composed of a cylindrical core with $f_{ads,1}$ and $f_{cat,1}$ and of cylindrical shell characterized by $f_{ads,2} \neq f_{ads,1}$ and $f_{cat,2} \neq f_{cat,1}$ (Fig. 3a), placing more sorbent near the wall (i.e. $f_{ads,2} > f_{ads,1}$) could be more advantageous due to the lower temperature near the wall, which favors adsorption. This approach, however, is also disadvantageous, because the adsorbent near the wall has lower thermal conductivity, which negatively impacts the efficiency of heat transfer, thereby worsening the apparent wall heat transfer coefficient. The key factor increasing sorption efficiency is the intensified heat removal through the wall.

Even with the assumption made here about the constant character of $f_{ads,1}$ and $f_{ads,2}$, respectively in the cylindrical core and surrounding shell, the number of viable solutions is essentially infinite, because an additional design parameter is the radius of the core. For this reason, to determine the radial distribution of the sorbent, which could give a higher sorption efficiency than the uniform and layered bed, an optimization problem was solved. The average value of CO_2 adsorbed in the bed up to the breakthrough time, $Q_{\mathrm{CO_2}}$, was chosen as the objective function, therefore as a result, the problem became:

$$\max_{f_{ads,1}, R_c} Q_{\mathrm{CO_2}} \tag{34}$$

In the above equation, $f_{ads,1}$ is the volume fraction of sorbent in the core, and R_c is the radius of the core. Given that for a fixed value of the ratio of sorbent to catalyst (here 5:1), $f_{ads,2}$ depends on $f_{ads,1}$, the constraints of the problem can be written as follows:

$$f_{ads,2} = \frac{f_{ads,tot} - f_{ads,1}(V_1/V_{tot})}{(V_2/V_{tot})} \tag{35}$$

where $f_{ads,tot} = ads\text{-}to\text{-}cat/(ads\text{-}to\text{-}cat - 1)$ is the total volumetric fraction allocated to the adsorbent in the reactor, V_1 and V_2 are respectively the volumes of the inner bed core and the outer bed shell, whereas V_{tot} is the total volume of the reactor. Moreover, both $f_{ads,1}$ and $f_{ads,2}$ must be constrained to be equal to or greater than 0 and less than or equal to 1. These inequalities combined with Eq. (35), divide the region of the space spanned by all the combinations of $f_{ads,1}$ and R_c into a feasible and an unfeasible region, which is displayed in Fig. 7.

Since the solution of the optimization problem at this research stage is mainly illustrative, the problem was solved using a brute force approach. Some experimental work to validate the model results is currently being designed for future work based on the results of this numerical analysis. Figure 7 shows feasible solutions of the problem defined by Eq. (34) and

(35) in the space of design parameters determined by direct simulation of the dynamics of the hybrid bed model until its breakthrough. In addition, the optimal pair of design parameters, namely $f_{ads,1} = 1$ and $R_c/R_r = 0.5$ (hence $R_c = 1.25 \cdot 10^{-2}$ m), for which $Q_{CO_2} = 1.431$ mol/kg, are marked in the figure with a bullet. For such a solution, given the adopted value of the adsorbent to catalyst ratio (5:1) throughout the apparatus, $f_{ads,2} = 0.78$. The optimum point can be seen as a compromise between improving the wall heat transfer and the radial heat conductivity. In fact, since both effects are influenced by the conductivity of the bed material (see Eq. (14) and (28)), for a constant adsorbent to catalyst volume ratio, improving one effect inevitably worsens the other. As a result, if the catalyst is positioned entirely near the wall, the heat generated in the bed will have difficulty reaching the higher conductivity layer, making it more difficult to extract and reducing the performance of the adsorbent bed.

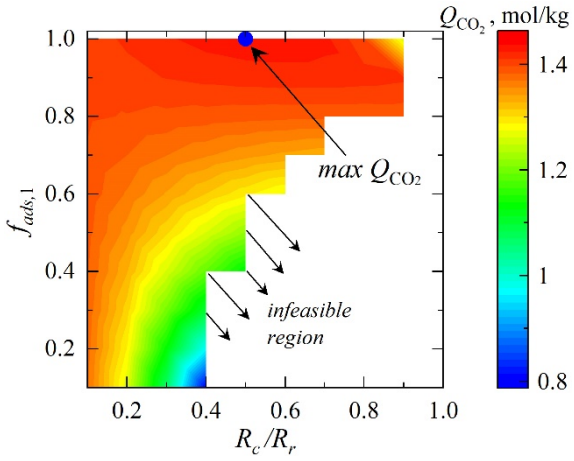

Fig. 7. Objective function, Q_{CO_2}, for optimizing the structure of nonadiabatic bed with the radially nonuniform distribution of adsorbent, comprising two decision variables, i.e., core radius, R_c, and volume fraction of sorbent particles in the core, $f_{ads,1}$, together with its maximum (denoted with bullet). Optimization was done by setting $T_w = 298.15$ K and the adsorbent-to-catalyst ratio equal to 5:1.

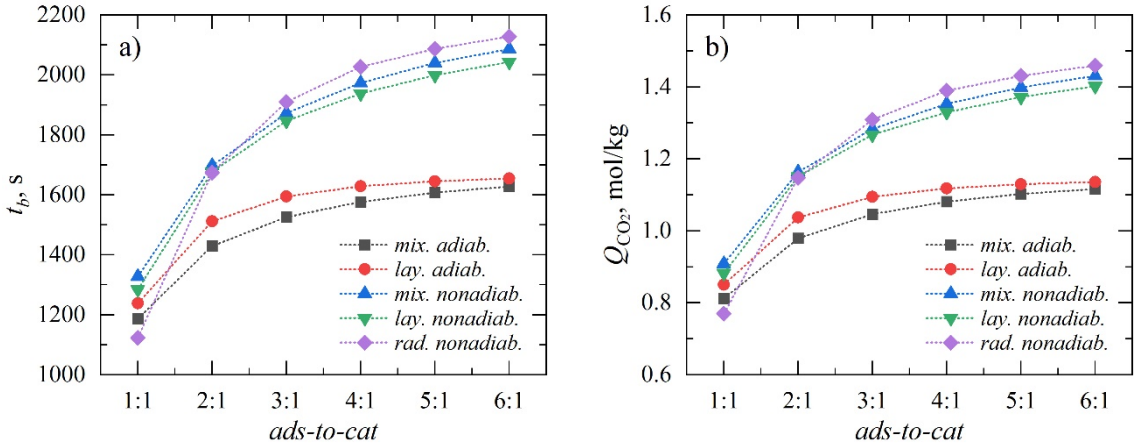

Fig. 8. Bed breakthrough time, t_b (a), and corresponding values of the average adsorbate concentration in the sorbent, Q_{CO_2} (b), determined for different configurations of hybrid bed depending on adsorbent-to-catalyst ratio, where *mix*. denotes a bed made of uniform mixture of particles, *lay*. corresponds to a bed made of six alternating layers, and *rad*. denotes bed with optimal radially nonuniform distribution of adsorbent.

In Fig. 8, the resulting configuration (denoted by *rad. nonadiab.*) is compared with the results obtained for the layered bed (denoted by *lay. adiab.* and *lay. nonadiab.*) and the uniform bed (denoted by *mix. adiab.* and *mix. nonadiab.*). The results are shown as a function of the sorbent to catalyst ratio. It can be observed that in the case of the aforementioned ratio equal to 5:1 (which was addressed by the solved optimization problem) the radial nonuniform distribution of the sorbent allows to increase both the t_b and Q_{CO_2} when compared to the mixed or layered configuration. Although the increase is not large, it indicates a potentially important direction for structuring hybrid beds in adsorptive reactors. Figures 9 and 10 show, respectively, the spatial distributions of temperature and CO_2 concentration in the solid phase (expressed per unit volume of the column) at breakthrough (Fig. 9) and shortly after the start of the process, i.e. for $t = 10$ min (Fig. 10). The figures show both the distributions for the optimal solution (Fig. 9a and 9b, and Fig. 10a and 10b) and for the case with the same value of R_c where most of the sorbent is located near the wall (Fig. 9c and 9d, and Fig. 10c and 10d, where $f_{ads,1} = 0.4$ and $f_{ads,2} = 0.98$). It can be observed that both at the beginning of the process (Fig. 10) and at the breakthrough of the bed (Fig. 9), both the front of the concentration wave and the thermal wave for the optimal solution are much more flattened than those obtained for the second case shown here.

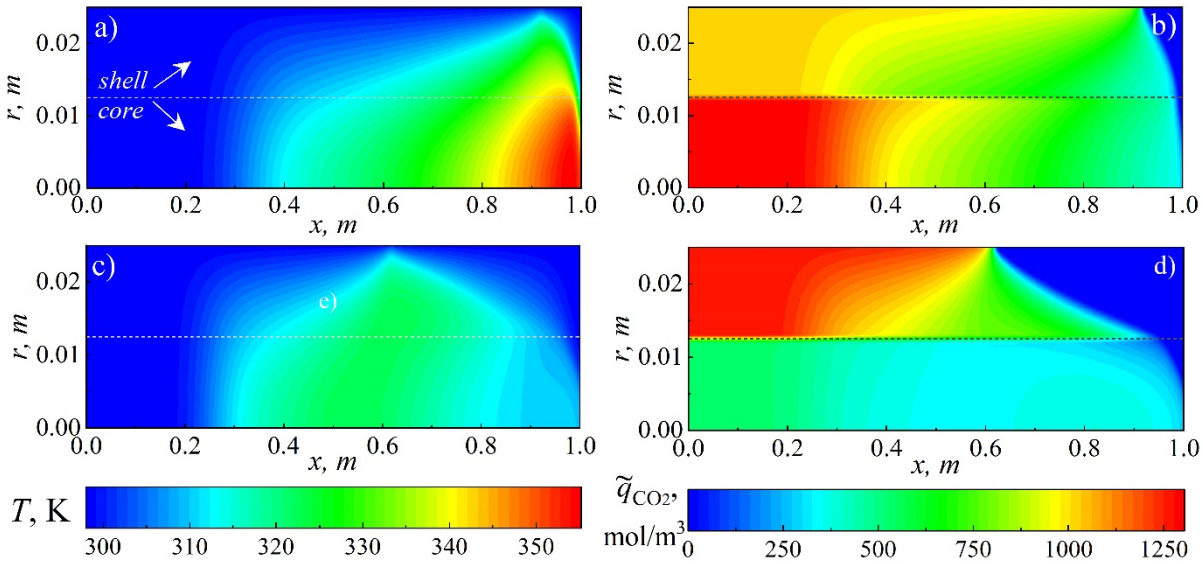

Fig. 9. Spatial distributions of temperature (left column) and solid-phase concentration of CO_2 (right column) expressed in moles per cubic meter of hybrid reactor at t_b for bed with radially nonuniform distribution of adsorbent: (a)-(b) optimal design with $f_{ads,1} = 1$ and $R_c/R_r = 0.5$ ($t_b = 2087.29$ s), and (c)-(d) configuration with $f_{ads,1} = 0.4$ and $R_c/R_r = 0.5$ ($t_b = 1639.39$ s). In both cases, the bed is nonadiabatic ($T_w = 298.15$ K), and the adsorbent-to-catalyst ratio is 5:1.

There are two reasons for this: For the optimal solution, heat removal from the core is difficult but in this zone, there is more sorbent available for the CO_2. As a result, the axial mass dispersion flattens the longitudinal concentration wave to a lesser extent because the adsorbate is effectively adsorbed by the solid. At the same time, the more effective heat removal from the cylindrical shell (characterized by higher nickel content) reduces the width of the thermal wave near the apparatus wall, which can be observed most clearly in Figure 10. For the optimal solution (Fig. 10a and 10b), the heat removal from the core is difficult, but in this zone, there is more sorbent available for the CO_2. As a result, the axial mass dispersion flattens the concentration wave in the longitudinal direction to a lesser extent, as can be seen by comparing Figure 10b and 10d, since the adsorbate is effectively adsorbed by the solid. In addition, the bed zone characterized by a lower fraction of adsorbent performs better in the optimal case (Fig. 10b), showing higher CO_2 concentration in the solid phase than in the sub-optimal case (Fig 10d). At the same time, more effective heat removal from the cylindrical shell (characterized by higher nickel content) reduces the width of thermal wave near the apparatus wall (Fig. 10a).

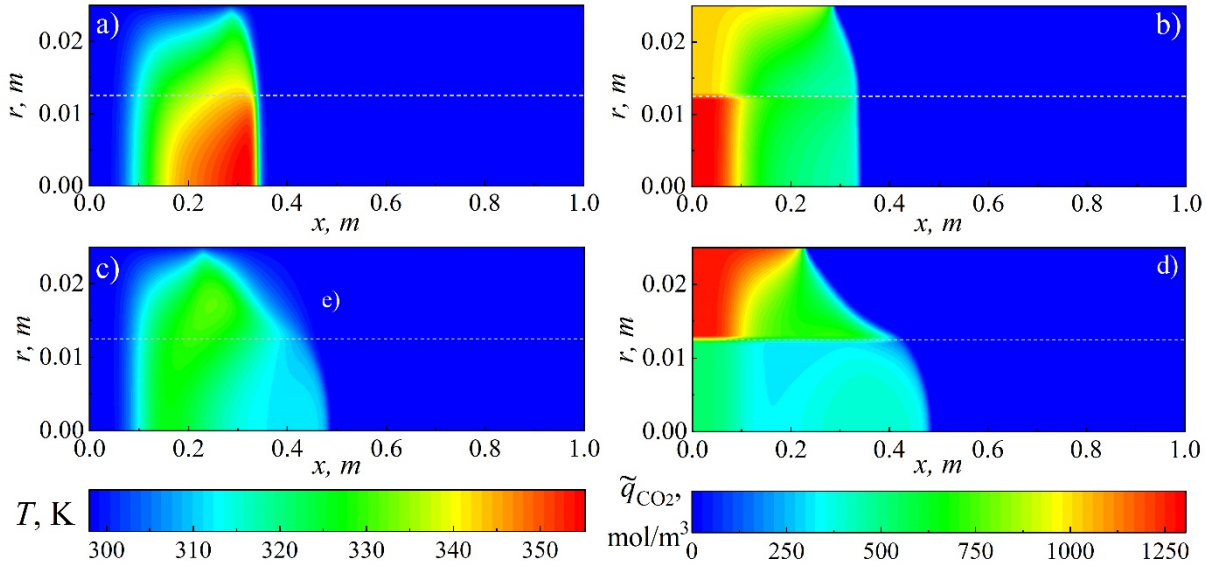

Fig. 10. Spatial distributions of temperature (left column) and solid-phase concentration of CO_2 (right column) expressed in moles per cubic meter of hybrid reactor determined for nonadiabatic (T_w = 298.15 K) hybrid bed with radially nonuniform distribution of adsorbent, and with adsorbent-to-catalyst ratio equal to 5:1 at t = 10 min: (a)-(b) optimal design with $f_{ads,1}$ = 1 and R_c/R_r = 0.5, and (c)-(d) configuration with $f_{ads,1}$ = 0.4 and R_c/R_r = 0.5.

Furthermore, Fig. 9 and 10 show that by radially distributing materials with different capacities and thermal conductivities, it is possible to significantly modify both the shape and the intensity of the heat wave generated inside the bed, in this case due to adsorption. This new ability to manage heat can be exploited even more during the subsequent reactive phase. In the latter, the heat release must be carefully balanced in order to avoid the formation of hot spots, thus preventing too rapid desorption and achieving the minimum temperature required for catalytic reaction to take place.

4.4.4 Conclusions

In this study, the dynamics of a nonadiabatic and adiabatic hybrid bed were analysed using a two-dimensional mathematical model to account for both longitudinal and radial distributions of concentration and temperature. The effect of different sorbent and catalyst spatial arrangements in the hybrid bed on its performance during the CO_2 adsorption step was investigated.

It was shown that, in both the adiabatic and nonadiabatic case, a bed with alternating layers of adsorbent and catalyst and a bed in the form of a physical mixture of the two types of particles outperforms–a standard adsorption bed in terms of bed breakthrough time and sorption capacity. Although the latter was not explicitly studied in the paper, the structure analysed, with two axial layers, is equivalent to a classical adsorption column, but with a sorption inert zone located near the outlet. The improvement in the performance was attributed to the influence of the catalyst on the heat transport inside the bed; in fact, the catalyst, as opposed to the adsorbent, is characterized by both a higher thermal conductivity and a higher heat capacity, thus acting locally as a heat sink.

The optimization problem was solved for a configuration with radially nonuniform adsorbent distribution, and it was further shown that placing more catalysts (characterized by higher thermal conductivity) close to the wall allows to extend the bed breakthrough time and the sorption capacity. This is due to the much more efficient removal from the bed of the heat generated in the exothermic adsorption process.

Since the hybrid apparatus analysed in this paper is intended to be used in the second step of the cyclic process for the CO_2 methanation, additional questions arise that will be the subject of further research. Indeed, it is clear that the optimization of the hybrid bed must be carried out for the entire two-step process, i.e. adsorption and reactive regeneration. This is a multicriteria problem, where the objective functions could be the sorption capacity of the bed (for the adsorption step) and the degree of conversion of CO_2 in the reaction with the hydrogen fed to the bed (for the regeneration step). Regarding the latter, given exothermic nature of the methanation process, it is expected to be advantageous to place more catalyst close to the walls of the apparatus. However, a core containing only sorbent (which is the mass source at the adsorption stage) may not be the best solution due to limited radial mass transport.

Acknowledgements

The research was financed by the Polish National Science Centre under the research project:" Experimental and numerical analysis of mass and heat transport in "tailor-made" fixed beds for gas-solid processes", no. UMO-2021/42/E/ST8/00313.

Symbols

a, a_0 - parameters in the Toth isotherm equation (Eq. (7) and (8)), mol/(kg·kPa)

a_{ax}, a_{rad} –parameters of the convective term in the expression for determination, respectively, of axial and radial thermal conductivity (Eq. (12) and (13))

A – slope of the function defined by Eq. (29) and Eq. (30)

b, b_0 – parameters in the Toth isotherm equation (Eq. (7) and (8)), 1/kPa

c – parameter in the Toth isotherm equation (Eq. (7) and (8)), K

c_g – gas specific heat capacity, J/(kg·K)

$c_{g,ads}$ – adsorbed phase specific heat capacity, J/(kg·K)

c_{lim} – ratio of molar fractions in Eq. (31), -

c_s – solid specific gas capacity, J/(kg·K)

C_{CO_2} – molar concentration of CO_2 in gas phase, mol/m^3

C_{f,CO_2} – molar concentration of CO_2 in gas phase at the inlet, mol/m^3

d_p – particle diameter, m

d_{pore} – mean pore diameter, m

D_{ax} – axial mass dispersion coefficient, m^2/s

D_e – effective diffusion coefficient, m^2/s

D_K – Knudsen diffusion coefficient, m^2/s

D_m – molecular diffusion coefficient, m^2/s

D_r – reactor diameter, m

D_{rad} – radial mass dispersion coefficient, m^2/s

E – parameter in the Toth isotherm equation (Eq. (7) and (8)), K

f_{ads} – volume fraction of adsorbent in the bed, -

f_{cat} – volume fraction of catalyst in the bed, -

h_w – apparent wall heat transfer coefficient, W/(m^2·K)

k – mass transfer coefficient in LDF model given by Eq. (5) and (6), 1/s

K_{ax} – axial effective thermal conductivity, W/(m·K)

K_{rad} – radial effective thermal conductivity, W/(m·K)

K_{ax}^0 – axial static effective thermal conductivity, W/(m·K)

K_{rad}^0 – radial static effective thermal conductivity, W/(m·K)

L – reactor length, m

M – number of sorbent and catalyst layers in the layered bed, -

N_{ax} – number of discretization nodes along the bed length, -

N_{rad} – number of discretization nodes along the bed radius, -

Nu – Nusselt number, -

p – total pressure,

p_{CO_2} – CO_2 partial pressure,

Pr – Prandtl number, -

r – radial coordinate, m

r_p – particle radius, m

R – universal gas constant, J/(mol·K)

R_c – radius of the cylindrical core, m

R_r – reactor radius, m

Re_p – particle Reynolds number, -

q_{CO_2} – concentration of CO_2 adsorbed in the solid phase, mol/kg

$q^*_{CO_2}$ – equilibrium concentration of CO_2 adsorbed in the solid phase, mol/kg

$\tilde{q}_{CO_2}$ – concentration of CO_2 adsorbed in the solid phase expressed per unit volume of the column defined by Eq. (33), mol/m^3

Q_{CO_2} – average concentration of adsorbed CO_2 at t_b defined by Eq. (32), mol/kg

Sc – Schmidt number, -

t – time, s

t_b – time of breakthrough of the bed, s

T – temperature, K

T_0 – initial bed temperature, K

T_f – gas temperature at the inlet, K

T_w – wall temperature, K

u – superficial gas velocity, m/s

V – volume, m^3

$y_{CO_2,in}$ – molar fraction of CO_2 in the gas stream at the inlet, -

$\tilde{y}_{CO_2,out}$ – average molar fraction of CO_2 in the gas stream at the outlet, -

x – axial coordinate, m

Greek symbols

β – parameter in the correlation for static effective thermal conductivity (Eq. (14))

γ – parameter in the correlation for static effective thermal conductivity (Eq. (14))

Γ_{heat} – parameter in the mass balance equation (1) defined by Eq. (3)

Γ_{mass} – parameter in the mass balance equation (2) defined by Eq. (4)

ΔH_{ads} – isosteric enthalpy of CO_2 adsorption, J/mol

ε_b – bed porosity, -

ε_p – particle porosity, -

ε_t – total porosity of the bed, -

κ – the ratio of the thermal conductivity of a solid to a gas, -

λ_g – thermal conductivity of the gas, W/(m·K)

λ_s – thermal conductivity of the solid, W/(m·K)

μ_g – gas viscosity, kg/m^3

ρ_g – gas density, kg/m^3

ρ_b – bed bulk density, kg/m^3

τ, τ_0 – parameters in the Toth isotherm equation (Eq. (7) and (8)), -

τ_p – tortuosity factor, -

ψ_t – parameter in the correlation for static effective thermal conductivity (Eq. (14))

Subscripts

1 – refers to the inner part (core) of the fixed bed

2 – refers to the outer part (shell) of the fixed bed

ads – refers to adsorbent or adsorbate

cat – refers to catalyst

tot – refers to total

4.5 Development of data-driven models in application to numerical simulation of adsorption processes

4.5.1 Research objective

In addition to extensive work in the field of catalytic and adsorptive reactors modeling (adsorption stage), intensive work was carried out in the field of surrogate modeling of multicomponent adsorption. Due to the typically multicomponent nature of mixtures purified in adsorption columns or fed into adsorptiv4 reactors, knowledge of multicomponent equilibrium is essential for modeling such processes. The research activity was aimed at developing and applying a data-driven models of multicomponent adsorption isotherms that may be potentially used for efficient numerical simulation of adsorption processes with chemical reaction. The study was carried out mainly making use of self-produced software on MATLAB platform. The predominantly modeling nature of the work performed and the lack of directly accessible experimental data, made it unavoidable to conduct an in-depth literature study of both the materials used in adsorptive (hybrid) reactors, and thus to the physical and mathematical models describing their operation, and the data-driven methods employed in the development of the self-produced software.

4.5.2 Literature study

This section reports and reviews literature references related to the multicomponent adsorption model and the data-driven methodology used.

The study of adsorption processes with reaction is becoming increasingly addressed in the literature, fitting into the context of technologies for Carbon Capture and Utilization - CCU (IEA (2023); Koytsoumpa et al., 2021). The simulation of adsorption processes with reaction can be distinguished into two steps. A first step, addressed so far during research activities, is related to the simulation of pure adsorption processes, based on data obtained from the scientific literature. In a second step, which will be addressed later within the research activities, models for simulating reactive processes are instead analyzed. Such processes can benefit from the adsorption step because it can act actively by removing reaction byproducts, and because during the regeneration of the adsorbent, it can be exploited as sources of reactant species (Gunia et al., 2023). Indeed, the design and analysis of the behavior of adsorption columns and adsorptive (hybrid) reactors requires information about the adsorption equilibrium, which in the case of multicomponent adsorption is obtained

experimentally (Myers and Prausnitz, 1965). It is therefore necessary to refer to models that are based on the application of the more established thermodynamic theories of adsorption. In particular case studied within this study, the attention was focused on the adsorption of gaseous mixtures of CO_2-N_2 and CO_2-CH_4 with the objective of simulating processes such as post-combustion CO_2 capture and biogas upgrading on zeolites (ZSM-5 and 5A). Data on single-component adsorption isotherms were obtained from the scientific literature (Hefti et al., 2015; Mendes et al., 2017). The adsorption of CO_2 and N_2 on zeolite ZSM-5 was described using Sips equation (Hefti et al., 2015),

$$q^{\circ} = q_{sat}\frac{(bp)^n}{1+(bp)^n}, \quad q_{sat} = q_{sat,0}\exp\left[\chi\left(T/T_0 - 1\right)\right]$$
$$b = b_0\exp\left(-\Delta H/(RT)\right), \quad n = n_0 + \alpha\left(T/T_0 - 1\right) \tag{1}$$

whereas the adsorption of CO_2 and CH_4 on zeolite 5A was described using Toth equation (Mendes et al., 2017):

$$q^{\circ} = q_{sat}\frac{bp}{\left[1+(bp)^n\right]^{1/n}}, \quad b = b_0\exp\left(-\Delta H/(RT)\right) \tag{2}$$

The parameters of the adsorption isotherm equations are presented in Table 1.

Table 1. Parameters of the adsorption isotherm for binary mixtures of carbon dioxide and nitrogen on zeolites ZSM-5 and 13X and CO_2/CH_4 on 5A zeolite (Hefti et al., 2015 and Mendes et al., 2017).

ZSM-5 and 13X	CO_2	N_2	5A zeolite	CO_2	CH_4
$q_{(sat,0)}$, mol/kg	2,775	2,027	$q_{(sat,0)}$, mol/kg	5,11	4,28
χ	0	0	b_0, 1/bar	2.1e-5	2.0e-4
b_0, 1/bar	1.7e-5	6.8e-5	-ΔH, kJ/mol	38,1	17,2
-ΔH, kJ/mol	26,98	17,31	n	0,61	1,09
n_0	0,71	0,91			
α	0	0			

The model chosen for the description of multicomponent adsorption is the one based on ideal adsorption solution theory (IAST). In this theory, based on the data of single-component isotherms available in the literature, the thermodynamic conditions at the equilibrium between gas-phase and adsorbed species are derived. This multicomponent equilibrium is obtained by solving the system of nonlinear equations, given below (Sharma et al., 2023):

$$py_i = p_i^{\circ}(\eta) \cdot x_i, \;\; i = 1, \ldots, N_c \tag{3}$$

$$\sum_{i=1}^{K} x_i = 1 \tag{4}$$

$$\eta = \eta_1 = \eta_2 = \ldots = \eta_{N_c} \tag{5}$$

Equations (1) represent the equivalent of Raoult's law for ideal liquid mixtures. Equations (3), on the other hand, describe the multicomponent equilibrium at a given temperature, which is obtained by equalizing the reduced grand potentials of the mixture with those of the pure components. p_i°, in Eq. (1), is the partial adsorption pressure of the pure (*i*-th) component if it had the same reduced grand potential and temperature as the gas mixture, and it appearns as the integration extreme in the calculation of the reduced grand potential:

$$\eta = \int_0^{p_i^{\circ}} \frac{q_i^{\circ}(p_i)}{p_i} dp_i \tag{6}$$

Therefore, IAST is based on the calculation of reduced grand potential, which has the units of mol/kg and is calculated from the grand potential. The grand potential (expressed in J/kg) physically represents the change in free energy associated with the immersion of adsorbent, fully discharged, within the gas. The reduced grand potential is equal to the ratio of the grand potential to the *RT* product (where *R* is universal gas constant, and *T* is temperature expressed in K). In addition, the absolute value of grand potential is the minimum work under isothermal conditions required to clean the adsorbent. (Sharma et al., 2023). However, solving the IAST problem while performing numerical simulations of adsorbent particles or the adsorption process taking place in adsorption column or adsorptive reactor can involve time-consuming calculations.

For this reason, in order to explore innovative and computationally efficient solutions, two data-driven methods including artificial neural networks (ANN) and Kriging, known as

Gaussian process regression (GPR), were analyzed for building surrogate models (Forrester et al., 2008b) with the goal of predicting multicomponent adsorption accurately.

ANNs, which emulate the learning process of biological neural systems, are recognized as a tool with great flexibility in approximating nonlinear functions. These can be characterized by a relatively simple structure of nodes, which can be adjusted during the training phase. ANNs are able to learn both correlations and patterns in the analyzed data, even in the presence of noise and uncertainty (Bizon et al., 2011).

In the work of Ghalandari et al., (2020) a feed-forward neural network with a hidden layer was presented for the prediction of multicomponent adsorption of a mixture of N_2, CO_2 and CH_4 on activated carbon. The network was trained with experimental data of single-component isotherms and shown to predict the amount adsorbed as temperature, pressure, gas type and specific surface area of the adsorbent varied. The results showed how a simple feed-forward network with just nine neurons can predict the data with a mean square error (MSE) of $4 \cdot 10^{-3}$. Nogueira and colleagues, (2022) investigated the dynamic behavior of the concentration profile of a fixed-bed isothermal adsorbent column by employing a neural network to replace multicomponent isotherms. The adsorbed amount of the single component at equilibrium was chosen as the output of the network, while the concentrations in the liquid phase of the two adsorbed components (propanol and n-propyl propionate) were provided as input. The authors proposed feed-forward neural networks to calculate the adsorption equilibrium and mass transport coefficients. A neural network consisting of a hidden layer of seven neurons with hyperbolic tangent ('tansig') as the activation function was trained for each component. An MSE of 0.067 was obtained by comparing the results of the proposed hybrid model against experimental data. Kareem and colleagues, (2018), employed ANN modeling to predict the adsorption of binary and ternary mixtures of CO_2, CH_4 and H_2O on zeolite 13X and demonstrated that a feed-forward neural network can fit the training data with a single hidden layer of 14 neurons, with sigmoidal activation functions. This network was trained using experimental data obtained with different compositions of the gas mixture and different operating conditions, namely a temperature of 343 K and a total pressure of up to 10 bar.

Kriging or GPR can be seen as an empirical model, its use is attractive when, due to limited time or resources, there can only be a limited number of sampling points. There are several methods for deriving accurate predictions from observations. In particular, Kriging also

known as best linear unbiased predictor, has been initially employed in geostatistics since 1951 (Forrester et al., 2008a). The definition of "best linear unbiased predictor" is related to the minimum value of prediction variance that characterizes GPR compared with linear predictors (Forrester et al., 2008a). To predict a new function value at point $\mathbf{x_0}$ - that is, $Z^*(\mathbf{x}_0)$, the Kriging model uses a weighted average of all known data (Wackernagel, 2003). Kriging uses most of the information in the data to obtain the new unknown value optimally. Therefore, the following relationship can be used to estimate the new value of the function (Wackernagel, 2003):

$$Z^*(\mathbf{x}_0) = \lambda_0 + \sum_{i=1}^{n} \omega_i \, Z(\mathbf{x}_i) \tag{7}$$

where *n* is the number of observations; ω_i are the weights; $Z^*(\mathbf{x}_0)$ is the estimated value of the function at a new location; meanwhile, $Z(\mathbf{x}_i)$ is the response of the function (or measure) at the sampled point with coordinates $\mathbf{x}_i$; and λ_0 is the mean or expected value of the function in the domain of interest. Finding the best linear unbiased prediction is equivalent to finding the optimal weights ω_i that minimize the variance of the prediction subject to the unbiasedness condition; therefore, the following minimization problem can be stated (Wackernagel, 2003):

$$\min_{\omega_i} \mathrm{Var}\big(Z(\mathbf{x}_0) - Z^*(\mathbf{x}_0)\big) \tag{8}$$

where $Z(\mathbf{x}_0)$ is the expected value of the function at the new point of coordinates $\mathbf{x}_0$.

Mukherjee and colleagues, (2023) used Gaussian Process Regression (GPR) to obtain surrogate models of multicomponent adsorption through data obtained from grand canonical Montecarlo (GCMC) simulations, which is a rigorous model of adsorption at the molecular level (Yun et al., 2002). Through GCMC, the authors generated a large number of data, in particular 5000 and 50000 cycles were used for initialization and generation of the data set, respectively. The authors state that GPRs differ from other machine learning models in that they are flexible nonparametric models that can emulate any distribution with less starting data while providing an estimate of the standard deviation along with the required output. In addition, GPRs have shown better performance for smaller starting data sets than models such as Bayesian neural networks (BNNs) or neural network ensembles, which can also provide uncertainty estimates. Moreover, Mukherjee and colleagues, (2023) have found that

the best kernels for obtaining accurate models for their data are those based on Radial Basis Functions (RBF).

The combination of Kriging and multilinear free energy regression models was employed by Zhao and colleagues, (2022) to predict the adsorption capacity of organic pollutants by bio-char and resin. After analyzing models built with neural networks as well, the authors concluded that the ones built with Kriging are more faithful with the measurements, allowing them to increase the accuracy in predicting the adsorption efficiency of pollutants in aqueous solutions by about 10 percent.

4.5.3 Development of data-driven models

This section gives hints about the implementation of the code: the MATLAB tools used and the procedure followed. The code allowed the IAST problem to be solved numerically for a wide range of component partial pressures and system temperatures, being and input of the surrogate models. The data obtained were used to construct two surrogate models using ANN and Kriging. The resulting models were compared and analyzed in terms of accuracy against the results obtained via IAST.

Among the different sampling strategies that can be applied to select samples for surrogate model construction, uniform sampling was used, specifically dividing the feature space as follows:

- partial pressures of CO_2 and CH_4 in a first case study, and of CO_2 and N_2 in a second case study, were sampled at 21 points divided logarithmically between the decades 10^{-1} and $10^{0.69}$ [bar].
- temperature was sampled at 21 points linearly divided between 303 and 363 [K].

Adsorption isotherms (both single and multicomponent) have a steeper trend for lower pressures, which flattens out as the pressure increases. For this reason, a logarithmic scale was chosen for sampling partial pressures. As outputs, the values of the adsorbed amounts of the individual component were used for the construction of surrogate models. Kriging models and feed-forward neural networks were built separately for each individual adsorbed component. This allowed the model error to be reduced.

For the construction of the ANN the MATLAB toolbox "*Neural Net Fitting*" was used, which allows, having defined the architecture of the network and the input and output data, to train it optimally. For the construction of the model based on Kriging, the function *"fitrgp"* was

used. Several models were tested by varying the number of neurons of the neural network and the kernel functions of the Kriging models. In particular, a feed-forward network with 15 neurons in the hidden layer was chosen, characterized by the *"tansig"* (*hyperbolic tangent*) activation functions; meanwhile, the *"ARDExponential"* function was the best choice as a kernel for Kriging-based models.

4.5.4 Results

The adsorption isotherms of the binary mixtures were determined on the basis of the isotherms of the pure components (Fig. 1). The results obtained through IAST, solving the system expressed by Eqs. (3-5) for a wide range of values of partial pressures and temperatures of the gas mixture, were compared with those obtained from surrogate models.

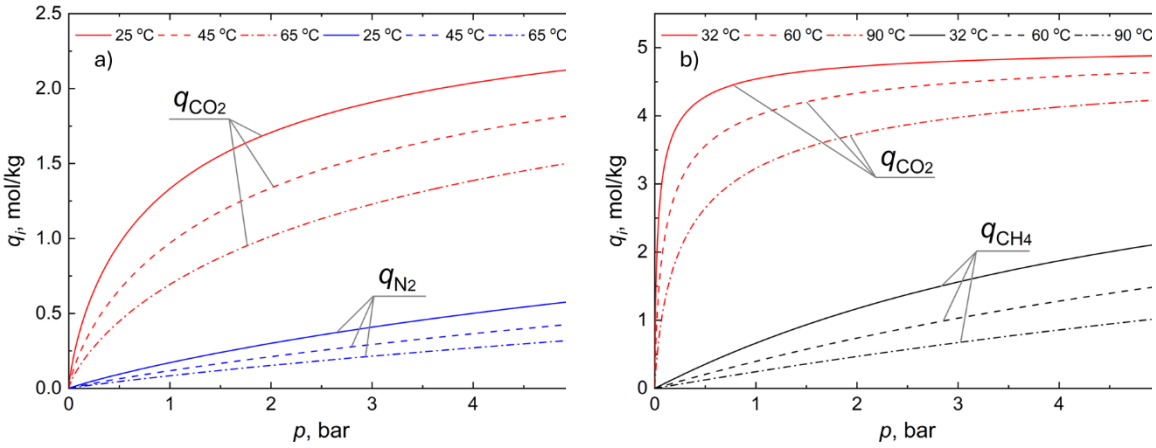

Figure.1. a) sorption isotherms on zeolite ZSM-5 of pure CO_2 and N_2, Sips; b) sorption isotherms on zeolite 5A of pure CO_2 and N_2, Toth model

Fig. 2 shows the multicomponent isotherms calculated using IAST for two representative values of the analyzed temperatures (T = 25 °C for Fig. 2a; T = 32°C in Fig. 2band for a range of partial pressures of the individual components contained in the mixtures, used as an input to the surrogate model. The analogous surfaces obtained using ANN and Kriging are virtually the same, therefore are not reported here.

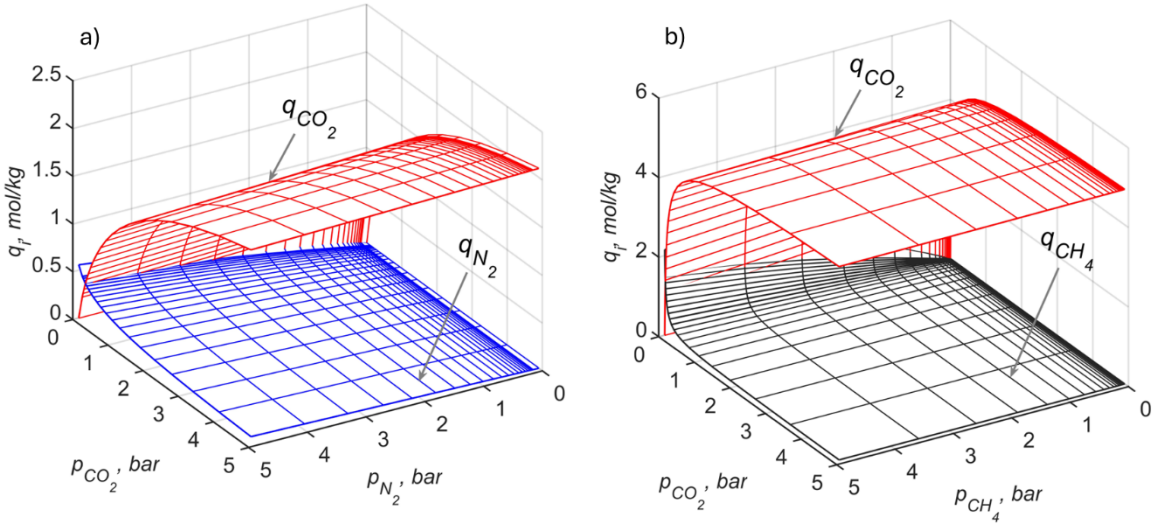

Figure. 2 a) CO_2 and N_2 adsorption isotherms on zeolite ZSM-5 in binary mixture, Sips' model; b) CO_2 and CH_4 adsorption isotherms on zeolite 5A in binary mixture, Toth's model

In fact, both ANN and Kriging-based models showed high accuracy with a root square mean error (RSME) value on the order of 10^{-6}-10^{-5}, in the approximation of multicomponent isotherms.

In addition, Fig. 3 shows the calculated absolute error isolines for the two proposed surrogate models. While both models have an absolute error always below 10^{-3}, for all partial pressure values considered, the Kriging-based model shows a more uniform error, going up only for very low CO_2 partial pressure values (on the order of 10^{-1} bar).

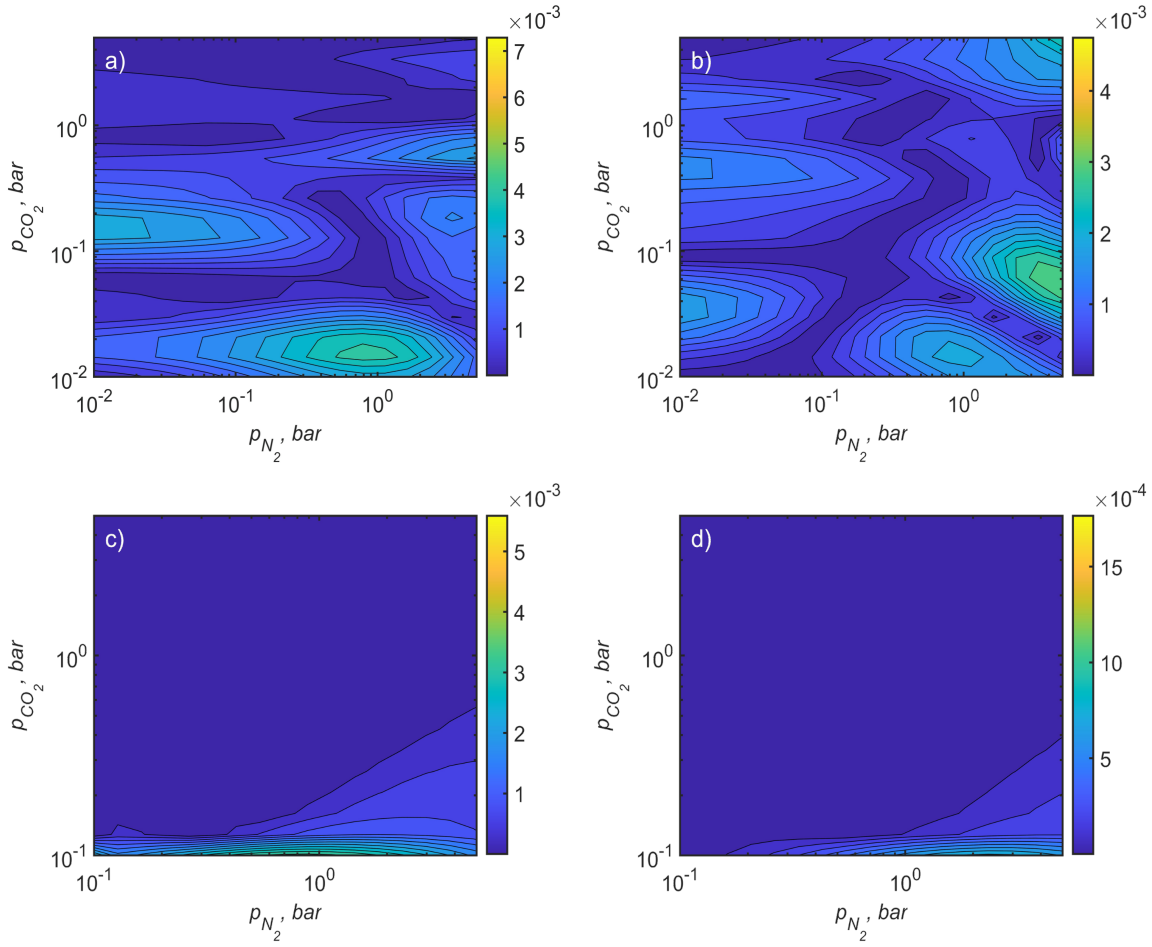

Fig.3. Computed absolute error in predicting the amount adsorbed by ANN (with 15 neurons) and Kriging (with exponential kernel function): (a) CO_2 ANN; (b) N_2 ANN; (c) CO_2 Kriging (d) N_2 Kriging

4.5.5 Discussion and future developments

This study examined the possibility of using ANN and Kriging to approximate multicomponent adsorption isotherms. Surrogate models can accurately predict the multicomponent adsorption equilibrium as the thermodynamic properties of the mixture change. The goal of further research is to develop efficient hybrid models to simulate either the spent flue gas treatment or biogas upgrading process, considering the impact of individual components (N_2, NO_x, CO, H_2, H_2O, etc.) on CO_2 capture efficiency. The methodology will also be extended to the modeling and simulation of adsorbent reactors, i.e., reactors with a bed consisting of a dual-function sorbent-catalyst material or a physical

mixture of adsorbent and catalyst particles, for the cyclic sequestration of CO_2 and its methanation by reactive bed regeneration, using H_2 produced from excess renewable energy.

Chapter 5
Results: Analysis of self-ignition systems through Full and Reduced-Order Models

5.1 Analysis of an innovative sampling strategy based on k-means clustering algorithm for POD and POD-DEIM reduced-order models of a 2-D reaction-diffusion system[5]

Enrico Alberto Cutillo[a]*, Gianmarco Petito*[a]*, Katarzyna Bizon*[b]**, Gaetano Continillo*[a]

[a]*Dipartimento di Ingegneria, Università degli Studi del Sannio, Piazza Roma 21, 82100 Benevento, Italy*

[b]*Faculty of Chemical Engineering and Technology, Cracow University of Technology, ul. Warszawska 24, 31-155 Kraków, Poland,*

**corresponding author: katarzyna.bizon@pk.edu.pl, ORCID: 0000-0001-7600-4452*

Abstract

In this work, a model-order reduction methodology based on proper orthogonal decomposition (POD) and Galërkin projection is presented and applied to the simulation of the self-ignition of a stockpile of solid fuel. Self-ignition is a phenomenon associated with steep changes in space and time, yielding high gradients of state variables which demand grid refinement and, thus, increase of the computational burden. To cope with this difficulty, first, a full order model (FOM), generated by finite-difference discretization of the PDEs constituting the differential model, is employed to generate reference solutions. Two different POD-based formulations are proposed: the classical POD-Galërkin is employed to generate reduced-order models (ROM), then discrete empirical interpolation method (DEIM) is employed to deal with nonlinearities in a more efficient manner. These reduction techniques are further supplemented with an innovative sampling approach based on *k*-means clustering. The resulting agile ROM is validated against the FOM.

Both model-order reduction strategies, particularly the POD-DEIM model, reproduce the FOM solutions with high accuracy and much lower computational cost: The results of the application of a combination of the DEIM algorithm and *k*-means clustering show that the computational time for the calculation of one solution reduces up to 1020 times, while

[5] Published in: *Combustion theory and modelling* 27.4 (2023): 508-535. https://doi.org/10.1080/13647830.2023.2174451

remaining able to reproduce all bifurcation points found with the FOM, thus demonstrating quantitative and qualitative agreement.

Keywords: Reaction-diffusion system; model-order reduction; POD-Galërkin; *k*-means clustering; discrete empirical interpolation method.

5.1.1 Introduction

Spontaneous combustion in stocks of bulk solid and dust materials is still a topical problem. Storage and treatment of organic solid compound is a key step in the waste treatment and in the energy production industry. Normal operations in composting facilities, power plant mills, or wastewater treatment plants involve carrying and storing substantial amounts of flammable materials. Piles of municipal solid waste, agroforestry residues, or sewage sludge can lead to the phenomenon of self-heating and self-ignition. To understand and avoid those phenomena is crucial, as they may lead to catastrophic consequences and financial losses (Medic Pejic et al., 2015; Putranto and Chen, 2017; Schwarzer et al., 2021). Piles of solid flammable materials left alone for weeks or even days may have a temperature increase with no heat input from the surrounding ambient. If the heat generated inside the pile cannot escape quickly, the internal temperature rises until it reaches the critical level of self-ignition (Fernandez-Anez et al., 2021). There are many factors that may contribute to spontaneous combustion, among the others: pile size, type and composition of the bulk, internal heat and oxygen transfer, specific chemical kinetics, stock geometry, and atmospheric moisture content (Brooks and Glasser, 1986). Those factors characterize the heterogeneous and porous structure of all kinds of different flammable materials, which greatly influence the transport and conversion mechanisms of matter and energy. Temperature gradients transport heat away from the solid bulk through conduction and convection. Diffusion and convection mechanisms transport gaseous reactants and products like carbon dioxide, oxygen and water to/from the atmosphere surrounding the stockpile. The differences in atmospheric pressure cause forced convection on the surface of the pile, while differences in temperature cause natural convection between the pile and the surrounding air (Brooks et al., 1988). The main heat source is provided by the low-temperature oxidation of the solid matrix in contact with the atmospheric oxygen, which is the cause of uncontrolled and mainly undesired changes in the thermal properties of the pile. Further exothermic processes, such as microbial

metabolism, can also contribute to the self-heating of the stockpile. In fact, in a pile of urban waste, it might be necessary to consider the biological reactions due to the formation of colonies of fungi and bacteria. In this case the model should incorporate those reactions to verify their influence on the self-heating process (Luangwilai et al., 2011). Other mechanisms of self-heating are adsorption-desorption of water due to differences between effective and equilibrium moisture concentrations of lignite and air, and oxidation of pyrite (Lohrer et al., 2005).

Aim of this work is to apply, in the study of the self-ignition phenomenon, a methodology that helps conduct the analysis of such complex systems in a more efficient manner. To better understand and predict the dynamical behavior of a reaction-diffusion system, one must solve the infinite dimensional mathematical model (a system of nonlinear PDEs). The most straightforward approach to solve this system is to operate a finite difference approximation of the spatial derivatives, thus generating a large set of ODEs, hereafter called full order model (FOM). For a one-time calculation this is a feasible solution, but when the system must be repeatedly solved, the need of a more efficient and hence faster solution procedure may arise. This happens for example in real-time simulations, control applications, detailed parametrical studies, or within an optimization algorithm.

To reduce the computational burden of the process of deriving FOM solutions coming from heavy calculations, one may think of building data-driven models, such as artificial neural networks (ANN) or reduced-order models (ROM). The first ones may be seen as black boxes providing an input-output relation that permits to simulate the system response quickly and accurately. On the other hand, ROMs are based on the original physical model and have the capability of predicting the system behavior in parameter regions that are not explored during the model construction. ROMs have proven to be fast and accurate in many applications from aerospace to chemical engineering problems (Amsallem et al., 2007; Bizon and Continillo, 2021a).

In this work, two formulations of reduced-order models via proper orthogonal decomposition (POD) and Galërkin-projection are introduced for a bidimensional reaction-diffusion system that models the self-ignition of combustible solid materials. Firstly, the classical POD-Galërkin approach is applied to the mathematical model of the system, thus yielding the reduced-order model (ROM) for the “base case.” Successively, the bottleneck operation of evaluating the nonlinear reaction terms in the FOM domain is addressed. This

procedure may lead to ROM simulations that turn out to be even slower than the corresponding FOM, because the evaluation of the nonlinear function is computationally expensive. To address this problem, various methods of hyper-reduction of the original ROM have been proposed in the literature, such as the classic discrete empirical interpolation method (DEIM), Gauss–Newton approximated tensors (GNAT), or Gappy POD. Gappy POD (Sirovich and Everson, 1995) is mostly used for hyper-reduced models originating from finite element discretized FOM, while GNAT is based on Petrov-Galërkin projection (Brands et al., 2019). DEIM, introduced by Chaturantabut and Sorensen (2010), is employed in the present work, and attention is focused on the possibility of increasing its robustness and accuracy by exploring different sampling strategies of the snapshot matrix to build the empirical basis function set. There is no unique and general method to collect the snapshots from the FOM solutions, but it is known that a proper choice of those solutions can lead to lower errors and more robust ROMs. Another issue of the classical POD technique, which is addressed in this work, is the desirable property of globality of the ROM. Classical ROMs may fail when employed far from the conditions at which the snapshots are collected. In other words, the constructed ROM loses accuracy in presence of large deviations of values of the model parameters from the set used to generate the ROM. A ROM that can capture the global behavior of the system, also varying the values of the parameters inside their field of existence, is called global ROM (Lu et al., 2019).

5.1.2 Mathematical model

The mathematical model for the description of the diffusion-reaction system under study consists of a set of mass and energy balance equations. In principle, these equations must be formulated for the gas phase that diffuses in the bulk of the pile, and for the solid fuel, that in this case can be described as a porous medium. The mathematical model of a diffusion-reaction system can be further simplified by considering some assumptions: consumption of the solid reactant may be neglected, given the much faster evolution of gas-phase phenomena; thermal equilibrium between the two phases may be considered, hence the same temperature may be assumed for gas and solid phase. Then, only one mass balance equation for the gaseous reactant and only one energy balance equation is sufficient to describe the whole system. The simplest chemical reaction can be represented by a first-order one-step

kinetic expression, with the classic Arrhenius exponential expression describing the temperature dependence of the reaction rate.

Based on the above assumptions, the model equations, in dimensionless form, are:

$$\frac{\partial c}{\partial t} = \mathrm{Le}\left(\frac{\partial^2 c}{\partial x^2} + \frac{\partial^2 c}{\partial y^2}\right) - \varphi^2 c \exp\left(-\frac{\gamma}{T}\right) \tag{1}$$

$$\frac{\partial T}{\partial t} = \left(\frac{\partial^2 T}{\partial x^2} + \frac{\partial^2 T}{\partial y^2}\right) + \beta\varphi^2 c \exp\left(-\frac{\gamma}{T}\right) \tag{2}$$

where c is the dimensionless concentration of the gaseous reactant, T is the dimensionless temperature, Le, i.e., the Lewis number, is the ratio between mass and heat diffusivities, β is a dimensionless heat of reaction, φ is the Thiele modulus, and γ is a dimensionless activation energy. The associated initial and boundary conditions complete the system of partial differential equations, which can then be solved numerically. In this study, diffusion-reaction problems related to a stockpile of solid fuel are analyzed. It is assumed that the pile can be described by an infinitely long slab with rectangular cross section. With the chosen geometry and for symmetric initial and boundary conditions, the problem is symmetrical. Figure 1 shows the geometric representation of the problem with the relevant boundary conditions.

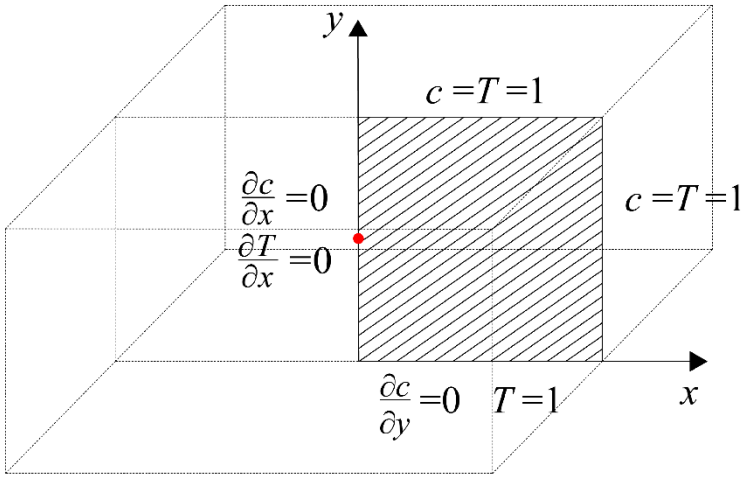

Figure 1. Geometric representation of the problem with the relevant boundary conditions. The red dot indicates the point in the domain for which time series are reported in the time-dependent plots.

The boundary conditions defined for this problem are:

$$\frac{\partial c}{\partial x} = \frac{\partial T}{\partial x} = 0 \quad \text{at} \quad x = 0 \tag{3a}$$

$$\frac{\partial c}{\partial y} = 0 \quad \text{and} \quad T = 1 \quad \text{at} \quad y = 0 \tag{3b}$$

$$c = 1, \quad T = 1 \quad \text{at} \quad x = 1 \tag{3c}$$

$$c = 1, \quad T = 1 \quad \text{at} \quad y = 1 \tag{3d}$$

Finally, the problem is completed with the following initial conditions:

$$c(x, y, t = 0) = 1, \quad T(x, y, t = 0) = 1 \tag{4}$$

5.1.3 Model order reduction of nonlinear dynamical systems

- POD-ROM formulation

Considering the two PDEs (Eq. (1) and (2)) introduced above along with boundary and initial conditions (Eq. (3) and (4)), such system can be approximated by a large set of ODEs deriving from the discretization of the spatial derivatives (more details on the discretized model are given in Appendix A). In a compact matrix formulation, the system can be expressed as:

$$\frac{d}{dt}\mathbf{u} = \mathbf{A}\mathbf{u} + \mathbf{F}(\mathbf{u}), \quad \mathbf{u}(0) = \mathbf{u}_{init} \tag{5}$$

This is the so-called full order model (FOM), where $\mathbf{u} = [u_1, u_2, ..., u_{N_x \cdot N_y}]^{\mathrm{T}}$ is a state variable vector, $\mathbf{A} \in \mathbf{R}^{N_x \cdot N_y \times N_x \cdot N_y}$ is a coefficient matrix, and $\mathbf{F} \in \mathbf{R}^{N_x \cdot N_y}\mathbf{R}^{N_x \cdot N_y}$ is a vector defined as $\mathbf{F} = [F(u_1), F(u_2), ..., F(u_{N_x \cdot N_y})]^{\mathrm{T}}$ with F being a nonlinear function. The product of the number of grid points in the x direction by the number of grid points in the y direction, $N_x \cdot N_y$ hereafter is denoted as N. The subsequent introduction of the POD methodology is applied to both temperature and concentration, and the ROM equations that are obtained are coupled through the nonlinear terms and thus they must be solved simultaneously.

The generic state variable vector **u**, following the Galërkin projection method, can be approximated as a linear combination of orthonormal basis vectors and time dependent coefficients:

$$\mathbf{u} \approx \tilde{\mathbf{u}} = \sum_{k=1}^{K} \phi_k c_k = \mathbf{\Phi}_K \mathbf{c}_K \quad \text{with} \quad \mathbf{\Phi}_K \in \mathbf{R}^{N \times K} \tag{6}$$

In Eq. (6), the unknowns are the time dependent coefficients c_i. Substituting $\tilde{\mathbf{u}}$ in Eq. (5) and projecting the coefficient matrix **A** and the vector **F** onto the basis $\mathbf{\Phi}_K$, yields the following system of equations, referred to as the reduced-order model (ROM):

$$\mathbf{\Phi}_K^{\mathrm{T}} \frac{d}{dt} \mathbf{\Phi}_K \mathbf{c}_K = \mathbf{\Phi}_K^{\mathrm{T}} \mathbf{A} \mathbf{\Phi}_K \mathbf{c}_K + \mathbf{\Phi}_K^{\mathrm{T}} \mathbf{F}(\mathbf{\Phi}_K \mathbf{c}_K) \tag{7}$$

Noting that the modes $\mathbf{\Phi}_K$ are only functions of space, and that $\mathbf{\Phi}_K^{\mathrm{T}} \mathbf{\Phi}_K = \mathbf{I}$, where **I** is the identity matrix, Eq. (7) can be rewritten as:

$$\frac{d}{dt} \mathbf{c}_K = \mathbf{\Phi}_K^{\mathrm{T}} \mathbf{A} \mathbf{\Phi}_K \mathbf{c}_K + \mathbf{\Phi}_K^{\mathrm{T}} \mathbf{F}(\mathbf{\Phi}_K \mathbf{c}_K) \tag{8}$$

The reduced-order model has a much fewer number of equations with respect to the FOM, and in fact the aim of the approximation described above is to have $K << N$.

Generally, any type of orthogonal basis may be employed to build a reduced-order model. In this work, to improve the performance of the ROM, the basis vectors are derived from a set of solutions of the FOM. To obtain a reduced model, firstly the FOM is solved using the method of lines (MOL) (Bizon, 2017), which results into solving the set of ODEs shown in Eq. (5). The solutions, often called snapshots, represent the spatiotemporal complexity of the system and carry valuable information on its behavior. Such information is encoded in the basis vectors, which are obtained applying the proper orthogonal decomposition (POD) to a chosen set of snapshots. The basis vectors obtained from FOM solutions using POD are often called "empirical basis" or "modes" of the system, and are obtained by solving the following eigenvalue problem (Holmes et al., 1996):

$$\mathbf{C}\mathbf{\Phi} = \mathbf{\Lambda}\mathbf{\Phi} \tag{9}$$

Matrix **C** is called correlation matrix and is defined as follows:

$$\mathbf{C} = \frac{1}{M} \mathbf{U}\mathbf{U}^{\mathrm{T}} \tag{10}$$

where **U** is the matrix of the snapshots, and each of its columns contains the state variable vectors of the discretized system at a given time instant:

$$\mathbf{U} = \begin{bmatrix} u_1(t_1) & \cdots & u_1(t_M) \\ \vdots & \ddots & \vdots \\ u_N(t_1) & \cdots & u_N(t_M) \end{bmatrix} \tag{11}$$

Subscript M in the last column represents the total number of solutions (snapshots) that have been chosen to construct the empirical basis.

The output of Eq. (9) are the eigenvectors (i.e., modes) and their corresponding eigenvalues (arranged in the diagonal matrix $\mathbf{\Lambda}$). The most important modes are those which carry more information on the behavior of the system, whereas the other modes can be seen as noise for the purpose of the construction of the reduced-order model. To distinguish the most prominent modes from the least important, one must look at the eigenvalue that corresponds to each mode: in fact, eigenvalues are used to order the eigenvectors (modes) from the most important to the least important. In particular, the most important modes are associated with the highest eigenvalues, and so, if the eigenvalues are ordered in descending order, from the largest to the smallest, also the corresponding eigenvectors are ordered from the most important to the least important. To reduce the dimension of the model, less significant modes can be neglected. There are mainly two methods to find the threshold eigenvalue that discriminates the most important modes that must be considered in the construction of the ROM from those that can be neglected: an *a-priori* method and an empirical method, the second one being more accurate but more expensive in terms of computational cost.

The *a-priori* method consists of the evaluation of the so-called cumulative correlation energy defined as (Sirovich, 1987):

$$E_K = \sum_{k=1}^{K} \lambda_k \Big/ \sum_{k=1}^{N} \lambda_k \tag{12}$$

where λ_k are the ordered eigenvalues and E_k is usually chosen as at least 0.99 to build a sufficiently accurate model.

The empirical method consists of the construction of different ROMs, which are built with an increasing number of modes. For each ROM, the error is calculated between full and truncated solutions. This error must be smaller than a predefined value, given by the designer of the reduced-order model or by the requirements of the application. At the end of the procedure, the ROM is chosen that, among the others, leads to sufficiently accurate solutions, and yet is computationally convenient (Bizon, 2017; Bizon and Continillo, 2021a).

- *ROM globality and sampling strategies*

In the case of dynamical time-dependent systems, such as the one studied in this work, snapshots are classically sampled from the transient response, from oscillating regimes or, if they are available, from chaotic trajectories (Bizon et al., 2012c; Lu et al., 2019).

To seek ROM globality, in this work two sampling strategies are compared. The first one, the most straightforward, is uniform sampling, i.e., taking samples of the FOM solutions with a uniform time interval. The uniformly sampled snapshots include both the transient behavior of the system and its oscillating regimes. The system is simulated for a set of values of the parameter of interest (Table 1). For the system under study in this work (Eq. (1)-(4)), in all the simulations fixed values of parameters Le, φ and β are assumed while the parameter subject to modification in individual simulations is γ. The solutions found for different values of the selected key parameters are then combined in a single snapshot matrix, as shown in Eq. (13):

$$\mathbf{U}=\begin{bmatrix} u_1(t_1,\gamma_1) & \cdots & u_1(t_M,\gamma_1) & u_1(t_1,\gamma_2) & \cdots & u_1(t_M,\gamma_2) & u_1(t_1,\gamma_H) & \cdots & u_1(t_M,\gamma_H) \\ \vdots & \ddots & \vdots & \vdots & \ddots & \vdots & \vdots & \ddots & \vdots \\ u_N(t_1,\gamma_1) & \cdots & u_N(t_M,\gamma_1) & u_N(t_1,\gamma_2) & \cdots & u_N(t_M,\gamma_2) & u_N(t_1,\gamma_H) & \cdots & u_N(t_M,\gamma_H) \end{bmatrix} \tag{13}$$

To further increase the robustness of the ROM, with the aim of predicting the bifurcation points with respect to one parameter variation, and while keeping computational resources to a minimum, another sampling strategy is introduced, consisting of the application of the *k*-means clustering algorithm to the uniformly sampled solutions.

The *k*-means algorithm is one of the most popular clustering techniques, widely applied in science and engineering. In the field of chemical engineering, for example, the procedure has proven successful in a series of studies on parameter-dependent stationary problems, such as optimization problems on multifunctional fixed-bed catalytic reactors (Bizon et al., 2021; Bizon and Continillo, 2021a). The algorithm is based on the so-called Lloyd method (Lloyd, 1982), which consists of an iterative expectation-maximization type approach that attempts to address the following objective: given a set of Euclidean points and a positive integer number of clusters *k*, divide the points into *k* clusters so that the total sum of the squared Euclidean distances of each point to its nearest cluster center is minimized. Briefly, *k*-means operates a partition of the snapshot set by grouping together subsets of nearby observations from an ensemble; the observations are considered near in the sense of some mutual distance, for example, the Euclidean distance. The intuitive nature of the Lloyd method and the effectiveness of the *k*-means technique make this clustering algorithm the most popular and used in numerous applications in different fields of engineering.

However, the *k*-means clustering technique is not always applicable: for example, for systems with considerable amounts of data, the algorithm may not be particularly effective as it may be difficult to identify the relevant underlying structure (i.e., the *k* clusters). This may be due to the presence of many irrelevant characteristics in the initial dataset (Guyon et al., 2004). Furthermore, like many clustering methods, *k*-means clustering requires specification of the number of clusters *k* before starting the clustering procedure.

In this work, the set of Euclidean points are the state variables (concentration and temperature) within the bidimensional domain shown in Fig. 1, or in other words the FOM solutions considered above in the construction of the snapshot matrix. After partitioning the solutions profiles into *k* clusters, the snapshot matrix consists of the centroids of the clusters. The centroids are the arithmetic means of the solution profiles of a given cluster. The *k*-means clustering algorithm for generating centroids is shown in Fig. 2.

INPUT k number of clusters; solution profiles $\mathbf{U}=[\mathbf{u}(t_1,\gamma_1),\ldots,\mathbf{u}(t_M,\gamma_H)] \in \mathbb{R}^{N\times M\cdot H}$

1) choose k initial guess centroids $\mathbf{Z}=[\mathbf{z}_1,\ldots,\mathbf{z}_k]$ from the column of $\mathbf{U}$

2) **while** not converged **do**

3) **for** $i=1$ to $M\cdot H$

4) $\mathbf{a}_i \leftarrow 1$

5) **for** $j=1$ to k

6) **if** $\|\mathbf{u}_i-\mathbf{z}_i\|<\|\mathbf{u}_i-\mathbf{z}_{\mathbf{a}_i}\|$

7) $\mathbf{a}_i \leftarrow j$

8) **end**

9) **end**

10) **for** $j=1$ to k

11) move $\mathbf{z}_i$ to the mean of $\{\mathbf{u}_i : \mathbf{a}_i = j\}$

12) **end**

13) **end**

OUTPUT centroids of the k clusters: $\mathbf{Z}=[\mathbf{z}_1,\ldots,\mathbf{z}_k]$

Figure 2. The *k*-means algorithm, adapted from (Hamerly and Drake, 2015).

- The bottleneck of the evaluation of the nonlinear term: a hyper-reduction strategy via DEIM

Consider the nonlinear term in the ROM introduced in Eq. (8):

$$\mathbf{\Gamma} = \mathbf{\Phi}_K^{\mathrm{T}} \mathbf{F}(\mathbf{\Phi}_K \mathbf{c}_K) \tag{14}$$

It can be noted that the function $\mathbf{F}(\mathbf{\Phi}_K \mathbf{c}_K)$ must be evaluated in the full-order space having dimension N and, in fact, $\tilde{\mathbf{u}} = \mathbf{\Phi}_K \mathbf{c}_K$ is the state variable vector of N elements.

To proceed with DEIM, the first thing to do is the application of the POD method to approximate the nonlinear function, so, in the same way introduced earlier for the reduction of the model, here the matrix of snapshots of the nonlinear function is introduced:

$$\mathbf{U}_F = \left[\mathbf{F}_1, \ldots, \mathbf{F}_j, \ldots, \mathbf{F}_M \right] \quad \text{where} \quad \mathbf{F}_j = [F(u_1(t_j)), F(u_2(t_j)), ..., F(u_N(t_j))]^{\mathrm{T}} \tag{15}$$

where M is the total number of snapshots considered. In the case of uniform sampling, M is the number of samples collected directly from the FOM solutions, whereas, when clustering is employed, M is the total number of clusters (and of centroids). After solving the eigenvalue problem, the nonlinear function **F** can be approximated as:

$$\mathbf{F} \approx \tilde{\mathbf{F}} = \mathbf{\Psi}_J \mathbf{q}_J \tag{16}$$

The unknown set of time-dependent coefficients $\mathbf{q}_J$ is to be determined. They are calculated using the following equation:

$$\mathbf{P}^{\mathrm{T}} \mathbf{F} = \left(\mathbf{P}^{\mathrm{T}} \mathbf{\Psi}_J \right) \mathbf{q}_J \tag{17}$$

where **P** is the matrix of the interpolation indices defining the grid points at which the nonlinear function is evaluated. Eq. (17) can be rearranged as follows:

$$\mathbf{q}_J = \left(\mathbf{P}^{\mathrm{T}} \mathbf{\Psi}_J \right)^{-1} \mathbf{P}^{\mathrm{T}} \mathbf{F} \tag{18}$$

Considering that the following equality holds:

$$\mathbf{P}^{\mathrm{T}} \mathbf{F}(\mathbf{u}(t)) = \mathbf{F}(\mathbf{P}^{\mathrm{T}} \mathbf{u}(t)) \tag{19}$$

then Eq. (18) can be rewritten as:

$$\mathbf{q}_J = \left(\mathbf{P}^{\mathrm{T}} \mathbf{\Psi}_J \right)^{-1} \mathbf{F}\left(\mathbf{P}^{\mathrm{T}} \tilde{\mathbf{u}} \right) \tag{20}$$

Matrix **P** contains the interpolation indices and can be computed using the DEIM algorithm (Chaturantabut and Sorensen, 2010) reported in Fig. 3.

INPUT Projection basis of the nonlinear function $\boldsymbol{\Psi} = \left[\boldsymbol{\psi}_1, ..., \boldsymbol{\psi}_N\right] \in \mathbb{R}^{N \times N}$

1) $p_1 = i$ such that $\max\left\{\left|\boldsymbol{\psi}_1(\zeta_i)\right|,\ i = 1, ..., N\right\}$

2) $\boldsymbol{\Psi}_1 = \boldsymbol{\psi}_1 \in \mathbb{R}^N$, $\mathbf{p} = p_1 \in \mathbb{R}^N$, $\mathbf{P} = e_{p_1} \in \mathbb{R}^N$

3) **for** $j = 2$ to J

4) **solve** $(\mathbf{P}^{\mathrm{T}}\boldsymbol{\Psi}_j)\mathbf{q}_j = \mathbf{P}^{\mathrm{T}}\boldsymbol{\psi}_j$ for $\mathbf{q}_j$

5) $\mathbf{r} = \boldsymbol{\psi}_j - \boldsymbol{\Psi}_j\mathbf{q}_j$

6) $p_j = i$ such that $\max\left\{|\mathbf{r}|,\ i = 1, ..., N\right\}$

7) $\boldsymbol{\Psi}_j = \left[\boldsymbol{\psi}_1, ..., \boldsymbol{\psi}_j\right] \in \mathbb{R}^{N \times j}$, $\mathbf{p} = \left[p_1, ..., p_j\right]^{\mathrm{T}} \in \mathbb{R}^j$ $\mathbf{P} = \left[e_{p_1}, ..., e_{p_j}\right] \mathbb{R}^{N \times j}$

8) **end**

OUTPUT Vector of interpolation indices $\mathbf{p} = \left[p_1, ..., p_J\right]^{\mathrm{T}} \in \mathbb{R}^J$

Figure 3. The DEIM algorithm, adapted from (Bizon, 2017).

Finally, substituting Eq. (20) into Eq. (17) and then in the ROM Eq. (8), the hyper-reduced POD-DEIM model is obtained:

$$\frac{d}{dt}\mathbf{c}_K = \boldsymbol{\Phi}_K^{\mathrm{T}}\mathbf{A}\boldsymbol{\Phi}_K\,\mathbf{c}_K + \boldsymbol{\Phi}_K^{\mathrm{T}}\boldsymbol{\Psi}_J\left(\mathbf{P}^{\mathrm{T}}\boldsymbol{\Psi}_J\right)^{-1}\mathbf{F}\left(\mathbf{P}^{\mathrm{T}}\boldsymbol{\Phi}_K\mathbf{c}_K\right) \tag{21}$$

In Eq. (21) the second term on the right-hand side $\boldsymbol{\Phi}_K^{\mathrm{T}}\boldsymbol{\Psi}_J\left(\mathbf{P}^{\mathrm{T}}\boldsymbol{\Psi}_J\right)^{-1}\mathbf{F}\left(\mathbf{P}^{\mathrm{T}}\boldsymbol{\Phi}_K\mathbf{c}_K\right)$ contains two factors that can be computed offline: $\boldsymbol{\Phi}_K^{\mathrm{T}}\boldsymbol{\Psi}_J\left(\mathbf{P}^{\mathrm{T}}\boldsymbol{\Psi}_J\right)^{-1}$ and $\mathbf{P}^{\mathrm{T}}\boldsymbol{\Phi}_K$. More importantly, the nonlinear function is evaluated only $J << N$ times, making the solution of the ODEs system much faster.

The introduced POD-DEIM methodology comes with a price: there are two numerical parameters to be calibrated for each variable (in the case of this work the variables are two: concentration and temperature inside the pile). The numerical parameters are the number of POD modes K used to approximate the state variables, and the number of interpolation points J used to evaluate the nonlinear part of the operator. These parameters need be adjusted with the objective of building a fast and accurate ROM.

The accuracy of the model and the speed of the simulation are conflicting objectives: the search of the optimal ROM is a multi-objective optimization and as such there are infinitely many solutions to the problem. Most authors prefer to maintain low the number of J and K thus preserving the speed of the ROM (Bremer et al., 2017a; Sukuntee and Chaturantabut, 2020). Moreover, the accuracy and the speed of the simulation are not necessarily

monotonous function of J and K. For this reason, the full space of parameters J and K must be investigated. This makes the tuning of the introduced numerical parameters a heavy task.

5.1.4 Solution procedure and model parameters

To numerically solve the mathematical model, as stated above the PDE system that describes heat and mass balance is firstly transformed into a system of nonlinear ODE (the so called FOM); the whole procedure is reported in Appendix A. To reach the discretized final system, the space derivative terms are approximated by means of central difference formulae at N discrete nodes equally distributed along the bi-dimensional grid of the rectangular domain. After the transformation, the solution of the ODE system is obtained by employing the built-in variable time step solver '*ode15s*' of MATLAB®. A convergence study on successive refinements of the grid has been conducted to choose the appropriate number of uniformly spaced nodes in the x and y direction. To describe the system, $N = 100$ nodes were chosen for each dimension. This results into the transformation of the infinite dimensional model consisting of 2 PDEs into a large system of $2 \cdot 10^4$ ODEs. The system of ODEs is then integrated in the time interval $t \in [0, 5]$, and the solution is sampled with a uniform time-step equal to $\Delta t = 2 \cdot 10^{-4}$, resulting in 25001 snapshots.

The values of the parameters employed in the numerical simulations, chosen as typical for the self-combustion of coal stockpiles (Brooks et al., 1988), are reported in Table 1. The results are described and discussed in three subsections. Section 5.1 reports the results obtained by the FOM solution. Section 5.2 shows the application of reduced-order modelling via the classical POD-Galërkin. In this case the method allows to reduce the number of variables and equations, resulting in a set of $2 \times K$ ODEs (where K is the number of POD modes), with $K << N$. The third part of the results (sub-section 5.3) is focused on the application of the POD-DEIM methodology. These results are obtained by varying K (number of POD modes) and J (DEIM interpolation points), in the ranges defined in Table 1. This is necessary to reach the best accuracy of the POD and POD-DEIM solutions with respect to the base-case, represented by FOM solutions. This study can be seen as a parametric analysis on pairs of values of K and J to understand their influence on the accuracy of the reduced-order models. Furthermore, to choose the most representative solution samples from the FOM (i.e., the 25001 snapshots), and thus to determine a faithful POD basis, the k-means clustering algorithm is employed. The output of the k-means algorithm is a set of k centroids that are used to build a new matrix of snapshots. In all the

simulations involving the *k*-means clustering algorithm the number of centroids is set equal to 2000. The value of 2000 was a result of a parametric analysis on the influence of the number of centroids on the accuracy of the reduced-order models.

5.1.5 Results and discussion

In this work the choice of studying only the influence of γ follows from the fact that it has the strongest effects on the system behavior when compared to the other parameters (Schwarzer et al., 2021). This is due to the exponential nature of the Arrhenius expression, in which the dimensionless activation energy (i.e., γ) appears. To explore the worst-case scenario, the ROMs have been constructed to obtain accurate solutions for an interval of values of γ.

5.1.5.1 Influence of parameter γ on the FOM solutions

The influence of γ on the behavior of the system is analyzed by simulation, and the results of these simulations are collected in the solution diagram in Fig. 4 and reported as time series in Fig. 5.

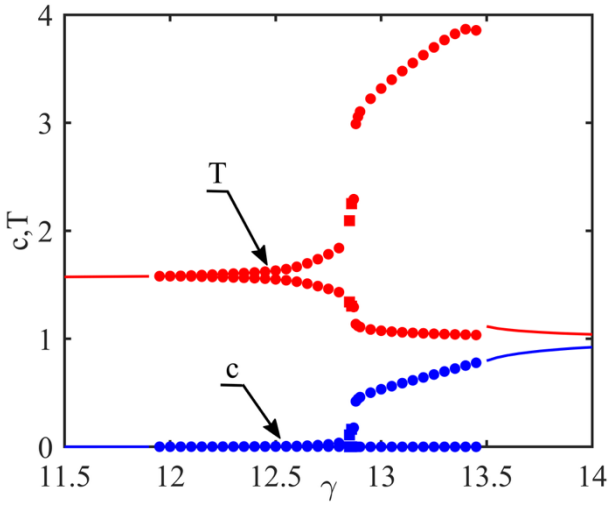

Figure 4. Solution diagram obtained with the FOM by varying the parameter γ with the method of brute force. Solid lines, dots and squares denote, respectively, steady-state solutions, maxima and minima of period-1, and period-2 solutions.

The system exhibits steady-state and oscillatory solutions within the parameter range explored in this work (i.e., 11.5 – 14).

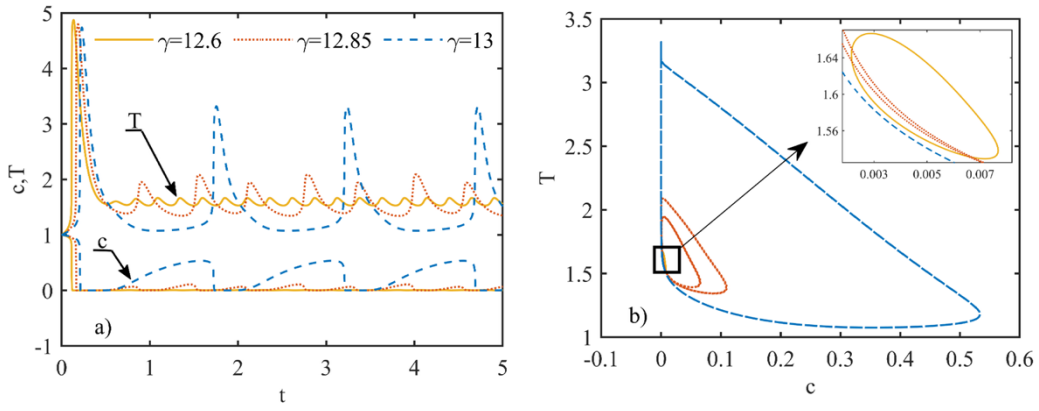

Figure 5. Time series (a) and phase space (b) solutions obtained employing the FOM.

Three γ values are particularly significant:

- γ = 11.95 where the simulation detects the first oscillatory solution
- γ = 12.85 where the simulation detects the first period-2 oscillatory solution
- γ = 13.5 where the system returns to a steady-state solution.

The presence of a period-2 oscillatory solution is not surprising. In the literature, the same physical system modeled with a one-dimensional geometry has shown the existence of period doubling bifurcations, resulting in quasi periodic (tori) and aperiodic attractors and metastable chaos (Continillo et al., 2000). The existence of such rich dynamics has not been confirmed in this work, but it is speculated that, as for the one-dimensional case, also bi-dimensional systems may exhibit chaotic behavior in a narrow window between γ = 12.85 and γ = 12.86.

As shown in Fig. 4, most solutions have an oscillatory behavior, particularly in the range of $\gamma \in [11.95, 13.45]$. This fact makes the simulation and analysis of the self-ignition of solid materials a computationally expensive task, as the presence of such oscillatory solutions requires longer computations from the adjustable step size ODE solver. The need for reduced-order models is even more emphasized if we consider that more complex models are needed to account for chemical or bio-chemical reaction networks and physical effects, e.g., microbial activity, consideration of heat of water adsorption, or more complex geometries (Sheng and Yao, 2022c).

The sensitivity of self-igniting systems to the dimensionless activation energy is well depicted in the solution diagram (Fig. 4). To better understand the physical phenomena, it is

useful to focus on the periodic solutions. Recall that Fig. 4 and Fig. 5 report simulation results for a single point, interior to the domain, which is located halfway on the symmetry axis as shown in Fig. 1.

The analysis of Fig. 5a permits to understand the phenomenon of self-ignition. Due to the high initial concentration of oxygen inside the pile, in the first instants there is a fast and sudden combustion (an explosion), that is similar for all three values analyzed for the dimensionless activation energy γ. After the early transient, the influence of γ on the system behavior is observed. By increasing γ, that may correspond to increasing the activation energy by changing the chemical composition of the combustible solid, as well as using a different reference temperature, the time lag between two consecutive peaks of temperature and concentration increases, with a meaningful variation of frequency and amplitude of the periodic solution.

For higher values of γ (the dashed curve of Fig. 5a), the system has an overall slower reaction rate. For this reason, the oxygen diffusing from the ambient is not consumed in the outer layers of the pile but rather diffuses and accumulates inside the solid porous material. If oxygen is not significantly consumed, its concentration slowly rises (from about 0.6 to 1.8 AUT). Meanwhile, also the temperature slightly increases, because the heat slowly generated by the reaction overcomes the heat lost through the boundaries. When the temperature reaches the critical value of self-ignition, a new rapid combustion event is observed (ca. 1.8 AUT). As represented by the assumed constant boundary conditions, oxygen is continuously supplied from the ambient atmosphere, while solid fuel depletion remains negligible. The ignition phenomenon repeats and, mathematically, the system is locked on to the limit cycle attractor. Moving the attention to a lower value of γ (solid curve in Fig. 5a), the reaction can occur at lower temperatures, oxygen is promptly consumed at the boundary of the domain, and this does not allow the growth of its bulk concentration; hence, in the analyzed point of the domain, solutions exhibit limit cycles with small amplitude (the magnified inset in Fig. 5b). Figure 5b highlights the presence of three dynamic attractors for the three values of γ analyzed. The existence of the period-two limit cycle (the dotted curve) can be explained by the contrasting tendencies of the system to be attracted both by the rapid reaction regime (small cycle, high frequency oscillations depicted by the solid curves in both diagrams) and by the slow reaction regime (large cycle, low frequency oscillations depicted by the dashed

curves) as γ is varied. The results agree with those reported by Continillo et al., (2000) for the one-dimensional model.

5.1.5.2 Evaluation of the POD-based solution

Generally, POD reduced-order models are accurate and efficient since they are empirically based. However, their empirical character brings in some limitations. Depending on the chosen set of solutions, i.e., snapshots, the empirical model loses accuracy as the parameter set moves away from the values employed in generating the snapshots. In this work, this traduces into how to find the most suitable dataset, based on one or more FOM solutions, obtained by variation of the value of γ, that combines accuracy and flexibility in terms of parameter values. The choice of the snapshot sampling strategy is targeted to the construction of a reduced-order model that is as global as possible, as discussed in Section 3. The desired property for a ROM is to reproduce the FOM as closely as possible, both quantitatively and qualitatively. For quantitative comparison, the following average error has been introduced:

$$\varepsilon_{K,avg} = \frac{1}{M} \cdot \sum_{i=1}^{M} \frac{1}{\sqrt{N}} \cdot \frac{\left\| \mathbf{u}(t_i) - \tilde{\mathbf{u}}(t_i) \right\|}{\left\| \mathbf{u}(t_i) \right\|} \tag{22}$$

where $\|\cdot\|$ is the L_2-norm, whereas $\mathbf{u}(t_i)$ and $\tilde{\mathbf{u}}(t_i)$ are respectively FOM and ROM solutions evaluated at time instant t_i, N is the number of spatial discretization nodes, and M is the total number of time samples.

Since temperature and concentration errors have the same order of magnitude and the same pattern, only temperature average errors are reported. Various strategies of snapshot sampling are evaluated, namely:

- 'γ Single Sol.': snapshots are sampled from FOM results obtained for only one value of the parameter (γ = 13) and using a uniform sampling strategy considering both transient and regime solutions.
- 'γ Mix': snapshots are sampled from FOM results obtained for two values of γ (γ = 13 and 12.6) and using a uniform sampling strategy considering both transient and regime solutions.
- 'γ Mix *k*-means': as in the previous case, to build the snapshots matrix two values of γ are employed (i.e., γ = 13 and 12.6). In this case, the snapshots are chosen automatically, employing the *k*-means clustering algorithm. The snapshots here are

the centroids of a predefined number (2000) of clusters, following from the results of a preliminary analysis of accuracy and convergence, conducted but not reported.

The choice to include in the snapshot matrix the information related to FOM solutions obtained for two values of the selected parameter has been made following the work of Bizon et al., (2008). Particularly, the basis function set was calculated by incorporating the two different dynamic attractors previously analyzed (i.e., small cycles, short periods, moderate gradients, found for $\gamma = 12.6$, and large cycles, long periods, steep gradients, found for $\gamma = 13$).

The first reduction technique considered is the classical POD approach. The error has been evaluated for three different values of γ: 12.6, 12.85 and 13, and reported in Fig. 6 as a function of the truncation order K. Note that the error is not reported for the lowest values of the numerical parameter K since there are no consistent results of simulations available.

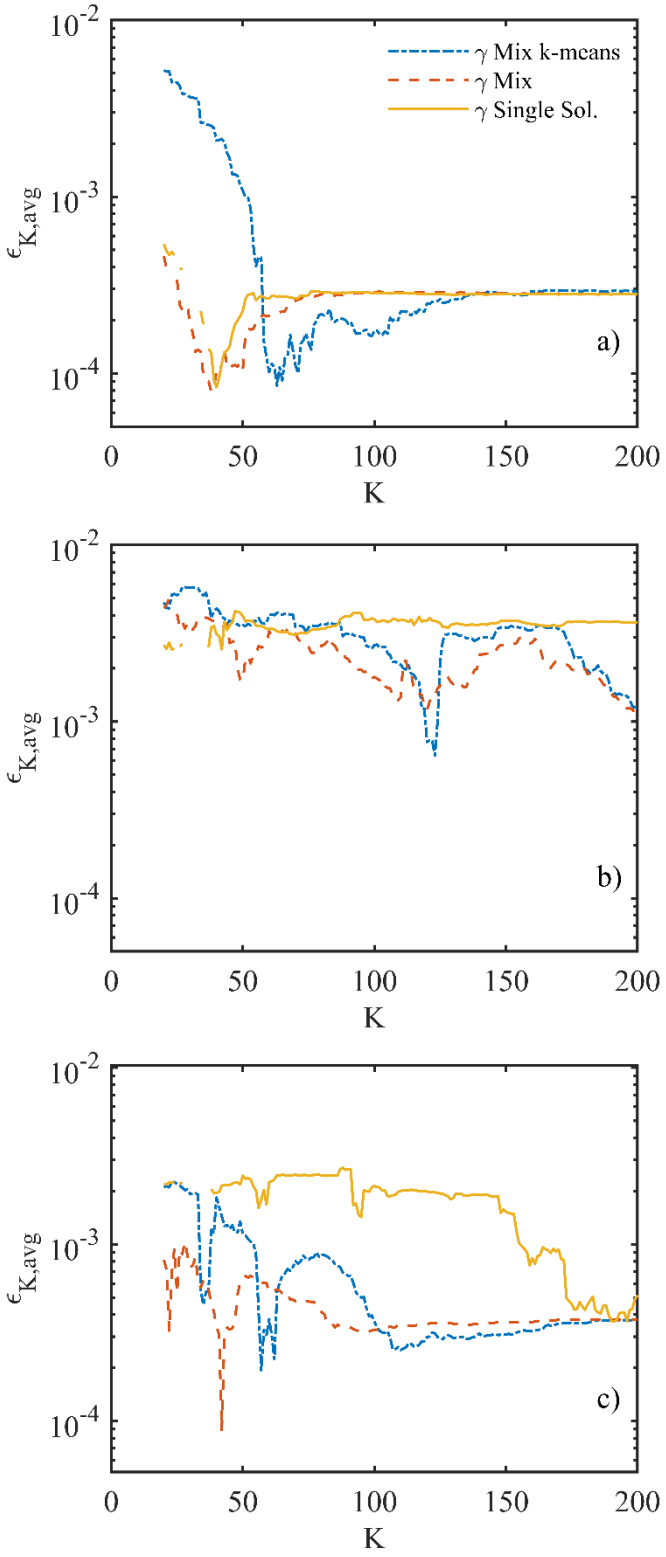

Figure 6. Computational errors in the approximation of the dimensionless temperature as a function of K, for three different values of γ: a) $\gamma = 13$, b) $\gamma = 12.85$, c) $\gamma = 12.6$, and for various snapshot sampling strategies.

Figure 6a reports the errors for $\gamma = 13$, that is the value of the parameter for which the snapshots were generated and included in all the POD basis sets. The three sampling strategies lead to comparable results. Particularly, the error curves obtained for the ROM constructed using 'γ Single Sol.' and 'γ Mix' sampling are very similar in terms of shape and of overall mean value (respectively equal to $2.76 \cdot 10^{-4}$ and $2.57 \cdot 10^{-4}$). This is an expected behavior, as the snapshot matrices have been built using solutions relative to $\gamma = 13$. Note that the *k*-means strategy has a slightly higher mean error ($7.21 \cdot 10^{-4}$): this is also expected since, with *k*-means, data reduction of about 12:1 is implemented by using, in place of each cluster grouping several snapshots, the relevant single cluster centroid.

Reduced-order models can lose validity if used for parameter values too much different from those for which the solutions were generated and sampled. This is exactly what can be noted in Fig. 6c. Here the error of the model built with the 'γ Single Sol.' strategy (solid line) is on average of $1.7 \cdot 10^{-3}$, one order of magnitude higher if compared to the one of Fig. 6a. To extend the validity of the ROM, the 'γ Mix' (dashed line) and 'γ Mix *k*-means' (dash-dot line) strategies are employed, successfully leading to lower errors (respectively of $4.26 \cdot 10^{-4}$ and $6.31 \cdot 10^{-4}$ on average).

Figure 6b reports the error of the reduced-order models simulated for a value of γ that was not employed in the construction of the sampled solutions for any of the ROMs. The accuracy of the ROMs in this case is expectedly lower for all the sampling strategies considered. As expected, both 'γ Mix' and 'γ Mix *k*-means' perform better than 'γ Single Sol.' In fact, 'γ Single Sol.' exhibits lower globality when used to simulate the system for different values of γ and, for this reason, from now on this strategy is no further analyzed in conjunction with DEIM.

Obviously, the main advantage of a reduced-order model is the lower computational cost required to achieve the same level of accuracy. Figure 7 reports the speedup ratio as a function of *K*.

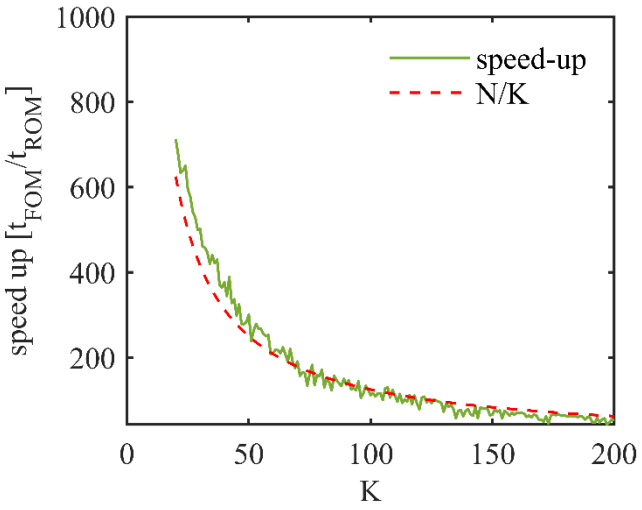

Figure 7. Speedup of the computational time achieved by simulating the system with the POD-ROM for γ=12.85. The N/K curve is reported for comparison.

Speedup as high as three orders of magnitude can be achieved with the least accurate POD-based model: however, this may lead to inaccurate and even unphysical solutions. By taking at least 120 modes, it is possible to reproduce the behavior computed with the FOM (here is where the minimum computed error for γ = 12.85 can be obtained). Yet, with 120 modes, the ROM solution can be computed two orders of magnitude faster than the corresponding FOM. The speedup factor (t_{FOM}/t_{ROM}) follows the N/K curve (showing the ratio of the number of FOM over ROM differential equations), as reported in Fig. 7. Further speedup of the calculations can be achieved using DEIM, as shown in the following subsection.

5.1.5.2 Evaluation of the POD-DEIM solution

A hyper-reduction of the nonlinear term made via the POD-DEIM algorithm permits to achieve a much higher speedup compared to the one achieved with classical POD. As a result of the considerations made above, POD-DEIM has been implemented considering only two of the three strategies introduced, namely 'γ Mix' and 'γ Mix k-means.' The first step of the algorithm to be employed to compute the DEIM interpolation points is the construction of the snapshot matrix of the nonlinear term. The nonlinear terms appearing in the two PDEs (Eq. (1) and Eq. (2)) differ just in some constant parameters:

$$F_1(c,T) = \beta\varphi^2 c \exp\left(-\frac{\gamma}{T}\right), \quad F_2(c,T) = -\varphi^2 c \exp\left(-\frac{\gamma}{T}\right) \tag{23}$$

These two nonlinear functions are treated separately with DEIM, using the same number of interpolation points, *J*, for the two functions. Following DEIM, firstly a set of basis functions is obtained for the nonlinear functions. The snapshot matrices $\mathbf{U}_{F_1}$ and $\mathbf{U}_{F_2}$ are computed using the solutions of the FOM simulations, sampled uniformly or with *k*-means as explained in the previous section. Then, the basis functions of the two nonlinear terms are obtained by solving the eigenvalue problem $\mathbf{C}_{F_i} = \mathbf{U}_{F_i}\mathbf{U}_{F_i}^{\mathrm{T}}$ $(i = 1, 2)$, where $\mathbf{C}_{F_i}$ is the correlation matrix. The positions of the interpolation points in the grid are then selected using the DEIM algorithm described in Fig. 3.

To understand the possible benefits of the clustering technique for the construction of the basis, the average error was calculated as done with the classical POD model. The DEIM methodology comes with a new parameter *J*, which adds complexity to the construction of the ROM in that both *K* and *J* must be determined. Fig. 8 reports the values of the calculated average error between the FOM and the DEIM solutions as a function of *K* (as done in the POD section). The results relate to two values of the parameter γ and to two different strategies of snapshot sampling. Each graph contains three curves, referring to three of the values of interpolation points considered in the study ($J = 100$, $J = 300$ and $J = 500$).

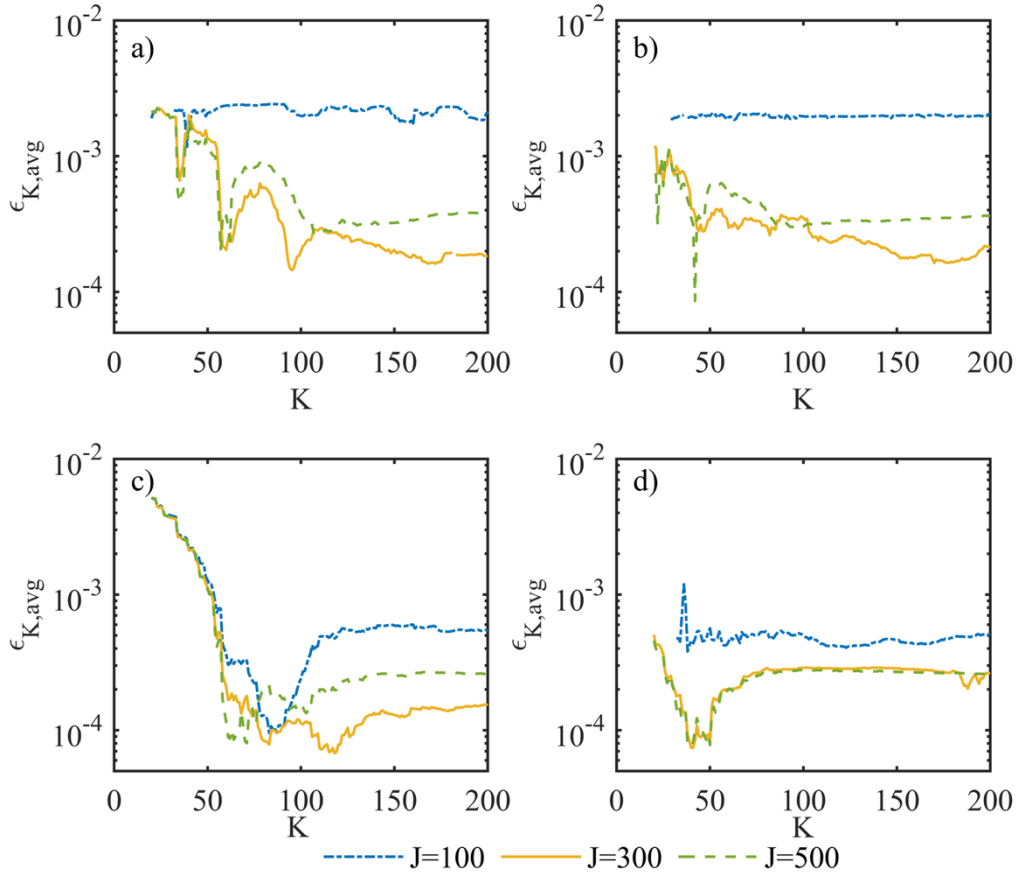

Figure 8. Computational errors in the approximation of the dimensionless concentration as a function of K, for three different values of the number of interpolation points J: a) $\gamma = 12.6$, 'γ Mix k-means,' b) $\gamma = 12.6$, 'γ Mix,' c) $\gamma = 13$, 'γ Mix k-means', d) $\gamma = 13$, 'γ Mix'.

Reading the graph from left to right, it can be observed that the errors have the same order of magnitude even if the ROM based on the combination of k-means and DEIM (Fig. 8a and 8c) is built with a much lower number of snapshots (2000 centroids) with respect to the uniformly sampled 25000 FOM solutions (Fig. 8b and 8d).

As observed earlier, errors are slightly higher when employing k-means as compared to uniform sampling. For example, the mean value of the k-means error calculated over the considered range of K, for $\gamma = 13$ and $J = 500$, is $7.3 \cdot 10^{-4}$, only slightly higher than the value of $2.5 \cdot 10^{-4}$ found with uniform sampling. This decrease in accuracy is expected for the ROM built with the k-means strategy when a small number of modes is considered (from $K = 20$ to $K = 60$), as the linear part of this ROM is built upon the POD model introduced in Subsection 5.2, which performs best when using uniform sampling. If the reduced-order model is built with a higher number of modes (i.e., $K > 60$), the error calculated for the k-means strategy and that calculated with the uniform strategy have the same order of

magnitude. In some cases, lower errors can be obtained with *k*-means, as seen by comparing the solid curves reported in Fig. 8c and Fig. 8d.

The error analysis is further extended to the values of γ that were not included in the snapshots (Fig. 9). The values of the parameters analyzed are $\gamma = 12.2$ (low amplitude oscillations), $\gamma = 12.85$ (period-doubling solution) and $\gamma = 13.4$ (high amplitude solution). This choice of γ values has been made to assess how DEIM is able to predict a system behavior not previously encountered in the simulations used for ROM construction, such as the period-doubling solution.

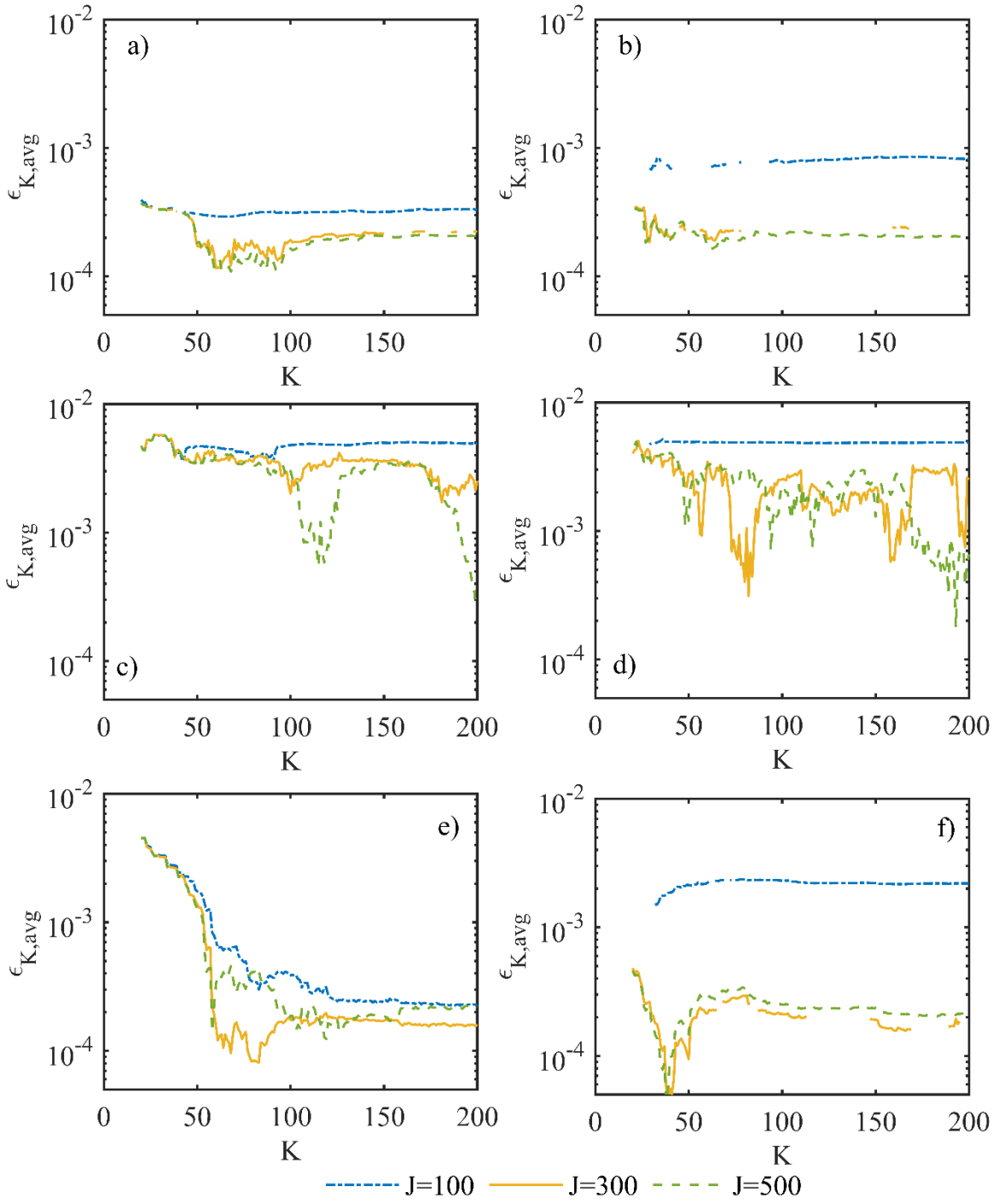

Figure 9. Computational errors in the approximation of the dimensionless concentration as a function of K, for three different values of the number of interpolation points J: a) $\gamma = 12.2$, 'γ Mix k-means', b) $\gamma = 12.2$, 'γ Mix', c) $\gamma = 12.85$, 'γ Mix k-means', d) $\gamma = 12.85$, 'γ Mix', e) $\gamma = 13.4$, 'γ Mix k-means', f) $\gamma = 13.4$, 'γ Mix'.

It is known from the literature (Bizon et al., 2008) that when moving away from the conditions at which a reduced-order model is constructed, the solutions are approximated with lower accuracy. As can be seen in Fig. 9, the errors appear to be of the same order of magnitude as those obtained for values of γ included in the snapshots (Fig. 8). Moreover, the hyper-reduced DEIM models succeed in capturing even the period-doubling solutions (Fig. 9c and 9d), although with a slightly higher error (of the order of 10^{-3}), with the most accurate ROM being in the range of $5 \cdot 10^{-4}$. This confirms the global character of this ROM, which can be used in applications such as parametric analysis.

Analyzing the ROMs computed with lower values of the number of interpolation points J, the strategy of 'γ Mix k-means' appears to be more robust. In fact, as it can be seen by looking at the curves corresponding to $J = 100$ and $J = 300$, the 'γ Mix' curves (right column of Fig. 9) are more irregular, and in many cases the error cannot be computed (in this case the ROM, using MATLAB® '*ode15s*', does not converge to a solution). This result enlightens the advantage of combining the k-means strategy and DEIM, that yields more stable models.

Analyzing the computational time of the DEIM-based ROM (Fig. 10) it must be said that - unlike the case of the classical POD method - the speedup does not follow the N/K trend observed in the previous subsection.

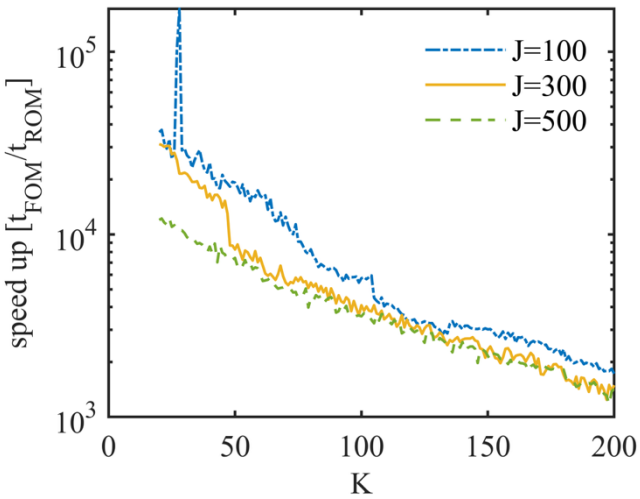

Figure 10. Speedup as a function of K, for three different values of the number of interpolation points J, $\gamma = 12.85$, and for the ROM constructed by using the 'γ Mix k-means' strategy.

The computation time, not reported, remains in the order of magnitude of seconds for any simulation and for every value of K and J chosen in the range of respectively [20 – 200] and [100 – 500]. This allows the use of relatively high values of J and K, to obtain accurate and global ROMs that still exhibit a more than remarkable speedup with respect to the FOM. Moreover, it must be noted that the speedup is not sensibly influenced by the value of J. This is an expected result, considering that, to integrate the FOM, at every time step the ODE solver must evaluate 20000 nonlinear terms, whereas when DEIM is applied the ODE solver must evaluate, at most, 1000 nonlinear terms. Considering this, a satisfactory result would be to achieve a speedup factor of about one thousand with a reasonably prescribed accuracy. This means that if the FOM solution is computed in $1.2 \cdot 10^4$ seconds (i.e., 3 hours), the corresponding DEIM solution should be computed in about 10 seconds. The time series reported in Fig. 11 have been calculated using $K = 200$ and $J = 500$ and setting up the k-means clustering with 2000 centroids, which resulted in a reliable POD-DEIM with a speedup of 1020 and an error of $1.49 \cdot 10^{-4}$.

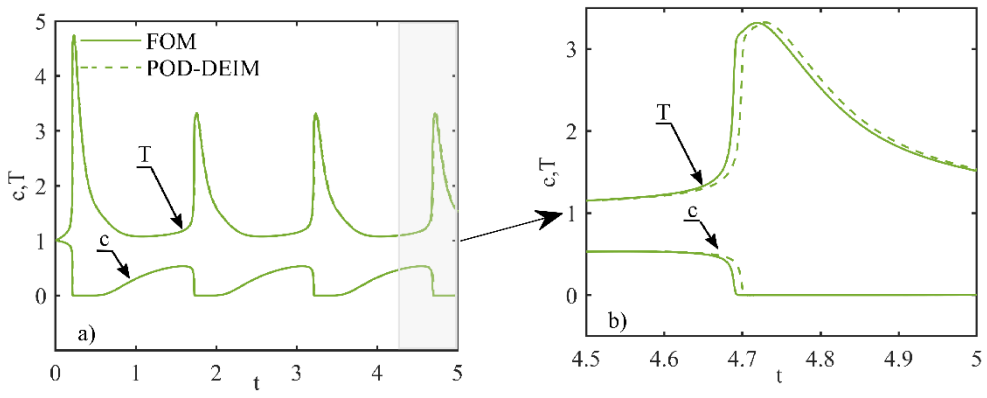

Figure 11: Comparison of temperature and concentration time series obtained using FOM and ROM at the point of the domain marked in Fig. 1, for $\gamma = 13$ (a). The inset (b) reports an explosion event.

The solutions obtained using FOM and DEIM practically overlap. However, although the reduced-order model captures accurately the dynamic evolution of the systems, the solutions appear to slightly drift out of phase as time passes (Fig. 11b).

It is now interesting to examine the solutions in the entire spatial domain. Figure 12 compares the dimensionless temperature distribution obtained from FOM (first row) and POD-DEIM (second row) at three different time instants.

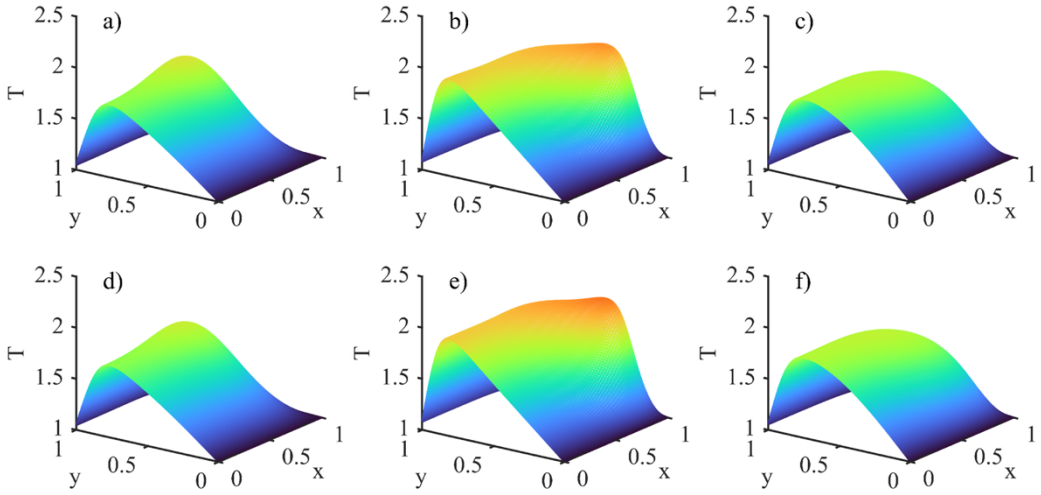

Figure 12: Comparison of temperature solutions for $\gamma = 12.6$ obtained from FOM (first row) and POD-DEIM (second row) at three different time instants: $t = 1.26$ (a, d), $t = 1.3198$ (b, e), $t = 1.36$ (c, f). These instants have been chosen as representative of pre and post ignition events.

The results are computed for $\gamma = 12.6$ and show how the spatiotemporal evolution of the state variables obtained from FOM and ROM are structurally the same and quantitatively comparable. This is a further proof of the satisfactory performance of POD-DEIM solutions, also when varying the parameter of interest.

5.1.6 Conclusions

In this work a set of reduced dynamic models has been built with the aim of approximating the state variable vectors of a bi-dimensional reaction-diffusion system. The system describes the self-ignition of a porous solid material, analyzed in different physical conditions that lead to different dynamical behavior. Particularly, the simulations have been conducted varying the value of the dimensionless activation energy γ, bringing the system from fast (low value of γ) to slow (high value of γ) reacting regimes (Continillo et al., 2000). It has been shown that the system is characterized by an oscillatory behavior for the values of γ between 11.95 and 13.45. This fact makes the simulation and analysis of the system a computationally expensive task, thus emphasizing the need for the construction of a reduced-order model (ROM). Two ROM formulations have been employed, namely the classical POD-Galërkin which allows the speedup of the simulations, and the discrete empirical interpolation method (DEIM) that enhances the computational savings by reducing the

number of online evaluations of the model nonlinearities. Although these methodologies have already proven to capture the essential dynamics of spatially distributed reactive systems (Bizon et al., 2008, 2012a; Bremer et al., 2017a), they are characterized by some issues, such as instabilities, accuracy and globality, that still need to be properly addressed.

In this work two sampling strategies have been compared for the selection of the snapshots, namely uniform sampling versus *k*-means. For quantitative evaluation, an expression for the mean error has been introduced and different ROMs have been evaluated. Considering that the parameter space needs to be sampled at different values to obtain a ROM capable of predicting the behavior of the system over the range of interest (Bizon et al., 2008), two different dynamic attractors of the system under study have been used to build the snapshot matrix. The FOM solutions used as snapshots have been obtained for a value of $\gamma = 12.6$, where the attractor of the system is characterized by small cycles and moderate gradients, and for a value of $\gamma = 13$, where the attractor is characterized by large cycles and steep gradients. The combination of these two information in the construction of the basis functions has resulted in ROMs capable of predicting even the bifurcation points of the analyzed system, thus demonstrating quantitative and qualitative agreement with the results of FOM (Cutillo et al., 2023). Furthermore, the two sampling strategies have shown similar patterns in terms of error between ROM and FOM, as the two numerical parameters of the reduced-order models (K and J) are varied. The *k*-means strategy allows to obtain a more stable ROM, especially when the DEIM methodology is employed. In fact, with the uniform sampling strategy the obtained models result unreliable for low values K and J. Thanks to the enhanced stability resulting from the application of *k*-means, it is possible to achieve a reduction in the burden of building and using reduced-order models for computationally challenging problems such as parametric analysis, optimization and control.

After assessing the sampling strategy, the best ROM has been chosen to report representative simulation results. The choice of the ROM has been made considering both accuracy and speedup with respect to the FOM. For this reason, a ROM built with the DEIM methodology and the *k*-means sampling strategy has been selected, with the values of the numerical parameters set to K=200 and J=500. The results show good agreement with the FOM for both the temporal evolution of the state variables at a single point within the domain and in the entire spatial domain, as expected due to the low mean error of the chosen ROM.

Furthermore, the chosen ROM allows to achieve a speedup of 1020 in comparison with the simulation CPU time of the original FOM.

5.1.7 Appendix A

Figure A1 shows the discretization performed on the bi-dimensional mesh with the nodes ordered from the bottom left to the top right. The application of central difference schemes to approximate the spatial partial derivatives in Eq. (1) and (2) with the boundary conditions defined by Eq. (3) results into a large system of ODEs.

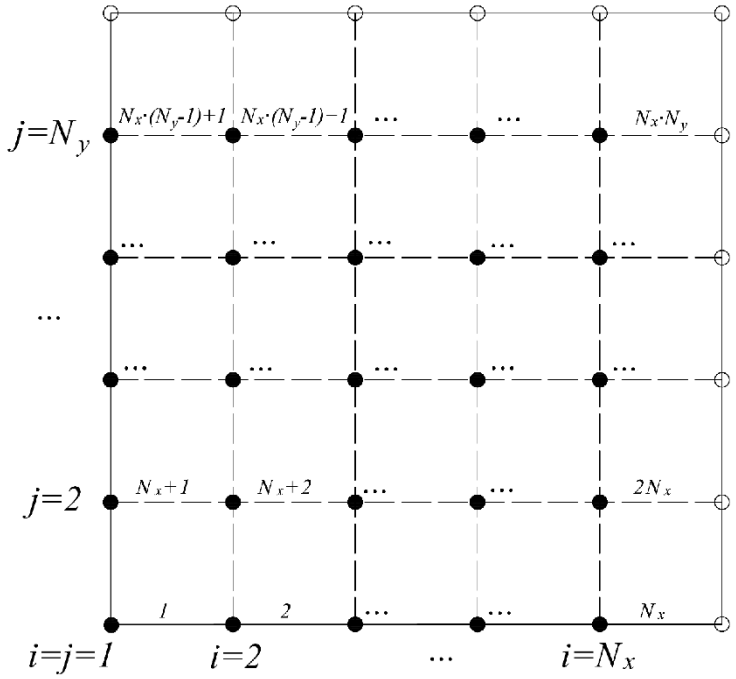

Figure A1. Bi-dimensional grid used to discretize spatial partial derivatives.

In Figure A1, for each solid circle the corresponding discretized equations are written, while the empty circles refer to the nodes where the Dirichlet boundary condition provide known values for the state variable. Furthermore, the Neumann boundary conditions defined in Eq. (3) are first discretized by application of finite differences and then substituted into the finite difference form of Eq. (1) and Eq. (2).

The Neumann boundary conditions (Eq. (3a) and Eq. (3b)) can be rewritten as:

$$\frac{c_{2,j}-c_{0,j}}{2\Delta x}=0 \;\Rightarrow\; c_{0,j}=c_{2,j} \text{ for } j=1,...,N_y \tag{A.1}$$

$$\frac{T_{2,j}-T_{0,j}}{2\Delta x}=0 \;\Rightarrow\; T_{0,j}=T_{2,j} \;\text{ for }\; j=1,...,N_y \tag{A.2}$$

$$\frac{c_{i,0}-c_{i,2}}{2\Delta x}=0 \;\Rightarrow\; c_{i,0}=c_{i,2} \;\text{ for i}=1,...,N_x \tag{A.3}$$

The Dirichlet boundary conditions of Eq. (3b), Eq. (3c) and Eq. (3d) can be rewritten as:

$$T_{i,0}=1 \;\text{ for }\; \mathrm{i}=1,...,N_x \tag{A.4}$$

$$c_{N_x+1,j}=1 \;,\; T_{N_x+1,j}=1 \;\text{ for }\; j=1,...,N_y \tag{A.5}$$

$$c_{i,N_y+1}=1 \;,\; T_{i,N_y+1}=1 \;\text{ for }\; i=1,...,N_x \tag{A.6}$$

Eq. (1) and Eq. (2) are discretized by applying central difference schemes as:

Node $i=1,\ j=1$ (bottom left corner)

$$\frac{dc_{1,1}}{dt}=\mathrm{Le}\left(\frac{-2c_{1,1}+2c_{2,1}}{\Delta x^2}+\frac{-2c_{1,1}+2c_{1,2}}{\Delta y^2}\right)-\varphi^2 c_{1,1}\exp\left(-\frac{\gamma}{T_{1,1}}\right) \tag{A.7}$$

$$\frac{dT_{1,1}}{dt}=0 \tag{A.8}$$

Nodes $i=2,\ldots,N_x-1,\ j=1$ (bottom central)

$$\frac{dc_{i,1}}{dt}=\mathrm{Le}\left(\frac{c_{i-1,1}-2c_{i,1}+c_{i+1,1}}{\Delta x^2}+\frac{-2c_{i,1}+2c_{i,2}}{\Delta y^2}\right)-\varphi^2 c_{i,1}\exp\left(-\frac{\gamma}{T_{i,1}}\right) \tag{A.9}$$

$$\frac{dT_{i,1}}{dt}=0 \tag{A.10}$$

Node $i=N_x,\ j=1$ (bottom right corner)

$$\frac{dc_{N_x,1}}{dt}=\mathrm{Le}\left(\frac{c_{N_x-1,1}-2c_{N_x,1}+1}{\Delta x^2}+\frac{-2c_{N_x,1}+2c_{N_x,2}}{\Delta y^2}\right)-\varphi^2 c_{N_x,1}\exp\left(-\frac{\gamma}{T_{N_x,1}}\right) \tag{A.11}$$

$$\frac{dT_{N_x,1}}{dt}=0 \tag{A.12}$$

Nodes $i=1,\ j=2,\ldots,N_y-1$ (left central)

$$\frac{dc_{1,j}}{dt} = \mathrm{Le}\left(\frac{-2c_{1,j} + 2c_{2,j}}{\Delta x^2} + \frac{c_{1,j-1} - 2c_{1,j} + c_{1,j+1}}{\Delta y^2} \right) - \varphi^2 c_{1,j} \exp\left(-\frac{\gamma}{T_{1,j}} \right)$$

(A.13)

$$\frac{dT_{1,j}}{dt} = \left(\frac{-2T_{1,j} + 2T_{2,j}}{\Delta x^2} + \frac{T_{1,j-1} - 2T_{1,j} + T_{1,j+1}}{\Delta y^2} \right) + \beta\varphi^2 c_{1,j} \exp\left(-\frac{\gamma}{T_{1,j}} \right)$$

(A.14)

Nodes $i = 2,..., N_x - 1,\ j = 2,\ldots, N_y - 1$ (internal nodes)

$$\frac{dc_{i,j}}{dt} = \mathrm{Le}\left(\frac{c_{i-1,j} - 2c_{i,j} + c_{i+1,j}}{\Delta x^2} + \frac{c_{i,j-1} - 2c_{i,j} + c_{i,j+1}}{\Delta y^2} \right) - \varphi^2 c_{i,j} \exp\left(-\frac{\gamma}{T_{i,j}} \right)$$

(A.15)

$$\frac{dT_{i,j}}{dt} = \left(\frac{T_{i-1,j} - 2T_{i,j} + T_{i+1,j}}{\Delta x^2} + \frac{T_{i,j-1} - 2T_{i,j} + T_{i,j+1}}{\Delta y^2} \right) + \beta\varphi^2 c_{i,j} \exp\left(-\frac{\gamma}{T_{i,j}} \right)$$

(A.16)

Nodes $i = N_x,\ j = 2,\ldots, N_y - 1$ (right central)

$$\frac{dc_{N_x,j}}{dt} = \mathrm{Le}\left(\frac{c_{N_x,j-1} - 2c_{N_x,j} + c_{N_x,j+1}}{\Delta x^2} + \frac{c_{N_x-1,j} - 2c_{N_x,j} + 1}{\Delta y^2} \right) - \varphi^2 c_{N_x,j} \exp\left(-\frac{\gamma}{T_{N_x,j}} \right)$$

(A.17)

$$\frac{dT_{N_x,j}}{dt} = \left(\frac{T_{N_x,j-1} - 2T_{N_x,j} + T_{N_x,j+1}}{\Delta x^2} + \frac{T_{N_x-1,j} - 2T_{N_x,j} + 1}{\Delta y^2} \right) + \beta\varphi^2 c_{N_x,j} \exp\left(-\frac{\gamma}{T_{N_x,j}} \right)$$

(A.18)

Node $i = 1,\ j = N_y$ (top left corner)

$$\frac{dc_{1,N_y}}{dt} = \mathrm{Le}\left(\frac{-2c_{1,N_y} + 2c_{2,N_y}}{\Delta x^2} + \frac{c_{1,N_y-1} - 2c_{1,N_y} + 1}{\Delta y^2} \right) - \varphi^2 c_{1,N_y} \exp\left(-\frac{\gamma}{T_{1,N_y}} \right)$$

(A.19)

$$\frac{dT_{1,N_y}}{dt} = \left(\frac{-2T_{1,N_y} + 2T_{2,N_y}}{\Delta x^2} + \frac{T_{1,N_y-1} - 2T_{1,N_y} + 1}{\Delta y^2} \right) + \beta\varphi^2 c_{1,N_y} \exp\left(-\frac{\gamma}{T_{1,N_y}} \right)$$

(A.20)

Nodes $i=2,\ldots,N_x-1,\ j=N_y$ (top central)

$$\frac{dc_{i,N_y}}{dt}=\mathrm{Le}\left(\frac{c_{i-1,N_y}-2c_{i,N_y}+c_{i+1,N_y}}{\Delta x^2}+\frac{c_{i,N_y-1}-2c_{i,N_y}+1}{\Delta y^2}\right)-\varphi^2 c_{i,N_y}\exp\left(-\frac{\gamma}{T_{i,N_y}}\right)$$

(A.21)

$$\frac{dT_{i,N_y}}{dt}=\left(\frac{T_{i-1,N_y}-2T_{i,N_y}+T_{i+1,N_y}}{\Delta x^2}+\frac{T_{i,N_y-1}-2T_{i,N_y}+1}{\Delta y^2}\right)+\beta\varphi^2 c_{i,N_y}\exp\left(-\frac{\gamma}{T_{i,N_y}}\right)$$

(A.22)

Node $i=N_x,\ j=N_y$ (top right corner)

$$\frac{dc_{N_x,N_y}}{dt}=\mathrm{Le}\left(\frac{c_{N_x-1,N_y}-2c_{N_x,N_y}+1}{\Delta x^2}+\frac{c_{N_x,N_y-1}-2c_{N_x,N_y}+1}{\Delta y^2}\right)-\varphi^2 c_{N_x,N_y}\exp\left(-\frac{\gamma}{T_{N_x,N_y}}\right)$$

(A.23)

$$\frac{dT_{N_x,N_y}}{dt}=\left(\frac{T_{N_x-1,N_y}-2T_{N_x,N_y}+1}{\Delta x^2}+\frac{T_{N_x,N_y-1}-2T_{N_x,N_y}+1}{\Delta y^2}\right)+\beta\varphi^2 c_{N_x,N_y}\exp\left(-\frac{\gamma}{T_{N_x,N_y}}\right)$$

(A.24)

Constant coefficients can be identified in the linear part of the system of discretized equations. Then it is possible to define a constant coefficient matrix that, multiplied by the state variables, allows writing the complete system of equations in the matrix form as in Eq. (5).

Definition of the three parameters *a*, *b* and *d* can ease the construction of the matrices:

$$a=-\frac{1}{\Delta x^2}$$

(A.27)

$$b=-\frac{1}{\Delta y^2}$$

(A.28)

$$d=2\left(a+b\right)$$

(A.29)

Considering the bi-dimensional grid of Fig. A1, that is made up of $N_x \cdot N_y$ nodes, two constant coefficient matrices for the discrete variables are obtained. Namely an $N_x \cdot N_y \times N_x \cdot N_y$ matrix denoted by **A** for the vector state variable **c**, and a matrix denoted by **B**, with the same dimensions of **A**, for the vector state variable **T**.

Matrices **A** and **B** are, respectively, defined as:

$$\mathbf{A} = \begin{array}{c} \begin{matrix} 1 & 2 & \dots & N_x & N_x+1 & N_x+2 & \dots & 2N_x & \dots & \dots & \dots & \dots & N_x\cdot(N_y-1)+1 & N_x\cdot(N_y-1)+2 & \dots & N_x\cdot N_y \end{matrix} \\ \begin{bmatrix} d & -2a & 0 & 0 & -2b & 0 & 0 & 0 & 0 & 0 & 0 & 0 & 0 & 0 & 0 & 0 \\ -a & d & -a & 0 & 0 & -2b & 0 & 0 & 0 & 0 & 0 & 0 & 0 & 0 & 0 & 0 \\ 0 & -a & d & -a & 0 & 0 & -2b & 0 & 0 & 0 & 0 & 0 & 0 & 0 & 0 & 0 \\ 0 & 0 & -a & d & 0 & 0 & 0 & -2b & 0 & 0 & 0 & 0 & 0 & 0 & 0 & 0 \\ -b & 0 & 0 & 0 & d & -2a & 0 & 0 & -b & 0 & 0 & 0 & 0 & 0 & 0 & 0 \\ 0 & -b & 0 & 0 & -a & d & -a & 0 & 0 & -b & 0 & 0 & 0 & 0 & 0 & 0 \\ 0 & 0 & -b & 0 & 0 & -a & d & -a & 0 & 0 & -b & 0 & 0 & 0 & 0 & 0 \\ 0 & 0 & 0 & -b & 0 & 0 & -a & d & 0 & 0 & 0 & -b & 0 & 0 & 0 & 0 \\ 0 & 0 & 0 & 0 & -b & 0 & 0 & 0 & d & -2a & 0 & 0 & -b & 0 & 0 & 0 \\ 0 & 0 & 0 & 0 & 0 & -b & 0 & 0 & -a & d & -a & 0 & 0 & -b & 0 & 0 \\ 0 & 0 & 0 & 0 & 0 & 0 & -b & 0 & 0 & -a & d & -a & 0 & 0 & -b & 0 \\ 0 & 0 & 0 & 0 & 0 & 0 & 0 & -b & 0 & 0 & -a & d & 0 & 0 & 0 & -b \\ 0 & 0 & 0 & 0 & 0 & 0 & 0 & 0 & -b & 0 & 0 & 0 & d & -2a & 0 & 0 \\ 0 & 0 & 0 & 0 & 0 & 0 & 0 & 0 & 0 & -b & 0 & 0 & -a & d & -a & 0 \\ 0 & 0 & 0 & 0 & 0 & 0 & 0 & 0 & 0 & 0 & -b & 0 & 0 & -a & d & -a \\ 0 & 0 & 0 & 0 & 0 & 0 & 0 & 0 & 0 & 0 & 0 & -b & 0 & 0 & -a & d \end{bmatrix} \begin{matrix} 1 \\ 2 \\ \dots \\ N_x \\ N_x+1 \\ N_x+2 \\ \dots \\ 2N_x \\ \dots \\ \dots \\ \dots \\ \dots \\ N_x\cdot(N_y-1)+1 \\ N_x\cdot(N_y-1)+2 \\ \dots \\ N_x\cdot N_y \end{matrix} \end{array}$$

$$\mathbf{B} = \begin{array}{c} \begin{matrix} 1 & 2 & \dots & N_x & N_x+1 & N_x+2 & \dots & 2N_x & \dots & \dots & \dots & \dots & N_x\cdot(N_y-1)+1 & N_x\cdot(N_y-1)+2 & \dots & N_x\cdot N_y \end{matrix} \\ \begin{bmatrix} 0 & 0 & 0 & 0 & 0 & 0 & 0 & 0 & 0 & 0 & 0 & 0 & 0 & 0 & 0 & 0 \\ 0 & 0 & 0 & 0 & 0 & 0 & 0 & 0 & 0 & 0 & 0 & 0 & 0 & 0 & 0 & 0 \\ 0 & 0 & 0 & 0 & 0 & 0 & 0 & 0 & 0 & 0 & 0 & 0 & 0 & 0 & 0 & 0 \\ 0 & 0 & 0 & 0 & 0 & 0 & 0 & 0 & 0 & 0 & 0 & 0 & 0 & 0 & 0 & 0 \\ -b & 0 & 0 & 0 & d & -2a & 0 & 0 & -b & 0 & 0 & 0 & 0 & 0 & 0 & 0 \\ 0 & -b & 0 & 0 & -a & d & -a & 0 & 0 & -b & 0 & 0 & 0 & 0 & 0 & 0 \\ 0 & 0 & -b & 0 & 0 & -a & d & -a & 0 & 0 & -b & 0 & 0 & 0 & 0 & 0 \\ 0 & 0 & 0 & -b & 0 & 0 & -a & d & 0 & 0 & 0 & -b & 0 & 0 & 0 & 0 \\ 0 & 0 & 0 & 0 & -b & 0 & 0 & 0 & d & -2a & 0 & 0 & -b & 0 & 0 & 0 \\ 0 & 0 & 0 & 0 & 0 & -b & 0 & 0 & -a & d & -a & 0 & 0 & -b & 0 & 0 \\ 0 & 0 & 0 & 0 & 0 & 0 & -b & 0 & 0 & -a & d & -a & 0 & 0 & -b & 0 \\ 0 & 0 & 0 & 0 & 0 & 0 & 0 & -b & 0 & 0 & -a & d & 0 & 0 & 0 & -b \\ 0 & 0 & 0 & 0 & 0 & 0 & 0 & 0 & -b & 0 & 0 & 0 & d & -2a & 0 & 0 \\ 0 & 0 & 0 & 0 & 0 & 0 & 0 & 0 & 0 & -b & 0 & 0 & -a & d & -a & 0 \\ 0 & 0 & 0 & 0 & 0 & 0 & 0 & 0 & 0 & 0 & -b & 0 & 0 & -a & d & -a \\ 0 & 0 & 0 & 0 & 0 & 0 & 0 & 0 & 0 & 0 & 0 & -b & 0 & 0 & -a & d \end{bmatrix} \begin{matrix} 1 \\ 2 \\ \dots \\ N_x \\ N_x+1 \\ N_x+2 \\ \dots \\ 2N_x \\ \dots \\ \dots \\ \dots \\ \dots \\ N_x\cdot(N_y-1)+1 \\ N_x\cdot(N_y-1)+2 \\ \dots \\ N_x\cdot N_y \end{matrix} \end{array}$$

The system of equations to be solved becomes:

$$\frac{d}{dt}\mathbf{c} = \mathbf{A}\mathbf{c} + \mathbf{F}_1(\mathbf{c},\mathbf{T})$$

(A.30)

$$\frac{d}{dt}\mathbf{T} = \mathbf{B}\mathbf{T} + \mathbf{F}_2(\mathbf{c}, \mathbf{T})$$

(A.31)

where:

$$\mathbf{c} = [c_{1,1}, c_{2,1}, ..., c_{N_x,1}, c_{1,2}, c_{2,2}, ..., c_{N_x,2}, ..., c_{1,N_y}, c_{2,N_y}, ..., c_{N_x \cdot N_y}]^{\mathrm{T}}$$

(A.32)

$$\mathbf{T} = [T_{1,1}, T_{2,1}, ..., T_{N_x,1}, T_{1,2}, T_{2,2}, ..., T_{N_x,2}, ..., T_{1,N_y}, T_{2,N_y}, ..., T_{N_x \cdot N_y}]^{\mathrm{T}}$$

(A.33)

Although the two set of differential equations are written separately to simplify both the discussion and the code development, the derived equations are coupled by the nonlinear terms $\mathbf{F}_1$ and $\mathbf{F}_2$, and for this reason must be solved simultaneously.

5.2 Assessing the effect of variable ambient temperature on the self-ignition of a reaction-diffusion system employing a reduced-order modelling methodology[6]

Enrico A. Cutillo[a,*], Katarzyna Bizon[b] and Gaetano Continillo[a]

[a]Dipartimento di Ingegneria, Univeristà degli studi del Sannio, Piazza Roma 21, Benevento, Italia
[b]Faculty of Chemical Engineering and TechnologyCracow University of Technology, Kraków, Poland
cutillo@unisannio.com

The system under study in this work is a self-igniting pile of solid material. To predict and understand the effect of steep changes of the state variables on such systems, a reaction-diffusion model is employed. These systems can exhibit complex oscillatory behaviour, and changes in ambient conditions over time may strongly impact the inherent oscillations. To simulate the unsteady evolution of the pile, both a classical numerical technique (method of lines) and a reduced-order approach are employed in combination with a stiff ODE solver. To account for circadian fluctuations in temperature, time-variable boundary conditions are assumed upon formulating the problem. The reduced-order model is introduced in view of understanding if an approximated formulation characterized by a much lower number of state variables can accurately predict the complex behaviour of the system even in the case of sudden, steep variations of the values of the state variables due to the phenomenon of self-ignition, intensified here by variable boundary conditions. The selected case studies have the goal of exploring the effect of stockpile properties on the self-ignition phenomenon. Numerical solutions show the anticipated coupling between the system intrinsic dynamics and the oscillating temperature imposed at the boundary. All the analysed cases are accurately replicated by the reduced-order model.

5.2.1 Introduction

Spontaneous ignition is a phenomenon whose danger must be carefully foreseen with a view to its prevention, to reduce the risk of material and economic losses in the storage of porous flammable materials. Today, storage of solid materials can be relevant to many industries. Traditional production processes such as energy production from coal, biobased processes where fossil sources are replaced by biomass (Thorenz et al., 2018), or waste treatment plants (Zambra et al., 2011), share the need of handling and storing porous flammable materials. The problem of spontaneous combustion and even explosion can also arise in the agricultural or food industry (Medic Pejic et al., 2015). Non-linear dynamical systems are often

[6] Published in: *Chemical Engineering Transactions* 99 (2023): 523-528.
https://doi.org/10.3303/CET2399088

employed to study and anticipate the occurrence of such unwanted phenomena via numerical simulations (Fu et al., 2021). In this study, the reaction-diffusion model adopted in Continillo et al. (2000), is used to investigate the effects of ambient temperature variations. To describe the spatial and temporal evolution of these initial-boundary value problem, finite difference approximations of spatial derivatives may be utilized, which feature a high number of discretization nodes, that are required to maintain a high level of accuracy even in the presence of steep changes in the state variables, either spatially or temporally, as occurs in the self-combustion of a solid stack (Cutillo et al., 2023). In this context, Reduced-Order Models (ROMs) are paramount to enable sound design and optimization activities of such high dimensional and computationally expensive systems (Jain et al., 2017). The methodology of model order reduction has been shown to be both fast and accurate in a variety of applications, ranging from aerodynamics (Krath et al., 2021) to chemical engineering problems (Bizon and Continillo, 2021a; Continillo et al., 2000). In this work it is shown how knowing non-trivial information about the system, such as the influence of the dimensionless activation energy γ upon the dynamics of the system, can help in deriving reduced-order models that are valid even outside of the parameter value domains for which they are built. In fact, if properly constructed, ROMs that are based on original physical models can predict system behaviour in areas of parameter space that were not explored during the model's development. In this study, a ROM based on Proper Orthogonal Decomposition (POD) and Galerkin projection is developed and utilized to simulate the impact of temperature changes on self-ignition phenomena.

5.2.2 Mathematical model and computational methods

- *Mathematical model of a self-igniting pile*

The problem of self-ignition of a stockpile is formulated under the following assumptions (Continillo et al., 2000): The lower side of the pile is in contact with the ground, while the upper side is exposed to ambient conditions. Given that the physical and geometrical properties of the pile in the horizontal directions are assumed constant, a one-dimensional model is appropriate to describe the problem. To account for reactant transport inside the porous medium, Fickian diffusion of the gas is considered. The chemical reaction between the reactant and the solid fuel is modelled using a first-order kinetic. The temperature dependence of the reaction rate is described using the classical Arrhenius exponential expression. Gas- and solid-phase are assumed to be in local thermal equilibrium, resulting

in a single energy balance equation. In addition, neglecting solid material consumption leads to the use of only one mass balance equation. Based on these assumptions, the problem is expressed using the following dimensionless model equations:

$$\frac{\partial c}{\partial t} = Le \frac{\partial^2 c}{\partial x^2} - \Phi^2 c \exp\left(-\frac{\gamma}{T}\right) \tag{1}$$

$$\frac{\partial T}{\partial t} = \frac{\partial^2 T}{\partial x^2} + \beta \Phi^2 c \exp\left(-\frac{\gamma}{T}\right) \tag{2}$$

The associated boundary and initial conditions are:

$$T(0,t) = A\sin(\omega t), \quad T(1,t) = 1, \quad c(0,t) = 1, \quad \left.\frac{\partial c}{\partial x}\right|_{x=1} = 0 \quad \text{for } t > 0 \tag{3}$$

$$T(x,0) = T_{ss}, \quad c(x,0) = c_{ss} \quad \text{for } x \in [0,1] \tag{4}$$

Following the work of Zambra et al., 2011), who analysed a pile of composting material under variable ambient conditions, the naturally occurring temperature oscillations throughout the day and night are formulated in this work using a sinusoidal boundary condition, as reported in Equation 3. The above system of partial differential equations is solved applying the finite difference method. Particularly, the discretization nodes employed in this study are N=200. The resulting system of ordinary differential equations (ODEs) is called Full Order Model (FOM) and is solved with a stiff ODE solver available in MATLAB (‘*ode15s’*).

- *Reduced-order model formulation*

The methodology employed in this work to build the reduced-order model is known as Proper Orthogonal Decomposition (Holmes et al., 1996) and can be seen as a method to extract the most important information about the dynamics of the system and to use that information to build a set of empirical basis functions that allow an efficient approximation of the state variables of the system. This method is based on the collection of experimental observations that in the case of this work come from numerical simulations performed with the FOM and will be referred to as snapshots. In general, it is recommendable that the experimental or simulation data coming from the FOM be chosen as representative of all different observed dynamic behaviours.

In this work, the set of snapshots chosen to build the ROM are sampled using a uniform sampling strategy. The snapshots are then collected in the following matrix: y(x,ti), x=[x1, x2, …,xn], i = 1, …, M (note that, for simplicity, the dependencies of y will not be indicated

in the following). To derive the set of empirical basis functions, the following eigenvalue problem is solved (Holmes et al., 1996):

$$C\Phi = \lambda C \tag{5}$$

where:

$$C = \left\langle \mathbf{y}\,\mathbf{y}^{\mathrm{T}} \right\rangle \tag{6}$$

is the correlation matrix and $\langle \cdot \rangle$ denotes an arithmetic mean of the standard inner product of the snapshot matrix. Then, the truncated state variables are expressed as a linear combination of a sub-set of first K determined basis functions:

$$\mathbf{y} = \sum_{j=1}^{K} a_j(t_i)\Phi_j(\mathbf{x}) \tag{7}$$

The POD method allows to extract N basis function, but only the most relevant are employed to build the reduced-order model. In fact, the basis function associated with the highest eigenvalues carries most of the information about the system dynamics. For this reason, it is possible to approximate the state variable with only K << N POD functions, leading to the desired reduction in the dimension of the original system. Following a previous work (Cutillo et al., 2023), the set of snapshots was sampled for values of the parameter γ equal to 11 and 13. These two values are located in the vicinity of a region of the parameter space where the system has chaotic behaviour, as earlier reported in Continillo et al. (2000). The choice of sampling the FOM solutions for these two parameter values stems from the fact that two fundamental pieces of information can be derived from the evolution of the state variables. The first is the characteristic behaviour of an ignition event with a subsequent stationary state, the second is the characteristic behaviour of an ignition event leading to a stable limit cycle. After sampling, the reduced-order model was built and, particularly, 11 modes were chosen for the approximation of the state variables. In this way, the original system with 400 differential equations was reduced to 22 differential equations. Like with the FOM, the reduced-order model was also solved using the method of lines, through the same stiff integrator in MATLAB (‘*ode15s*’).

5.2.3 Results and discussion

- *Key parameter values*

Although the model employed in this work was originally derived for simulating coal stockpiles, its crucial kinetic parameters can be adjusted to forecast the self-ignition of a

variety of materials used across multiple industries, including biomass. It is important to consider the potential implications of changing these parameters before using the model for new materials, for this reason the selection of parameter values used in the simulation was made with the goal of representing realistic materials and ambient conditions. The parameter values reported in Table 1 are typical of lignin-rich biomass such as the one studied in (Bach et al., 2017). Lignocellulosic biomass, in particular, is gaining attention as it is one of the key components of second-generation biofuels (De Blasio et al., 2022). Meanwhile, the values used in this study for the combustion enthalpy were taken from the research conducted by Krigstin and Wetzel (2016). The frequency of the oscillating temperature at the top boundary has been chosen to represent circadian oscillation; being a dimensionless variable, its value depends on L (the pile height), and its value can be computed as $\omega=2\pi L^2/(86400\cdot\alpha)$. For the other dimensionless variables, reference can be made to Continillo et al. (2000).

Table 1: Dimensionless and dimensional parameters employed

Parameter	Value	Parameter	Value
Φ^2	[0.45, 6.5]·10^5	D	$5\cdot10^{-5}$
β	[4.5-4.67]	α	$1.8\cdot10^{-4}$
γ	[13-17]	ω	0.396
Le	0.2722	ε	0.3
ΔH	[1.8, 2.0]·10^5	L	[0.8, 3]
E_a	[3.25, 4.25]·10^5	A	20

- *Simulation results*

The studied system can exhibit complex behaviour even without external variable forcing. In fact, Figure 1 shows the evolution of the system when a constant temperature value is applied to the outer boundary. The dimensionless parameter values used in the analyzed simulation are: $\Phi^2 = 5.9529\cdot10^5$, β = 4.5, γ= 17.0386, Le = 0.27, which are compatible with the following dimensional parameter values: ΔH = 1.88·105, E_a = 4.25·104, L = 2.9, while the other values are reported in Table 1. As it can be observed, after the transient regime has extinguished, the system starts oscillating around what is called a chaotic attractor. This regime is characterized by aperiodic behaviour that is strongly dependent on the initial

conditions. Although this behaviour has been already predicted in Continillo et al. (2000), in the cited work the simulations were carried out for different values of the parameters, that were representative of a coal stockpile, whereas in this work are characteristic of a stockpile of woody biomass. Because of the hypothesis made in deriving the model, such as: the consumption of the solid fuel is neglected; the properties of the pile are constant during the time of the simulation, while the concentration of oxidant is constant at the top of the domain; it is seen that the consumption of reactant caused by combustion is followed by a new build-up, and so on. This phenomenon can be found in the literature under the name of relaxation-oscillation regime, in which extremely slow build-up is followed by a sudden discharge (Strogatz, 2018). In systems characterized by relaxation-oscillation phenomena, the boundary conditions define the range of possible solutions that can be challenging in terms of numerical stability, and this of course can affect the applied method of the Proper Orthogonal Decomposition for the construction of the Reduced-Order Model. As seen in the following results, a change in boundary conditions can also affect the amplitude and frequency of the oscillations. When the boundary conditions are changed, the system may switch from an oscillatory to a non-oscillatory state or can switch between oscillatory states characterized by different amplitudes and frequency. For this reason, time-dependent boundary conditions have a significant impact on the behaviour of dynamic systems that exhibit relaxation-oscillation phenomena.

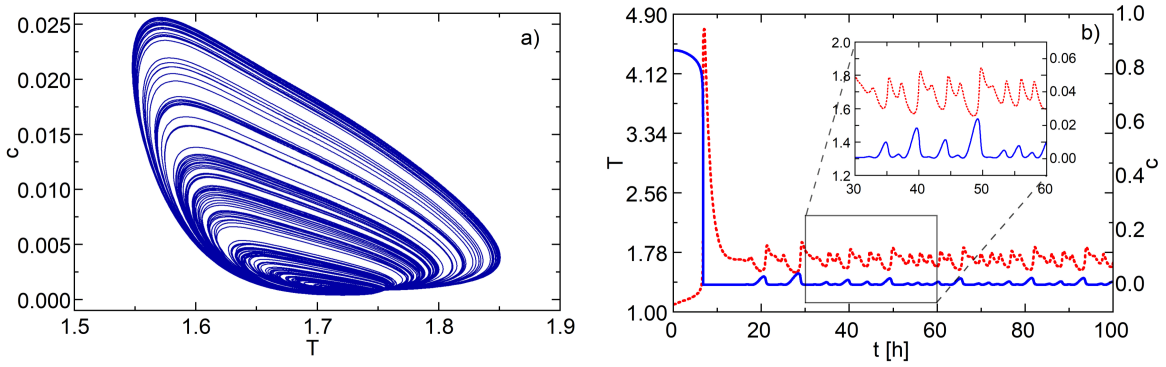

Figure 1: Chaotic orbit (a) and time series (b) representative of the evolution of the concentration and the temperature inside the porous matrix. The data is sampled at the middle of the domain (x = 0.5).

Figure 2 shows that, after forcing the system with sinusoidal boundary conditions, its dynamic behaviour switches from chaotic to more regular periodic oscillations, featuring

much larger bursts of peak temperature, resulting in more violent ignition phenomena, as opposed to the low amplitude oscillations that can be found without the periodic forcing, shown earlier in Figure 1b. Figure 2a shows how the "stresses" accumulated during the slow build-up are released during the sudden "discharge". Here, the "stress" is the concentration of reactant that accumulates within the porous matrix, resulting in a sudden "discharge" when the explosion happens. Figure 2a shows that the build-up takes almost 3 days. The occurring phenomenon can be visualized better by looking at Figure 2b, where snaps of the spatiotemporal evolution of temperature and concentration are reported.

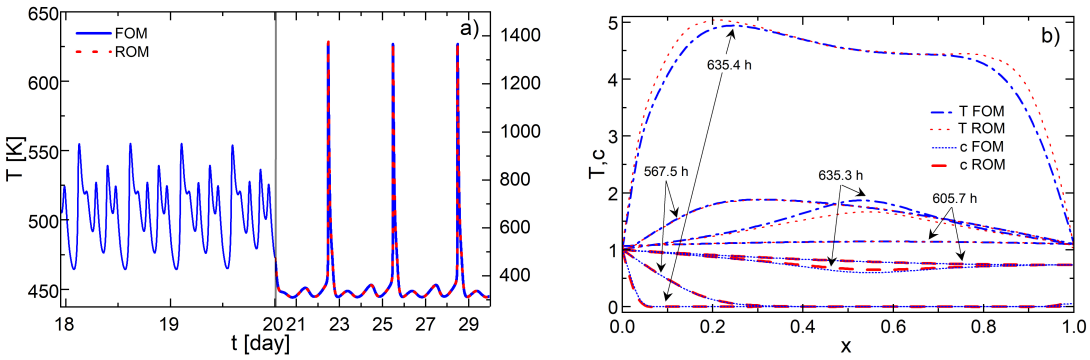

Figure 2: Temperature evolution at the middle of the domain before and after oscillating boundary condition are considered, mimicking circadian temperature variations (a), and state variables profiles along the domain in four different salient moments.

The first snapshot is taken at 567.5 h (or 23.64 days) from the beginning of time. Here the system has already gone through an ignition phenomenon (as it can be seen from Figure 2a): both temperature and concentration are decreasing inside the domain. This decrease is followed by a new, slow build up, as can be seen from the snap at 605.7 h (25.24 days). After this state, it takes almost 30 h for the system to achieve the right combination of temperature and concentration that allow for the combustion event to newly occur. At 635.3 h the combustion starts at the middle of the domain, and in less than 0.1 h (6 minutes), the front of the flame has spread throughout the whole domain, consuming the accumulated oxygen. Figure 2a reports the evolution of the system before and after the sinusoidal forcing is applied. After the forcing, the system is simulated both by the FOM and the ROM. In this case study, as emphasized by the overlapping curves, the ROM appropriately reproduces the dynamic behaviour analysed, which is remarkable if one thinks that this data-driven model has been built from solutions of the FOM derived with the hypothesis of constant boundary condition. Clearly, this accuracy arises from the fact that the Reduced-Order Model (built

from the original first principles model), maintains key information about the system dynamics.

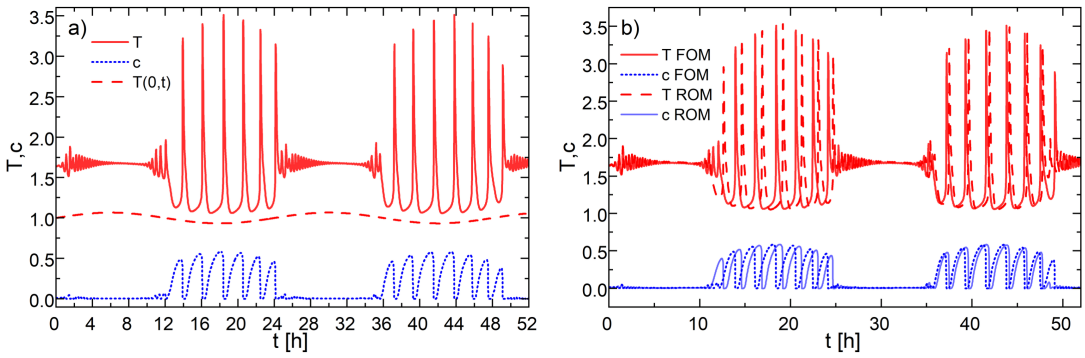

Figure 3: Time series representative of the evolution of the state variables inside the porous matrix. Comparison of FOM results with the time-varying boundary condition (a) and FOM with ROM (b). The data is sampled in a point at the middle of the domain (x = 0.5).

While keeping the oscillating boundary temperature, the behaviour of the system can drastically change as the values of the parameters of interest are varied. In fact, the results of the simulation reported in Figure 3 are obtained for the following values of the parameters: φ^2 = 4.5302·104, γ= 12.9894, which are compatible with the following dimensional parameter values: ΔH = 1.88·105, E_a = 3.24·104, L = 0.8, while maintaining constant the other parameters. Figure 3 shows that, in this case, self-ignition phenomena happen more frequently: taking as reference the oscillating boundary condition (reported as the dashed curve in Figure 3a), during one period of the sinusoidal boundary condition there are between six and seven combustion events which are followed by low amplitude and high frequency temperature and concentration oscillations. Moreover, the most energetic combustion events take place when the boundary temperature reaches its minimum. This is caused by the fact that, in this case, the concentration of oxidiser in the first layers of the pile cannot drop below the critical level of self-ignition because the lower temperature of the “night” inhibits the consumption of reactant in the first layer of the domain; hence the reactant is capable of filling the pile and self-ignite. During ignition, the combustion fronts travel along the domain. At the top of the domain the pile is already at low temperature, while in the bottom of the domain the pile is still violently burning. The concentration of the reactant keeps building up in the first layers and, as the combustion event is ended, a new one can start. Thus, multiple ignitions are observed during one night. As the temperature rises (during the day) the concentration no longer has the possibility to build up inside the pile and, for this

reason, impulsive combustion cannot be observed. With these parameter values the ROM appears to be less accurate than the previous case, and in fact the curves are not overlapped anymore but, as clearly shown in Figure 3b, the behaviour of the system is still well depicted in terms of frequency and amplitude of the oscillations of the state variables. The error between FOM and ROM is due to a phase shift, that is characteristic of ROMs built with POD method when they are used for the simulation of periodic regimes (Bizon et al., 2008).

5.2.5 Conclusions

The size chosen for the system under study does not require high computational costs for its numerical resolution, and this allowed to evaluate the performance of the ROMs under various conditions. Particularly, the reduced model was formulated in view of understanding what would happen if time-dependent boundary conditions were simulated, mimicking circadian phenomena, on top of relaxation-oscillation phenomena occurring with constant boundary conditions. This in some cases enhanced extreme ignition phenomena that might affect numerical stability: in this respect, the MATLAB *ode solver*, in association with the model reduction technique developed, proved robust and reliable. The system dynamics was shown to be clearly influenced by varying boundary conditions, and several parameter values, chosen as characteristic of second-generation biofuels, were investigated, and the system behaviour was described quantitatively (through the simulations) and physically (giving a physical explanation of the observed phenomenon). Particularly, the relaxation-oscillation behaviour has been found and described in the neighbourhood of chaotic solutions. Simulations results show that the non-stationary character of burning piles (i.e. braziers, stored biomasses, charcoal) already emerges from a simple reaction-diffusion model that neglects most of the real system complexity. Thanks to the ROM, it was possible to accurately reproduce the results of the classical model applied in the literature, with a reduction of the systemic order of magnitude (going from 400 equations to 22) with obvious savings in CPU time. The work will serve as a basis for extending the analysis to more complex systems, such as 2D or 3D domains, which may represent the fuel stack more accurately. It is expected that, in addition to the reduction in the system, significant savings in CPU time will allow the model to be applied to solve computationally onerous problems, such as parametric analysis, optimization or control studies, with a view to predicting and reducing the risks these systems pose in terms of economic or material losses.

Nomenclature

c – dimensionless reactant concentration, -

T – dimensionless temperature, -

φ – thermal Thiele modulus, -

Le – Lewis number, -

β – dimensionless heat reaction, -

γ – dimensionless activation energy, -

t – dimensionless time, -

L – layer thickness, m

D – mass diffusivity, m2/s

α – thermal diffusivity, m2/s

ΔH – enthalpy of reaction, J/mol

Ea – activation energy, J/mol

ε – porosity, -

cp – specific heat, kJ/(kg·K)

A – amplitude of circadian oscillations, -

ω – angular velocity of circadian oscillations, -

y – snapshots matrix, -

x – discretized coordinate vector, -

M – number of time samples, -

Φ – set of basis functions, -

a_j – modal coefficients, -

λ – eigenvectors associated with basis functions, -

N – number of discretization nodes, -

K – truncation order of the state variables, -

C – correlation matrix, -

Conclusions

This thesis has addressed the analysis, simulation, and optimization of reactive and adsorptive systems. It introduced reduced-order modeling techniques, with particular emphasis on methane reactors and self-ignition systems. The results consistently demonstrate that reduced-order methodologies, particularly those based on Proper Orthogonal Decomposition (POD) and POD-DEIM strategies, provide an effective and reliable framework for handling the intrinsic complexity of nonlinear, spatially distributed systems while substantiually reducing the computational effort.

A first major outcome concerns the dynamical characterization of an adiabatic fixed-bed methanation reactor with mass recycle. The identification of periodic oscillations arising from a Hopf bifurcation clarified the interplay between recycle-induced feedback and the inverse response typical of fixed-bed reactors. The analysis of inlet temperature and recycle ratio highlighted how operating conditions shape the global dynamics of the reactor, with direct implications for plant design and control. Building upon this understanding, the development of a reduced order model (ROM) for the same methanation reactor represented a substantial methodological advancement. The ROM allowed the reduction ot the system dimensions by one order of magnitude (from 1200 to 210 ODEs) while preserving the essential features of both stationary and periodic regimes with relative errors of the order of 10^{-3}. Speedups of 15 for steady-state solutions and 5 for periodic regimes were achieved, confirming that the reduced model retains the accuracy of the original high dimensional model while enabling significantly faster simulations. These results strongly support the use of ROMs as enabling tools for real-time control, parametric studies, and future extensions to more complex two-dimensional reactor descriptions.

The reduced order framework also proved highly valuable in the optimal structuring of non-isothermal fixed-bed reactors. In the context of process integration, the POD-ROM methodology allowed the exploration of bi-functional catalyst distribution at the pellet scale while lowering the computational costs. Although a relatively large number of POD modes was required to ensure accuracy, the approach enabled the practical assessment of design alternatives that would otherwise be computationally onerous. The adoption of optimal catalyst distribution was shown to enhance reactor performance and production efficiency,

demonstrating that model reduction is not merely a computational shortcut but a strategic enabler for reactor design and optimization

The numerical investigation of CO_2 adsorption in a hybrid fixed bed, composed of spatially arranged adsorbent and catalyst, highlighted the critical role of structural design and thermal management in improving adsorption performance. The two-dimensional model, accounting for both axial and radial gradients, demonstrated that alternating layers or physical mixtures of adsorbent and catalyst outperform standard adsorption beds in terms of breakthrough time and sorption capacity. The improvement was attributed to the higher thermal conductivity and heat capacity of the catalyst, which acts as a distributed heat sink, moderating the exothermic heat release during adsorption.

The optimization of radially nonuniform material distributions further showed that placing more catalyst near the reactor wall significantly enhances heat removal, thereby extending breakthrough time and increasing sorption capacity. The ability to shape the intensity and propagation of the heat wave through material distribution opens new possibilities for integrated adsorption-reaction processes, especially in cyclic CO_2 methanation systems.

However, the two-dimensional nature of the model makes optimization computationally demanding, despite the use of the open-source "*ADiGator*" package developed in MATLAB which allowed to numerically calculate a sparse Jacobian, significantly reducing the computational time. In this context, the reduced order modeling approach developed in this thesis emerges as a key enabler for future work. Extending POD-ROM or POD-DEIM methodologies to 2-D hybrid reactor models would allow efficient optimization of the full adsorption-reactive regeneration cycle, where sorption capacity and CO_2 conversion must be balanced. Such an approach would make feasible large-scale parametric analyses and structural optimization studies that are currently limited by computational costs, thereby accelerating the rational design of thermally managed hybrid reactors.

The development of data-driven surrogate models based on Artificial Neural Networks (ANN) and Kriging techniques demonstrated that multicomponent adsorption equilibria can be accurately approximated across varying thermodynamic conditions. These models provide a flexible and computationally efficient alternative to traditional thermodynamic formulations, especially when dealing with complex gas mixtures relevant to flue gas treatment or biogas upgrading.

The integration of data-driven models with first-principles dynamic models represents a promising hybrid modeling strategy. By replacing computationally expensive equilibrium calculations with accurate surrogates, the overall simulation burden of cyclic adsorption-reaction systems can be significantly reduced. This approach lays the foundation for efficient modeling of dual-function sorbent-catalyst reactors for CO_2 sequestration and methanation, enabling more comprehensive process simulations and optimization studies. The synergy between reduced order modeling and machine-learning-based surrogates constitutes a powerful paradigm for next-generation reactor modeling.

The self-ignition studies on two-dimensional reaction-diffusion systems further validated the robustness and efficiency of reduced order methodologies in highly nonlinear and oscillatory regimes. The system exhibited complex dynamical behavior, including oscillations and bifurcation phenomena, making full-order simulations computationally expensive. The adoption of POD-Galerkin models already provided significant acceleration, but the incorporation of the Discrete Empirical Interpolation Method (DEIM) proved decisive in further reducing computational cost by limiting the online evaluation of nonlinear terms.

The combination of DEIM with an optimized snapshot selection strategy based on k-means clustering yielded stable and accurate reduced models, capable of reproducing even bifurcation points with quantitative and qualitative agreement with the full model. A speedup of more than three orders of magnitude (≈1020) was achieved, demonstrating the dramatic impact of DEIM in nonlinear systems. Moreover, in the study of variable ambient temperature effects, the ROM reduced the system size from 400 to 22 equations while preserving accuracy and numerical robustness, enabling efficient exploration of time-dependent boundary conditions and relaxation-oscillation phenomena.

Overall, the self-ignition works confirm that the careful treatment of nonlinearities through DEIM is essential for achieving substantial computational savings without sacrificing stability or predictive capability. These findings reinforce the broader conclusion of the thesis: reduced order modeling - especially when combined with advanced sampling strategies and nonlinear approximation techniques - constitutes a powerful and versatile tool for the simulation, optimization, and control of complex reactive and adsorptive systems.

In summary, the thesis demonstrates that reduced order modeling is not only an effective strategy for accelerating simulations of methane reactors and reactive-adsorptive systems, but also a foundational methodology for enabling structural optimization, and advanced

dynamical analysis. The integration of physics-based reduction techniques with data-driven surrogates and nonlinear interpolation methods paves the way for computationally tractable, yet physically faithful, modeling of increasingly complex energy and environmental processes.

Bibliography

Abdul Kareem, F. A., Shariff, A. M., Ullah, S., Keong, L. K., and Mellon, N. (2018). Total and partial uptakes of multicomponent vapor-gas mixtures on 13X zeolite at 343K: Experimental and modeling study. *Microporous and Mesoporous Materials*, *258*, 95–113. https://doi.org/https://doi.org/10.1016/j.micromeso.2017.09.004

Adler, J., and Enig, J. W. (1964). The critical conditions in thermal explosion theory with reactant consumption. *Combustion and Flame*, *8*(2), 97–103. https://doi.org/10.1016/0010-2180(64)90035-5

Adrover, A., Cerbelli, S., and Giona, M. (2002). A spectral approach to reaction/diffusion kinetics in chaotic flows. *Computers and Chemical Engineering*, *26*(1), 125–139. https://doi.org/10.1016/S0098-1354(01)00761-X

Adrover, A., Continillo, G., Crescitelli, S., Giona, M., and Russo, L. (2000). Wavelet-like collocation method for finite-dimensional reduction of distributed systems. *Computers and Chemical Engineering*, *24*(12), 2687–2703. https://doi.org/10.1016/S0098-1354(00)00621-9

Adrover, A., and Giona, M. (2003). Modal reduction of PDE models by means of Snapshot Archetypes. *Physica D: Nonlinear Phenomena*, *182*(1–2), 23–45. https://doi.org/10.1016/S0167-2789(03)00120-9

Ali Abd, A., Roslee Othman, M., Helwani, Z., and Kim, J. (2024). An overview of biogas upgrading via pressure swing adsorption: Navigating through bibliometric insights towards a conceptual framework and future research pathways. *Energy Conversion and Management*, *306*, 118268. https://doi.org/10.1016/J.ENCONMAN.2024.118268

Amsallem, D., and Farhat, C. (2012). Interpolation Method for Adapting Reduced-Order Models and Application to Aeroelasticity. *Https://Doi.Org/10.2514/1.35374*, *46*(7), 1803–1813. https://doi.org/10.2514/1.35374

Amsallem, D., Farhat, C., and Lieu, T. (2007). Aeroelastic analysis of F-16 and F-18/A configurations using adapted CFD-based reduced-order models. *Collection of Technical Papers - AIAA/ASME/ASCE/AHS/ASC Structures, Structural Dynamics and Materials Conference*, *8*(April), 7943–7962. https://doi.org/10.2514/6.2007-2364

Antoulas, A. C., Ionutiu, R., Martins, N., ter Maten, E. J. W., Mohaghegh, K., Pulch, R., Rommes, J., Saadvandi, M., and Striebel, M. (2015). Model Order Reduction: Methods, Concepts and Properties. In M. Günther (Ed.), *Coupled Multiscale Simulation and Optimization in Nanoelectronics* (pp. 159–265). Springer Berlin Heidelberg. https://doi.org/10.1007/978-3-662-46672-8_4

Astrid, P. (2004). *Reduction of process simulation models : a proper orthogonal decomposition approach*. https://doi.org/10.6100/IR581728

Aversano, G., Bellemans, A., Li, Z., Coussement, A., Gicquel, O., and Parente, A. (2019). Application of reduced-order models based on PCA and Kriging for the development of digital twins of reacting flow applications. *Computers and Chemical Engineering*, *121*, 422–441. https://doi.org/https://doi.org/10.1016/j.compchemeng.2018.09.022

Azizi, Z., Rezaeimanesh, M., Tohidian, T., and Rahimpour, M. R. (2014). Dimethyl ether: A review of technologies and production challenges. *Chemical Engineering and Processing: Process Intensification*, *82*, 150–172. https://doi.org/10.1016/J.CEP.2014.06.007

B. R. Nogueira, I., V. Santana, V., Ribeiro, A. M., and Rodrigues, A. E. (2022). Using scientific machine learning to develop universal differential equation for multicomponent adsorption separation systems. *The Canadian Journal of Chemical Engineering*, *100*(9), 2279–2290. https://doi.org/https://doi.org/10.1002/cjce.24495

Bach, Q. V., Tran, K. Q., and Skreiberg, Ø. (2017). Combustion kinetics of wet-torrefied forest residues using the distributed activation energy model (DAEM). *Applied Energy*, *185*, 1059–1066. https://doi.org/10.1016/j.apenergy.2016.02.056

Bareschino, P., Cutillo, A. E., Tregambi, C., Pepe, F., Continillo, G., and Mancusi, E. (2022a). Periodic Oscillations in Methane Reactor: Effects of the Main Operating Parameters. *Computer Aided Chemical Engineering*, *51*, 1–6. https://doi.org/10.1016/B978-0-323-95879-0.50001-1

Bareschino, P., Cutillo, A. E., Tregambi, C., Pepe, F., Continillo, G., and Mancusi, E. (2022b). Periodic Oscillations in Methane Reactor: Effects of the Main Operating Parameters. *Computer Aided Chemical Engineering*, *51*, 1–6. https://doi.org/10.1016/B978-0-323-95879-0.50001-1

Bareschino, P., Mancusi, E., Tregambi, C., Pepe, F., Urciuolo, M., Brachi, P., and Ruoppolo, G. (2021). Integration of biomasses gasification and renewable-energies-driven water electrolysis for methane production. *Energy*, *230*, 120863. https://doi.org/https://doi.org/10.1016/j.energy.2021.120863

Bareschino, P., Mancusi, E., Urciuolo, M., Paulillo, A., Chirone, R., and Pepe, F. (2020). Life cycle assessment and feasibility analysis of a combined chemical looping combustion and power-to-methane system for CO2 capture and utilization. *Renewable and Sustainable Energy Reviews*, *130*(November 2019), 109962. https://doi.org/10.1016/j.rser.2020.109962

Bárkányi, Á., Chován, T., Németh, S., and Abonyi, J. (2021). Modelling for Digital Twins—Potential Role of Surrogate Models. *Processes 2021, Vol. 9, Page 476*, *9*(3), 476. https://doi.org/10.3390/PR9030476

Barrault, M., Maday, Y., Nguyen, N. C., and Patera, A. T. (2004). An 'empirical interpolation' method: application to efficient reduced-basis discretization of partial differential equations. *Comptes Rendus Mathematique*, *339*(9), 667–672. https://doi.org/10.1016/J.CRMA.2004.08.006

Bates, S. J., Sienz, J., and Langley, D. S. (2003). Formulation of the Audze–Eglais Uniform Latin Hypercube design of experiments. *Advances in Engineering Software*, *34*(8), 493–506. https://doi.org/10.1016/S0965-9978(03)00042-5

Ben-Mansour, R., Abuelyamen, A., and Qasem, N. A. A. (2020). Thermal design and management towards high capacity CO2 adsorption systems. *Energy Conversion and Management*, *212*, 112796. https://doi.org/10.1016/J.ENCONMAN.2020.112796

Benner, P., and Breiten, T. (2015). Two-Sided Projection Methods for Nonlinear Model Order Reduction. *SIAM Journal on Scientific Computing*, *37*(2), B239–B260. https://doi.org/10.1137/14097255X

Benner, P., Goyal, P., and Gugercin, S. (2018). H2-Quasi-Optimal Model Order Reduction for Quadratic-Bilinear Control Systems. *SIAM Journal on Scientific Computing*, *39*(2), 983–1032. https://doi.org/10.1137/16M1098280

Benner, P., Grivet-Talocia, S., Quarteroni, A., Rozza, G., Schilders, W., and Silveira, L. M. (2021). *1 Model order reduction: basic concepts and notation* (P. Benner, S. Grivet-Talocia, A. Quarteroni, G. Rozza, W. Schilders, and L. M. Silveira, Eds.; pp. 1–14). De Gruyter. https://doi.org/doi:10.1515/9783110498967-001

Bischoff, K. B. (1967). An extension of the general criterion for importance of pore diffusion with chemical reactions. *Chemical Engineering Science*, *22*(4), 525–530. https://doi.org/10.1016/0009-2509(67)80035-6

Bizon, K. (2010). *Spectral reduction of numerical models of combustion processes* (Marek. P. Berezowski, Gaetano. P. Continillo, R. A. R. Białecki, Bolesław. R. Tabiś, and Jan. R. Thullie, Eds.). http://repolis.bg.polsl.pl/dlibra/publication/edition/56935

Bizon, K. (2017). Assessment of a POD method for the dynamical analysis of a catalyst pellet with simultaneous chemical reaction, adsorption and diffusion: Uniform temperature case. *Computers and Chemical Engineering*, *97*, 259–270. https://doi.org/10.1016/J.COMPCHEMENG.2016.11.009

Bizon, K. (2023). A journey from mechanistic to data-driven models in process engineering: dimensionality reduction, surrogate and hybrid approaches, and digital twins. *Chemical and Process Engineering: New Frontiers*, *44*(No 3 (24th Polish Conference of Chemical and Process Engineering, 13-16 June 2023, Szczecin, Poland. Guest editor: Prof. Rafał Rakoczy and 8th European Process Intensification Conference, 31.05–2.06.2023, Warsaw, Poland.)), e24. https://doi.org/10.24425/cpe.2023.146726

Bizon, K., and Continillo, G. (2012). Reduced order modelling of chemical reactors with recycle by means of POD-penalty method. *Computers and Chemical Engineering*, *39*, 22–32. https://doi.org/10.1016/j.compchemeng.2011.10.001

Bizon, K., and Continillo, G. (2019). Determination of the optimal distribution of active centers in a multifunctional catalyst pellet using global searching combined with reduced-order modeling approach. In A. A. Kiss, E. Zondervan, R. Lakerveld, and L. Özkan (Eds.), *29th European Symposium on Computer Aided Process Engineering* (Vol. 46, pp. 1015–1020). Elsevier. https://doi.org/https://doi.org/10.1016/B978-0-12-818634-3.50170-3

Bizon, K., and Continillo, G. (2020). Optimal Design of a Non-isothermal Hybrid Catalyst Pellet based on POD-DEIM Reduced-order Methodology. *Computer Aided Chemical Engineering*, *48*, 271–276. https://doi.org/10.1016/B978-0-12-823377-1.50046-X

Bizon, K., and Continillo, G. (2021a). Efficient optimization of a multifunctional catalytic fixed-bed reactor via reduced-order modeling approach. *Chemical Engineering Research and Design*, *165*, 214–229. https://doi.org/10.1016/j.cherd.2020.11.007

Bizon, K., and Continillo, G. (2021b). Efficient optimization of a multifunctional catalytic fixed-bed reactor via reduced-order modeling approach. *Chemical Engineering Research and Design*, *165*, 214–229. https://doi.org/10.1016/j.cherd.2020.11.007

Bizon, K., Continillo, G., Berezowski, M., and Smua-Ostaszewska, J. (2012a). Optimal model reduction by empirical spectral methods via sampling of chaotic orbits. *Physica D: Nonlinear Phenomena*, *241*(17), 1441–1449. https://doi.org/10.1016/J.PHYSD.2012.05.004

Bizon, K., Continillo, G., Berezowski, M., and Smua-Ostaszewska, J. (2012b). Optimal model reduction by empirical spectral methods via sampling of chaotic orbits. *Physica D: Nonlinear Phenomena*, *241*(17), 1441–1449. https://doi.org/10.1016/j.physd.2012.05.004

Bizon, K., Continillo, G., Berezowski, M., and Smua-Ostaszewska, J. (2012c). Optimal model reduction by empirical spectral methods via sampling of chaotic orbits. *Physica D: Nonlinear Phenomena*, *241*(17), 1441–1449. https://doi.org/10.1016/j.physd.2012.05.004

Bizon, K., Continillo, G., Cutillo, E. A., and D'Onofrio, A. (2021). A POD-ROM Methodology for Optimal Structuring of a Non-isothermal Fixed-bed Reactor for Process Integration. *Computer Aided Chemical Engineering*, *50*, 307–312. https://doi.org/10.1016/B978-0-323-88506-5.50049-8

Bizon, K., Continillo, G., Mancaruso, E., Merola, S. S., and Vaglieco, B. M. (2010). POD-based analysis of combustion images in optically accessible engines. *Combustion and Flame*, *157*(4), 632–640. https://doi.org/https://doi.org/10.1016/j.combustflame.2009.12.013

Bizon, K., Continillo, G., Mancaruso, E., and Vaglieco, B. M. (2011). Reconstruction of in-cylinder pressure in a diesel engine from vibration signal using a RBF neural network model. *SAE Technical Papers*. https://doi.org/10.4271/2011-24-0161

Bizon, K., Continillo, G., Russo, L., and Smuła, J. (2008). On POD reduced models of tubular reactor with periodic regimes. *Computers and Chemical Engineering*, *32*(6), 1305–1315. https://doi.org/10.1016/j.compchemeng.2007.06.004

Bizon, K., Skrzypek-Markiewicz, K., Continillo, G., Bizon, K., Skrzypek-Markiewicz, K., and Continillo, G. (2020). Enhancement of the Direct Synthesis of Dimethyl Ether (DME) from Synthesis Gas by Macro- and Microstructuring of the Catalytic Bed. *Catalysts 2020, Vol. 10, 10*(8). https://doi.org/10.3390/CATAL10080852

Blasio, C. De, Salierno, G., and Özdenkci, K. (2022). Lignocellulosic Biomass for Biofuels Production, an Integrated Approach. *Enzymes in the Valorization of Waste*, 23–49. https://doi.org/10.1201/9781003187714-2

Brands, B., Davydov, D., Mergheim, J., and Steinmann, P. (2019). Reduced-Order Modelling and Homogenisation in Magneto-Mechanics: A Numerical Comparison of Established Hyper-Reduction Methods. *Mathematical and Computational Applications*, *24*(1), 20. https://doi.org/10.3390/mca24010020

Bremer, J., Goyal, P., Feng, L., Benner, P., and Sundmacher, K. (2017a). POD-DEIM for efficient reduction of a dynamic 2D catalytic reactor model. *Computers and Chemical Engineering*, *106*, 777–784. https://doi.org/10.1016/j.compchemeng.2017.02.032

Bremer, J., Goyal, P., Feng, L., Benner, P., and Sundmacher, K. (2017b). POD-DEIM for efficient reduction of a dynamic 2D catalytic reactor model. *Computers and Chemical Engineering*, *106*, 777–784. https://doi.org/10.1016/j.compchemeng.2017.02.032

Brooks, K., Balakotaiah, V., and Luss, D. (1988). Effect of natural convection on spontaneous combustion of coal stockpiles. *AIChE Journal*, *34*(3), 353–365. https://doi.org/10.1002/aic.690340302

Brooks, K., and Glasser, D. (1986). A simplified model of spontaneous combustion in coal stockpiles. *Fuel*, *65*(8), 1035–1041. https://doi.org/10.1016/0016-2361(86)90163-8

Browne, C. A. (1929). *The Spontaneous Combustion of Hay*. https://doi.org/10.22004/AG.ECON.157950

Brunton, S. L., and Kutz, J. N. (2021). 7 Data-driven methods for reduced-order modeling. In P. Benner, S. Grivet-Talocia, A. Quarteroni, G. Rozza, W. Schilders, and L. M. Silveira (Eds.), *Volume 2: Snapshot-Based Methods and Algorithms* (pp. 307–344). De Gruyter. https://doi.org/doi:10.1515/9783110671490-007

Brunton, S. L., Proctor, J. L., and Kutz, J. N. (2016). Discovering governing equations from data by sparse identification of nonlinear dynamical systems. *Proceedings of the National Academy of Sciences*, *113*(15), 3932–3937. https://doi.org/10.1073/pnas.1517384113

Canuto, C., Hussaini, M., Quarteroni, A., and Zang, T. (2006). *Spectral Methods: Fundamentals in Single Domains* (Vol. 23). https://doi.org/10.1007/978-3-540-30726-6

Carberry, J. J. . (2001). *Chemical and catalytic reaction engineering*. 642. https://books.google.com/books/about/Chemical_and_Catalytic_Reaction_Engineer.html?hl=itandid=arJLaKa4yDQC

Carras, J. N., and Young, B. C. (1994). Self-heating of coal and related materials: Models, application and test methods. *Progress in Energy and Combustion Science*, *20*(1), 1–15. https://doi.org/10.1016/0360-1285(94)90004-3

Chaturantabut, S., and Sorensen, D. C. (2010). Nonlinear model reduction via discrete empirical interpolation. *SIAM Journal on Scientific Computing*, *32*(5), 2737–2764. https://doi.org/10.1137/090766498

Chauhan, P. R., Kaushik, S. C., and Tyagi, S. K. (2022). A review on thermal performance enhancement of green cooling system using different adsorbent/refrigerant pairs. *Energy Conversion and Management: X*, *14*, 100225. https://doi.org/10.1016/J.ECMX.2022.100225

Chinesta, F., and Ladevèze, P. (2020). Proper generalized decomposition. *Snapshot-Based Methods and Algorithms*, 97–138. https://doi.org/10.1515/9783110671490-003

Colelli, L., Dell'Aversano, S., Bassano, C., Vanga, G., Gallucci, K., and Vilardi, G. (2026). Liquid e-fuels for a sustainable future: A comprehensive review of production, regulation, and technological innovation. *Energy Conversion and Management*, *347*, 120529. https://doi.org/10.1016/J.ENCONMAN.2025.120529

Continillo, G. (1995). *Dynamic Behaviour of Distributed-Parameter Models of Exothermic Reactions with Heat Transfer Effects*. 437–454.

Continillo, G., Faraoni, V., Maffettone, P. L., and Crescitelli, S. (2000). Non-linear dynamics of a self-igniting reaction-diffusion system. *Chemical Engineering Science*, *55*(2), 303–309. https://doi.org/10.1016/S0009-2509(99)00325-5

Continillo, G., Galiero, G., Maffettone, P. L., and Crescitelli, S. (1996). Characteriation of chaotic dynamics in the spontaneous combustion of coal stockpiles. *Symposium (International) on Combustion*, *26*(1), 1585–1592. https://doi.org/10.1016/S0082-0784(96)80382-1

Costa, A. L. H., and Bagajewicz, M. J. (2019). 110th Anniversary: On the Departure from Heuristics and Simplified Models toward Globally Optimal Design of Process Equipment. *Industrial and Engineering Chemistry Research*, *58*(40), 18684–18702. https://doi.org/10.1021/ACS.IECR.9B02611

Cutillo, Enrico A., Bizon, K., and Continillo, G. (2023). Assessing the Effect of Variable Ambient Temperature on the Self-ignition of a Reaction-diffusion System Employing a Reduced Order Modelling Methodology. *Chemical Engineering Transactions*, *99*, 523–528. https://doi.org/10.3303/CET2399088

Cutillo, E.A., Mancusi, E., Bizon, K., Bareschino, P., and Continillo, G. (2023). A Reduced Order Model for the Prediction of the Dynamics of a Methane Reactor. In *Computer Aided Chemical Engineering* (Vol. 52). https://doi.org/10.1016/B978-0-443-15274-0.50191-8

Cutillo, E. A., Neupauer, K., Continillo, G., and Bizon, K. (2025). *Enhancing carbon dioxide adsorption in a hybrid fixed bed via structuring and thermal management: a numerical study*. *1*. https://doi.org/10.17632/GK8TYZKC6D.1

Cutillo, Enrico Alberto, Petito, G., Bizon, K., and Continillo, G. (2023). Analysis of an innovative sampling strategy based on k-means clustering algorithm for POD and POD-DEIM reduced order models of a 2-D reaction-diffusion system. *Combustion Theory and Modelling*, *27*(4), 508–535. https://doi.org/10.1080/13647830.2023.2174451

Danckwerts, P. V. (1953). Continuous flow systems: Distribution of residence times. *Chemical Engineering Science*, *2*(1), 1–13. https://doi.org/10.1016/0009-2509(53)80001-1

Das, S., Deen, N. G., and Kuipers, J. A. M. (2018). Multiscale modeling of fixed-bed reactors with porous (open-cell foam) non-spherical particles: Hydrodynamics. *Chemical Engineering Journal*, *334*, 741–759. https://doi.org/10.1016/J.CEJ.2017.10.047

Dell'Aversano, S., Villante, C., Gallucci, K., Vanga, G., and Di Giuliano, A. (2024). E-Fuels: A Comprehensive Review of the Most Promising Technological Alternatives towards an Energy Transition. *Energies 2024, Vol. 17, Page 3995*, *17*(16), 3995. https://doi.org/10.3390/EN17163995

Demir, H., Mobedi, M., and Ülkü, S. (2010). The use of metal piece additives to enhance heat transfer rate through an unconsolidated adsorbent bed. *International Journal of Refrigeration*, *33*(4), 714–720. https://doi.org/10.1016/J.IJREFRIG.2009.12.032

Dixon, A. G. (1996). An improved equation for the overall heat transfer coefficient in packed beds. *Chemical Engineering and Processing: Process Intensification*, *35*(5), 323–331. https://doi.org/10.1016/0255-2701(96)80012-2

Dixon, A. G. (2012). Fixed bed catalytic reactor modelling—the radial heat transfer problem. *The Canadian Journal of Chemical Engineering*, *90*(3), 507–527. https://doi.org/https://doi.org/10.1002/cjce.21630

Dixon, A. G. (2017). Local transport and reaction rates in a fixed bed reactor tube: Endothermic steam methane reforming. *Chemical Engineering Science*, *168*, 156–177. https://doi.org/10.1016/J.CES.2017.04.039

Dixon, A. G., Nijemeisland, M., and Stitt, E. H. (2006). Packed Tubular Reactor Modeling and Catalyst Design using Computational Fluid Dynamics. *Advances in Chemical Engineering*, *31*, 307–389. https://doi.org/10.1016/S0065-2377(06)31005-8

Dones, I., Skogestad, S., and Preisig, H. A. (2011). Application of Balanced Truncation to Nonlinear Systems. *Industrial and Engineering Chemistry Research*, *50*(17), 10093–10101. https://doi.org/10.1021/IE200706D

Eglajs, V., and Audze, P. (1977). New approach to the design of multifactor experiments. *Problems of Dynamics and Strengths. Riga. Zinatne Publishing House.*, *35*, 104–107.

Elnashaie, S. S. E. H., and Elshishini, S. S. (1994). Modelling, Simulation and Optimization of Industrial Fixed Bed Catalytic Reactors. *Modelling, Simulation and Optimization of Industrial Fixed Bed Catalytic Reactors*, 1–510. https://doi.org/https://doi.org/10.1201/9780203746769

Eppinger, T., Jurtz, N., Kraume, M., Eppinger, T., Jurtz, N., and Kraume, M. (2021). Influence of Macroscopic Wall Structures on the Fluid Flow and Heat Transfer in Fixed Bed Reactors with Small Tube to Particle Diameter Ratio. *Processes 2021, Vol. 9, 9*(4). https://doi.org/10.3390/PR9040689

Eppinger, T., Wehinger, G. D., Jurtz, N., Aglave, R., and Kraume, M. (2016). A numerical optimization study on the catalytic dry reforming of methane in a spatially resolved fixed-bed reactor. *Chemical Engineering Research and Design*, *115*, 374–381. https://doi.org/10.1016/J.CHERD.2016.09.007

Ergun, S., and Orning, A. A. (1949). Fluid Flow through Randomly Packed Columns and Fluidized Beds. *Industrial and Engineering Chemistry*, *41*(6), 1179–1184. https://doi.org/10.1021/IE50474A011',

Esener, A. A., Roels, J. A., and Kossen, N. W. F. (1981). The influence of temperature on the maximum specific growth rate of Klebsiella pneumoniae. *Biotechnology and Bioengineering*, *23*(6), 1401–1405. https://doi.org/10.1002/BIT.260230620

F. D. Martins, V., Miguel, C. V., Gonçalves, J. C., Rodrigues, A. E., and Madeira, L. M. (2022). Modeling of a cyclic sorption–desorption unit for continuous high temperature CO2 capture from flue gas. *Chemical Engineering Journal*, *434*, 134704. https://doi.org/10.1016/J.CEJ.2022.134704

Fernandez-Anez, N., Castells-Somoza, B., Amez-Arenillas, I., and Garcia-Torrent, J. (2021). Self-ignition tendency of solid fuels: A gas emissions approach for early detection. *Journal of Loss Prevention in the Process Industries*, *71*(March), 104501. https://doi.org/10.1016/j.jlp.2021.104501

Finlayson, B. A. (2013). Chapter 1: Introduction. In *The Method of Weighted Residuals and Variational Principles* (pp. 3–14). Society for Industrial and Applied Mathematics. https://doi.org/doi:10.1137/1.9781611973242.ch1

Forrester, A., Sobester, A., and Keane, A. (2008a). *Engineering Design Via Surrogate Modelling: A Practical Guide*. https://doi.org/10.1002/9780470770801

Forrester, A., Sobester, A., and Keane, A. (2008b). Sampling Plans. In *Engineering Design via Surrogate Modelling: a practical guide* (pp. 1–31). John Wiley and Sons, Ltd. https://doi.org/https://doi.org/10.1002/9780470770801.ch1

Frank-Kamenetskii, D. A. (1955). Diffusion and heat exchange in chemical kinetics. *Diffusion and Heat Exchange in Chemical Kinetics*, first published (in Russian) in 1947, available in English since 1955, Last edition from Princeton University Press, 2016, ISBN 9780691626932

Froment, G., Bischoff, K., and De Wilde, J. (2011). Chapter 11: Fixed Bed Catalytic Reactors. *Chemical Reactor Analysis and Design*, 505–584. https://www.wiley.com/en-us/Chemical+Reactor+Analysis+and+Design%2C+3rd+Edition-p-9780470565414

FROMENT, G. F. (1972). *Analysis and Design of Fixed Bed Catalytic Reactors*. 1–55. https://doi.org/10.1021/BA-1972-0109.CH001

Fu, S., Chen, H., Watt, S. D., Sidhu, H. S., Luangwilai, T., and Shu, Y. (2021). Numerical Study on Effect of Ambient Humidity Variation on Self-heating and Spontaneous Ignition of the Eucalyptus Bark Pile. *Fire Technology*, *57*(4), 1803–1825. https://doi.org/10.1007/s10694-021-01091-4

Galerkin, B. G. (1915). Rods and plates. Series occurring in various questions concerning the elastic equilibrium of rods and plates. *Engineers Bulletin (Vestnik Inzhenerov)*, *19*, 897–908.

Ghalandari, V., Hashemipour, H., and Bagheri, H. (2020). Experimental and modeling investigation of adsorption equilibrium of CH4, CO2, and N2 on activated carbon and prediction of multi-component adsorption equilibrium. *Fluid Phase Equilibria*, *508*. https://doi.org/10.1016/j.fluid.2019.112433

Ghasemi, M., and Gildin, E. (2016). Model order reduction in porous media flow simulation using quadratic bilinear formulation. *Computational Geosciences*, *20*(3), 723–735. https://doi.org/10.1007/s10596-015-9529-0

Grande, C. A., Kaiser, A., and Andreassen, K. A. (2023). Methane storage in metal-organic framework HKUST-1 with enhanced heat management using 3D printed metal lattices. *Chemical Engineering Research and Design*, *192*, 362–370. https://doi.org/10.1016/J.CHERD.2023.03.003

Gray, P., Griffiths, J. F., and Moule, R. J. (1974). B. Thermokinetic oscillations. Thermokinetic oscillations accompanying propane oxidation. *Faraday Symposia of the Chemical Society*, *9*(0), 103–113. https://doi.org/10.1039/FS9740900103

Gray, P., and Lee, P. R. (1967). *Oxidation and Combustion Reviews* (C. F. H. Tipper, Ed.; Vol. 2, p. 1). Elsevier.

Grossmann, C., Roos, H.-G., and Stynes, M. (2007). Numerical Treatment of Partial Differential Equations. *Numerical Treatment of Partial Differential Equations*. https://doi.org/10.1007/978-3-540-71584-9

Grünewald, M., and Agar, D. W. (2004). Enhanced catalyst performance using integrated structured functionalities. *Chemical Engineering Science*, *59*(22–23), 5519–5526. https://doi.org/10.1016/j.ces.2004.07.072

Gu, C. (2011). QLMOR: A projection-based nonlinear model order reduction approach using quadratic-linear representation of nonlinear systems. *IEEE Transactions on Computer-Aided Design of Integrated Circuits and Systems*, *30*(9), 1307–1320. https://doi.org/10.1109/TCAD.2011.2142184

Guffanti, S., Visconti, C. G., and Groppi, G. (2020). Model Analysis of the Effects of Active Phase Distribution at the Pellet Scale in Catalytic Reactors for the Direct Dimethyl Ether Synthesis. *Industrial and Engineering Chemistry Research*, *59*(32), 14252–14266. https://doi.org/10.1021/acs.iecr.0c01938

Guffanti, S., Visconti, C. G., van Kampen, J., Boon, J., and Groppi, G. (2021). Reactor modelling and design for sorption enhanced dimethyl ether synthesis. *Chemical Engineering Journal*, *404*(May 2020). https://doi.org/10.1016/j.cej.2020.126573

Gunia, M., Ciećko, J., and Bizon, K. (2023). Assessment of the bed macrostructuring and thermal waves impact on carbon dioxide adsorption efficiency in a hybrid fixed-bed reactor. *Chemical and Process Engineering: New Frontiers*, *44*(No 3 (24th Polish Conference of Chemical and Process Engineering, 13-16 June 2023, Szczecin, Poland. Guest editor: Prof. Rafał Rakoczy and 8th European Process Intensification Conference, 31.05–2.06.2023, Warsaw, Poland.)), e13–e13. https://doi.org/10.24425/cpe.2023.144699

Guyon, I., Gunn, S., Ben-Hur, A., and Dror, G. (2004). Result Analysis of the NIPS 2003 Feature Selection Challenge. In L. Saul, Y. Weiss, and L. Bottou (Eds.), *Advances in Neural Information Processing Systems* (Vol. 17). MIT Press. https://proceedings.neurips.cc/paper_files/paper/2004/file/5e751896e527c862bf67251a474b3819-Paper.pdf

Hamerly, G., and Drake, J. (2015). Accelerating lloyd's algorithm for k–means clustering. *Partitional Clustering Algorithms*, 41–78. https://doi.org/10.1007/978-3-319-09259-1_2/FIGURES/10

Hayer, F., Bakhtiary-Davijany, H., Myrstad, R., Holmen, A., Pfeifer, P., and Venvik, H. J. (2011). Synthesis of dimethyl ether from syngas in a microchannel reactor—Simulation and experimental study. *Chemical Engineering Journal*, *167*(2–3), 610–615. https://doi.org/10.1016/J.CEJ.2010.09.080

Hefti, M., Marx, D., Joss, L., and Mazzotti, M. (2015). Adsorption equilibrium of binary mixtures of carbon dioxide and nitrogen on zeolites ZSM-5 and 13X. *Microporous and Mesoporous Materials*, *215*, 215–228. https://doi.org/https://doi.org/10.1016/j.micromeso.2015.05.044

Hoff, M. J. H. van't. (1884). Etudes de dynamique chimique. *Recueil Des Travaux Chimiques Des Pays-Bas*, *3*(10), 333–336. https://doi.org/10.1002/RECL.18840031003

Holmes, P., Lumley, J. L., and Berkooz, G. (1996). Turbulence, Coherent Structures, Dynamical Systems and Symmetry. In *Cambridge Monographs on Mechanics*. Cambridge University Press. https://doi.org/DOI: 10.1017/CBO9780511622700

Hotelling, H. (1933). Analysis of a complex of statistical variables into principal components. *Journal of Educational Psychology*, *24*(6), 417–441. https://doi.org/10.1037/H0071325

IEA (2023), The Role of E-fuels in Decarbonising Transport, IEA, Paris https://www.iea.org/reports/the-role-of-e-fuels-in-decarbonising-transport, Licence: CC BY 4.0. (n.d.).

Jackson, R. (1977). *Transport in Porous Catalysts* (Vol. 4). Elsevier Scientific Publishing Company.

Jain, S., Tiso, P., Rutzmoser, J. B., and Rixen, D. J. (2017). A quadratic manifold for model order reduction of nonlinear structural dynamics. *Computers and Structures*, *188*, 80–94. https://doi.org/10.1016/j.compstruc.2017.04.005

Jarczewski, S., Barańska, K., Drozdek, M., Michalik, M., Bizon, K., and Kuśtrowski, P. (2022). Energy-balanced and effective adsorption-catalytic multilayer bed system for removal of volatile organic compounds. *Chemical Engineering Journal*, *431*, 133388. https://doi.org/10.1016/J.CEJ.2021.133388

Jones, D. R. (1974). Convective effects in enclosed, exothermically reacting gases. *International Journal of Heat and Mass Transfer*, *17*(1), 11–21. https://doi.org/10.1016/0017-9310(74)90034-9

Kaganov, S. A. (1967). The stability of the steady — state solutions in the theory of thermal explosions: PMM vol. 31, no. 6, 1967, pp. 1081–1085. *Journal of Applied Mathematics and Mechanics*, *31*(6), 1083–1087. https://doi.org/10.1016/0021-8928(67)90214-6

Kammerer, S., Borho, I., Jung, J., and Schmidt, M. S. (2022). Review: CO2 capturing methods of the last two decades. *International Journal of Environmental Science and Technology 2022 20:7*, *20*(7), 8087–8104. https://doi.org/10.1007/S13762-022-04680-0

Kapoor, R., Ghosh, P., Kumar, M., and Vijay, V. K. (2019). Evaluation of biogas upgrading technologies and future perspectives: a review. *Environmental Science and Pollution Research 2019 26:12*, *26*(12), 11631–11661. https://doi.org/10.1007/S11356-019-04767-1

Karhunen, K. (1946). Über lineare Methoden in der Wahrscheinlichkeitsrechnung. *Annals of Academic Science Fennicae, Series A1 Mathematics and Physics*, *37*, 3–79.

Keenan, J. H., and Keyes, F. G. (1936). Thermodynamic properties of steam : including data for the liquid and solid phases. In *(No Title)*. J. Wiley Chapman and Hall. https://cir.nii.ac.jp/crid/1970304959884089361

Kiewidt, L. (2017). *Solid sponges as support for heterogeneous catalysts in gas-phase reactions*. https://api.semanticscholar.org/CorpusID:102628098

Kosambi, D. D. (1943). Statistics in function space. *Journal of Indian Mathematical Society*, *7*, 76–88.

Koytsoumpa, E. I., Magiri – Skouloudi, D., Karellas, S., and Kakaras, E. (2021). Bioenergy with carbon capture and utilization: A review on the potential deployment towards a European circular bioeconomy. *Renewable and Sustainable Energy Reviews*, *152*, 111641. https://doi.org/https://doi.org/10.1016/j.rser.2021.111641

Kramer, B., Peherstorfer, B., and Willcox, K. E. (2024). Learning Nonlinear Reduced Models from Data with Operator Inference. *Annual Review of Fluid Mechanics*, *56*(Volume 56, 2024), 521–548. https://doi.org/10.1146/ANNUREV-FLUID-121021-025220/CITE/REFWORKS

Kramer, B., and Willcox, K. E. (2019). Nonlinear model order reduction via lifting transformations and proper orthogonal decomposition. *AIAA Journal*, *57*(6), 2297–2307. https://doi.org/10.2514/1.J057791

Krath, E. H., Houchens, B. C., Marian, D. V., Pol, S. U., and Westergaard, C. (2021). Multivariate Design and Optimization of the AeroMINE Internal Turbine Blade. *AIAA Propulsion and Energy Forum, 2021*. https://doi.org/10.2514/6.2021-3368

Krigstin, S., and Wetzel, S. (2016). A review of mechanisms responsible for changes to stored woody biomass fuels. *Fuel*, *175*, 75–86. https://doi.org/10.1016/j.fuel.2016.02.014

Kumar, K., and Kostina, E. (2024). Optimal Parameter Estimation Techniques for Complex Nonlinear Systems. *Differential Equations and Dynamical Systems*. https://doi.org/10.1007/s12591-024-00688-9

Kutz, J. N. (2023). Machine Learning Methods for Reduced Order Modeling. *Lecture Notes in Mathematics*, *2328*, 201–228. https://doi.org/10.1007/978-3-031-29563-8_4/FIGURES/7

Kuznetsov, Y. (1998). Elements of applied bifurcation theory. In *Elements of Applied Bifurcation Theory*. Springer New York. https://doi.org/10.1007/978-0-387-22710-8_8

Kwan, T. H., and Yao, Q. (2022). Numerical analysis on the geometrical design of liquid cooling based carbon capture by adsorption for higher thermal efficiency. *International Communications in Heat and Mass Transfer*, *139*, 106459. https://doi.org/10.1016/J.ICHEATMASSTRANSFER.2022.106459

Lass, O., and Volkwein, S. (2014). Adaptive POD basis computation for parametrized nonlinear systems using optimal snapshot location. *Computational Optimization and Applications*, *58*(3), 645–677. https://doi.org/10.1007/S10589-014-9646-Z/TABLES/6

Leonzio, G., and Shah, N. (2024). Recent advancements and challenges in carbon capture, utilization and storage. *Current Opinion in Green and Sustainable Chemistry*, *46*, 100895. https://doi.org/10.1016/J.COGSC.2024.100895

Levenspiel, O. (1998). Chemical Reaction Engineering, 3rd Edition | Wiley. *New York*, 704. https://www.wiley.com/en-us/Chemical+Reaction+Engineering%2C+3rd+Edition-p-9780471254249

Lian, Y., Deng, S., Li, S., Guo, Z., Zhao, L., and Yuan, X. (2019). Numerical analysis on CO2 capture process of temperature swing adsorption (TSA): Optimization of reactor geometry. *International Journal of Greenhouse Gas Control*, *85*, 187–198. https://doi.org/10.1016/J.IJGGC.2019.03.029

Lin, X., Li, X., Liu, H., Boczkaj, G., Cao, Y., and Wang, C. (2024). A review on carbon storage via mineral carbonation: Bibliometric analysis, research advances, challenges, and perspectives. *Separation and Purification Technology*, *338*, 126558. https://doi.org/10.1016/J.SEPPUR.2024.126558

Liu, H., Ong, Y.-S., and Cai, J. (2018). A survey of adaptive sampling for global metamodeling in support of simulation-based complex engineering design. *Structural and Multidisciplinary Optimization*, *57*(1), 393–416. https://doi.org/10.1007/s00158-017-1739-8

Lloyd, S. P. (1982). Least Squares Quantization in PCM. *IEEE Transactions on Information Theory*, *28*(2), 129–137. https://doi.org/10.1109/TIT.1982.1056489

Loéve, M. (1945). Fonctions aléatoires du second ordre. *Comptes Rendus de l'Académie Des Sciences*, *220*(469).

Lohrer, C., Schmidt, M., and Krause, U. (2005). A study on the influence of liquid water and water vapour on the self-ignition of lignite coal-experiments and numerical simulations. *Journal of Loss Prevention in the Process Industries*, *18*(3), 167–177. https://doi.org/10.1016/j.jlp.2005.03.006

Lu, K., Jin, Y., Chen, Y., Yang, Y., Hou, L., Zhang, Z., Li, Z., and Fu, C. (2019). Review for order reduction based on proper orthogonal decomposition and outlooks of applications in mechanical systems. *Mechanical Systems and Signal Processing*, *123*, 264–297. https://doi.org/https://doi.org/10.1016/j.ymssp.2019.01.018

Luangwilai, T., Sidhu, H., and Nelson, M. (2011). A two dimensional, reaction-diffusion model of compost piles. *The Proceedings of ANZIAM*, *53*, C34–C52. https://doi.org/10.21914/anziamj.v53i0.5083

Luangwilai, T., Sidhu, H. S., and Nelson, M. I. (2013). Biological self-heating in compost piles: A Semenov formulation. *Chemical Engineering Science*, *101*, 533–542. https://doi.org/10.1016/j.ces.2013.07.015

Luangwilai, T., Sidhu, H. S., Nelson, M. I., and Chen, X. D. (2010). Modelling air flow and ambient temperature effects on the biological self-heating of compost piles. *Asia-Pacific Journal of Chemical Engineering*, *5*(4), 609–618. https://doi.org/10.1002/APJ.438

Lucia, D. J., Beran, P. S., and Silva, W. A. (2004). Reduced-order modeling: new approaches for computational physics. *Progress in Aerospace Sciences*, *40*(1–2), 51–117. https://doi.org/10.1016/J.PAEROSCI.2003.12.001

Luyben, W. L. . (2007). *Chemical reactor design and control*. 419. https://books.google.com/books/about/Chemical_Reactor_Design_and_Control.html?id=P-zvB8z3djYC

Malling, G. F., and Thodos, G. (1967). Analogy between mass and heat transfer in beds of spheres: Contributions due to end effects. *International Journal of Heat and Mass Transfer*, *10*(4), 489–498. https://doi.org/10.1016/0017-9310(67)90169-X

Mancusi, E., Acampora, L., Marra, F. S., and Altimari, P. (2015). Hysteresis in autothermal methane reforming over Rh catalysts: Bifurcation analysis. *Chemical Engineering Journal*, *262*, 1052–1064. https://doi.org/10.1016/J.CEJ.2014.10.061

Mancusi, E., Bareschino, P., Brachi, P., Coppola, A., Ruoppolo, G., Urciuolo, M., and Pepe, F. (2021a). Feasibility of an integrated biomass-based CLC combustion and a renewable-energy-based methanol production systems. *Renewable Energy*, *179*, 29–36. https://doi.org/10.1016/j.renene.2021.06.114

Mancusi, E., Bareschino, P., Brachi, P., Coppola, A., Ruoppolo, G., Urciuolo, M., and Pepe, F. (2021b). Feasibility of an integrated biomass-based CLC combustion and a renewable-energy-based methanol production systems. *Renewable Energy*, *179*, 29–36. https://doi.org/10.1016/j.renene.2021.06.114

Mancusi, E., Piso, G., Shah, H. H., Pepe, F., Tregambi, C., and Bareschino, P. (2025). Modelling of a continuous sorption-enhanced methanation process in an adiabatic packed-bed reactor system. *Chemical Engineering Science*, *301*, 120800. https://doi.org/10.1016/J.CES.2024.120800

Mancusi, E., Russo, L., Brasiello, A., Crescitelli, S., and Di Bernardo, M. (2007). Hybrid modeling and dynamics of a controlled reverse flow reactor. *AIChE Journal*, *53*(8), 2084–2096. https://doi.org/10.1002/AIC.11216

Maria, G., and Stefan, D. N. (2010). Variability of operating safety limits with catalyst within a fixed-bed catalytic reactor for vapour-phase nitrobenzene hydrogenation. *Journal of Loss Prevention in the Process Industries*, *23*(1), 112–126. https://doi.org/10.1016/J.JLP.2009.06.007

Matkowsky, B. J., and Sivashinsky, G. I. (1978). Propagation of a Pulsating Reaction Front in Solid Fuel Combustion. *SIAM Journal on Applied Mathematics*, *35*(3), 465–478. https://doi.org/10.1137/0135038

Matray, V., Amlani, F., Feyel, F., and Néron, D. (2024). *A hybrid numerical methodology coupling Reduced Order Modeling and Graph Neural Networks for non-parametric geometries: applications to structural dynamics problems*. https://arxiv.org/abs/2406.02615

McLaughlin, H., Littlefield, A. A., Menefee, M., Kinzer, A., Hull, T., Sovacool, B. K., Bazilian, M. D., Kim, J., and Griffiths, S. (2023a). Carbon capture utilization and storage in review: Sociotechnical implications for a carbon reliant world. *Renewable and Sustainable Energy Reviews*, *177*, 113215. https://doi.org/10.1016/J.RSER.2023.113215

McLaughlin, H., Littlefield, A. A., Menefee, M., Kinzer, A., Hull, T., Sovacool, B. K., Bazilian, M. D., Kim, J., and Griffiths, S. (2023b). Carbon capture utilization and storage in review: Sociotechnical implications for a carbon reliant world. *Renewable and Sustainable Energy Reviews*, *177*, 113215. https://doi.org/10.1016/J.RSER.2023.113215

Mears, D. E. (1971). Diagnostic criteria for heat transport limitations in fixed bed reactors. *Journal of Catalysis*, *20*(2), 127–131. https://doi.org/10.1016/0021-9517(71)90073-X

Mears, D. E. (1976). On Criteria for Axial Dispersion in Nonisothermal Packed-Bed Catalytic Reactors. *Industrial and Engineering Chemistry Fundamentals*, *15*(1), 20–23. https://doi.org/10.1021/I160057A004/ASSET/I160057A004.FP.PNG_V03

Medic Pejic, L., Fernandez Anez, N., García Torrent, J., and Ramírez-Gómez, Á. (2015). Determination of spontaneous combustion of thermally dried sewage sludge. *Journal of Loss Prevention in the Process Industries*, *36*, 352–357. https://doi.org/10.1016/j.jlp.2015.01.013

Mendes, P. A. P., Ribeiro, A. M., Gleichmann, K., Ferreira, A. F. P., and Rodrigues, A. E. (2017). Separation of CO2/N2 on binderless 5A zeolite. *Journal of CO2 Utilization*, *20*, 224–233. https://doi.org/https://doi.org/10.1016/j.jcou.2017.05.003

Merzhanov, A. G., and Shtessel, E. A. (1973). Free Convection And Thermal Explosion In Reactive Systems. *Acta Astronautica*, *18*, 191–199.

Mhadmhan, S., Ngamcharussrivichai, C., Hinchiranan, N., Kuchonthara, P., Li, Y., Wang, S., and Reubroycharoen, P. (2022). Direct biogas upgrading via CO2 methanation to high-quality biomethane over NiMg/CNT-SiO2 fiber catalysts. *Fuel*, *310*, 122289. https://doi.org/10.1016/J.FUEL.2021.122289

Miguel, C. V., Soria, M. A., Mendes, A., and Madeira, L. M. (2017). A sorptive reactor for CO2 capture and conversion to renewable methane. *Chemical Engineering Journal*, *322*, 590–602. https://doi.org/10.1016/J.CEJ.2017.04.024

Miyawaki, N., Fukushima, T., Mizuno, T., Inoue, M., and Takisawa, K. (2021). Effect of wood biomass components on self-heating. *Bioresources and Bioprocessing*, *8*(1), 1–6. https://doi.org/10.1186/S40643-021-00373-7/FIGURES/9

Monazam, E. R., Shadle, L. J., and Shamsi, A. (1998). Spontaneous Combustion of Char Stockpiles. *Energy and Fuels*, *12*(6), 1305–1312. https://doi.org/10.1021/EF980094M

Moore, B. C. (1981). Principal Component Analysis in Linear Systems: Controllability, Observability, and Model Reduction. *IEEE Transactions on Automatic Control*, *26*(1), 17–32. https://doi.org/10.1109/TAC.1981.1102568

Moraga, N. O., Corvalán, F., Escudey, M., Arias, A., and Zambra, C. E. (2009). Unsteady 2D coupled heat and mass transfer in porous media with biological and chemical heat

generations. *International Journal of Heat and Mass Transfer*, *52*(25–26), 5841–5848. https://doi.org/10.1016/J.IJHEATMASSTRANSFER.2009.07.027

Mukherjee, K., Osaro, E., and Colón, Y. J. (2023). Active learning for efficient navigation of multi-component gas adsorption landscapes in a MOF. *Digital Discovery*, *2*(5), 1506–1521. https://doi.org/10.1039/D3DD00106G

Myers, A. L., and Prausnitz, J. M. (1965). Thermodynamics of mixed-gas adsorption. *AIChE Journal*, *11*(1), 121–127. https://doi.org/https://doi.org/10.1002/aic.690110125

Narasingam, A., Siddhamshetty, P., and Sang-Il Kwon, J. (2017). Temporal clustering for order reduction of nonlinear parabolic PDE systems with time-dependent spatial domains: Application to a hydraulic fracturing process. *AIChE Journal*, *63*(9), 3818–3831. https://doi.org/https://doi.org/10.1002/aic.15733

Nguyen, V. B., Tran, S. B. Q., Khan, S. A., Rong, J., and Lou, J. (2020). POD-DEIM model order reduction technique for model predictive control in continuous chemical processing. *Computers and Chemical Engineering*, *133*, 106638. https://doi.org/10.1016/J.COMPCHEMENG.2019.106638

Nicolae, A., and Maria, G. (2007). Sensitivity and risk analysis of an industrial fixed-bed catalytic reactor for benzene oxidation. *Revista de Chimie -Bucharest- Original Edition-*, *58*, 427–435.

Nordon, P. (1979). A model for the self-heating reaction of coal and char. *Fuel*, *58*(6), 456–464. https://doi.org/10.1016/0016-2361(79)90088-7

Partopour, B., and Dixon, A. G. (2017). An integrated workflow for resolved-particle packed bed models with complex particle shapes. *Powder Technology*, *322*, 258–272. https://doi.org/10.1016/J.POWTEC.2017.09.009

Patak, H. N. (1973). *Statistische Untersuchung von Schüttschichten und Simulation der darin auftretenden Dispersion*. ETH Zurich.

Pearson, K. (1901). LIII. On lines and planes of closest fit to systems of points in space. *The London, Edinburgh, and Dublin Philosophical Magazine and Journal of Science*, *2*(11), 559–572. https://doi.org/10.1080/14786440109462720

Peherstorfer, B., and Willcox, K. (2016). Data-driven operator inference for nonintrusive projection-based model reduction. *Computer Methods in Applied Mechanics and Engineering*, *306*, 196–215. https://doi.org/10.1016/J.CMA.2016.03.025

Perry, R. H., and Green, D. W. (1997). Sec. 22: Membrane Separation Processes. In *Perry's Engineers' Handbook*. http://pubs.acs.org/doi/pdf/10.1021/ed027p533.1

Pfeffer, R. (1964). Heat and mass transport in multiparticle systems. *Industrial and Engineering Chemistry Fundamentals*, *3*(4), 380–383. https://doi.org/10.1021/I160012A018/ASSET/I160012A018.FP.PNG_V03

Putranto, A., and Chen, X. D. (2017). A new model to predict diffusive self-heating during composting incorporating the reaction engineering approach (REA) framework. *Bioresource Technology*, *232*, 211–221. https://doi.org/10.1016/j.biortech.2017.01.065

Qian, E., Kramer, B., Peherstorfer, B., and Willcox, K. (2020). Lift and Learn: Physics-informed machine learning for large-scale nonlinear dynamical systems. *Physica D: Nonlinear Phenomena*, *406*, 132401. https://doi.org/10.1016/J.PHYSD.2020.132401

Ray, Y. C., Jiang, T. S., and Wen, C. Y. (1987). Particle attrition phenomena in a fluidized bed. *Powder Technology*, *49*(3), 193–206. https://doi.org/10.1016/0032-5910(87)80128-6

Restuccia, F., Fernandez-Anez, N., and Rein, G. (2019). Experimental measurement of particle size effects on the self-heating ignition of biomass piles: Homogeneous samples of dust and pellets. *Fuel*, *256*, 115838. https://doi.org/10.1016/J.FUEL.2019.115838

Rönsch, S., Schneider, J., Matthischke, S., Schlüter, M., Götz, M., Lefebvre, J., Prabhakaran, P., and Bajohr, S. (2016a). Review on methanation - From fundamentals to current projects. *Fuel*, *166*, 276–296. https://doi.org/10.1016/j.fuel.2015.10.111

Rönsch, S., Schneider, J., Matthischke, S., Schlüter, M., Götz, M., Lefebvre, J., Prabhakaran, P., and Bajohr, S. (2016b). Review on methanation - From fundamentals to current projects. *Fuel*, *166*, 276–296. https://doi.org/10.1016/j.fuel.2015.10.111

Russo, L., Adrover, A., Continillo, G., Crescitelli, S., and Giona, M. (2000). Dynamic behavior of a reaction/diffusion system: Wavelet-like collocations and approximate inertial manifolds. *International Conference on Control of Oscillations and Chaos, Proceedings*, (2), 356–359. https://doi.org/10.1109/COC.2000.873990

Saha, B. B., Uddin, K., Pal, A., and Thu, K. (2019). Emerging sorption pairs for heat pump applications: an overview. *JMST Advances 2019 1:1*, *1*(1), 161–180. https://doi.org/10.1007/S42791-019-0010-4

Sahyoun, S., and Djouadi, S. (2013a). Local Proper Orthogonal Decomposition based on space vectors clustering. *2013 3rd International Conference on Systems and Control, ICSC 2013*, 665–670. https://doi.org/10.1109/ICoSC.2013.6750930

Sahyoun, S., and Djouadi, S. (2013b). Local Proper Orthogonal Decomposition based on space vectors clustering. *2013 3rd International Conference on Systems and Control, ICSC 2013*, 665–670. https://doi.org/10.1109/ICoSC.2013.6750930

Salinger, A. G., Aris, R., and Derby, J. J. (1994). Modeling the spontaneous ignition of coal stockpiles. *AIChE Journal*, *40*(6), 991–1004. https://doi.org/10.1002/AIC.690400610

Sánchez-Contador, M., Ateka, A., Ibáñez, M., Bilbao, J., and Aguayo, A. T. (2019). Influence of the operating conditions on the behavior and deactivation of a CuO-ZnO-ZrO2@SAPO-11 core-shell-like catalyst in the direct synthesis of DME. *Renewable Energy*, *138*, 585–597. https://doi.org/10.1016/J.RENENE.2019.01.093

Sansana, J., Joswiak, M. N., Castillo, I., Wang, Z., Rendall, R., Chiang, L. H., and Reis, M. S. (2021). Recent trends on hybrid modeling for Industry 4.0. *Computers and Chemical Engineering*, *151*, 107365. https://doi.org/10.1016/J.COMPCHEMENG.2021.107365

Schmal, D., Duyzer, J. H., and van Heuven, J. W. (1985). A model for the spontaneous heating of coal. *Fuel*, *64*(7), 963–972. https://doi.org/10.1016/0016-2361(85)90152-8

Schmid, P. J. (2010). Dynamic mode decomposition of numerical and experimental data. *Journal of Fluid Mechanics*, *656*, 5–28. https://doi.org/DOI: 10.1017/S0022112010001217

Schnitzlein, K., and Hofmann, H. (1987). An alternative model for catalytic fixed bed reactors. *Chemical Engineering Science*, *42*(11), 2569–2577. https://doi.org/10.1016/0009-2509(87)87008-2

Schwarzer, L., Jensen, P. A., Wedel, S., Glarborg, P., Karlström, O., Holm, J. K., and Dam-Johansen, K. (2021). Self-heating and thermal runaway of biomass – Lab-scale experiments and modeling for conditions resembling power plant mills. *Fuel*, *294*(January). https://doi.org/10.1016/j.fuel.2021.120281

Semenoff, N. (1928). Zur Theorie des Verbrennungsprozesses. *Zeitschrift Für Physik 1928 48:7*, *48*(7), 571–582. https://doi.org/10.1007/BF01340021

Shampine, L. F., and Reichelt, M. W. (2006). The MATLAB ODE Suite. *Https://Doi.Org/10.1137/S1064827594276424*, *18*(1), 1–22. https://doi.org/10.1137/S1064827594276424

Sharma, S., Balestra, S. R. G., Baur, R., Agarwal, U., Zuidema, E., Rigutto, M. S., Calero, S., Vlugt, T. J. H., and Dubbeldam, D. (2023). RUPTURA: simulation code for breakthrough, ideal adsorption solution theory computations, and fitting of isotherm models. *Molecular Simulation*, *49*(9), 893–953. https://doi.org/10.1080/08927022.2023.2202757

Sheng, C., and Yao, C. (2022a). Review on Self-Heating of Biomass Materials: Understanding and Description. *Energy and Fuels*, *36*(2), 731–761. https://doi.org/10.1021/ACS.ENERGYFUELS.1C03369/SUPPL_FILE/EF1C03369_SI_001.PDF

Sheng, C., and Yao, C. (2022b). Review on Self-Heating of Biomass Materials: Understanding and Description. *Energy and Fuels*, *36*(2), 731–761. https://doi.org/10.1021/ACS.ENERGYFUELS.1C03369

Sheng, C., and Yao, C. (2022c). Review on Self-Heating of Biomass Materials: Understanding and Description. *Energy and Fuels*, *36*(2), 731–761. https://doi.org/10.1021/ACS.ENERGYFUELS.1C03369/SUPPL_FILE/EF1C03369_SI_001.PDF

Shtessel', E. A., Pribytkova, K. V., and Zhukova, L. A. (1979). Characteristics of thermal self-ignition under conditions of natural convection. *Combustion, Explosion, and Shock Waves*, *15*(5), 555–562. https://doi.org/10.1007/BF00740583/METRICS

Sirovich, L. (1987). Turbulence and the dynamics of coherent structures. II. Symmetries and transformations. *Quarterly of Applied Mathematics*, *45*(3), 573–582. https://doi.org/10.1090/QAM/910463

Sirovich, L., and Everson, R. (1995). Karhunen–Loève procedure for gappy data. *JOSA A, Vol. 12, Issue 8, Pp. 1657-1664*, *12*(8), 1657–1664. https://doi.org/10.1364/josaa.12.001657

Solsvik, J., and Jakobsen, H. A. (2012a). A Survey of Multicomponent Mass Diffusion Flux Closures for Porous Pellets: Mass and Molar Forms. *Transport in Porous Media*, *93*(1), 99–126. https://doi.org/10.1007/s11242-012-9946-7

Solsvik, J., and Jakobsen, H. A. (2012b). A Survey of Multicomponent Mass Diffusion Flux Closures for Porous Pellets: Mass and Molar Forms. *Transport in Porous Media*, *93*(1), 99–126. https://doi.org/10.1007/S11242-012-9946-7/METRICS

Solsvik, J., Tangen, S., and Jakobsen, H. A. (2012). On the consistent modeling of porous catalyst pellets: Mass and molar formulations. *Industrial and Engineering Chemistry Research*, *51*(24), 8222–8236. https://doi.org/10.1021/IE3007853;WGROUP:STRING:ACHS

Stegehake, C., Riese, J., and Grünewald, M. (2018). Aktueller Stand zur Modellierung von Festbettreaktoren und Möglichkeiten zur experimentellen Validierung. *Chemie Ingenieur Technik*, *90*(11), 1739–1758. https://doi.org/https://doi.org/10.1002/cite.201800130

Stegehake, C., Riese, J., and Grünewald, M. (2019). Modeling and Validating Fixed-Bed Reactors: A State-of-the-Art Review. *ChemBioEng Reviews*, *6*(2), 28–44. https://doi.org/https://doi.org/10.1002/cben.201900002

Stott, J. B. (1960). Influence of Moisture on the Spontaneous Heating of Coal. *Nature 1960 188:4744*, *188*(4744), 54–54. https://doi.org/10.1038/188054a0

Strogatz, S. H. (2018). NONLINEAR DYNAMICS AND CHAOS: With Applications to Physics, Biology, Chemistry, and Engineering. *Nonlinear Dynamics and Chaos: With Applications to Physics, Biology, Chemistry, and Engineering*, 1–513. https://doi.org/10.1201/9780429492563

Strogatz, S. H. (2024). *Nonlinear Dynamics and Chaos: With Applications to Physics, Biology, Chemistry, and Engineering* (3rd, Ed.). Chapman and Hall/CRC. https://doi.org/10.1201/9780429398490

Sukuntee, N., and Chaturantabut, S. (2020). Parametric Nonlinear Model Reduction Using K - Means Clustering for Miscible Flow Simulation. *Journal of Applied Mathematics*, *2020*. https://doi.org/10.1155/2020/3904606

Szyc, M., and Nowak, W. (2014). Operation of an adsorption chiller in different cycle time conditions. *Chemical and Process Engineering*, *Vol. 35*(nr 1), 109–119. https://doi.org/10.2478/CPE-2014-0008

Takeno, T., and Sato, K. (1980). Effect of oxygen diffusion on ignition and extinction of self-heating porous bodies. *Combustion and Flame*, *38*(C), 75–87. https://doi.org/10.1016/0010-2180(80)90038-3

Terragni, Filippo, and Vega, J. M. (2014). Construction of Bifurcation Diagrams Using POD on the Fly. *Https://Doi.Org/10.1137/130927267*, *13*(1), 339–365. https://doi.org/10.1137/130927267

Terragni, F., and Vega, J. M. (2014). Efficient computation of bifurcation diagrams via adaptive ROMs. *Fluid Dynamics Research*, *46*(4), 041412. https://doi.org/10.1088/0169-5983/46/4/041412

Tezzele, M., Demo, N., Mola, A., and Rozza, G. (2022). *An integrated data-driven computational pipeline with model order reduction for industrial and applied mathematics*. 179–200. https://doi.org/10.1007/978-3-030-96173-2_7

Theodoropoulos, C. (2011). Optimisation and Linear Control of Large Scale Nonlinear Systems: A Review and a Suite of Model Reduction-Based Techniques. In A. N. Gorban and D. Roose (Eds.), *Coping with Complexity: Model Reduction and Data Analysis* (pp. 37–61). Springer Berlin Heidelberg.

Thorenz, A., Wietschel, L., Stindt, D., and Tuma, A. (2018). Assessment of agroforestry residue potentials for the bioeconomy in the European Union. *Journal of Cleaner Production*, *176*, 348–359. https://doi.org/10.1016/j.jclepro.2017.12.143

Tursi, A. (2019). A review on biomass: importance, chemistry, classification, and conversion. *Biofuel Research Journal*, *6*(2), 962–979. https://doi.org/10.18331/BRJ2019.6.2.3

Ullmann, M., Prüfert, U., Seidel, J., Ernst, O. G., and Hasse, C. (2014). Application of proper orthogonal decomposition methods in reactive pore diffusion simulations. *The Canadian Journal of Chemical Engineering*, *92*(9), 1552–1560. https://doi.org/https://doi.org/10.1002/cjce.22018

Van Antwerpen, W., Du Toit, C. G., and Rousseau, P. G. (2010). A review of correlations to model the packing structure and effective thermal conductivity in packed beds of mono-sized spherical particles. *Nuclear Engineering and Design*, *240*(7), 1803–1818. https://doi.org/10.1016/j.nucengdes.2010.03.009

Wackernagel, H. (2003). *Multivariate geostatistics: an introduction with applications*. Springer Science and Business Media.

Wakao, N., Kaguei, S., and Funazkri, T. (1979). Effect of fluid dispersion coefficients on particle-to-fluid heat transfer coefficients in packed beds: Correlation of nusselt numbers. *Chemical Engineering Science*, *34*(3), 325–336. https://doi.org/10.1016/0009-2509(79)85064-2

Wehinger, G. D., Klippel, F., and Kraume, M. (2017). Modeling pore processes for particle-resolved CFD simulations of catalytic fixed-bed reactors. *Computers and Chemical Engineering*, *101*, 11–22. https://doi.org/10.1016/J.COMPCHEMENG.2017.02.029

Wei, J., Yao, C., and Sheng, C. (2023). Modelling Self-Heating and Self-Ignition Processes during Biomass Storage. *Energies 2023, Vol. 16, Page 4048*, *16*(10), 4048. https://doi.org/10.3390/EN16104048

Weisz, P. B., and Hicks, J. S. (1962). The behaviour of porous catalyst particles in view of internal mass and heat diffusion effects. *Chemical Engineering Science*, *17*(4), 265–275. https://doi.org/10.1016/0009-2509(62)85005-2

Weisz, P. B., and Prater, C. D. (1954). Interpretation of Measurements in Experimental Catalysis. *Advances in Catalysis*, *6*(C), 143–196. https://doi.org/10.1016/S0360-0564(08)60390-9

Xu, J., and Froment, G. F. (1989a). Methane steam reforming, methanation and water-gas shift: I. Intrinsic kinetics. *AIChE Journal*, *35*(1), 88–96. https://doi.org/10.1002/aic.690350109

Xu, J., and Froment, G. F. (1989b). Methane steam reforming, methanation and water-gas shift: I. Intrinsic kinetics. *AIChE Journal*, *35*(1), 88–96. https://doi.org/10.1002/aic.690350109

Yin, C., Wang, Y., Fang, Q., Chen, X., Yan, H., and Ma, L. (2024). Self-heating and spontaneous ignition of biomass storage piles: Towards a reliable prediction tool. *Renewable Energy*, *228*, 120683. https://doi.org/10.1016/J.RENENE.2024.120683

Young, L. C., and Finlayson, B. A. (1973). Axial Dispersion in Nonisothermal Packed Bed Chemical Reactors. *Industrial and Engineering Chemistry Fundamentals*, *12*(4), 412–422. https://doi.org/10.1021/I160048A004/ASSET/I160048A004.FP.PNG_V03

Yun, J.-H., He, Y., Otero, M., Düren, T., and Seaton, N. A. (2002). Adsorption equilibrium of polar/non-polar mixtures on MCM-41: experiments and Monte Carlo simulation. In F. Rodriguez-Reinoso, B. McEnaney, J. Rouquerol, and K. Unger (Eds.), *Studies in Surface Science and Catalysis* (Vol. 144, pp. 685–692). Elsevier. https://doi.org/https://doi.org/10.1016/S0167-2991(02)80197-5

Zambra, C. E., Moraga, N. O., and Escudey, M. (2011). Heat and mass transfer in unsaturated porous media: Moisture effects in compost piles self-heating. *International Journal of Heat*

and Mass Transfer, *54*(13–14), 2801–2810. https://doi.org/10.1016/j.ijheatmasstransfer.2011.01.031

Zhang, J., Ren, T., Liang, Y., and Wang, Z. (2016a). A review on numerical solutions to self-heating of coal stockpile: Mechanism, theoretical basis, and variable study. *Fuel*, *182*, 80–109. https://doi.org/10.1016/J.FUEL.2016.05.087

Zhang, J., Ren, T., Liang, Y., and Wang, Z. (2016b). A review on numerical solutions to self-heating of coal stockpile: Mechanism, theoretical basis, and variable study. *Fuel*, *182*, 80–109. https://doi.org/10.1016/J.FUEL.2016.05.087

Zhang, X., Witte, J., Schildhauer, T., and Bauer, C. (2020). Life cycle assessment of power-to-gas with biogas as the carbon source. *Sustainable Energy and Fuels*, *4*(3), 1427–1436. https://doi.org/10.1039/C9SE00986H

Zhao, Y., Fan, D., Li, Y., and Yang, F. (2022). Application of machine learning in predicting the adsorption capacity of organic compounds onto biochar and resin. *Environmental Research*, *208*, 112694. https://doi.org/https://doi.org/10.1016/j.envres.2022.112694

Zimmermann, R. T., Bremer, J., and Sundmacher, K. (2022a). Load-flexible fixed-bed reactors by multi-period design optimization. *Chemical Engineering Journal*, *428*(January 2021), 130771. https://doi.org/10.1016/j.cej.2021.130771

Zimmermann, R. T., Bremer, J., and Sundmacher, K. (2022b). Load-flexible fixed-bed reactors by multi-period design optimization. *Chemical Engineering Journal*, *428*(January 2021), 130771. https://doi.org/10.1016/j.cej.2021.130771